

**APPLIED
COMPUTATIONAL
ELECTROMAGNETICS
SOCIETY
JOURNAL**

September 2018
Vol. 33 No. 9
ISSN 1054-4887

The ACES Journal is abstracted in INSPEC, in Engineering Index, DTIC, Science Citation Index Expanded, the Research Alert, and to Current Contents/Engineering, Computing & Technology.

The illustrations on the front cover have been obtained from the research groups at the Department of Electrical Engineering, The University of Mississippi.

THE APPLIED COMPUTATIONAL ELECTROMAGNETICS SOCIETY

<http://aces-society.org>

EDITORS-IN-CHIEF

Atef Elsherbeni

Colorado School of Mines, EE Dept.
Golden, CO 80401, USA

Sami Barmada

University of Pisa, ESE Dept.
56122 Pisa, Italy

ASSOCIATE EDITORS-IN-CHIEF: REGULAR PAPERS

Mohammed Hadi

Kuwait University, EE Dept.
Safat, Kuwait

Antonio Musolino

University of Pisa
56126 Pisa, Italy

Marco Arjona López

La Laguna Institute of Technology
Torreon, Coahuila 27266, Mexico

Alistair Duffy

De Montfort University
Leicester, UK

Abdul A. Arkadan

Colorado School of Mines, EE Dept.
Golden, CO 80401, USA

Paolo Mezzanotte

University of Perugia
I-06125 Perugia, Italy

Wenxing Li

Harbin Engineering University
Harbin 150001, China

Salvatore Campione

Sandia National Laboratories
Albuquerque, NM 87185, USA

Luca Di Rienzo

Politecnico di Milano
20133 Milano, Italy

Maokun Li

Tsinghua University
Beijing 100084, China

Wei-Chung Weng

National Chi Nan University, EE Dept.
Puli, Nantou 54561, Taiwan

Rocco Rizzo

University of Pisa
56123 Pisa, Italy

Mauro Parise

University Campus Bio-Medico of Rome
00128 Rome, Italy

Alessandro Formisano

Seconda Università di Napoli
81031 CE, Italy

Lei Zhao

Jiangsu Normal University
Jiangsu 221116, China

Yingsong Li

Harbin Engineering University
Harbin 150001, China

Piotr Gas

AGH University of Science and Technology
30-059 Krakow, Poland

Sima Noghianian

University of North Dakota
Grand Forks, ND 58202, USA

ASSOCIATE EDITORS-IN-CHIEF: EXPRESS PAPERS

Lijun Jiang

University of Hong Kong, EEE Dept.
Hong, Kong

Steve J. Weiss

US Army Research Laboratory
Adelphi Laboratory Center (RDRL-SER-M)
Adelphi, MD 20783, USA

Amedeo Capozzoli

Univerita di Napoli Federico II, DIETI
I-80125 Napoli, Italy

Shinichiro Ohnuki

Nihon University
Tokyo, Japan

Jiming Song

Iowa State University, ECE Dept.
Ames, IA 50011, USA

Yu Mao Wu

Fudan University
Shanghai 200433, China

Kubilay Sertel

The Ohio State University
Columbus, OH 43210, USA

Maokun Li

Tsinghua University, EE Dept.
Beijing 100084, China

EDITORIAL ASSISTANTS

Matthew J. Inman

University of Mississippi, EE Dept.
University, MS 38677, USA

Shanell Lopez

Colorado School of Mines, EE Dept.
Golden, CO 80401, USA

EMERITUS EDITORS-IN-CHIEF

Duncan C. Baker

EE Dept. U. of Pretoria
0002 Pretoria, South Africa

Allen Glisson

University of Mississippi, EE Dept.
University, MS 38677, USA

Ahmed Kishk

Concordia University, ECS Dept.
Montreal, QC H3G 1M8, Canada

Robert M. Bevensee

Box 812
Alamo, CA 94507-0516, USA

Ozlem Kilic

Catholic University of America
Washington, DC 20064, USA

David E. Stein

USAF Scientific Advisory Board
Washington, DC 20330, USA

EMERITUS ASSOCIATE EDITORS-IN-CHIEF

Yasushi Kanai
Niigata Inst. of Technology
Kashiwazaki, Japan

Levent Gurel
Bilkent University
Ankara, Turkey

Erdem Topsakal
Mississippi State University, EE Dept.
Mississippi State, MS 39762, USA

Mohamed Abouzahra
MIT Lincoln Laboratory
Lexington, MA, USA

Sami Barmada
University of Pisa, ESE Dept.
56122 Pisa, Italy

Alexander Yakovlev
University of Mississippi, EE Dept.
University, MS 38677, USA

Ozlem Kilic
Catholic University of America
Washington, DC 20064, USA

Fan Yang
Tsinghua University, EE Dept.
Beijing 100084, China

EMERITUS EDITORIAL ASSISTANTS

Khaled ElMaghoub
Trimble Navigation/MIT
Boston, MA 02125, USA

Anne Graham
University of Mississippi, EE Dept.
University, MS 38677, USA

Christina Bonnington
University of Mississippi, EE Dept.
University, MS 38677, USA

Mohamed Al Sharkawy
Arab Academy for Science and Technology, ECE Dept.
Alexandria, Egypt

SEPTEMBER 2018 REVIEWERS: REGULAR PAPERS

Shahid Ahmed
Rezaul Azim
David Chen
Fangyuan Chen
Qian Ding
Pasquale Dottorato
Ondrej Franek
Evgeni Frishman
Michael Johnson
Arkom Kaewrawang
Kun-Chou Lee
Wang-Sang Lee
Haiwen Liu
Franklin Manene
Omid Manoochehri
Antonino Musolino
Roberto Ovando

Francoise Paladian
Mark Panitz
M. Periyasamy
Andrew Peterson
Konstantinos Prokopidis
C.J. Reddy
Qiang Ren
Rachid Saadane
Srikumar Sandeep
Wei Song
Chalasan Subba Rao
Christopher Trueman
Jiangong Wei
Wei-Chung Weng
Qi Wu
Xingqiu Yuan
Xiaoyan Zhang

SEPTEMBER 2018 REVIEWERS: EXPRESS PAPERS

Fangyuan Chen
George Kyriacou

TABLE OF CONTENTS – REGULAR PAPERS

A Finite Difference Time Domain Method for Passive Intermodulation Analysis of Nonlinear Metal-Metal Contact
Tuanjie Li, Wangmin Zhai, Xiangyang Li, Xiaofei Ma, and Jie Jiang 935

SSD Accelerated Parallel Out-of-Core Higher-Order Method of Moments and Its Large Applications
Zhongchao Lin, Sheng Zuo, Xunwang Zhao, Yu Zhang, and Weijun Wu..... 943

Design Optimization of Electromagnetic Devices using an Improved Quantum inspired Particle Swarm Optimizer
Obaid U. Rehman, Shanshan Tu, Sadaqat U. Rehman, Shafiullah Khan, and Shiyong Yang 951

An Efficient Method to Study Shielding Effectiveness of Rectangular Enclosure with Wire Penetration
Pu-Yu Hu and Xiao-Ying Sun..... 957

Robustness Evaluation of Split Ring Resonator Antenna System for Wireless Brain Care in Semi-Anatomical Ellipsoid Head Model
Shubin Ma, Leena Ukkonen, Lauri Sydänheimo, and Toni Björninen 966

Multiple Human Targets Detection and Localization Using Leaky Coaxial Cable Sensing Technique
Qiao Guan, Hongmin Lu, Chongchong Chen, and Chuanxia He 973

Conformal Load-Bearing Antenna Structure for MIMO Applications
David L. Zeppettella and Mohammad Ali 979

Wideband Dual-polarized Vivaldi Antenna with Gain Enhancement
Huanhuan Lv, Qiulin Huang, Jianqiang Hou, and Jinlin Liu 990

UWB Gain Enhancement of Horn Antennas Using Miniaturized Frequency Selective Surface
Mehmet A. Belen, Filiz Güneş, Peyman Mahouti, and Aysu Belen 997

A Low-Profile Miniaturized Frequency Selective Surface with Insensitive Polarization
Meiyu Wang, Lei Zhao, Jun Wang, Xinhua Liang, Shengjun Zhang, Yingsong Li, and Wenhua Yu 1003

The Design of a High Gain Dual-Polarized Quad-Ridged Circular Horn Antenna for Wideband EMC Test Applications Bekir Solak, Mustafa Secmen, and Ahmet Tekin	1009
Air Gap Effect on Antenna Characteristics of Slitline and Stripline Dipoles on an Extended Hemispherical Lens Substrate Truong Khang Nguyen and Huy Hung Tran.....	1018
Optimization and Design of Multi-ring Pole Pieces for Small-sized Permanent Magnetic Resonance Imaging Magnet Yi-Yuan Cheng, Tao Hai, Yang-Bing Zheng, Bao-Lei Li, and Ling Xia.....	1026
Loss Analysis of Wideband RF MEMS Shunt Capacitive Switch in T and Π -Match Configurations Santhanam Suganthi, Palavesanadar Thiruvalar Selvan, and Singaravelu Raghavan	1034
Interference Effects of Via Interconnect in Three Layer Printed Circuit Board Avali Ghosh, Sisir Kumar Das, and Annapurna Das	1040

TABLE OF CONTENTS – EXPRESS PAPERS

Data-Driven Arbitrary Polynomial Chaos for Uncertainty Quantification in Filters Osama J. Alkhateeb and Nathan Ida	1048
---	------

A Finite Difference Time Domain Method for Passive Intermodulation Analysis of Nonlinear Metal-Metal Contact

Tuanjie Li¹, Wangmin Zhai¹, Xiangyang Li¹, Xiaofei Ma², and Jie Jiang³

¹ School of Mechano-Electronic Engineering
Xidian University, Xi'an, 710071, China
tjli888@126.com, wang0min@163.com, 1950973447@qq.com

² Xi'an Institute of Space Radio Technology
Xi'an, 710000, China
maxf041600@sina.com

³ Honghe University
Mengzi, 661100, China
jiangjie_uoh@163.com

Abstract — The passive intermodulation (PIM) has gradually become a serious electromagnetic interference in the high-power and high-sensitivity RF/microwave communication system with the existence of the nonlinear metal-to-metal (MM) contacts. This paper proposes a finite difference time domain (FDTD) method for PIM analysis of nonlinear MM contacts. There are two kinds of models, the power series model and the equivalent circuit model, to describe the nonlinear MM contacts. Then the FDTD method is applied to analyze the nonlinear models so that the nonlinear current through the MM contact can be determined. For the microwave transmission devices, the PIM power level can be obtained by fast Fourier transform of the nonlinear current. For the microwave radiation devices such as antennas, the nonlinear currents are taken as a new electromagnetic transmitting source, the far-field scattering and PIM power level can be obtained by the FDTD method. Finally, a comparison between the simulation and experimental results is illustrated to verify the validity of the proposed method.

Index Terms — Equivalent circuit model, metal-to-metal contact, passive intermodulation, power level, power series model, time domain finite difference method.

I. INTRODUCTION

With the development of higher power, wider band, and higher receiving-sensitivity communication systems, the passive intermodulation (PIM) has become a serious problem that cannot be ignored because PIM noise signals will fall into the receiving band [1]. The passive intermodulation products (PIMP) are generated for the inherent nonlinear I-V response curve of passive devices.

When the nonlinear passive devices are excited by two- or multi-carriers, many intermodulation distortion signals are generated in the system. Basically there are two types of passive nonlinearities in communication system: contact nonlinearity and material nonlinearity [2]. The existing researches showed the nonlinear metal-to-metal (MM) contact is one of potential PIM sources in passive devices. Up to now, two mathematical models have been proposed to describe the nonlinear MM contacts. One is the power series model applied to represent the nonlinear I-V response curve of the MM contacts [3, 4]. The other is the equivalent circuit model applied to reveal the PIM power level caused by nonlinear MM contacts [5].

One of the difficulties when trying to locate PIM is that the nonlinearity that gives rise to them does not manifest itself at low input signal levels which is because PIM levels are normally low and at low power levels the PIMP may fall below the thermal noise level. Testing for PIM signal, measuring them and also locating sources can be a tough challenge for test equipment. So it's a more convenient and reasonable method to analyze and predict the PIM power level through the mathematical models to design the microwave devices and high frequency circuits.

The PIM power level of the nonlinear MM contact model is transformed into that of the nonlinear circuit. The harmonic balance method [6], the finite difference time domain (FDTD) method [7] and the large-signal-small-signal analysis method [8] are adopted to solve the nonlinear circuit. For instance, the advanced design system (ADS) is the electronic design software to analyze the I-V response of nonlinear circuits using the harmonic balance method [9]. The FDTD method, as a full wave

analysis, can analyze the current, voltage and electric field strength of nonlinear devices. Since it is a time-domain method, FDTD solutions can cover a wide frequency range with a single simulation run. What's more, FDTD calculates the E and H fields everywhere in the computational domain as they evolve in time. It lends itself to providing animated displays of the electromagnetic field movement through the model. The FDTD method is suitable to analyze the field-circuit coupling PIM problems with multiple carriers, nonlinearity, and wide frequency band characteristics.

This paper proposes a PIM analysis method of MM contacts based on the FDTD method. First, two nonlinear MM contact models are discussed. Second, the FDTD method for PIM analysis of nonlinear MM contacts is developed based on the power series and equivalent circuit models. Finally, two simulation examples are illustrated to verify the validity of the proposed method.

II. NONLINEAR MM CONTACT MODELS

Two mathematical models have been proposed to describe the nonlinear I-V characteristic of MM contacts. And the proposed mathematical models contribute to the calculation of PIM power level.

A. Power series model of nonlinear MM contacts

Assuming the microwave components with nonlinear MM contacts are excited by two signals with frequencies f_1 and f_2 , an expression for its input voltage can be written as:

$$V_{in} = V_1 \cos(2\pi f_1 t) + V_2 \cos(2\pi f_2 t), \quad (1)$$

where V_{in} is the combined input signals, V_1 and V_2 are the amplitudes of two signals.

The transfer function of nonlinear passive components caused by MM contacts may be represented by the polynomial series method [10] as follows.

$$I = \sum_{k=0}^K a_k V_{in}^k, \quad (2)$$

where I is the total nonlinear current, a_k is the coefficient which depends on the nonlinear properties of components.

Substituting Eq. (1) into Eq. (2) and solving for all intermodulation and harmonic components of nonlinear current, we can get the spectrum of I . PIMP are generated at frequencies described by the following equation [11]:

$$f = mf_1 + nf_2, \quad (3)$$

where m and n can be negative as well as positive integers and the sum $|m| + |n|$ defines the order of the PIMP.

Once the I-V response curve of passive components with nonlinear MM contacts is measured, the spectrum of nonlinear current is easily transformed by the fast Fourier transformation (FFT). Then the PIM power level

caused by nonlinear contacts can be calculated with the power series model.

B. Equivalent circuit model of nonlinear MM contacts

Due to the roughness of contact surfaces, the real contact occurs only at some points and the real contact area is much less than the nominal contact area. The MM micro-contact is shown in Fig. 1 [12, 13]. Two main regions including the contact and non-contact zones can be clearly differentiated. To reveal the electrical circuit characteristics of nonlinear MM contacts accurately, Vicente and Hartnagel established the equivalent circuit model [5].

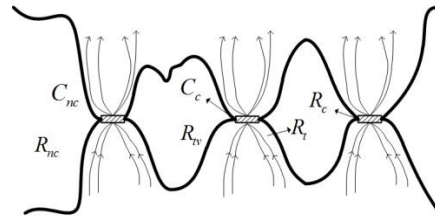


Fig. 1. Micro-schematic diagram of MM contact.

There exist some resistances and capacitances to describe the electrical characteristics of MM contact as shown in Fig. 2.

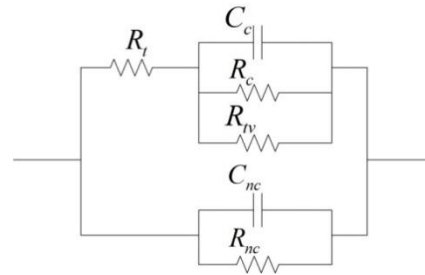


Fig. 2. Equivalent circuit of MM contact.

The constriction resistance R_t result from current constriction effect, it includes Maxwell resistance R_m and Sharvin resistance R_s . It can be calculated as follows:

$$R_t = f(\lambda/r_a) \frac{\rho}{2r_a} + \frac{4\rho\lambda}{3A_r}, \quad (4)$$

where $f(\lambda/r_a) = (1 + 0.83(\lambda/r_a)) / (1 + 1.33(\lambda/r_a))$ is interpolation function which reveals the relationship between R_m and R_s . λ is electron free path for the contact material, ρ is contact metal resistivity, $R_m = \rho/2r_a$ is Maxwell resistance, $R_s = 4\rho\lambda/(3A_r)$ is Sharvin resistance. r_a is the average radius of the asperity contact circle, and A_r is real area of contact. The metal

contact resistance R_c , generates in contact zone because the outer adsorbed film cracks under the action of contact force. The formula for calculating the contact resistance R_c of asperity with a plurality of MM contact spots is as follows:

$$R_c = \frac{\rho}{2r_{MM}N_c} f\left(\frac{r_{MM}}{r_a}\right), \quad (5)$$

where r_{MM} is the equivalent MM contact circle radius of a single asperity and N_c is the quantity of micro asperities, $f(r_{MM}/r_a)$ is a function of the contraction scale considering the current constriction effect and its expression is as follows:

$$f\left(\frac{r_{MM}}{r_a}\right) = 1 - 1.41581\left(\frac{r_{MM}}{r_a}\right) + 0.06322\left(\frac{r_{MM}}{r_a}\right)^2 + 0.15261\left(\frac{r_{MM}}{r_a}\right)^3 + 0.19998\left(\frac{r_{MM}}{r_a}\right)^4. \quad (6)$$

The tunnel resistance R_{tv} and contact capacitance C_c , produce in the zone that the adsorbed film does not crack. The tunnel resistance is based on tunnel current. The tunnel current density is nonlinear and voltage dependent. That is [14]:

$$R_{tv} = \frac{V}{A_s J_{tv}}, \quad (7)$$

$$J_{tv} = \frac{e}{2\pi h s^2} (\varphi_0 e^{-4\pi\sqrt{\frac{2m\varphi_0}{h^2}}s} - (\varphi_0 + eV)e^{-4\pi\sqrt{\frac{2m(\varphi_0 + eV)}{h^2}}s}),$$

where, J_{tv} is the tunnel current density, A_s is the tunnel area, φ_0 is the work function of metal, s is the thickness of barrier in the Fermi level, h is the Planck constant, m is the mass of electron. The tunnel current is the dominant nonlinear source in MM contact [15]. The contact capacitance is $C_c = \varepsilon_r \varepsilon_0 A_n A^* / s$, where ε_r is the relative dielectric constant of the insulating film on the metal, ε_0 is the vacuum dielectric constant, A_n is the nominal contact area and A^* is the dimensionless ratio of real contact area A_r and nominal contact area A_n . The non-contact resistance R_{nc} and the non-contact capacitance C_{nc} exist in the non-contact zone. The non-contact resistance is very large. The non-contact capacitance is $C_{nc} = \varepsilon_0 (A_n - A_r) / d$, where d is the distance of up and down non-contact area.

As shown in Fig. 1, in the contact zone, R_c , R_{tv} and C_c are parallel connection, and they are connected with the constriction resistance R_t in series. In the non-contact zone, R_{nc} and C_{nc} are connected in parallel. The non-contact resistance is very large, and the generation mechanism includes the field emission and the gas

breakdown etc. The non-contact resistance can be regarded as an open circuit when analyzed. It can be seen from Fig. 1 that the circuits in the contact and non-contact zones are connected in parallel. Then, the equivalent circuit model of MM contact can be established as shown in Fig. 2, which can be used to describe the nonlinear I-V response of MM contact.

III. FDTD METHOD FOR PIM ANALYSIS OF NONLINEAR MM CONTACT

A. FDTD method for PIM analysis of power series model

The coaxial connector is as an example to illustrate the FDTD method for simulating the PIM power level of passive components. Coaxial connectors are one kind of common microwave components frequently used in communication system. Also they are the dominant contributors to PIM distortion in high frequency networks. Once the I-V response of connectors is measured, the PIM power level is conveniently calculated by FDTD method without considering the shape of connectors and PIM source location. When the PIM power level is simulated by FDTD, the I-V relationship of connectors can be taken as the I-V relationship of a lumped component in the FDTD meshes.

The lumped element at the node $(i, j, k+1/2)$ and at time $t = (n+1/2)\Delta t$ can be derived by the Maxwell's curl-H equation as follows [4]:

$$E_z^{n+1}\left(i, j, k + \frac{1}{2}\right) = E_z^n\left(i, j, k + \frac{1}{2}\right) + \frac{\Delta t}{\varepsilon_0} (\nabla \times H)_z \Big|_{i, j, k+1/2}^{n+1/2} - \frac{\Delta t}{\varepsilon_0 \Delta x \Delta y} I_{zL}^{n+1/2}\left(i, j, k + \frac{1}{2}\right), \quad (8)$$

where Δt is the time step, ε_0 is the permittivity in vacuum.

The voltage $V_{zL}^{n+1/2}$ across the lumped element can be derived from the electric field E_z at the node $(i, j, k+1/2)$ as follows:

$$V_{zL}^{n+1/2}\left(i, j, k + \frac{1}{2}\right) = \frac{\Delta z}{2} \left[E_z^{n+1}\left(i, j, k + \frac{1}{2}\right) + E_z^n\left(i, j, k + \frac{1}{2}\right) \right]. \quad (9)$$

Substituting Eq. (9) into Eq. (2), the current through the component can be expressed in discrete form as follows:

$$I_{zL}^{n+1}\left(i, j, k + \frac{1}{2}\right) = \sum_{k=0}^K a_k \left(\frac{1}{2} \Delta z (E_z^{n+1}\left(i, j, k + \frac{1}{2}\right) + E_z^n\left(i, j, k + \frac{1}{2}\right)) \right)^k. \quad (10)$$

Substituting Eq. (10) into Eq. (8), we can obtain the passive device's FDTD iterative formula of electric field at the node $(i, j, k+1/2)$ as follows:

$$E_z^{n+1}(i, j, k + \frac{1}{2}) = E_z^n(i, j, k + \frac{1}{2}) + \frac{\Delta t}{\varepsilon_0} (\nabla \times H)_z \Big|_{i, j, k + 1/2}^{n+1/2} - \frac{\Delta t}{\varepsilon_0 \Delta x \Delta y} \sum_{q=0}^w a_q \left(\frac{1}{2} \Delta z (E_z^{n+1}(i, j, k + \frac{1}{2}) + \frac{1}{2} E_z^n(i, j, k + \frac{1}{2})) \right)^q. \quad (11)$$

Then the nonlinear current of passive device is calculated as follows:

$$\begin{cases} J = \sigma E \\ I = J \Delta x \Delta y \end{cases}, \quad (12)$$

where J is the current density, σ is the conductivity.

The obtained time domain current I is transformed to frequency domain by FFT. Finally the PIM power level with frequency of f is calculated as follows:

$$P_f = I_f^2 Z, \quad (13)$$

where I_f is the current amplitude with frequency of f , Z is the resultant impedance of lumped circuit.

B. FDTD method for PIM analysis of equivalent circuit model

The FDTD iterative formula of each element in equivalent circuit model should be derived firstly. Then all FDTD iterative formulas of elements are combined according to the topology of equivalent circuit. If the lumped element is a constriction resistance or contact resistance, the current through the liner resistance is:

$$I_{zL}^{n+1/2}(i, j, k + \frac{1}{2}) = \frac{V_{zL}^{n+1/2}(i, j, k + \frac{1}{2})}{R}, \quad (14)$$

where V_{zL} is the voltage across the lumped element, R is the constriction resistance R_l or contact resistance R_c .

The relationship between V_{zL} and the electric field E_z at the node $(i, j, k+1/2)$ is as shown in Eq. (9).

Substituting Eqs. (9) and (14) into Eq. (8), we can obtain the resistor's FDTD iterative formula of electric field at the node $(i, j, k+1/2)$ as follows:

$$E_z^{n+1}(i, j, k + \frac{1}{2}) = \frac{1 - \frac{\Delta t \Delta z}{2R\varepsilon_0 \Delta x \Delta y}}{1 + \frac{\Delta t \Delta z}{2R\varepsilon_0 \Delta x \Delta y}} E_z^n(i, j, k + \frac{1}{2}) + \frac{\Delta t / \varepsilon_0}{1 + \frac{\Delta t \Delta z}{2R\varepsilon_0 \Delta x \Delta y}} (\nabla \times H)_z \Big|_{i, j, k + 1/2}^{n+1/2}. \quad (15)$$

If the lumped element is a contact capacitance or non-contact capacitance, the current through the capacitance is:

$$I_C = C \frac{dU}{dt}, \quad (16)$$

where C is contact capacitance or non-contact capacitance, U is the voltage across the capacitance.

The relationship between the I and E_z at the node $(i, j, k+1/2)$ is:

$$I_{zL}^{n+1/2}(i, j, k + \frac{1}{2}) = \frac{C \Delta z}{\Delta t} (E_z^{n+1}(i, j, k + \frac{1}{2}) - E_z^n(i, j, k + \frac{1}{2})). \quad (17)$$

Substituting Eq. (17) into Eq. (8), we can obtain the capacity's FDTD iterative formula of electric field at the node $(i, j, k+1/2)$ as follows:

$$E_z^{n+1}(i, j, k + \frac{1}{2}) = E_z^n(i, j, k + \frac{1}{2}) + \frac{\Delta t / \varepsilon_0}{1 + \frac{C \Delta z}{\varepsilon_0 \Delta x \Delta y}} (\nabla \times H)_z \Big|_{i, j, k + 1/2}^{n+1/2}. \quad (18)$$

For the tunnel resistance, the relationship between the voltage and electric field of tunnel resistance at the node $(i, j, k+1/2)$ is as shown in Eq. (9).

Substituting Eqs. (7) and (9) into Eq. (8), we can obtain the tunnel resistance's FDTD iterative formula of electric field at the loaded node as follows:

$$E_z^{n+1}(i, j, k + \frac{1}{2}) = E_z^n(i, j, k + \frac{1}{2}) + \frac{\Delta t}{\varepsilon_0} (\nabla \times H)_z \Big|_{i, j, k + 1/2}^{n+1/2} - J_{nv}^{n+1}(i, j, k + \frac{1}{2}). \quad (19)$$

According to the above analysis of lumped elements, we may calculate the circuit shown in Fig. 2 and obtain the nonlinear current through the MM contact in Matlab software [16].

When the equivalent circuit model reveals the I-V relationship of nonlinear MM contacts in high frequency circuit, the PIM power level can be calculated by Eqs. (12) and (13). However, like as wire mesh reflectors, the PIM sources caused by nonlinear MM contacts can also be modeled in equivalent circuit, and the PIM power level transmitted by mesh reflectors can be simulated by FDTD. Firstly, the nonlinear current through the MM contacts is calculated by FDTD. Secondly, the calculated nonlinear current is regarded as the excitation source to simulate the PIM scattered field of the far field in FDTD method. Finally, the PIM scattered field of the far field is transformed to PIM power level of mesh reflectors by Friis transmission equation.

IV. SIMULATION EXAMPLES AND VERIFICATION

A. PIM simulation of power series model

The nonlinear I-V relationship of a passive device may be described by power series. The nonlinear current through the passive device is calculated by Eq. (11) and

(12). The PIM power level is determined by Eq. (13).

For instance, an N-type coaxial connector, as shown in Fig. 3, is used to evaluate the 3rd-order PIM power level by the proposed method and experimental test. The Rosenberger IM-26P PIM analyzer is used to measure the 3rd-order PIM power level of the coaxial connector which is excited by two signals with the frequencies of 2.62GHz and 2.69GHz in a reflection configuration at 43dBm input power, as shown in Fig. 4. The measured result is -99.8dBm.



Fig. 3. An N-type coaxial connector.

The nonlinear I-V characteristic of the N-type coaxial connector is measured and then expressed by a 3rd order power series as follows:

$$I = -10.081V^3 - 12.9439V^2 + 5.4809V - 9.4723 \times 10^{-4}. \quad (20)$$

Combining Eqs. (11), (12), (13) and (20), the PIM power levels of the coaxial connector calculated by the proposed FDTD method are illustrated in Fig. 5. The 3rd-order PIM power level is -103.2 dBm. The error of the 3rd-order PIM power level is 3.4 dB compared with the test result, which sufficiently shows the accuracy of the proposed FDTD method. It can be concluded that the FDTD method for PIM analysis of MM contacts can address the field-circuit coupling electromagnetism simulation problem, which offers a solution for the PIM analysis of mesh reflectors as described below.



Fig. 4. A measuring system composed of a PIM analyzer, a computer and device under test.

B. PIM analysis of MM contacts in mesh reflectors

The mesh reflector is made of three wires of tungsten (twisted together) with an individual core diameter of 15 microns. The overcoat covering each micro-wire is made of gold (thickness of 0.25 micron) lying over an intermediate layer of nickel (thickness of 0.2 micron). These loose MM contact points of mesh reflectors belonging to contact nonlinearities are important PIM sources. The dimension of the wire mesh sample measured is 1m×1m. The sample shown in Fig. 6 has a nominal tension of 300g/m. The frequencies of the carriers are 2.16GHz and 2.21GHz with a power of 43dBm. The result of a PIM test in the radiated mode indicates the seventh-order PIM value of the sample is -139dBm.

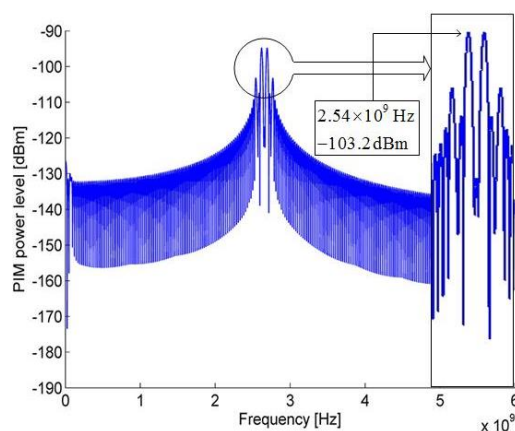


Fig. 5. PIM power levels evaluated by the proposed FDTD method.

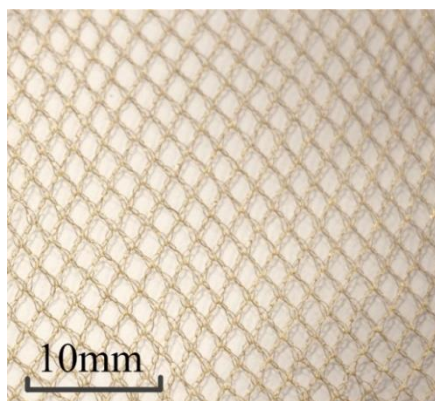


Fig. 6. Wire mesh sample.

There exists the gold-gold contact between two wires. The Poisson's ratio, elastic modulus, hardness, and resistivity of gold are 0.42, 79GPa, 275MPa, and $2.4 \times 10^{-8} \Omega m$, respectively. The mean free path of electrons is 38nm. The parameters of metal surface include the micro-asperity density $\eta = 7 \times 10^{15} / m^2$, the standard deviation of

surface height $\sigma = 5\text{nm}$, the mean of asperity height $z = 8\text{nm}$, and the relative dielectric constant $\epsilon_r = 3$. As shown in Fig. 7, the FEM model of wire mesh unit is established in ANSYS software, and the contact force and actual contact area can be obtained from the simulation result. The parameters are used to calculate R_t , R_c , C_c , C_{nc} , and R_{iv} in the equivalent circuit.

The contact force of single junction of wire mesh is calculated by fractal mechanics [17]. The parameters of circuit elements in the equivalent circuit model are calculated according to the contact force and the material parameters based on the expressions of each element in the equivalent circuit shown in Fig. 2. For example, if the contact force of two wire mesh is $5 \times 10^{-8}\text{N}$, the nonlinear current through the contact junction is calculated by the FDTD method shown in Fig. 8.

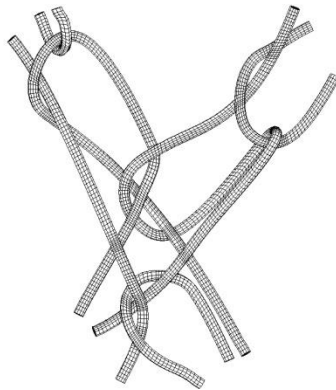


Fig. 7. The FEM model of wire mesh unit.

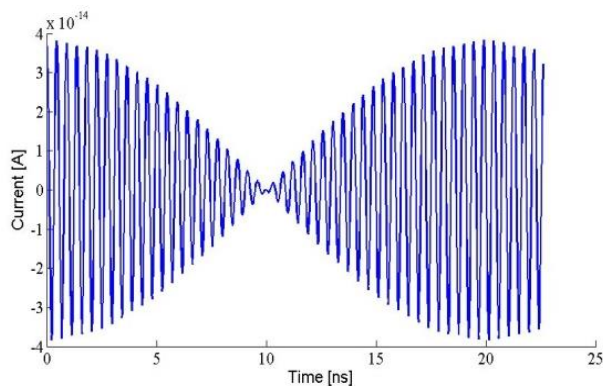


Fig. 8. Nonlinear current through the MM contact point.

Based on the nonlinear currents through contact junction, the far-field PIM power level of wire mesh can be simulated by the FDTD method. The analytical procedure is as follows:

(1) Taking the nonlinear current as a new electromagnetic wave source such as monopole antenna,

the scattered field of the far field can be obtained by the FDTD method.

(2) The calculated time-domain electric field intensity is converted into the frequency-domain one by FFT. In the form of absolute amplitude, the electric field intensity E of the scattered field is $10\lg E$ with a unit of $\text{dB}\mu\text{V}/\text{m}$.

(3) The far-field scattered field is an electric field E with a unit of $\mu\text{V}/\text{m}$, while the resulted analysis is to obtain the PIM power level P_r with a unit of mW. The transformation relationship between E and P_r is as follows [18]:

$$10\lg P_r = 20\lg E - 20\lg f + 10\lg G_r - 77.21, \quad (21)$$

where G_r is the gain of antenna.

(4) Consider all contact junctions of wire mesh in the most serious cases of the independent and phase uncorrelated PIM source, the received PIM power with a unit of dBm is:

$$P_f = 10\lg(P_{r1} + P_{r2} + \dots + P_{rN}), \quad (22)$$

where P_{ri} ($i = 1, 2, \dots, N$) is the PIM power level arising from the i th contact point, N is the total number of contact points in the wire mesh.

As shown in Fig. 6, the mesh reflector is composed of many weaving units, one of which is shown in Fig. 7. Each weaving unit contains 18 contact junctions. According to the direction of force acting on the contact junction, the junctions are classified into two categories, in plane and out of plane. The nonlinear current is calculated through each contact junction. However, there exist millions of contact junctions in mesh reflectors. The computing scale is too huge to calculate. Because the size of the weaving unit is far smaller than the wavelength, the phase difference caused by the positions of contact junctions can be ignored. Hence, the equivalent current of monopole antenna is the sum of same category contact junctions in the weaving unit. As shown in Fig. 9, the nonlinear currents existing in a weaving unit are equivalent to two emitters.

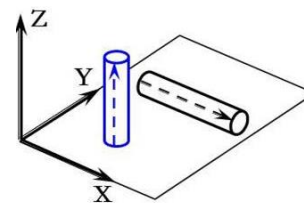


Fig. 9. Two equivalent emitters.

We consider the symmetry of wire mesh and the limitation of computing resources, we divide one quarter of the whole wire mesh into 19 groups and there are 82 weaving units in each group.

According to the above analytical procedure, the scattered field of the nonlinear current shown in Fig. 8 is obtained by Eq. (21), as shown in Fig. 10. The corresponding 7th-order PIM power level is -346.50 dBm. For the $1\text{m}\times 1\text{m}$ wire mesh, the 7th-order PIM power level is -130.77dBm by Eq. (22). The error is 5.9% compared with the test result -139dBm, which sufficiently validate the feasibility of the proposed approach.

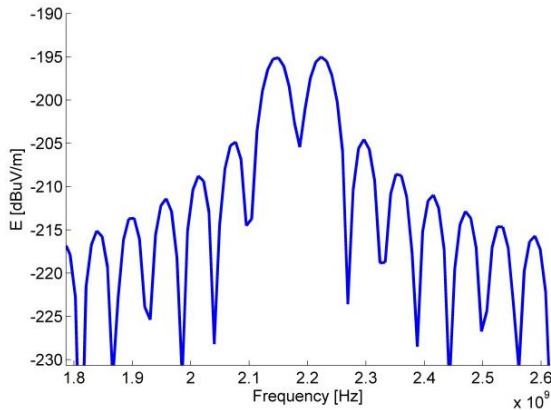


Fig. 10. Frequency-domain scattered field of the MM contact junction.

V. CONCLUSION

(1) The nonlinear MM contact is described by the power series model and equivalent circuit model respectively. The FDTD iterative formulas of two models are derived.

(2) The nonlinear current and PIM power level of power series model are developed by the FDTD method. The simulation and test results show the feasibility of the FDTD method.

(3) The nonlinear MM contact of mesh reflector is represented as the equivalent circuit model. The nonlinear current and PIM power level of wire mesh are solved by the FDTD method. The simulation result indicates the effectiveness of the proposed FDTD method which is suitable for solving the field-circuit coupling PIM problem.

ACKNOWLEDGMENT

The authors thank the anonymous reviewers for their valuable comments on the manuscript. This research was supported by the National Natural Science Foundation of China (Grant No. U1537213 and 61801175).

REFERENCES

- [1] P. L. Lui and A. D. Rawlins, "Passive nonlinearities in antenna systems," *IEE Colloquium on Passive Intermodulation Products in Antennas & Related Structures*, London, pp. 6/1-6/7, 1989.
- [2] F. Arazm and F. A. Benson, "Nonlinearities in metal contacts at microwave frequencies," *IEEE Transactions on Electromagnetic Compatibility*, vol. EMC-22, no. 3, pp. 142-149, 1980.
- [3] J. Jiang, T. J. Li, and Y. C. Liu, "Passive intermodulation scattering analysis of reflector considering contact nonlinearity," *Chinese Journal of Aeronautics*, vol. 26, no. 2, pp. 463-469, 2013.
- [4] W. Sui, D. A. Christensen, and C. H. Durney, "Extending the two-dimensional FDTD method to hybrid electromagnetic systems with active and passive lumped elements," *IEEE Transactions on Microwave Theory and Techniques*, vol. 40, no. 4, pp. 724-730, 1992.
- [5] C. Vicente and H. L. Hartnagel, "Passive-intermodulation analysis between rough rectangular waveguide flanges," *IEEE Transactions on Microwave Theory & Techniques*, vol. 53, no. 8, pp. 2515-2525, 2005.
- [6] F. N. Zghoul, "Analyzing single and multitone nonlinear circuits using a modified harmonic balance method," University of Idaho, Idaho, 2006.
- [7] P. Ciampolini, P. Mezzanotte, L. Roselli, and R. Sorrentino, "Accurate and efficient circuit simulation with lumped-element FDTD technique," *IEEE Transactions on Microwave Theory and Techniques*, vol. 44, no. 12, pp. 2207-2215, 1996.
- [8] H. Jokinen, "Computation of the steady-state solution of nonlinear circuits with time-domain and large-signal-small-signal analysis methods," *Acta Polytechnica Scandinavica Electrical Engineering*, vol. 87, pp. 1-75, 1997.
- [9] B. R. Poole, S. D. Nelson, and S. Langdon, "Advanced electric and magnetic material models for FDTD electromagnetic codes," *Particle Accelerator Conference*, Knoxville, Tennessee, pp. 2639-2680, 2005.
- [10] V. Golikov, S. Hienonen, and P. Vainikainen, "Passive intermodulation distortion measurements in mobile communication antennas," *IEEE 54th Vehicular Technology Conference*, vol. 4, pp. 2623-2625, 2001.
- [11] J. Jiang, T. J. Li, and X. F. Ma, "A nonlinear equivalent circuit method for analysis of passive intermodulation of mesh reflectors," *Chinese Journal of Aeronautics*, vol. 27, no. 4, pp. 924-926, 2014.
- [12] S. A. Maas, *Nonlinear Microwave and RF Circuits*. Artech House Publishers, Norwood, MA, 2003.
- [13] O. Rezvanian, M. A. Zikry, C. Brown, and J. Krim, "Surface roughness, asperity contact and gold RF MEMS switch behavior," *Journal of Micro-mechanics and Microengineering*, vol. 19, no. 10, pp. 2006-2015, 2007.
- [14] J. G. Simmons, "Generalized formula for the electric tunnel effect between similar electrodes separated by a thin insulating film," *Journal of*

Applied Physics, vol. 34, no. 6, pp. 1973-1803, 1963.

- [15] M. Vladimirescu, R. Kwiatkowski, and K. Engel, "Passive intermodulation distortion in RF coaxial electro-mechanical switches for space applications," *The 4th International ESA Multipactor, Corona and Passive Intermodulation Workshop*, Noordwijk, Netherlands, 2003.
- [16] A. Z. Elsherbeni and V. Demir, *The Finite-Difference Time-Domain Method for Electromagnetics with MATLAB Simulations*. 2nd edition, The SciTech Publishing, UK, 2015.
- [17] T. J. Li, J. Jiang, T. T. Shen, and Z. W. Wang, "Analysis of mechanical properties of wire mesh for mesh reflectors by fractal mechanics," *International Journal of Mechanical Sciences*, vol. 92, no. 3, pp. 90-97, 2015.
- [18] S. Y. Liao, "Measurements and computations of electric field intensity and power density," *IEEE Transactions on Instrumentation & Measurement*, vol. 26, no. 1, pp. 53-57, 1977.



intermodulation.

Tuanjie Li received his Ph.D. degree from Xi'an University of Technology in 1999. He now is a Professor and Ph.D. Supervisor at School of Mechano-electronic Engineering, Xidian University. His main research interests are space deployable structures and passive



Wangmin Zhai received his diploma in 2017 from Xidian University. He now is a master of Mechanical Engineering in Xidian University. His current research interests include microwave technique and passive intermodulation.

SSD Accelerated Parallel Out-of-Core Higher-Order Method of Moments and Its Large Applications

Zhongchao Lin¹, Sheng Zuo¹, Xunwang Zhao¹, Yu Zhang¹, and Weijun Wu²

¹ Shaanxi Key Laboratory of Large Scale Electromagnetic Computing
Xidian University, Xi'an, Shaanxi 710071, China
xwzhao@mail.xidian.edu.cn

² Science and Technology on Electromagnetic Compatibility Laboratory
China Ship Development and Design Center, Wuhan 430064, China

Abstract — The performance of the parallel out-of-core Higher-order Method of Moments (HoMoM) is analysed in this paper. The I/O to hard disks significantly affects the performance of the out-of-core algorithm. In order to reduce the I/O time, solid state drives (SSD) with high read and write speeds are utilized. The size of the in-core buffer allocated to each process, IASIZE, is tuned to achieve the optimum performance of the out-of-core algorithm. Numerical results show that the out-of-core algorithm using SSD exhibits better performance than that using SAS hard drives. As a challenging application, a slot array with 2068 elements is analysed using this method.

Index Terms — HoMoM, out-of-core algorithm, SAS, slot arra, SSD.

I. INTRODUCTION

The method of moments (MoM) is a numerically accurate method for solving electromagnetic radiation and scattering problems [1-3]. However, for large complex objects, MoM needs a large amount of physical memory to deal with the dense impedance matrix. The matrix is usually too large to be stored in the main memory (RAM) of the system. One choice is using fast algorithms combined with iterative solvers, such as the multilevel fast multipole algorithm (MLFMA) [4]. However, slow convergence or even divergence often occurs when an object contains complex structures or diverse materials specially dealing with radiation problems. Other choice is using fast direct solver incorporate compression [5] to reduce the amount of data that has to be stored. However, the low rank property of the matrix is indispensable in this method, so it will expire most of time.

An alternative solution is developing an out-of-core computation method using low-cost hard disks instead of memory to store data and using a direct solver like LU factorization for avoiding the slow convergence issue or

the demand for low rank property of the matrix. The out-of-core algorithm is designed according to the multi-layered memory hierarchies of the computation machines, which uses memory as in-core buffer and hard disks to store large matrices. The major task of developing an out-of-core algorithm is adding an efficient hard-disk I/O interface to an in-core algorithm, including both matrix filling and matrix equation solving procedures.

The state of the art high performance computing (HPC) technique can be employed to further improve the capability of the out-of-core algorithm. Due to the overhead of hard-disk I/O, the out-of-core algorithm typically requires more simulation time than its in-core counterpart. To reduce the I/O time, the high-speed SSD are utilized to accelerate the I/O [6, 7]. The radiation of an airborne antenna array is simulated to test the optimum IASIZE. Numerical results show that the performance of the out-of-core algorithm is affected by the value of IASIZE, the simulation time of the algorithm using SSD is reduced compared with that using SAS hard drives, and the developed parallel codes have excellent stability.

II. HIGHER-ORDER METHOD OF MOMENTS

A. Integral equations

The method is based on the solution of Surface Integral Equations (SIEs) [8] in the frequency domain for equivalent electric and magnetic currents over dielectric boundary surfaces and electric currents over perfect electric conductors (PECs). The integral equation employed is the Poggio-Miller-Chang-Harrington-Wu (PMCHW) formulation [9, 10], which is solved in frequency domain for equivalent electric and magnetic currents over dielectric boundary surfaces and electric currents over perfect electric conductors (PECs). The set of integral equations are solved by using MoM, specifically the Galerkin's method.

For the case when one of the two domains sharing a common boundary surface is a PEC, the magnetic currents are equal to zero at the boundary surface and therefore, the PMCHW formulation degenerates into the electric field integral equation (EFIE) [11].

B. Higher-order basis functions

Higher-order polynomials over bilinear quadrilateral patches are used as basis functions over relatively large subdomains [9],

$$F_{ij}(p, s) = \frac{\alpha_s}{|\alpha_p \times \alpha_s|} p^i s^j, \quad (1)$$

$$\alpha_p = \frac{\partial \mathbf{r}(p, s)}{\partial p}, \quad \alpha_s = \frac{\partial \mathbf{r}(p, s)}{\partial s}, \quad (2)$$

where, p and s are local coordinates, i and j are orders of basis functions, and α_p and α_s are covariant unitary vectors. The basis orders can be adapted to deal with nonuniform patches; that is to say for each patch may have completely different order in two directions. A quadrilateral patch is illustrated in Fig. 1.

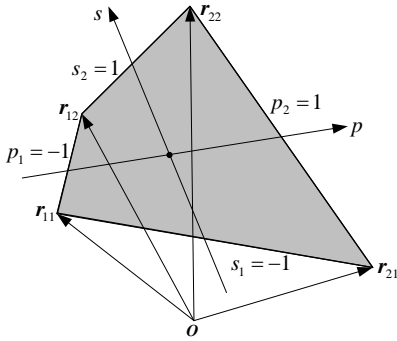


Fig. 1. Bilinear quadrilateral patch defined by four vertices with the position vectors of \mathbf{r}_{11} , \mathbf{r}_{21} , \mathbf{r}_{12} , \mathbf{r}_{22} .

The orders can be adjusted according to the electrical size of the geometric element. The orders become higher as the element size increases. The electrical size of the geometric element can be as large as two wavelengths. Typically, the number of unknowns for the HOBs is reduced by a factor of 5–10 compared with that for traditional piecewise basis functions, e.g., the RWG basis functions [12], and thus the use of HOBs drastically reduces the computational amount and memory requirement. Note that the polynomials can also be used as basis functions for wire structures. In this case, truncated cones are used for geometric modeling.

For bilinear surfaces, the surface current is decomposed into its p and s -components; p and s being the two parametric coordinates of the unit quadrangle, $p, s \in [-1, 1]$. The approximation for the s -component of the electric current is (analogous expressions hold for the

p -component of the electric current and for the magnetic current):

$$\mathbf{J}_s(p, s) = \sum_{i=0}^{N_p} \left[c_{i1} \mathbf{E}_{i1}(p, s) + c_{i2} \mathbf{E}_{i2}(p, s) + \sum_{j=2}^{N_s} a_{ij} \mathbf{P}_{ij}(p, s) \right], \quad (3)$$

$$-1 \leq p \leq 1 \quad -1 \leq s \leq 1, \quad (4)$$

where N_p and N_s are the degrees of the approximations along the coordinates, and a_{ij} , c_{i1} and c_{i2} are the unknown coefficients.

Expression (3) stands for the representation of the current in terms of edge basis functions $\mathbf{E}_i(p, s)$ and interior or patch basis functions $\mathbf{P}_{ij}(p, s)$ which can be compactly expressed as:

$$\mathbf{E}_{ik}(p, s) = \frac{\alpha_s}{|\alpha_p \times \alpha_s|} \begin{cases} p^i N(s), & k=1 \\ p^i N(-s), & k=2 \end{cases}, \quad (5)$$

$$\mathbf{P}_{ij}(p, s) = \frac{\alpha_s}{|\alpha_p \times \alpha_s|} p^i S_j(s), \quad (6)$$

$$N(s) = \frac{1-s}{2}, \quad S_i(s) = \begin{cases} s^{i-1} & i \text{ is even} \\ s^i - s & i \text{ is odd} \end{cases}. \quad (7)$$

Edge basis functions \mathbf{E}_{i2} and patch basis functions \mathbf{P}_{ij} are zero along the first edge ($s=-1$); being \mathbf{E}_{i1} and \mathbf{P}_{ij} zero along the second edge ($s=1$). Thus, the continuity equation can easily be imposed on a common edge.

Figure 2 shows the different polynomial orders in use for the simulation of a microstrip antenna and the orders range from 1 to 4. The orders of the basis functions over the patches that close to the feed are higher than those over other patches, because the current distribution on these patches changes much faster than that over other patches, as shown in the inserted figure inside Fig. 2.

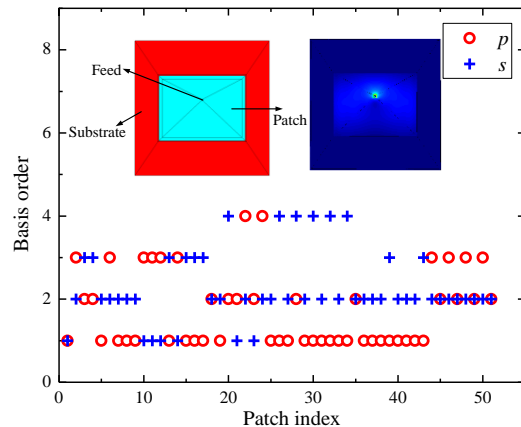


Fig. 2. Basis orders along p and s directions of each quadrilateral patch of the microstrip antenna. The basis orders are adaptive to the patch size along p and s local coordinates.

III. PARALLEL OUT-OF-CORE ALGORITHM

The MoM is based on the solution of Surface Integral Equations (SIEs) [8, 13], and the integral equations are discretized into $N \times N$ dense matrix equations in a general form of:

$$\mathbf{A}\mathbf{X} = \mathbf{B}, \quad (8)$$

where \mathbf{A} is the complex dense matrix, \mathbf{X} is the unknown vector to be solved for, and \mathbf{B} is the excitation vector.

The MoM is parallelized through partitioning the large dense matrix into blocks, which are uniformly distributed to Message Passing Interface (MPI) processes in a block-cyclic manner. As an example, assume that matrix A is divided into 6×6 matrix blocks, and distributed it to six processes in the 2×3 process grid. Figure 3 presents the block-cyclic distribution methodology based on ScaLAPACK math libraries. Two factors, process grid and block size, significantly affects the performance of the parallel algorithm. The reader is referred to [14] for more detailed discussion of the theory.

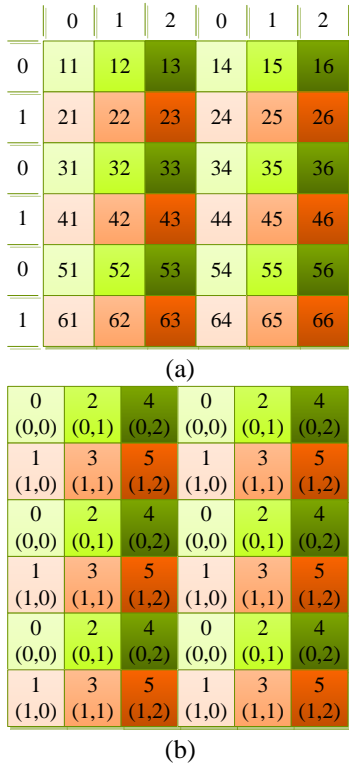


Fig. 3. Block-cyclic distribution scheme: (a) a matrix consisting of 6×6 blocks; (b) rank and coordinates of each process owning the corresponding blocks in (a).

The main idea of designing an out-of-core filling algorithm is to modify the in-core filling algorithm structure and fill a portion of the matrix at a time instead of the whole matrix. The detail procedure is shown in Fig. 4. When performing an out-of-core LU factorization,

each portion of the matrix is read into the RAM and the LU decomposition is started. On completion, the result of the LU factorization of this portion of the matrix is written back to the hard disk (HD). The code then proceeds with the next portion of the matrix until the entire matrix is LU factored. The memory is used as the in-core buffer for the out-of-core algorithm, and the buffer size, IASIZE, determines the number of portions. A larger value of IASIZE will lead to higher CPU usage, and this will result in faster computation. However, reading/writing a large file from/to the hard disk will need more time if the memory is not properly allocated. Therefore, the value of IASIZE is a critical factor for obtaining optimum performance. In the following sections, we investigate how the performance of a cluster is affected by the choice of the IASIZE parameter.

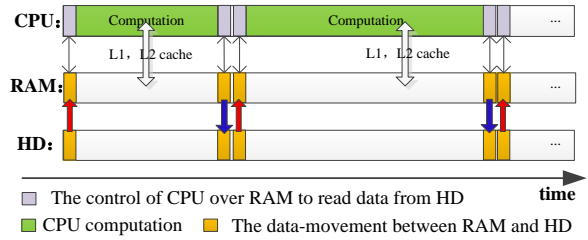


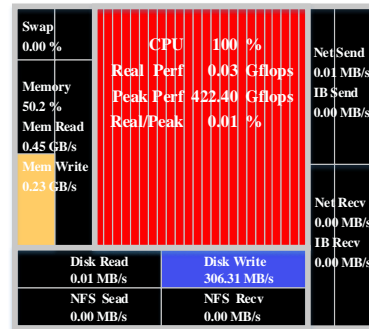
Fig. 4. The out-of-core algorithm.

The left-looking variant of LU factorization, which requires less hard-disk I/O amount than the right-looking variant, is used and the total amount of I/O required is [2, 13]:

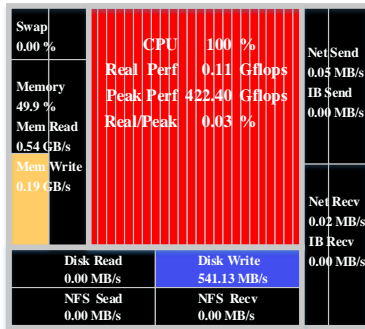
$$\frac{M^3}{2n_b} \left[1 + O\left(\frac{n_b}{M}\right) \right] R + 2M^2 \left[1 + O\left(\frac{n_b}{M}\right) \right] W, \quad (9)$$

where M is the order of the dense matrix, n_b is the matrix block size, and R and W are the time required to read and write one matrix element, respectively.

The read and write speeds of SAS and SSD that be monitored by paramon software [15] are shown in Fig. 5 and Fig. 6. And the read and write speeds of SSD are higher than those of ordinary hard drives, e.g., SAS. Therefore, R and W in (9) can be reduced by using SSD.

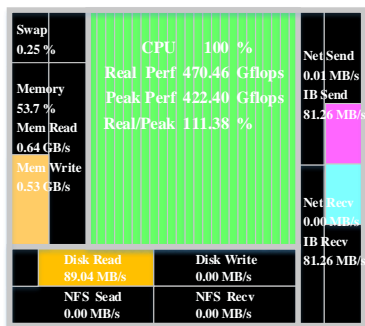


(a)

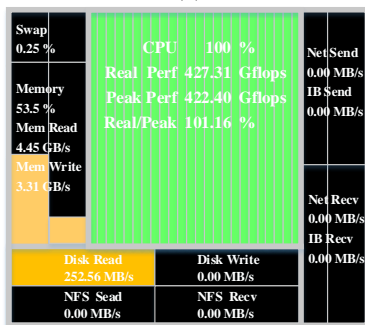


(b)

Fig. 5. Write speeds of hard disk: (a) SAS and (b) SSD.



(a)



(b)

Fig. 6. Read speeds of hard disk: (a) SAS and (b) SSD.

IV. NUMERICAL RESULTS

The computational platform used in this paper is a HPC cluster with 64 computing nodes. Each computing node has two 12-core Intel Xeon E5-2692v2 2.2 GHz EM64T processors (12×256 KB L2 Cache and 30 MB L3 Cache), 64 GB RAM. Among these 64 computing nodes, 32 computing nodes include SSD and each computing node has two 400 GB Intel MLC SSD, and the other 32 computing nodes include SAS hard disks and each computing node has two 600 GB 10K rpm SAS hard disks. The nodes are connected with Infiniband switches.

A. Correctness of the out-of-core algorithm

To validate the accuracy and efficiency of the HoMoM, the monostatic analysis of the NASA almond is considered. The parametric equations that define the geometry of the NASA almond are well known and available in the literature [16]. The Non-Uniform Rationale B-Spline (NURBS) model is shown in Fig. 7. The comparison between the computed result and the measurement for 9.92 GHz is shown in Fig. 8. The results agree with each other very well.

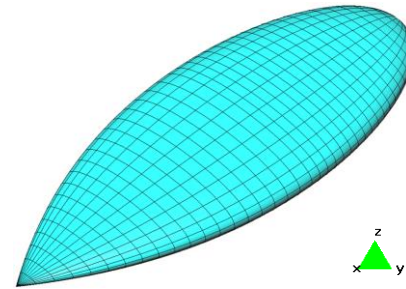
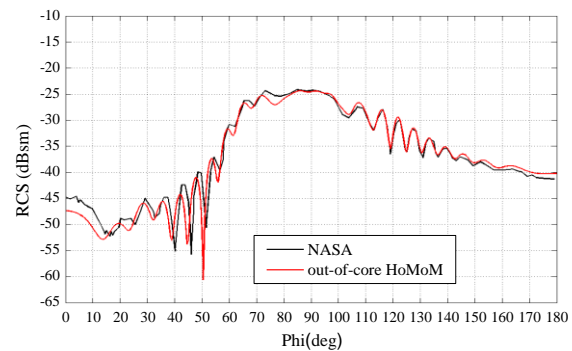


Fig. 7. NASA almond.

Fig. 8. VV polarized monostatic RCS of NASA almond at 9.92 GHz (0° starts from the x -axis in the xoy -plane).

B. IASIZE optimization

To find optimum IASIZE of the out-of-core algorithm using SSD and SAS, we calculate the radiation pattern of an airborne antenna array operating at 440 MHz as shown in Fig. 9. The antenna is a microstrip patch antenna array with 333 units and the material parameters of the substrate are $\epsilon_r = 4.2$ and $\mu_r = 1.0$. The dimensions of the airplane and the array are 54.0 m×53.8 m×10.5 m and 10.0 m×2.5 m×0.018 m, respectively. The number of unknowns (NUN) of the airborne array is 308,371. In all the simulation, the number of computing nodes used is 8, namely 192 CPU cores. The result is given in Fig. 10.

The time using different IASIZE is listed in Table 1. The measured wall time as a function of IASIZE is plotted in Fig. 11 and Fig. 12. From comparison, we can

see that the total time and matrix solving time of the out-of-core algorithm using SSD is evidently reduced compared with that using SAS, and the optimum IASIZE of the out-of-core algorithm using SSD and SAS are 3.0 GB and 2.3 GB, respectively.

Note that the optimum value of the IASIZE will vary slightly for the same platform when using different basis functions, or when running different projects with the same basis function. Also, the optimum value of the IASIZE may not be the same for different computational platforms. It is always advisable for the user to choose the proper IASIZE that 80%~90% of available memory size to avoid using virtual memory of the computer.

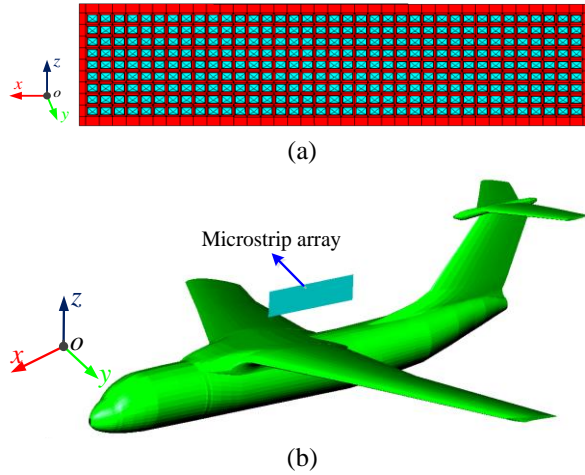


Fig. 9. Airborne array model: (a) the rectangular patch antenna array with 37×9 elements, and (b) the antenna array above an airplane.

Table 1: Wall times when using different IASIZE

IASIZE (GB)	Total Time(s)		LU Time(s)	
	SSD	SAS	SSD	SAS
2.0	31538	35360	25788	29528
2.1	30811	34194	25841	29086
2.2	30920	34047	25938	28960
2.3	31289	33524	26319	28488
2.4	31342	33846	26177	28806
2.5	30254	33961	26068	29705
2.6	30210	35717	25986	30803
2.7	30121	34507	25868	30228
2.8	30272	37172	26000	32715
2.9	30048	37123	25763	32460
3.0	30008	38894	25734	33062
3.1	30414	39344	26100	34177

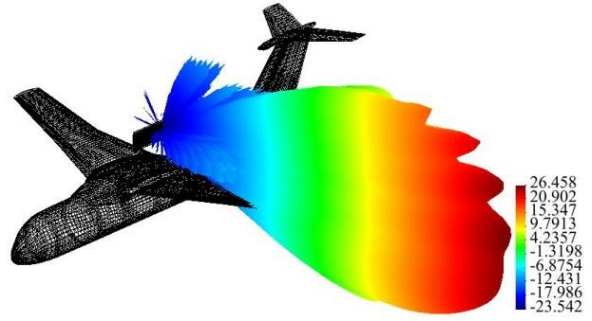


Fig. 10. 3D radiation pattern of the airborne antenna array.

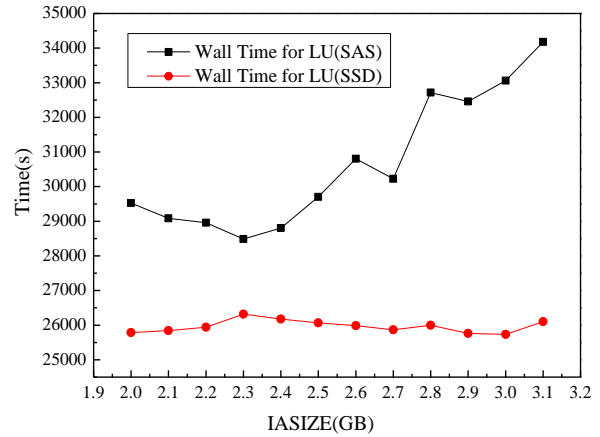


Fig. 11. Wall time for matrix solving when using different IASIZE.

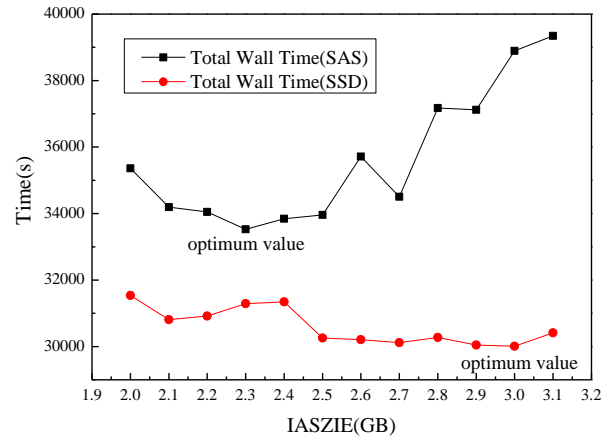


Fig. 12. Total wall time when using different IASIZE.

C. Performance comparison of SSD, SAS and RAM

In this section, we use the optimum IASIZE obtained in previous section to ensure best performance. We present one set of electromagnetic scattering results for demonstrating the performance of the out-of-core algorithm using SSD and SAS. The results of the in-core

algorithm are also given for comparison. The airplane model with dimensions of 11.6 m×7.0 m×2.93 m is shown in Fig. 13. The range of simulation frequency is from 600 MHz to 2.3GHz and the corresponding numbers of unknowns are given in Table 2, where the time for matrix filling and matrix equation solving is listed. The results in Fig. 14 illustrate that the out-of-core algorithm does not result in loss of numerical accuracy of the MoM.

According to Table 2, the performance comparison of the three solving approaches is evaluated and shown in Fig. 15. For the process of matrix filling, it can be seen that the in-core solver is the fastest, followed by the out-of-core solver using SSD, and out-of-core solver using SAS is the slowest. With the number of unknowns increasing, the difference among three approaches is more and more obvious. From the process of matrix equation solving, it can be seen that the performance of out-of-core algorithm using SSD is obviously better than using SAS and very close to the in-core algorithm. Because the matrix equation solving time is much longer than the matrix filling time, it can be concluded that the out-of-core algorithm using SSD achieves nearly the same performance as the in-core algorithm.

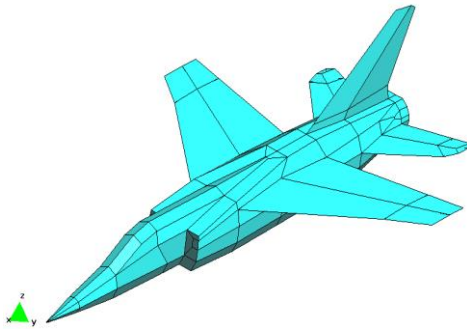


Fig. 13. An airplane model.

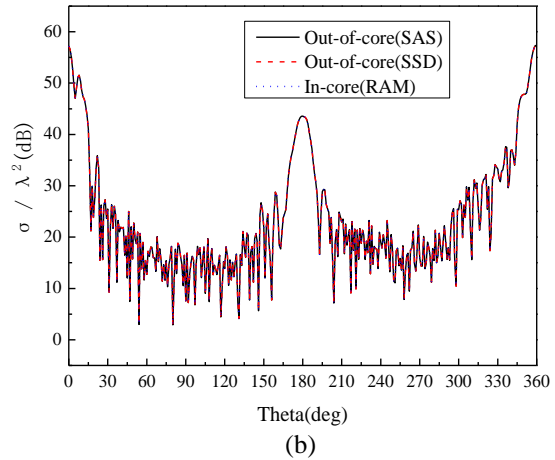
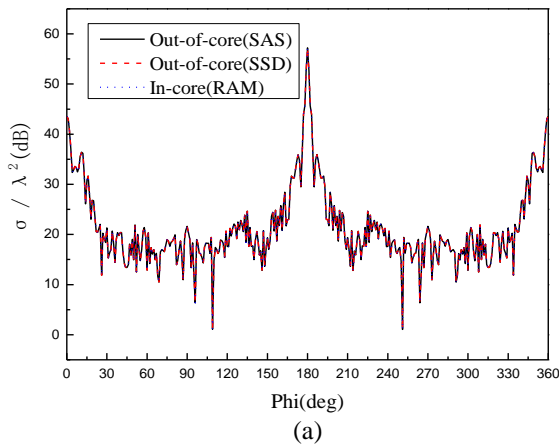


Fig. 14. Bistatic RCS of the airplane at 2 GHz: (a) xoy plane and (b) xoz plane. The plane wave is incident along $-x$ axis.

Table 2: Simulation time for the airplane

NUN	Matrix Filling Time(s)			Matrix Equation Solving Time(s)		
	SSD	SAS	RAM	SSD	SAS	RAM
14482	4.07	4.06	3.66	7.80	7.88	7.45
18689	4.76	4.79	4.16	13.27	13.90	12.75
23293	7.53	7.55	6.66	20.88	21.01	20.39
26943	10.38	10.33	9.11	29.50	29.39	28.47
33415	14.32	14.39	12.60	50.85	49.59	47.41
38964	22.14	22.08	19.35	73.26	72.63	69.28
47411	31.10	31.13	27.35	121.7	120	114.7
53307	32.63	32.55	27.93	165.1	163.4	156.6
61515	41.82	42.09	35.57	262.0	258.1	251.8
67552	46.35	46.53	39.35	325.2	321.9	320.4
76459	62.05	61.28	51.17	450.7	445.6	435.8
84059	74.00	75.69	62.88	610.8	651.3	575.7
93509	95.82	105.2	79.08	828.5	861	783.8
105905	114.1	126.1	94.89	1187	1243	1064
115934	157.2	171.6	116.4	1542	1703	1400
129012	202.6	221.6	146.3	2144	2548	1949
145483	209.7	229.7	175.8	3071	4042	2677
160770	380.1	493.4	228.2	4119	4903	3615

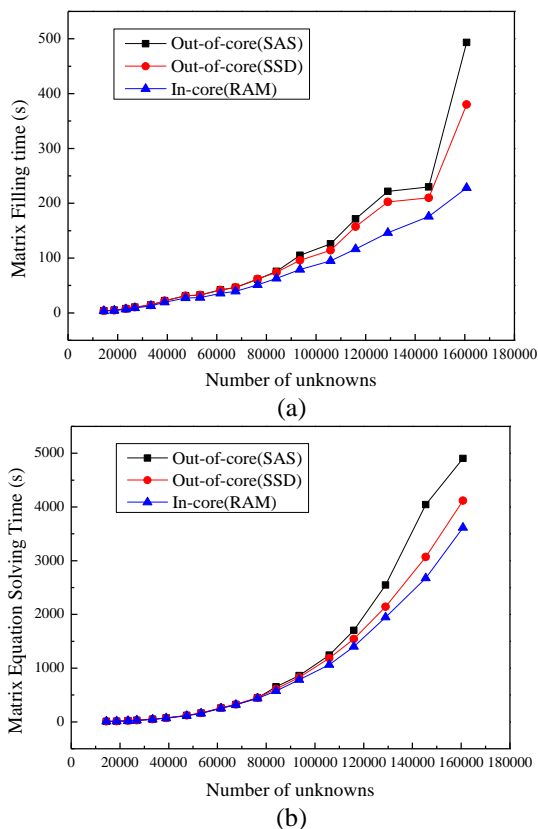


Fig. 15. Performance comparison of the out-of-core algorithm using SSD and SAS and the in-core algorithm: (a) matrix filling time, and (b) matrix equation solving time.

D. Radiation calculation of a waveguide slot antenna

In order to validate the stability of the parallel out-of-core algorithm and further confirm the acceleration performance of SSD, the radiation problem of a waveguide slot antenna operating at 35GHz as shown in Fig. 16 is calculated. The antenna model is composed of 24 waveguide components with a total 2068 slots, for an overall dimension of 66λ by 17λ . The total number of unknowns for this antenna is 660,779, which requires approximately 6.3 TB of storage to analyze the problem using double precision arithmetic. The general computer is unable to provide enough memory, so we use the parallel out-of-core MoM with higher-order basis functions.

The computational parameters are listed in Table 3. We can see that the required memory of this simulation is about 6.3 TB and the provided memory of the CPUs is 2.0 TB, so the parallel out-of-core algorithm has broken the limitation of the memory of the CPUs. Compared with the out-of-core algorithm using SAS hard drives, the acceleration percentage of the out-of-core algorithm using SSD is about 18.66%. The overall speedup does

not seem that good, but the hard disk only affects the time of reading and writing files in the out-of-core algorithm, so it is in line with expectations. Actually, acceleration of 18.66% can also reduce a lot of computing time for very large problem. The SSD is used to accelerate out-of-core algorithm in here is mainly want to reduce the performance loss that caused by reading/writing hard disk compared with the in-core algorithm. The result is given in Fig. 17. This simulation demonstrates that the code is stable and can be used for even more unknowns as long as sufficient hard disk is available.

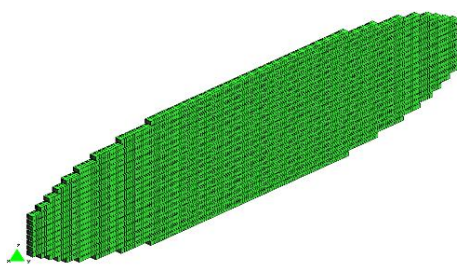


Fig. 16. Waveguide slot antenna model.

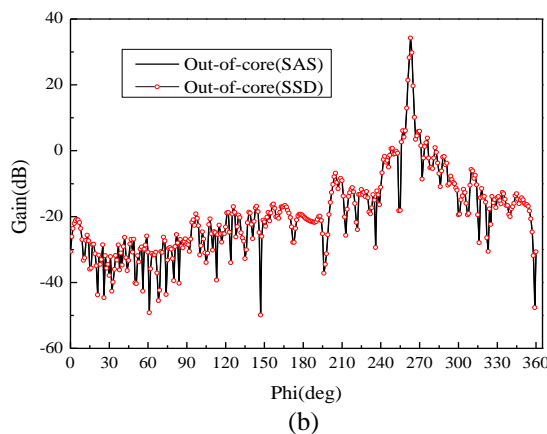
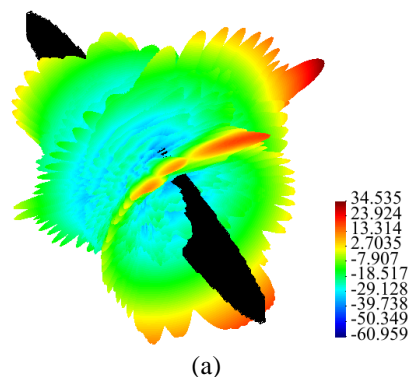


Fig. 17. Radiation patterns of the waveguide slot antenna: (a) 3D radiation pattern, and (b) xoy plane radiation pattern.

Table 3: Computational parameters for the antenna

NUN	Storage (TB)	Computational Resources	Total Wall Time(s)
660,779	6.354	32 nodes with SSD	387,319
		32 nodes with SAS	476,156

V. CONCLUSION

The performance of the parallel out-of-core MoM is improved through SSD, and the sensitivity of the speedup on IASIZE is much less with the SSD than with the SAS disks. The proposed algorithm allows matrices to be written to the hard disk and is no longer limited to the size of the memory. The algorithm does not suffer from slow-convergence issue, and thus it is suitable for accurately modeling large electromagnetic problems including complex structures and diverse materials.

ACKNOWLEDGMENT

This work was supported in part by the National Key Research and Development Program of China under Grant 2017YFB0202102, in part by the China Postdoctoral Science Foundation funded project under Grant 2017M613068, in part by the National Key Research and Development Program of China under Grant 2016YFE0121600, in part by the National High Technology Research and Development Program of China (863 Program) under Grant 2014AA01A302, in part by the Key Research and Development Program of Shandong Province under Grant 2015GGX101028, and in part by the Special Program for Applied Research on Super Computation of the NSFC-Guangdong Joint Fund (the second phase) under Grant No.U1501501.

REFERENCES

- [1] R. F. Harrington, *Field Computation by Moment Methods*. in IEEE Series on Electromagnetic Waves. New York: IEEE, 1993.
- [2] Y. Zhang, Z. Lin, X. Zhao, and T. K. Sarkar, "Performance of a massively parallel higher-order method of moments code using thousands of CPUs and its applications," *IEEE Transactions on Antennas and Propagation*, vol. 62, no. 12, pp. 6317-6324, 2014.
- [3] Z. Lin, Y. Zhang, S. Jiang, X. Zhao, and J. Mo, "Simulation of airborne antenna array layout problems using parallel higher-order MoM," *International Journal of Antennas and Propagation*, vol. 2014, Article ID 985367, 11 pages, 2014.
- [4] S. Velamparambil and W. C. Chew, "Analysis and performance of a distributed memory multilevel fast multipole algorithm," *IEEE Transactions on Antenna and Propagation*, vol. 53, no. 8, pp. 2719-2727, 2005.
- [5] J. Shaeffer, "Direct solve of electrically large integral equations for problem sizes to 1 M unknowns, [J], *IEEE Transactions on Antennas & Propagation*, 56(8):2306-2313, 2008.
- [6] J. No, S.-S. Park, and C.-S. Lim, "ReHypar: A recursive hybrid chunk partitioning method using NAND-flash memory SSD," *The Scientific World Journal*, vol. 2014, Article ID 658161, 9 pages, 2014.
- [7] J. Liu, Y. Lan, J. Liang, Q. Cheng, C.-C. Hung, C. Yin, and J. Sun, "An efficient schema for cloud systems based on SSD cache technology," *Mathematical Problems in Engineering*, vol. 2013, Article ID 109781, 9 pages, 2013.
- [8] P. Ylä-Oijala, M. Taskinen, and S. Järvenpää, "Analysis of surface integral equations in electromagnetic scattering and radiation problems," *Engineering Analysis with Boundary Elements*, vol. 32, no. 3, pp.196-209, 2008.
- [9] Y. Zhang and T. K. Sarkar, *Parallel Solution of Integral Equation Based EM Problems in the Frequency Domain*. Hoboken, NJ: Wiley, 2009.
- [10] R. F. Harrington, "Boundary integral formulations for homogenous material bodies," *Journal of Electromagnetic Waves and Applications*, vol. 3, no. 1, pp. 1-15, 1989.
- [11] John L. Volakis and Kubilay Sertel, *Integral Equation Methods for Electromagnetics*. Raleigh, NC: SciTech Pub., 2012.
- [12] S. M. Rao, D. R. Wilton, and A. W. Glisson, "Electromagnetic scattering by surfaces of arbitrary shape," *IEEE Trans. Antennas Propag.*, vol. 30, pp. 409-418, May 1982.
- [13] Y. Kuo, S. W. Tian, Z. Z. Ying, and T. M. Song, "Electromagnetic analysis for inhomogeneous interconnect and packaging structures based on volume-surface integral equations," *IEEE Transactions on Components, Packaging and Manufacturing Technology*, vol. 3, no. 8, pp. 1364-1371, 2013.
- [14] J. J. Dongarra, S. Hammarling, and D. W. Walker, "Key concepts for parallel out-of-core LU factorization," *Parallel Computing*, vol. 23, pp. 49-70, 1997.
- [15] <http://www.paratera.com/>
- [16] A. Woo, H. Wang, M. Schuh, and M. Sanders, "EM programmer's notebook-benchmark radar targets for the validation of computational electromagnetics programs," *IEEE Antennas and Propagation Magazine*, vol. 35, no. 1, pp. 84-89, Feb. 1993.

Design Optimization of Electromagnetic Devices using an Improved Quantum inspired Particle Swarm Optimizer

Obaid U. Rehman¹, Shanshan Tu^{2,*}, Sadaqat U. Rehman³, Shafiullah Khan⁴,
and Shiyong Yang⁵

¹Department of Electrical Engineering
Sarhad University of Science and IT, Peshawar, Kpk, 25000, Pakistan
obaid.ee@suit.edu.pk

²Faculty of Information Technology
Beijing University of Technology, Beijing, 100124, China
*sstu@bjut.edu.cn

³Department of Electronic Engineering
Tsinghua University, Beijing, 100084, China
enr.sidkhan@gmail.com

⁴Department of Electronics
Islamia College University, Peshawar, Kpk, 25000, Pakistan
shafielectronics@icp.edu.pk

⁵College of Electrical Engineering
Zhejiang University, Hangzhou, Zhejiang, 310027, China
eesyyang@zju.edu.cn

Abstract — Quantum inspired particle swarm optimization (QPSO) is widely used global convergence algorithm for complex design problems. But it may trap into local optima due to premature convergence because of insufficient diversity at the later stage of search process. In this regard, to intensify the QPSO performance in preventing premature convergence to local optima. This work presents a novel QPSO approach using student t probability distribution method with mutation operator on particle with global best position. In addition, a new dynamic control parameter is proposed to tradeoff between the exploration and exploitation searches. The proposed method will intensify the improvement in its convergence behavior and solution quality. The proposed improve QPSO called IQPSO is tested on an electromagnetic design problem namely, the TEAM workshop benchmark problem 22. The experimental results showcase the merit and efficiency of the proposed method.

Index Terms — Electromagnetic design, mutation, particle swarm optimization, quantum mechanics.

I. INTRODUCTION

Most real-world problems in electrical engineering

required optimization of multi objective functions with different constraints. However, the deterministic optimization techniques fail to find the global optimum solutions of these types of problems. In last few years, much efforts have been devoted to investigate and developed new stochastic optimal methods such as, genetic algorithm, differential evolution, tabu search method, cross entropy, simulated annealing, ant colony method and particle swarm optimization method etc., have all been successfully applied to electromagnetic design problems. Some latest optimization techniques for engineering application is reported in the following paragraph.

An adaptive null-steering beamformer based on Bat Algorithm (BA) for Uniform Linear Array (ULA) antennas to suppress the interference was proposed in [1]. In [2], for the design and optimization of radome-enclosed antenna arrays, a fast-numerical optimization technique is proposed to compensate the distortion error of radome-enclosed antenna arrays by correcting amplitude and phase of the excitations. A radiation pattern synthesis of non-uniformly excited planar arrays with the lowest relative side lobe level (SLL) was presented in [3]. A time dependent discrete adjoint

method is applied on electromagnetic problems [4]. A hybrid approach by combining a genetic algorithm (GA) with particle swarm optimization (PSO) is applied to solve electromagnetic problems [5]. An opposition based differential evolution algorithm is used for the optimization of elliptical array antenna [6]. In [7], the comparison of two well-known evolutionary algorithms is presented for the optimization of ships degaussing coil currents.

Though, there is no global optimal algorithm that has been efficient for all engineering design problems. Thus, there is a need to research and develop a global optimization technique for the study of electromagnetic design problems. In this regard, particle swarm optimization method is worthy for further studies.

The particle swarm optimization is an addition to the evolutionary algorithms. It was originated by Kennedy and Eberhart in 1995 [8]. PSO is inspired from the social behavior of bird flocking and school of fishes for hunting their food. PSO is very simple in notion and implementation but it traps into local minima when solving complex optimization problems. This is due to improper balance between exploration and exploitation searches [9]. To address this deficiency in particle swarm optimization, a quantum behaved particle swarm optimization (QPSO) was proposed [10]. Nevertheless, there are still some issues in QPSO that should be solved.

In this context, in this work an improved quantum inspired particle swarm optimization method (IQPSO) has proposed for the study of electromagnetic design problems. In the proposed method, a new mutation strategy with student t probability distribution method is applied on the particle with global best position. In addition, a new parameter updating formulae is proposed to tradeoff between global and local searches.

II. QPSO METHOD

Particle Swarm Optimization (PSO) is a population based stochastic process where individuals are referred to as particles and the population as a swarm. Each particle in a swarm represents a potential solution of the optimization problem. As, the particles move towards the global best point over the multi-dimensional region, the position and velocity are updated according to its own experience and that of its neighbor particles.

Consider a N dimensional design space. The velocity and position of the N^{th} dimension of the i^{th} particle is updated by using the following equations:

$$V_i^n = w \times V_i^n + c_1 \times rand1_i^n \times (pbest_i^n - X_i^n) + c_2 \times rand2_i^n \times (gbest^n - X_i^n), \quad (1)$$

$$X_i^n = X_i^n + V_i^n, \quad (2)$$

where, $V_i^n = (V_i^1, V_i^2, \dots, V_i^N)$ represents the velocity of the particle i . $X_i^n = (X_i^1, X_i^2, \dots, X_i^N)$ is the position of the i^{th} particle. $pbest_i = (pbest_i^1, pbest_i^2, \dots, pbest_i^N)$ is the

personal best position having the best fitness value for the i^{th} particle and $gbest = (gbest^1, gbest^2, \dots, gbest^N)$ is the best position found by the entire population. c_1 and c_2 are the two acceleration coefficients, $rand1_i^n$ and $rand2_i^n$ are the two uniform random numbers within the interval $[0,1]$.

The parameter w represents the inertia weight which is used to balance the local and global searches [11]. The value of w is decreasing linearly according to the following equation:

$$w = w_{max} - t \times (w_{max} - w_{min}) / T, \quad (3)$$

where T represents the maximum number of iterations and t is the current iteration.

QPSO was encouraged by analysis of the convergence of the classic PSO and Quantum model. However, unlike PSO, the position and velocity cannot be determined simultaneously in quantum model according to the uncertainty principle. In the quantum time space context, the quantum state of a particle is represented by a wave function $\Psi(x, t)$. It can be absorbed from the probability of the individuals appearing in position x from probability density function $|\Psi(x, t)|^2$, the form of which depends on the field where the particles lie in.

Sun [10] employed Delta potential model with the center on point $p = (p_1, p_2, \dots, p_D)$ to constraint the quantum particles in PSO in order that the particles can converge to their local p without explosion. In delta potential well, the wave function is given by:

$$\Psi(x) = \frac{1}{\sqrt{L}} \exp(-|p-x|/L), \quad (4)$$

and the probability density function is given by:

$$Q(x) = |\Psi(x)|^2 = \frac{1}{L} \exp(-2|p-x|/L). \quad (5)$$

Applying Monte Carlo method, the position of the particle can be measured as:

$$X_i^n(t) = p \pm 0.5 \times L \times \ln(1/u), \quad (6)$$

where u is a random number with uniform distribution within the range $[0, 1]$ and parameter L as evaluated in [8], is given by the following equation:

$$L(t+1) = 2 \times \beta \times |Mbest - X_i^n(t)|, \quad (7)$$

where β is a contraction expansion coefficient to control the convergence speed of the algorithm. Generally, it is given by:

$$\beta = 0.5 + (1.0 - 0.5) \times (Maxiter - t) / Maxiter. \quad (8)$$

The global point known as Mean best ($Mbest$) of the swarm is defined as the mean of the personal best and global best positions of all particles, and is given by:

$$Mbest = \frac{1}{M} \sum_{n=1}^M pbest_i^n + gbest^n, \quad (9)$$

where M is the size of the population.

Moreover, for the particles to converge to the global best position, the coordinates of each particle are determined by:

$$p = \varphi \times pbest_i^n + (1 - \varphi) \times gbest^n, \quad (10)$$

where φ is a uniform random number within the interval [0, 1].

Thus, the particles will be updated according to the following equation:

$$X_i^n(t+1) = p \pm \alpha \times |Mbest - X_i^n(t)| \times \ln(1/u), \quad (11)$$

III. PROPOSED IQPSO METHOD

To further intensify the QPSO performance in terms of solution quality and convergence speed different approaches such as Gaussian, exponential, Cauchy, beta and other probability distributions methods are used to produced random numbers and improve the position update equation of QPSO. In this work, following the same line of study, new outcomes are presented for the mutation operator in QPSO by using the student t probability distribution method. As, the mutation phenomena have been brought from the evolutionary methods to maintain the diversity. This is because at the early stage of evolution process the diversity of the population is high but later on it reduces quickly. One of the main reason is the improper balance between the local and global searches. Thus, to maintain a good balance between exploration and exploitation searches and to keep the diversity of the population high a new method of mutation is proposed in this work as follows.

A. Mutation strategy

In order to intensify the global searching capability of the proposed IQPSO method, some mutation operation is added to the particle with global best position as follows:

$$Gbest = mut(gbest), \quad (12)$$

where mut is obtained by the selection of a best fittest value of $gbest$ particle with student t random function.

The $Gbest$ is the new global best particle that will further take part in the optimization process to jump from local and achieve a global optimal solution.

The new global best particle $Gbest$ will combine with the mutation operator using a modification of parameters c_1 and c_2 of Equation (10) with modifications given by the following equation:

$$p = \frac{st_1 \times pbest_i^n + st_2 \times Gbest^n}{2}, \quad (13)$$

where st_1 and st_2 are the two random numbers generated with student t probability distribution method.

The generation of random numbers with student t probability distribution function provides a good cooperation between the probability of having a large number of small amplitude around the current point and a small probability holding higher amplitude that will

help the particles to escape from local optimum and accomplish the global optimum solution.

B. Updating parameter formulae

Moreover, the contraction expansion coefficient β is the only control parameter for QPSO and is used to tune the algorithm. The β plays an important role to control the convergence behavior of the algorithm. Therefore, different researchers have proposed different strategies to bring a good balance between exploration and exploitation searches to adjust the β parameter [12]. The most common value of β is to initially set to 1 and reduced linearly to 0.5. Also, β plays a vital role to keep balance between the local and global searches of the algorithm. However, improper adjustment of β will make the local and global searches disturb, as a result the algorithm trapped into local minima. Thus, to address this kind of issues, a proper adjustment of the value of β is important so that to jump the algorithm from local optima and achieve a global optimum solution. Thus, in this work, a new dynamic control parameter is proposed that will keep balance between the exploration and exploitation searches and will avoid the algorithm to trap into local minima. The proposed dynamic control parameter is given as:

$$\beta = 0.5 - \cos(rand / 2) \left(\frac{M_{iter} - t}{M_{iter}} \right), \quad (14)$$

where $rand$ is a uniform random number within range [0,1], M_{iter} is the maximum number of iteration and t is the current iteration.

Consequently, on the bases of cosine function values the coefficient expansion β parameter also varies to guarantee a tradeoff between the exploration and exploitation searches.

IV. NUMERICAL APPLICATION

To evaluate the performance of the proposed QPSO method for electromagnetic problems. It is used to solve a well-known benchmark TEAM workshop Problem 22 as stated in [13]-[18]. The TEAM workshop problem is a SMES (superconducting magnetic energy storage system) design optimization as shown in Fig. 1. The system consists of two concentric coils carrying current in the opposite directions. The inner main solenoid and the outer shielding solenoid that is used to minimize the stray field. The optimal design of SMES is to achieve a desired stored energy with minimal stray field. Therefore, the design should fulfil:

- (1) The energy stored in the device should be 180 MJ;
- (2) The generated magnetic field inside the solenoids must not violate certain physical condition to ensure the superconductivity;

(3) The mean stray field at 22 measurement points along line A and line B at distance of 10 m should be as small as possible.

To guarantee the superconductivity of the superconductors, the constraint equation between the current density of the two solenoids and magnetic flux density should fulfil:

$$J_i \leq (-6.4|B_{\max}|_i + 54)(A/mm^2) \quad (i=1,2), \quad (15)$$

where J_i and B_{\max} are the current density and maximal magnetic flux density in the i^{th} coil.

In the three-parameter optimization problem of SMES design, the inner solenoid is fixed at $r_1 = 2m$, $h_1/2 = 0.8m$, $d_1 = 0.27m$. The dimensions of the outer solenoid are optimized following the constraints as: $2.6m < r_2 < 3.4m$, $0.204m < h_2/2 < 1.1m$, $0.1m < d_2 < 0.4m$. Furthermore, the current densities for the two coils are set to be $22.5 A/mm^2$ in opposite directions. Also, for the convenience of numerical implementation, (15) can be simplified to $|B_{\max}| \leq 4.92T$. Under such simplification, the optimization problem is expressed as:

$$\min f = \frac{B_{\text{stray}}^2}{B_{\text{norm}}^2} + \frac{|Energy - E_{\text{ref}}|}{E_{\text{ref}}} \quad \text{subject to}$$

$$|B_{\max}| \leq 4.92T, \quad (16)$$

where $E_{\text{ref}} = 180MJ$, $B_{\text{norm}} = 3 \times 10^{-3}T$, $Energy$ is the energy stored in SMES device, B_{\max} is the maximum magnetic flux density, B_{stray}^2 is evaluated at 22 equidistance points along line A and line B as shown in Fig. 1, using the following equation:

$$B_{\text{stray}}^2 = \sum_{i=1}^{22} B_{\text{stray},i}^2 / 22. \quad (17)$$

In this case study, the performance parameter as required by Equations (16) and (17) are determined using two-dimensional finite element analysis.

For performance comparison, this case study is solved using the proposed IQPSO method, original QPSO [10], GQPSO [19] and MQPSO [20]. The optimal results of different stochastic approaches for 10 random runs are tabulated in Table 1.

The numerical results in Table 1 and statistical analysis as shown in Fig. 2, demonstrating the superiority of the proposed IQPSO method on other well-designed stochastic approaches. The convergence plot of Fig. 2, also illustrates that the convergence performance of the proposed IQPSO is faster than other tested optimal methods and the proposed IQPSO converges quickly at the initial iterations of the evolution process. Furthermore, it can jump from the local minima to further discover the search space.

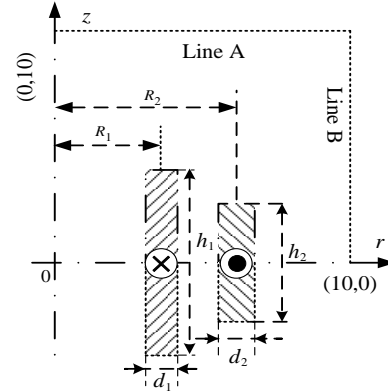


Fig. 1. SMES configuration.

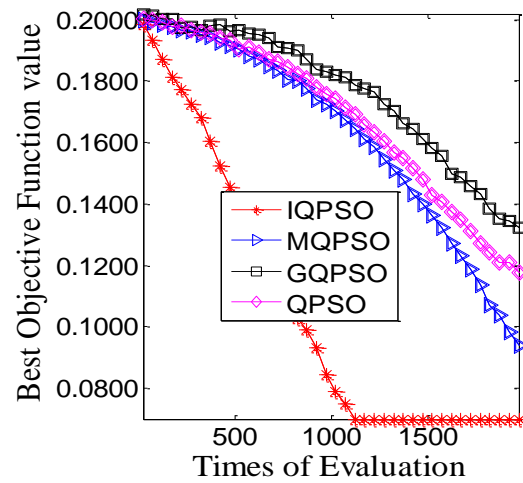


Fig. 2. Convergence comparison of different stochastic methods on Team problem 22.

Table 1: Performance comparison of different stochastic methods on Team workshop problem 22

Optimizer	r_2	$h_2/2$	d_2	Cost Function	Function Calls
GQPSO	3.1723	0.2319	0.3892	0.1222	2000
QPSO	3.0786	0.2414	0.3795	0.1077	2000
MQPSO	3.1198	0.3008	0.3079	0.0903	2000
IQPSO	3.1407	0.3149	0.2886	0.0796	2000

Thus, one can analyze from these numerical outcomes, that the performance of proposed IQPSO is extensively better than other tested stochastic approaches in terms of both solution quality and convergence speed (number of iterations).

V. CONCLUSION

In this paper, a new approach of mutation using student t probability distribution function and updated parameter control formulae is proposed to intensify the performance of QPSO algorithm. The new method

has been validated by using an electromagnetic design problem. The experimental outcomes on the case study demonstrates that the proposed method has high global searching capability and used less number of iterations for convergence as compared to other tested optimal methods. Consequently, it showcases the merit and high applicability of the proposed IQPSO method. Moreover, for future work it should be investigated to find other optimal methods for the study of electromagnetic design problems and the proposed method will be applied on other engineering electromagnetic problems.

ACKNOWLEDGEMENT

This work was supported in part by the National Natural Science Foundation of China (No. 61801008), Beijing Natural Science Foundation National (No. L172049), Beijing Science and Technology Planning Project (No. Z171100004717001).

REFERENCES

- [1] T. V. Luyen and T. V. B. Giang, "Null steering beamformer using bat algorithm," *Applied Computational Electromagnetics Society (ACES) Journal*, vol. 33, no. 1, pp. 23-29, 2018.
- [2] C. Zhai, X. Zhao, Y. Wang, Y. Zhang, and M. Tian, "PSO algorithm combined with parallel higher order MoM to compensate the influence of radome on antennas," *Applied Computational Electromagnetics Society (ACES) Journal*, vol. 32, no. 3, pp. 215-220, 2017.
- [3] R. Bera, D. Mandal, R. Kar, and S. P. Ghoshal, "Optimal design of elliptical array antenna using opposition based differential evolution technique," *Applied Computational Electromagnetics Society (ACES) Journal*, vol. 32, no. 9, pp. 833-841, 2017.
- [4] X. Zhang, J. C. Newman III, W. Lin, and W. K. Anderson, "Time dependent adjoint formulation for metamaterial optimization using Petrov Galerkin method," *ACES Express Journal*, vol. 1, no. 7, pp. 201-204, 2016.
- [5] O. Kilic and Q. M. Nguyen, "Enhanced artificial immune system algorithm and its comparison to bio-inspired optimization techniques for electromagnetic applications," *ACES Express Journal*, vol. 1, no. 3, pp. 97-100, 2016.
- [6] R. Bera, D. Mandal, R. Kar, and S. P. Ghoshal "Optimal design of elliptical array antenna using opposition based differential evolution technique," *Applied Computational Electromagnetics Society (ACES) Journal*, vol. 32, no. 9, pp. 833-841, 2017.
- [7] S. M. Makouie and A. Ghorbani "Comparison between genetic and particle swarm optimization algorithms in optimizing ships degaussing coil currents," *Applied Computational Electromagnetics Society (ACES) Journal*, vol. 31, no. 5, pp. 516-523, 2016.
- [8] S. Chakraborty, T. Senjyu, A. Yona, A. Y. Saber, and T. Funabashi, "Solving economic load dispatch problem with valve point effects using a hybrid quantum mechanics inspired particle swarm optimization," *IET Generation Transmission Distribution*, vol. 5, pp. 1042-1052, 2011.
- [9] J. Kennedy and R. Eberhart, "Particle swarm optimization," in *Proc. of the IEEE International Conference on Neural Network*, pp. 1942-1948, 1995.
- [10] J. Sun, B. Feng, and W. B. Xu, "Particle swarm optimization with particles having quantum behavior," in *Proc. of the IEEE Congress on Evolutionary Computation (CEC)*, pp. 325-331, 2004.
- [11] Y. Shi and R. C. Eberhard, "A modified particle swarm," in *Proceedings of IEEE International Conference on Evolutionary Computation*, Piscataway, NJ, pp. 1945-1950, 1999.
- [12] J. Sun, W. Xu, and B. Feng, "Adaptive parameter control for quantum behaved particle swarm optimization on individual level," in *Proceedings of IEEE International Conference on Systems, Man and Cybernetics*, Piscataway, NJ, pp. 3049-3054, 2005.
- [13] "SMES optimization benchmark," Team Workshop Problem 22 [Online]. Available: http://www.igte.tugraz.at/archive/team_new/description.php
- [14] S. L. Ho, S. Yang, G. Ni, and J. Huang, "A quantum-based particle swarm optimization algorithm applied to inverse problems," *IEEE Transaction on Magnetics*, vol. 49, no. 5, pp. 2069-2072, May 2013.
- [15] S. An, S. Yang, S. L. Ho, T. Li, and W. Fu, "A modified tabu search method applied to inverse problems," *IEEE Transaction on Magnetics*, vol. 47, no. 5, pp. 1234-1237, May 2011.
- [16] L. S. Coelho and P. Alotto, "Global optimization of electromagnetic devices using an exponential quantum behaved particle swarm optimizer," *IEEE Transaction on Magnetics*, vol. 44, no. 6, pp. 1074-1077, June 2008.
- [17] O. U. Rehman, J. Yang, Q. Zhou, S. Yang, and S. Khan, "A modified QPSO algorithm applied to an engineering inverse problem in electromagnetics," *International Journal of Applied Electromagnetics and Mechanics*, vol. 54, pp. 107-121, 2017.
- [18] L. D. S. Coelho and P. Alotto, "Electromagnetic optimization based on an improved diversity-guided differential evolution approach and adaptive mutation factor," *COMPEL-International Journal of Computation and Mathematics in Electrical and Electronics Engineering*, vol. 28, pp. 1112-1120, 2009.
- [19] L. D. S. Coelho, "Gaussian quantum behaved particle swarm optimization approaches for constrained engineering design problems," *Expert*

Systems with Applications, vol. 37 pp. 1676-1683, 2010.

- [20] O. U. Rehman, S. Yang, and S. Khan, "A modified quantum-based particle swarm optimization for engineering inverse problem," *COMPEL-The International Journal of Computation and Mathematics in Electrical and Electronic Engineering*, vol. 36, pp. 168-187, 2017.



Obaid Rehman received the B.S. degree from the NWFP University of Engineering and Technology, Peshawar, Pakistan, in 2003, in Electrical Engineering and the M.S. degree from University of Liverpool, Liverpool, UK, in 2006, in Computing and the Ph.D. degree

in Electrical Engineering from Zhejiang University, Hangzhou, China, in 2018.

He is currently Assistant Professor at Department of Electrical Engineering, Sarhad University of Science and IT, Peshawar, Pakistan.

His current research interests include the computational electromagnetics and numerical methods for electromagnetic applications etc.



Shanshan Tu received the Ph.D. degree from the Computer Science Department, Beijing University of Post and Telecommunication, in 2014. He is currently an Assistant Professor with the Faculty of Information Technology, Beijing University of Technology, China.

He was with the Department of Electronic Engineering, Tsinghua University as a Post-Doctoral Researcher from 2014 to 2016. He visited the University of Essex for joint doctoral training from 2013 to 2014. His research interests are in the areas of cloud computing security and Deep learning.



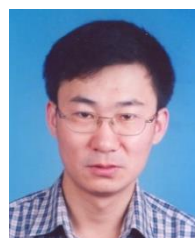
Pakistan in 2014.

He is currently a Doctoral Researcher in the Department of Electronic Engineering, Tsinghua University, Beijing, China.



Shafiullah Khan received the B.S. and M.S. degrees from the University of Peshawar, Pakistan in 2007 and 2009, respectively, and the Ph.D. degree in Electrical Engineering from Zhejiang University, Hangzhou, China, in 2017.

He is currently an Assistant Professor at Islamia College University, Peshawar, Pakistan.



Shiyou Yang received his B.Eng. degree in Automatic Control Engineering from Liaoning University of Technology, China in 1985, and M. Eng. and Ph.D. degrees in Electrical Engineering from Shenyang University of Technology, China, in 1990 and 1995, respectively.

He has been a Professor at the College of Electrical Engineering, Zhejiang University since 2001. Currently, his research interests include Computational Electromagnetics in both high and low frequency domains, the application of numerical techniques in electronic and electromagnetic devices.

An Efficient Method to Study Shielding Effectiveness of Rectangular Enclosure with Wire Penetration

Pu-Yu Hu and Xiao-Ying Sun

College of Communication Engineering
Jilin University, Changchun, 130022, P.R. China
18643125804@163.com, sunxy@jlu.edu.cn

Abstract — This paper presents a reliable and efficient analytical model to calculate the shielding effectiveness (SE) of a rectangular enclosure with wire penetration under plane wave illumination over frequency range of 0 to 2.5GHz. The wire is equivalent to monopole antenna, and the four-element lumped-parameter equivalent circuit for monopole antenna is established to represent the coupling process between electric field and the wire. Based on dynamic Green function, the approximate solution of the electric field distribution in the enclosure excited by the internal wire is derived, and Bethe's theory is used to calculate the approximate solution of the electric field distribution in the enclosure excited by the aperture when the aperture size is not negligible. Several cases are presented to verify the validity of the model. The effects of the length of the wire inside and outside the enclosure, wire penetration and observation point position as well as incident direction of plane wave on the SE are discussed in detail. Simulation result of the proposed model are in good agreement with that of the transmission line matrix (TLM) method.

Index Terms — Equivalent dipole, rectangular enclosure, shielding effectiveness, wire penetration.

I. INTRODUCTION

Shielding is one of the most important technologies in electromagnetic compatibility, which is widely used to protect electronic equipment from external electromagnetic radiation interference [1]. There is great interest in determination of shielding performance of the metallic enclosure, which is quantified by shielding effectiveness (SE). In real devices, there always exist aperture and wire penetration on the shielding enclosure to meet with internal electronic equipment power supply, data transmission and other practical needs. The external wire will induce external electromagnetic energy, and couple to the enclosure through internal wire. Meanwhile, when the size of the wire-penetrated aperture is big enough, aperture will also be an important electromagnetic coupling path and cannot be ignored. These two coupling paths will greatly reduce the shielding performance of

the shielding enclosure [2]. For these reasons, the study of the coupling effect of the enclosure with wire penetration becomes necessary in the shielding enclosure design.

The SE can be directly measured by the experiment [3, 4]. However, the experiment method is inefficient and expensive, which limits its applicability. Generally, numerical methods [5-7] and analytical formulations [8] are main ways to calculate SE. Numerical methods are suitable for calculating the SE of complex structures. Compared to numerical methods, analytical formulations require far less computational cost and are more suitable for regularity research. Zheng et al. applied Norton's equivalence theorem to study the electromagnetic coupling of an incident plane wave through a wire-penetrated electrically small aperture in an infinite conducting screen [9]. A transmission line model of the structure composed by a semi-infinite metallic screen with wire penetration on the ground plane was derived based on the scattering parameter by Daniele et al. [10]. Thomas et al. proposed a very efficient model to compute the coupling of external electromagnetic fields to the contents of an enclosure via wire penetrations using multiple-mode transmission line theory. The simulation results indicated a good consistency with the experimental data [11-13]. In this model, the wire was connected to enclosure through BNC connectors, and therefore the coupling effect of the wire-penetrated aperture was not taken into account. But in some applications, wires of the electronic device inside an enclosure will pass through the enclosure directly through aperture without connectors. Leone and Monich provided inductive coupling model and resonant dipole-antenna model to study the radiation of the enclosure by both wire and aperture [14]. Lertsirimit et al. developed an efficient hybrid method for analyzing the coupling to printed circuit board inside an enclosure via wire penetration using a combination of transmission-line analysis and full-wave solver [15]. Li solved the similar problem by a hybrid numerical analysis method of the partial element equivalent circuit (PEEC) and the method of moment (MoM), and the results of the hybrid

method were in good agreement with those of test [16].

In this paper, a reliable and efficient analytical model is developed to calculate the SE of rectangular enclosure with wire penetration under plane wave illumination. The coupling of external electromagnetic fields to an enclosure via both wire and wire-penetrated aperture is considered. The SE at any point within enclosure can be calculated efficiently and reliably. Simulation results of the presented model are in good agreement with that of the CST software over a wide frequency range (0~2.5GHz), which verifies the validity of the model. The effects of the length of the wire inside and outside the enclosure, wire penetration and observation point position as well as incident direction of plane wave on the SE are discussed in detail based on the model.

II. ANALYTICAL MODEL

The physical structure of a metallic rectangular enclosure with a z -direction wire penetration is depicted in Fig. 1. The dimensions of the rectangular enclosure are $x_e \times y_e \times z_e$. The whole wire can be divided into two segments, named wire A and wire B. The length of the wire A outside the enclosure is l_A and the length of the wire B inside the enclosure is l_B . The radius of the wire and aperture are r_d and r_a . The penetration point of the wire is located at $W(x_a, y_a, 0)$, and the central position of the internal wire is located at $S(x_a, y_a, l_B/2)$. The monitor point is located at $P(x_p, y_p, z_p)$ within the enclosure.

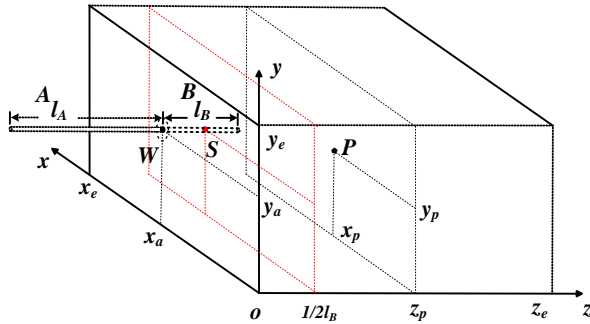


Fig. 1. Geometry of an enclosure with a wire penetration.

The enclosure is irradiated by an oblique plane wave with arbitrary incidence and polarization direction, as shown in Fig. 2. The electric field strength components of the plane wave can be described as:

$$E_x = E_0 \sin \alpha \sin \varphi + \cos \alpha \cos \varphi \sin \vartheta, \quad (1)$$

$$E_y = E_0 \cos \alpha \cos \vartheta, \quad (2)$$

$$E_z = E_0 \cos \alpha \sin \varphi \sin \vartheta - \sin \alpha \cos \varphi, \quad (3)$$

where E_0 is the electric field amplitude, φ is azimuth angle, ϑ is elevation angle and α is polarization angle. The related H-field can be calculated by:

$$\mathbf{H} = \frac{1}{\eta} \mathbf{k} \times \mathbf{E}, \quad (4)$$

where \mathbf{k} is the wave vector direction vector, and η is the characteristic impedance of the medium.

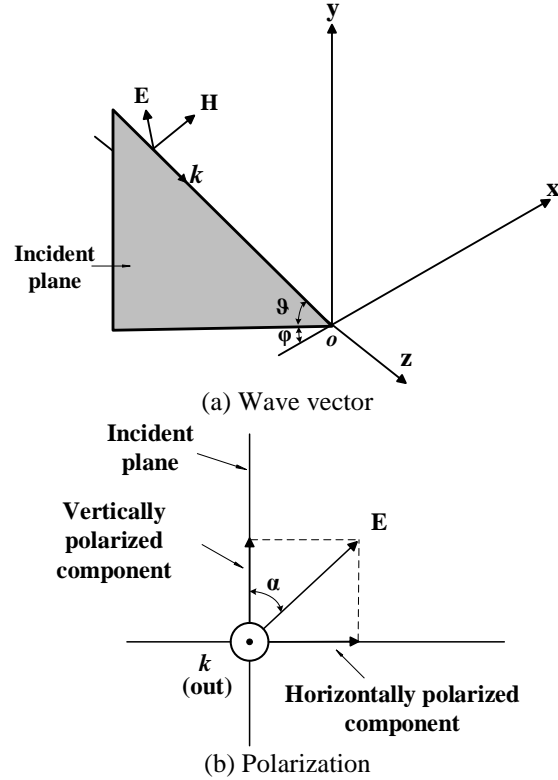


Fig. 2. Definition of the plane wave.

A. Analytical model of wire

Assuming that the wire-penetrated aperture is small enough and can be ignored, the external wire is the main way to couple the electromagnetic energy. The coupling of electromagnetic energy to the enclosure is achieved by the internal wire. In order to calculate the induced energy of the external wire, we consider the wire as monopole antenna. For a dipole or monopole antenna, it can be modelled as an equivalent circuit containing frequency dependent lumped elements over a wide frequency range [17]. The geometry and the four-element circuit model of a dipole antenna are shown in Fig. 3. The length and the diameter of the dipole antenna are $2h$ and $2r$ respectively. The equivalent circuit consists of the capacitance C_0 in series with a frequency dependent resistance called radiation resistance which is formed from a parallel connection circuit of C_1 , R_1 and L_1 . The equivalent impedance of the circuit is expressed as:

$$Z_d(j\omega) = \frac{1}{j\omega C_0} + \frac{j\omega(1/C_1)}{j\omega(1/C_1 R_1) + (1/L_1 C_1) - \omega^2}. \quad (5)$$

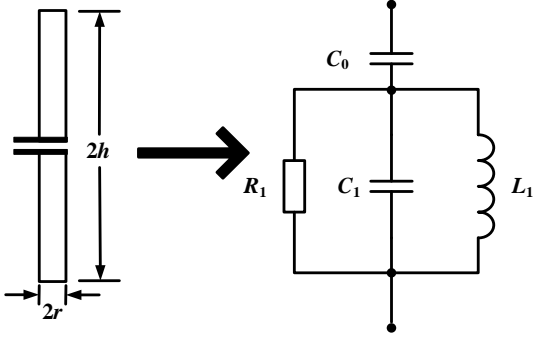


Fig. 3. The equivalent circuit model of a dipole antenna.

The values of R_1 , C_0 , C_1 , and L_1 up to the full-wave resonant frequency are given by [12]:

$$R_1 \approx [578.626] \ln(h/r) - [1675.1817] \Omega, \quad (6)$$

$$C_0 \approx [31.85] h / (\ln(h/r) - [0.6943]) \text{ pF}, \quad (7)$$

$$C_1 \approx [9.433] h / (\ln(h/r) - [2.458]) \text{ pF}, \quad (8)$$

$$L_1 \approx h ([119.58] \ln(h/r) - [147.07]) \text{ nH}, \quad (9)$$

where the contents in the square brackets represent empirical values.

The effective length of dipole antenna is given by [11]:

$$h_e(j\omega) = h\omega_h^2 / (\omega_h^2 + 2j\omega\delta_h - \omega^2), \quad (10)$$

where $\omega_h = 2\pi f_h$, f_h is expressed as:

$$f_h \approx ([7.609] \ln(h/r) + [92.57]) / h \text{ MHz}, \quad (11)$$

the damping frequency δ_h is expressed as:

$$\delta_h \approx \frac{h\omega_h}{2|he|_{\max}} \text{ rads/s}, \quad (12)$$

where $|he|_{\max}$ is:

$$|he|_{\max} \approx h ([0.7063] \ln(h/r) + [0.1387]). \quad (13)$$

For a monopole above ground the self-impedance and effective length is exactly half of that given by (5) and (13) where h is the monopole length [11]. So the self-impedance Z_A and Z_B of the wire A and B are half of that obtained by substituting l_A , l_B and r_d into formula (5)-(9), and the effective length h_{Ae} of the wire A is half of that obtained by substituting l_A and r_d into formula (10)-(13). Finally, the source current of the wire can be approximately expressed as [11]:

$$I_s = \frac{E_z h_{Ae}(j\omega)}{Z_A + Z_B}. \quad (14)$$

When the length of the internal wire is less than the wavelength, we neglect the influence of the current distribution of wire B and the complex coupling process between the aperture and the wire, the wire B is approximately equivalent to a z -direction electric dipole inside the enclosure with dipole effective length h_{Be} and current source I_s at the central position of the internal

wire. The electric field E in a rectangle enclosure contributed by the electric current distributions J inside the enclosure can be represented as [18]:

$$E(r) = -j\omega\mu_0 \iiint_V G_e(r, r') J(r') dV', \quad (15)$$

where μ_0 is the permeability of the medium, G_e is the dyadic Green's function, and V is the volume which sources occupy.

The electric field components at point $P(x_p, y_p, z_p)$, which are excited by the z -direction equivalent electric dipole located at the central position of the internal wire $S(x_a, y_a, l_B/2)$, are given by [19]:

$$E_{sz}(x_p, y_p, z_p) = \frac{-\varepsilon_{0m}\varepsilon_{0n}j\omega\mu_0(h_{Be}I_s)}{2k^2(x_e y_e)} \cdot \sum_{m=0}^{\infty} \sum_{n=0}^{\infty} \left\{ \frac{\Gamma_{mn} \cos k_{mn}(z_p + l_B/2 - z_e)}{k_{mn} \sin(k_{mn} z_e)} + \frac{\Gamma_{mn} \cos k_{mn}(|z_p - l_B/2| - z_e)}{k_{mn} \sin(k_{mn} z_e)} \right\}, \quad (16)$$

$$E_{sy}(x_p, y_p, z_p) = \frac{-\varepsilon_{0m}\varepsilon_{0n}j\omega\mu_0(h_{Be}I_s)}{2k^2(x_e y_e)} \cdot \sum_{m=0}^{\infty} \sum_{n=0}^{\infty} \left\{ \frac{\Gamma'_{mn} \sin k_{mn}(z_e - z_p - l_B/2)}{\sin(k_{mn} z_e)} + \frac{\Gamma'_{mn} \operatorname{sgn}(z_p - l_B/2) \sin k_{mn}(z_e - |z_p - l_B/2|)}{\sin(k_{mn} z_e)} \right\}, \quad (17)$$

$$E_{sx}(x_p, y_p, z_p) = \frac{-\varepsilon_{0m}\varepsilon_{0n}j\omega\mu_0(h_{Be}I_s)}{2k^2(x_e y_e)} \cdot \sum_{m=0}^{\infty} \sum_{n=0}^{\infty} \left\{ \frac{\Gamma''_{mn} \sin k_{mn}(z_e - z_p - l_B/2)}{\sin(k_{mn} z_e)} + \frac{\Gamma''_{mn} \operatorname{sgn}(z_p - l_B/2) \sin k_{mn}(z_e - |z_p - l_B/2|)}{\sin(k_{mn} z_e)} \right\}, \quad (18)$$

where

$$k_{mn} = \sqrt{k^2 - (m\pi/x_e)^2 - (n\pi/y_e)^2}, \quad (19)$$

$$\Gamma_{mn} = \left[(m\pi/x_e)^2 + (n\pi/y_e)^2 \right] \sin(m\pi x_a/x_e) \cdot \sin(n\pi y_a/y_e) \sin(m\pi x_p/x_e) \sin(n\pi y_p/y_e), \quad (20)$$

$$\Gamma'_{mn} = (n\pi/y_e) \sin(m\pi x_a/x_e) \sin(n\pi y_a/y_e) \cdot \sin(m\pi x_p/x_e) \cos(n\pi y_p/y_e), \quad (21)$$

$$\Gamma''_{mn} = (m\pi/x_e) \sin(m\pi x_a/x_e) \sin(n\pi y_a/y_e) \cdot \cos(m\pi x_p/x_e) \sin(n\pi y_p/y_e), \quad (22)$$

where $\operatorname{sgn}(\)$ represents sign function. ε_{0m} and ε_{0n} are Neumann factors which can be expressed as:

$$\varepsilon_{0m} = \begin{cases} 1, & m = 0 \\ 2, & m \neq 0 \end{cases}, \quad (23)$$

$$\varepsilon_{0n} = \begin{cases} 1, & n = 0 \\ 2, & n \neq 0 \end{cases}. \quad (24)$$

The electric field and SE at observation point are:

$$E_{ps} = \sqrt{(E_{sx})^2 + (E_{sy})^2 + (E_{sz})^2}, \quad (25)$$

$$SE_{ps} = -20 \log_{10} |E_{ps} / E_0|. \quad (26)$$

B. Analytical model of wire-penetrated aperture

When the size of the wire-penetrated aperture is big enough, the leakage electric field from wire-penetrated aperture cannot be ignored and need to be considered. Here we ignore the complex coupling relations between the wire and aperture, and the total electric field at point $P(x_p, y_p, z_p)$ inside the enclosure is expressed as:

$$E_t = E_{ps} + E_{pa}, \quad (27)$$

where E_{pa} is the leakage electric field from wire-penetrated aperture without wire, as shown in Fig. 4.

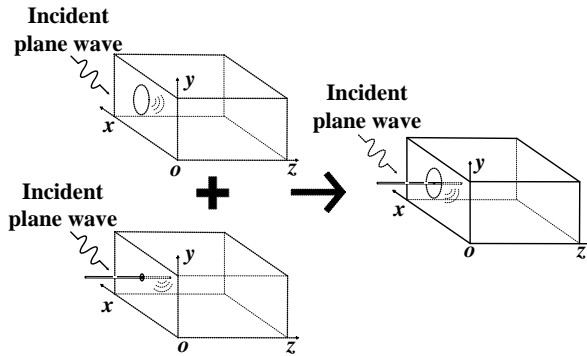


Fig. 4. The coupling of electric fields to the enclosure via both wire and wire-penetrated aperture.

We apply Bethe's theory and replace the aperture with electric and magnetic dipoles located on both sides of the perfectly electric conducting surface which fill the aperture [20]. The electric dipole \mathbf{p} and magnetic dipoles \mathbf{m} are outside the completely closed enclosure, while the mirrored dipoles \mathbf{m}' and \mathbf{p}' are inside the enclosure, as shown in Fig. 5.

The electric dipole is normal to the plane of the aperture, and the magnetic dipoles are parallel to the plane of the aperture. Dipole strengths are given by [19]:

$$\mathbf{p} = \mathbf{p}' = \alpha_e \varepsilon_0 E_{SCz} \hat{\mathbf{z}}, \quad (28)$$

$$\mathbf{m} = \mathbf{m}' = -\alpha_{mx} H_{SCx} \hat{\mathbf{x}} - \alpha_{my} H_{SCy} \hat{\mathbf{y}}, \quad (29)$$

where ε_0 is the dielectric constant. E_{SC} and H_{SC} are the short circuited electric field and magnetic field at the perfectly electric conducting surface in the absence of the aperture, which are two times of the electric field and magnetic field of the incident plane wave. For a circular

aperture with radius of r_a , the magnetic polarizabilities α_{mx} , α_{my} and electric polarizabilities α_e are given by:

$$\alpha_e = 2r_a^3 / 3, \quad (30)$$

$$\alpha_{mx} = \alpha_{my} = 4r_a^3 / 3. \quad (31)$$

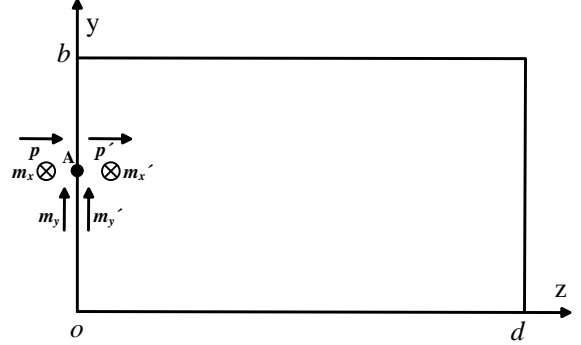


Fig. 5. Enclosure with equivalent dipole located at both sides of the wire-penetrated aperture.

The electric field components at point $P(x_p, y_p, z_p)$, which are excited by the z -direction electric dipole inside a completely closed enclosure located at the center point of the wire-penetrated aperture $W(x_a, y_a, 0)$, are [19]:

$$E_{ez}(x_p, y_p, z_p) = \frac{-\varepsilon_{0m} \varepsilon_{0n} j \omega \mu_0 (j \omega p')}{k^2(x_e y_e)} \cdot \sum_{m=0}^{\infty} \sum_{n=0}^{\infty} \frac{\Gamma_{mn}}{k_{mn}} \frac{\cos(k_{mn}(z_p - z_e))}{\sin(k_{mn} z_e)}, \quad (32)$$

$$E_{ey}(x_p, y_p, z_p) = \frac{-\varepsilon_{0m} \varepsilon_{0n} j \omega \mu_0 (j \omega p')}{k^2(x_e y_e)} \cdot \sum_{m=0}^{\infty} \sum_{n=0}^{\infty} \Gamma'_{mn} \frac{\sin(k_{mn}(z_e - z_p))}{\sin(k_{mn} z_e)}, \quad (33)$$

$$E_{ex}(x_p, y_p, z_p) = \frac{-\varepsilon_{0m} \varepsilon_{0n} j \omega \mu_0 (j \omega p')}{k^2(x_e y_e)} \cdot \sum_{m=0}^{\infty} \sum_{n=0}^{\infty} \Gamma''_{mn} \frac{\sin(k_{mn}(z_e - z_p))}{\sin(k_{mn} z_e)}. \quad (34)$$

The electric field components excited by the x -direction magnetic dipole are given by [21, 22]:

$$E_{mxz}(x_p, y_p, z_p) = \frac{\varepsilon_{0m} \varepsilon_{0n} j \omega \mu_0 m'_x}{x_e y_e} \cdot \sum_{m=0}^{\infty} \sum_{n=0}^{\infty} \frac{\Gamma'_{MNx}}{k_{mn}} \frac{\cos(k_{mn}(z_p - z_e))}{\sin(k_{mn} z_e)}, \quad (35)$$

$$E_{mxy}(x_p, y_p, z_p) = \frac{\varepsilon_{0m} \varepsilon_{0n} j \omega \mu_0 m'_x}{x_e y_e} \cdot \sum_{m=0}^{\infty} \sum_{n=0}^{\infty} \Gamma''_{MNx} \frac{\sin(k_{mn}(z_e - z_p))}{\sin(k_{mn} z_e)}, \quad (36)$$

$$E_{mxx}(x_p, y_p, z_p) = 0, \quad (37)$$

where

$$\Gamma'_{MNx} = \frac{n\pi}{y_e} \sin\left(\frac{m\pi x_a}{x_e}\right) \cos\left(\frac{n\pi y_a}{y_e}\right) \cdot \sin\left(\frac{m\pi x_p}{x_e}\right) \sin\left(\frac{n\pi y_p}{y_e}\right), \quad (38)$$

$$\Gamma''_{MNx} = \sin\left(\frac{m\pi x_a}{x_e}\right) \cos\left(\frac{n\pi y_a}{y_e}\right) \cdot \sin\left(\frac{m\pi x_p}{x_e}\right) \cos\left(\frac{n\pi y_p}{y_e}\right). \quad (39)$$

Similarly, we can easily calculate the value of E_{myz} , E_{myy} and E_{myx} due to the y -direction magnetic dipole.

The total leakage electric field components from the aperture and wire at observation point $P(x_p, y_p, z_p)$ can be obtained by:

$$E_{tx} = E_{sx} + E_{ex} + E_{mxx} + E_{myx}, \quad (40)$$

$$E_{ty} = E_{sy} + E_{ey} + E_{mxy} + E_{myy}, \quad (41)$$

$$E_{tz} = E_{sz} + E_{ez} + E_{mxz} + E_{myz}. \quad (42)$$

The total electric field and SE at $P(x_p, y_p, z_p)$ are:

$$E_t = \sqrt{(E_{tx})^2 + (E_{ty})^2 + (E_{tz})^2}, \quad (43)$$

$$SE_t = -20 \log_{10} |E_t / E_0|. \quad (44)$$

III. EXAMPLE AND ANALYSIS

In this section, the simulation results of the proposed model are compared with the results of the CST software based on transmission line matrix (TLM) method covering frequency range 0~2.5GHz. In TLM simulation, the material of the rectangle enclosure is aluminum with conductivity of 3.56×10^7 S/m, and the dimension of the enclosure are $x_e \times y_e \times z_e = 300\text{mm} \times 260\text{mm} \times 120\text{mm}$. The wire is good conductor with a radius of 4mm. Boundary conditions are set to absorbing boundary. We set the plane wave as the excitation source and electric field probes to calculate the electric field within the enclosure. Automatic meshing is adopted, and the accuracy is set to -80dB. Six cases are considered to verify the validity of the model, with various external and internal wire length, penetration point position, observation point position, incident direction of the plane wave and aperture radius listed in Table 1.

Table 1: Specific parameter settings

Case	External and Internal Wire Length (mm) (l_A, l_B)	Aperture Radius (mm) r_a	Wire Penetration Point Position (mm) (x_a, y_a)	Observation Point Positions (mm) (x_p, y_p, z_p)	Elevation Angle ($^\circ$) ϑ
1	(80, 50)	4.1	(150, 100)	(150, 215, 60)	90
2	(80, 50)	4.1	(225, 140)	(65, 90, 70)	90
3	(60/100, 50)	4.1	(150, 100)	(150, 215, 60)	90
4	(80, 10/30)	4.1	(150, 100)	(150, 215, 60)	90
5	(80, 50)	4.1	(150, 100)	(150, 215, 60)	20/45
6	(80, 50)	30	(150, 100)	(150, 215, 60)	90

Cases 1-5 are designed to study the coupling of electromagnetic field to the enclosure achieved by wire. We set the radius of the wire-penetrated aperture to 4.1mm, which is small enough to ignore the leakage electric field from aperture. Case 6 is designed to study the coupling of electromagnetic field to the enclosure obtained by both wire and aperture.

For case 1, the length of the external wire A and internal wire B are 80mm and 50mm respectively. The plane wave travels uniformly along the negative direction of the y -axis, with azimuth angle $\varphi=90^\circ$, elevation angle $\vartheta=90^\circ$, and polarization angle $\alpha=0^\circ$. The electric field is parallel to the external wire which is the worst case for shielding according to the formula (14). The simulation results of the proposed model and TLM method are shown in Fig. 6. The results obtained from the two methods are nearly the same, except discrepancies at low frequency. This may be due to the neglect of the current distribution of the internal wire and the complex

coupling process between the aperture and the wire in the model. SE results of the enclosure with aperture radius of 4.1mm and without wire are also shown in Fig. 6. Comparing the results under two conditions, we can see that the coupled electric field from the wire will lead to a significant reduction in SE of the enclosure, for example the reduction is 40dB at 500MHz. The leakage electric field from aperture is very few, which prove that we can just ignore it.

For case 2, penetration point and observation point position have changed compared to case 1. The simulation results of the proposed model and TLM method are shown in Fig. 7. The comparison between two methods demonstrates that the proposed method is applicable and effective. Compared with the results of case 1 and case 2, it can be found that the change of penetration point and observation point position has a little influence on the amplitude of the SE, but some higher order resonant modes will occur.

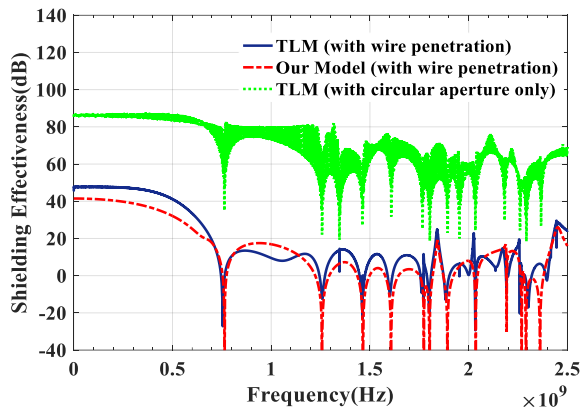


Fig. 6. SE result of case 1.

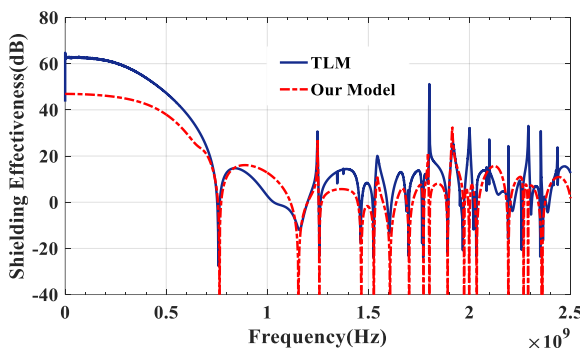


Fig. 7. SE result of case 2.

For case 3, the trend of SE along with change of the length of the external wire is analyzed. Here we select the model of case 1, and the lengths of the external wire are 60mm and 100mm respectively. From the simulation results shown in Fig. 8 and Fig. 9, we can see that the proposed model and TLM method are in good agreement. Combined with the results of case 1, we can find that as the external wire length decreases, the SE of the enclosure increases continuously within 1GHz. But at frequencies higher than about 1.25GHz, the SE of the enclosure gradually decreases with the decrease of external wire length, as shown in Fig. 10.

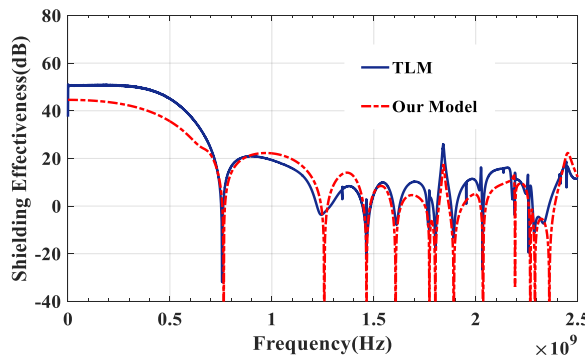


Fig. 8. SE result of case 3 ($l_A=60\text{mm}$).

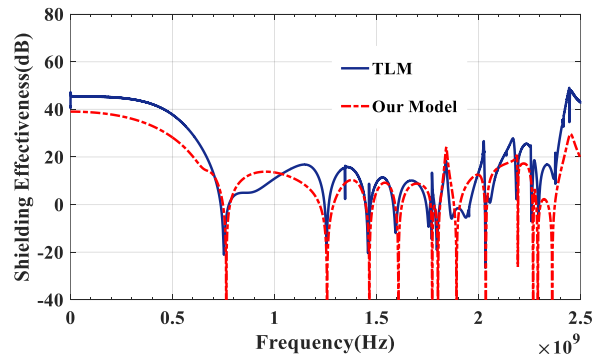


Fig. 9. SE result of case 3 ($l_A=100\text{mm}$).

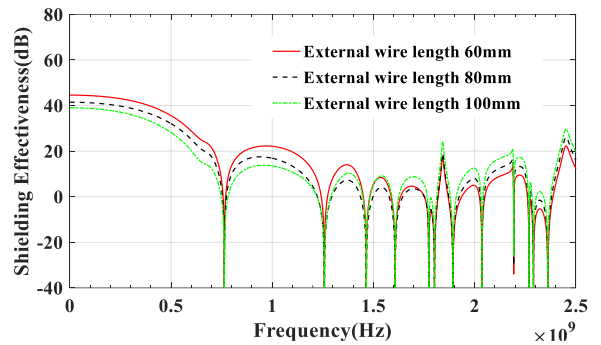


Fig. 10. SE results of the enclosure with different external wire length.

For case 4, the trend of SE along with change of the length of the internal wire is discussed. The enclosure model in case 1 is selected, the lengths of the internal wire are 10mm and 30mm respectively. The simulation results of the proposed model and TLM method are shown in Fig. 11 and Fig. 12. Simulation results show a good consistency between the two methods. Combined with the results of case 1, we can conclude that as the internal wire length decreases, the SE of the enclosure will increase continuously, as shown in Fig. 13. In comparison with case 3, we can find that the influence of the internal wire on SE is larger than that of external wire.

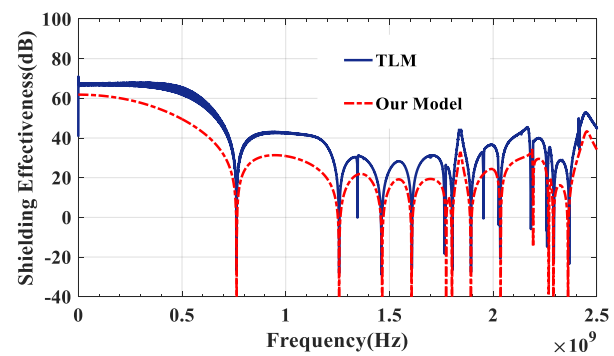


Fig. 11. SE result of case 4 ($2l_B=10\text{mm}$).

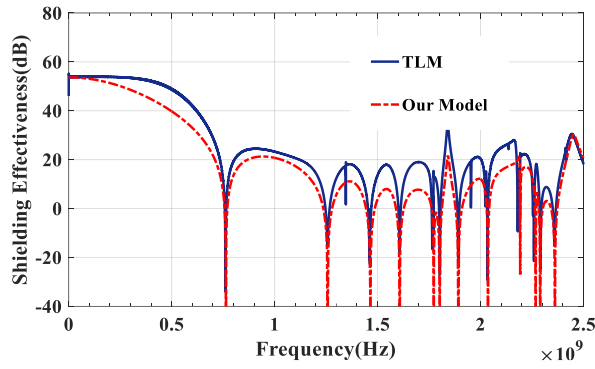


Fig. 12. SE result of case 4 ($2l_B=30\text{mm}$).

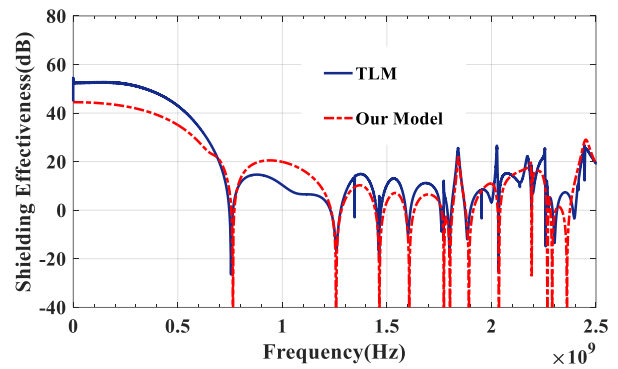


Fig. 15. SE result of case 5 (Elevation angle is 45°).

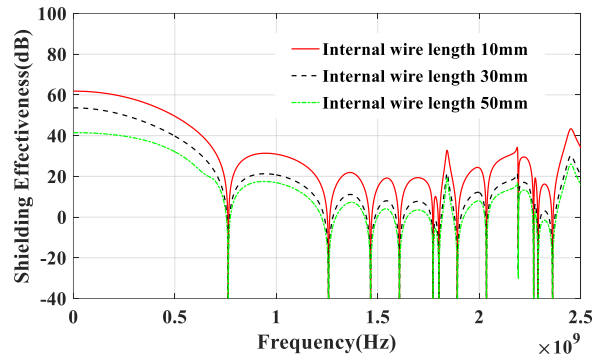


Fig. 13. SE results of the enclosure with different internal wire length.

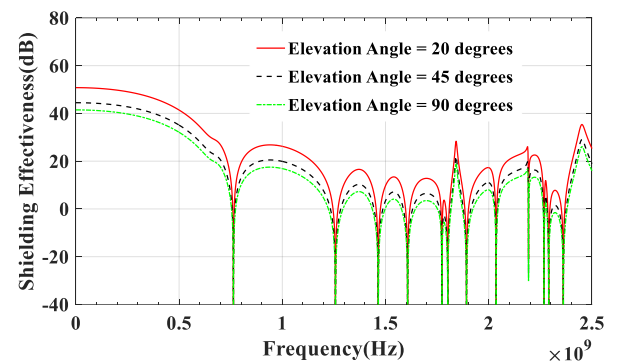


Fig. 16. SE results of the enclosure with different elevation angle.

For case 5, the influence of elevation angle on SE under vertical polarization is discussed. The model of case 1 is selected, here we set the elevation angles to 20 and 45 degrees. The simulation results shown in Fig. 14 and Fig. 15 show that the SE derived from the proposed model are basically consistent with that of TLM method, and as the elevation angle decreases, the SE of the enclosure will increase continuously. The worst case for shielding is when electric field parallel to the external wire, as shown in Fig. 16.

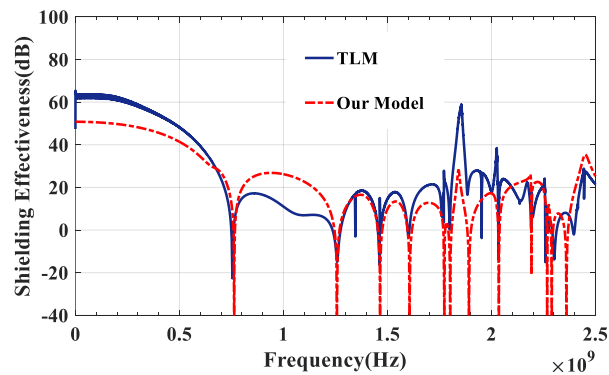


Fig. 14. SE result of case 5 (Elevation angle is 20°).

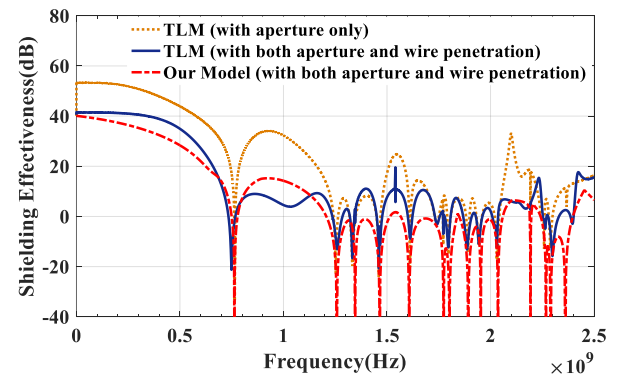


Fig. 17. Comparison of the SE results of the enclosure with both wire and aperture and with aperture only.

For case 6, the effect of aperture is taken into account. When the size of the aperture is big enough, the coupling of external electromagnetic fields to the enclosure via both wire and aperture need to be considered. Here we select the model of case 1. The radius of the circular aperture is $r_a=30\text{mm}$. From the simulation results of the proposed model and TLM method shown in Fig. 17, we can see that the two methods also have a good agreement and wire-

penetration significantly reduces the SE of the enclosure, especially at low frequency. In such a case, the SE of the enclosure with wire and aperture is reduced by about 10dB-20dB compared with the SE of the enclosure with aperture only at frequencies below 1.25GHz.

IV. CONCLUSION

In order to study the shielding performance of a metallic rectangular enclosure with wire penetration, we present a novel analytical model in this paper. The couplings of external electromagnetic fields to the enclosure via both wire and aperture are analyzed using monopole antenna equivalent circuit modeling and Bethe's theory. Various parameters such as the length of the wire inside and outside the enclosure, wire penetration and observation point position as well as incident direction of plane wave are taken into account. By this model, the SE of the enclosure with wire penetration under plane wave illumination can be calculated quickly and accurately over a wide frequency range (0~2.5G). Several cases have been presented to demonstrate the validity and accuracy of the model. The overall simulation results of the model match well with those of CST simulation software using TLM method, expect discrepancies existing at low frequency. The analysis shows that (1) the wire penetration will greatly reduce the SE of the enclosure; (2) both the length of the wire inside and outside the enclosure will affect the SE of the enclosure, but the influence of the internal wire on SE is larger than that of external wire. The SE decreases with the increase of the length of internal wire; (3) the condition where electric field is parallel to the external wire is the worst case for shielding. Compared with TLM method and other numerical algorithms, the proposed method has higher computation speed and higher computational efficiency, and therefore has its values on shielding enclosure design.

REFERENCES

- [1] T. Cvetkovic, V. Milutinovic, N. Doncov, and B. Milovanovic, "Numerical investigation of monitoring antenna influence on shielding effectiveness characterization," *Appl. Comp. Electro. Society (ACES) Journal*, vol. 29, no. 11, pp. 837-846, Nov. 2014.
- [2] G. Manara, M. Bandinelli, and A. Monorchio, "Electromagnetic penetration and coupling to wires through apertures of arbitrary shape," *IEEE Trans. Electromagn. Compat.*, vol. 40, no. 4, pp. 391-396, Nov. 1998.
- [3] S. Z. Sapuan and M. Z. M. Jenu, "Shielding effectiveness and S21 of a rectangular enclosure with aperture and wire penetration," *2007 Asia-Pacific Conference on Applied Electromagnetics*, pp. 1-5, Dec. 2007.
- [4] K. Yusoff, M. Z. M. Jenu, W. R. W. Abdullah, and B. M. Shariff, "Experimental study of the electromagnetic coupling to an enclosure via a wire penetration," *2005 Asia-Pacific Conference on Applied Electromagnetics*, pp. 172-174, Dec. 2005.
- [5] S. T. Song, H. Jiang, and Y. L. Huang, "Simulation and analysis of HEMP coupling effect on a wire inside an apertured cylindrical shielding cavity," *Appl. Comp. Electro. Society (ACES) Journal*, vol. 27, no. 6, pp. 505-515, June 2012.
- [6] R. Araneo and G. Lovat, "Analysis of the shielding effectiveness of metallic enclosures excited by internal sources through an efficient method of moment approach," *Appl. Comp. Electro. Society (ACES) Journal*, vol. 25, no. 7, pp. 600-611, July 2010.
- [7] G. Wu, Z. Q. Song, X. G. Zhang, and B. Liu, "Study on coupling characteristics of electromagnetic wave penetrating metallic enclosure with rectangular aperture," *Appl. Comp. Electro. Society (ACES) Journal*, vol. 26, no. 7, pp. 611-618, July 2011.
- [8] C. C. Wang, C. Q. Zhu, X. Zhou, and Z. F. Gu, "Calculation and analysis of shielding effectiveness of the rectangular enclosure with apertures," *Appl. Comp. Electro. Society (ACES) Journal*, vol. 28, no. 6, pp. 535-545, June 2013.
- [9] E. Zheng, R. F. Harrington, and J. R. Mautz, "Electromagnetic coupling through a wire-penetrated small aperture in and infinite conducting plane," *IEEE Trans. Electromagn. Compat.*, vol. 35, no. 2, pp. 295-300, May 1993.
- [10] V. Daniele, M. Gilli, and S. Pignari, "EMC prediction model of a single wire transmission line crossing a circular aperture in a planar screen," *IEEE Trans. Electromagn. Compat.*, vol. 38, no. 2, pp. 117-126, May 1996.
- [11] D. W. P. Thomas, A. Denton, T. M. Benson, and C. Christopoulos, "Electromagnetic coupling to an enclosure via a wire penetration," *IEEE Int. Symp. on Electromagn. Compat.*, pp. 183-188, Aug. 2001.
- [12] A. Nanni, D. W. P. Thomas, C. Christopoulos, T. Konefal, J. Paul, and L. Sandrolini, et al., "Electromagnetic coupling between wires and loops inside a rectangular cavity using multiple-mode transmission line theory," *IEEE Int. Symp. on Electromagn. Compat.*, pp. 609-614, Sep. 2004.
- [13] T. Konefal, J. F. Dawson, A. C. Denton, and T. M. Benson, et al., "Electromagnetic coupling between wires inside a rectangular cavity using multiple-mode-analogous-transmission-line circuit theory," *IEEE Trans. Electromagn. Compat.*, vol. 43, no. 3, pp. 273-281, Aug. 2001.
- [14] M. Leone and G. Monich, "Coupling of apertures in enclosures to external cabling structures," *IEEE*

- Trans. Electromagn. Compat.*, vol. 46, no. 1, pp. 107-110, Feb. 2004.
- [15] C. Lertsirimit, D. R. Jackson, and D. R. Wilton, "An efficient hybrid method for calculating the EMC coupling to a device on a printed circuit board inside a cavity by a wire penetrating an aperture," *Electromagnetics*, vol. 25, no. 7-8, pp. 637-654, Oct. 2005.
- [16] P. Li, F. R. Yang, and W. Y. Xu, "An efficient approach for analyzing shielding effectiveness of enclosure with connected accessory based on equivalent dipole modeling," *IEEE Trans. Electromagn. Compat.*, vol. 58, no. 1, pp. 103-110, Feb. 2016.
- [17] T. G. Tang, Q. M. Tieng, and M. W. Gunn, "Equivalent circuit of a dipole antenna using frequency-independent lumped elements," *IEEE Trans. Antennas Propag.*, vol. 41, no. 1, pp. 100-103, Jan. 1993.
- [18] L. W. Li, P. S. Kooi, M. S. Leong, and T. S. Yeo, "On the eigenfunction expansion of electromagnetic dyadic green's functions in rectangular cavities and waveguides," *IEEE Trans. Microw. Theory Tech.*, vol. 43, no. 3, pp. 700-702, Mar. 1995.
- [19] F. M. Tesche, M. V. Ianoz, and T. Karlsson, *EMC Analysis Methods and Computational Models*. Wiley, New York, 1997.
- [20] P. Y. Hu and X. Y. Sun, "Study of the calculation method of shielding effectiveness of rectangle enclosure with an electrically large aperture," *Progress In Electromagnetics Research M*, vol. 61, pp. 85-96, 2017.
- [21] S. K. Goudos, E. E. Vafiadis, and J. N. Sahalos, "Monte Carlo simulation for the prediction of

the emission level from multiple sources inside shielded enclosures," *IEEE Trans. Electromagn. Compat.*, vol. 44, no. 2, pp. 291-308, May 2002.

- [22] R. J. H. Crawhall, "EMI potential of multiple sources within a shielded enclosure," University of Ottawa, Ph.D., 1993.



EMC and EM protection.

Pu-Yu Hu received the B.S. degree in Electronic and Information Engineering from Changchun University of Technology, China, in 2015. He is currently working toward the Ph.D. degree in Communication and Information System in Jilin University. His research interests include



Xiao-Ying Sun received the Ph.D. degrees in Communication and Information System from Jilin University, Jilin, China, in 2005. Now he is a Professor and the Dean of College of Communication Engineering in Jilin University, Changchun, Jilin, China.

From 1996 to 2004, he was a Lecturer in the School of Radio Engineering, Jilin University, China. From 2005 to 2009, he was an Associate Professor in the School of Communication Engineering, Jilin University, China. His research interests include EMC, EM protection, array signal processing and tactile representation.

Robustness Evaluation of Split Ring Resonator Antenna System for Wireless Brain Care in Semi-Anatomical Ellipsoid Head Model

Shubin Ma, Leena Ukkonen, Lauri Sydänheimo, and Toni Björninen

BioMediTech Institute and Faculty of Biomedical Sciences and Engineering
Tampere University of Technology
Tampere, Finland
{shubin.ma, leena.ukkonen, lauri.sydanheimo, toni.bjorninen}@tut.fi

Abstract — Robustness evaluation is a critical part to verify the applicability of wireless implantable devices. In this work, we present a semi-anatomical ellipsoid head model to evaluate the robustness of a split ring resonator inspired antenna system toward variable implant location, tissue layer thicknesses, and antenna orientation with respect to the human head. The system consists of a passive wearable part placed on the scalp and a cortical implant that carries a passive UHF RFID microsystem. According to our results, the antenna system is robust toward variability: it enables the remote powering of a -18 dBm RFID microsystem at distance between 0.5 and 1.1 meter at various locations and orientations with respect to the head and for skull thickness up to 1 cm.

Index Terms — Antennas, brain modelling, implantable biomedical devices, RFID, robustness.

I. INTRODUCTION

With more than 86 billion neurons and other supportive glial cells constituting the cerebrum, the brainstem and the cerebellum, the human brain forms the central nervous system that regulates all our daily physiological activities. Thus, any injury to the brain usually leads to serious deterioration of physical and mental capacity. In the pursue toward better life quality for those suffering from debilitating neurological conditions, researchers have recently found wireless brain care based on implantable sensors and stimulators a compelling approach to achieve a long term intracranial physiological monitoring, prosthesis controlling and treatment for neurological disorders [1-3].

Among the wireless modalities for the data transfer, modulated backscattering or RFID-inspired approaches are compelling as they offer low-power data communications that is pertinent to battery-free implants [4-6]. To establish effective far field communications with a cortical backscattering implant, we have recently proposed a spatially distributed split-ring resonator inspired antenna system composed of a small, thin and

flexible implantable part that couples to a head-worn part acting as a performance booster [7]. Human body is an extremely complex operation environment for antennas, and thus computational electromagnetics and appropriate human body models are indispensable in the assessment of the electromagnetic performance of implantable and wearable antennas. In the aforementioned work, due to the difficulty of building a multiple-layer head phantom in practice, we used a simple homogenous block model to conduct the first feasibility evaluation of our antenna system and obtained a good agreement between the simulation and experimental results. That model included an average estimation for the dielectric properties of the human head, but due to its simplified geometry, it cannot be used to predict the impact of variation of the tissue layer thickness or radiation properties of the antenna system at different locations on the head or when its orientation with respect to the head changes. In practice, these are all crucial aspects, as the location of the implant varies according to the application and its exact orientation is hard to control during surgery. Thus, the antenna system must be robust toward these factors. It must also remain functional under anatomical variability since the tissue layer thicknesses are different for different individuals. Consequently, computational modelling of the human head with more details is pertinent to verify the applicability of the antenna system.

Currently, high-resolution medical imaging based computational models offer the most detailed structural information for computational modelling. However, for this reason they are not only computationally heavy, but reflect the anatomical details of a certain scanned individual with no possibility for adjusting the tissue layer thickness to assess the impact of anatomical variability. To overcome these limitations and to achieve holistic robustness evaluation of our system, we present modelling results obtained from a semi-anatomical human head model, which we have built by integrating a seven-layer ellipsoid with the anatomical head model of an adult male. Meanwhile, various electromagnetic CAD tools based on various numerical methods are available

to provide extremely good accuracy [8]. In this journal, we chose Ansys HFSS 17.0 to conduct the simulation and analysis.

II. SIMULATION SETUP

A. Antenna system

The antenna system is based on the split ring resonator structure with an implantable and wearable parts. Figure 1 shows the antenna structure and its geometrical dimensions. The implant part provides the self complex-conjugate matching with the IC that is connected to feed point in Fig. 1. The fully passive wearable part is for antenna gain improvement [7]. The cross-sectional view in Fig. 2 shows its implementation in intracranial environment. We assume the implant to be affixed to the dura, which is a tough fibrous membrane that forms the sack enclosing the subarachnoid space (SAS) and that wearable part is concentrically placed on the scalp. We use 35 μm thick copper as the conductor for the antenna system and the substrates for the wearable and implant parts are 2 mm thick EPDM (Ethylene-Propylene-Diene-Monomer) ($\epsilon_r=1.26$, $\tan\delta=0.007$ at 915 MHz) and 50 μm thick flexible polyethylene ($\epsilon_r=2.25$, $\tan\delta=0.001$ at 915 MHz), respectively. The coating material for the implant part is 1 mm thick silicone ($\epsilon_r=2.2$, $\tan\delta=0.007$ at 915 MHz). The RFID microchip in the simulation is modelled by the parallel connection of the resistance and capacitance of 2.85 k Ω and 0.91 pF, respectively [9].

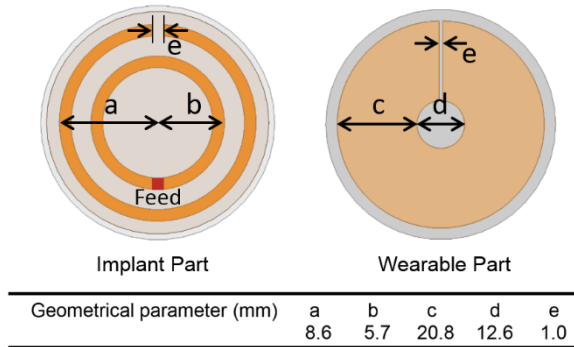


Fig. 1. Antenna system with its geometrical dimensions.

B. Antenna performance indicators

In the antenna development for passive RFID tags, the attainable read range (d_{tag}) between the tag and the off-body reader is one of the most important performance indicators. Friis' transmission equation can be used to estimate d_{tag} as:

$$d_{tag} = \frac{\lambda}{4\pi} \sqrt{\frac{D e_r \tau EIRP}{P_{ic0}}}, \quad (1)$$

where the d_{tag} is in inverse proportion to RFID IC wake-up power (P_{ic0}) and proportional to antenna directivity

(D), radiation efficiency (e_r), power transfer efficiency (τ), and the equivalent isotropically radiated power limitation ($EIRP$). The power transfer efficiency defined in (2) measures the portion of the power delivered from the antenna to the IC relative to the maximum power available from the antenna. It is given by:

$$\tau = \frac{4\text{Re}(Z_A)\text{Re}(Z_C)}{|Z_A + Z_C|^2}, \quad (2)$$

where Z_A and Z_C are the antenna and IC impedances, respectively. In other words, $0 < \tau \leq 1$ quantifies the goodness of the complex conjugate impedance matching between the antenna and the IC.

Among all the five variables shown in (1), except for P_{ic0} and $EIRP$, which are fixed by the IC design and the regional wireless communication regulatory committee, other parameters can be optimized to maximize d_{tag} . Therefore, in this work we will focus on the analysis of D , e_r and τ in the semi-anatomical human head model.

C. Semi-anatomical head model

We built the semi-anatomical human head model by integrating a seven-layer ellipsoid with the ANSYS anatomical human head model. The seven layers of the ellipsoid were constructed as ellipsoid shells with an adjustable thicknesses representing skin, fat, muscle, skull, dura, CSF (cerebrospinal fluid) and brain (grey matter). To model the relative permittivity and the electromagnetic energy dissipation in the biological matter, we used the four-term Cole-Cole relaxation model introduced in [10]. The loss model accounts for both loss sources: polarizability and ohmic loss due to conduction current. All the model parameters are available in [11] and Table 1 lists the dielectric properties of each tissue type at 950 MHz.

Table 1: Dielectric properties of human tissues at 950 MHz

Tissue	ϵ_r	σ (S/m)
Skin	41.405	0.867
Fat (not infiltrated)	5.462	0.051
Muscle	55.032	0.943
Skull (cancellous)	20.788	0.340
Dura	44.426	0.961
CSF	68.638	2.413
Brain (grey matter)	52.725	0.942

Figure 2 illustrates the semi-anatomical head model and six different placements of the antenna system in four different regions: the frontal anterior (FA), frontal posterior (FP) with upper and lower positions, parietal anterior (PA) with upper and lower positions and parietal posterior (PP). At each location, we defined the nominal antenna orientation such that a line drawn through the middle of the split gap in the wearable part intersects the minor axis of the ellipsoid pointing along the person's height.

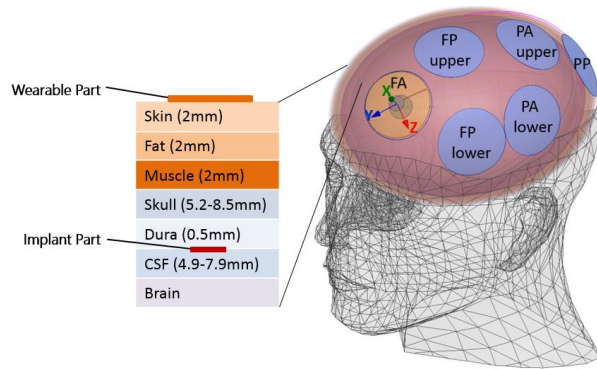


Fig. 2. Semi-anatomical human head model with the layered ellipsoid.

The thicknesses of skin, fat, and muscle tissue layers are almost independent of the positions on the head and thus we set a fixed value of 2 mm for each layer in this model [12]. The thickness of dura layer also varies over small range from 0.3 mm to 0.8 mm [13] and therefore we fixed the thickness of this layer to 0.5 mm. However, the thicknesses of the skull and the cerebrospinal fluid (CSF) layers vary greatly depending on the location. Hence, we measured these values over several cross-sectional slices of the anatomical head model to obtain averaged values. The thinner regions of the skull tend to coincide with wider SAS. Moreover, since we consider affixing the implant to the dura, the range for the skull thickness we present in Fig. 2 is the mean minimum thickness over the cross-sections, whereas the CSF layer thickness is the mean maximum SAS width. This selection was made, because we consider its benefit for both safety and wireless performance to maximize/minimize the distance between the implant and the cortex/wearable part.

Table 2 lists the thickness of each tissue layer within the four regions we have considered in our model. In order to model the antenna at a specific region, we have assigned the corresponding layer thicknesses over the whole ellipsoid. However, since the separation between the implant and wearable part (and the material composition at this location) is dominant for the system's performance, we expect the thickness variations at other regions to have comparatively negligible impact on it.

Table 2: Tissue thickness in different location [mm]

Position \ Tissue	FA	FP	PA	PP
Skin	2	2	2	2
Fat	2	2	2	2
Muscle	2	2	2	2
Skull	5.2	4.0	3.9	8.5
Dura	0.5	0.5	0.5	0.5
CSF	6.1	7.2	7.9	4.9

III. RESULTS AND DISCUSSION

ANSYS HFSS uses the finite element method (FEM) to generate the electromagnetic field solutions. To obtain a high-level accuracy, the mesh size needs to be small enough. HFSS uses iterative process to refine the mesh by minimizing the change in the solution between consecutive iterations. In HFSS, the default parameter to evaluate the convergence of the solution of a problem with a single excitation port is the S-parameter magnitude. Typically, it converges before the far field parameters. Therefore, in this work, we monitored the expression cache of τ , D and e_r in each iteration to ensure the accuracy and reliability of the results. In the last iteration of the mesh refinement, all these parameters were changing less than 0.07%.

For comparison, we also modelled the antenna system in a seven-layer block phantom with a surface area of $30 \times 30 \text{ cm}^2$. The layer thicknesses in the block phantom were identical to those in semi-anatomical model. Here the brain layer thickness was set to 7.5 cm so that the total thickness of the block was 25.2 cm. In our previous work, we have shown thorough experiments in liquid phantom [7] that the antenna system is robust toward moderately large rotational and translational misalignments between the wearable and implant parts [7] and thus we omit this analysis here.

A. Impact of antenna location

To facilitate the implementation of the wearable part on the curved surface of the ellipsoid, we flattened the contact surface between the two locally. However, since the curvature radius is large in comparison with the size of the wearable part, we expect this to introduce minimal impact on the results. In order to evaluate the impact of the antenna location on its electromagnetic performance judiciously, we first set the thickness for each layer of the head model to the values from the FP position. In this way, we can isolate the impact of the location (different curvature radii and impact of the anatomical part of the model) from the impact of variable tissue layer thicknesses. For comparison, we performed the same simulation in the layered block model with identical layer thicknesses.

Figure 3 shows the simulated power transfer efficiency with different implant locations. The results verify that the implant position has negligible impact on τ . This is because only the dielectric properties of tissue types closest to the antenna are determinant for its impedance. For the same reason, the result from the block phantom, shown with the black dashed line, also matches closely with those from the semi-anatomical model. This implies that the simple block phantom model is adequate for initial antenna impedance tuning.

Figure 4 shows the antenna radiation efficiency with different implant locations. The location causes a clear level shift in the radiation efficiency, but does not change

its peak frequency. Generally, the highest efficiency occurs in PP region, with the peak value of 0.60% at 925 MHz. The lowest efficiency occurs in the FP region at the lower location with its maximum value of 0.38%. The result from the block phantom model lies close to the mean value of those from the semi-anatomical model, but there is a difference in the frequency of the peak value, which shifts to 880 MHz in the block model.

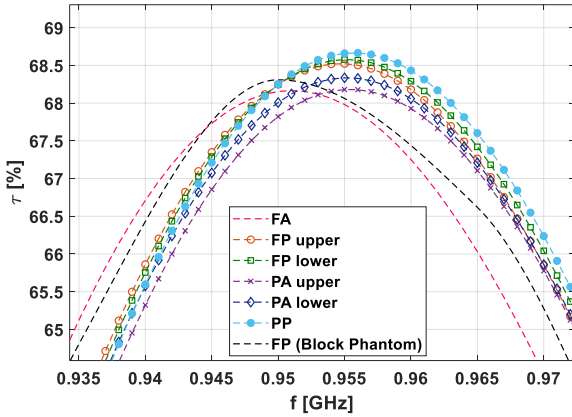


Fig. 3. Simulated power transfer efficiency in the semi-anatomical head model and the block phantom model.

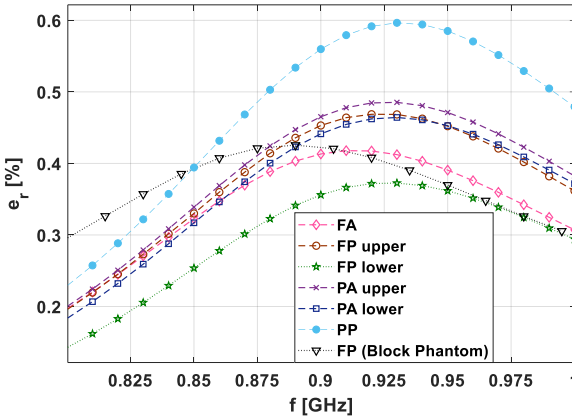


Fig. 4. Simulated antenna radiation efficiency in the semi-anatomical head model and the block phantom model.

As shown in Fig. 5, the antenna directivity varies up to 1.5 dB between the different implant locations. In comparison, the block phantom model underestimates it over the whole frequency range. Overall, we conclude that although 1.5 dB maximum variation in D between the six locations is clearly noticeable, it is relatively smaller than that observed in the radiation efficiency (Fig. 4).

Figure 6 shows the attainable read range computed from Equation (1) with the simulated quantities from the six locations and the block phantom. The peak value of

d_{tag} varies from 0.9 m to 1.1 m around the frequency 930 MHz. Here the peak value of the result from the block phantom is close to the minimum of those from the semi-anatomical model.

In general, the implant location has relatively larger influence on D and e_r and very little impact on τ . Nonetheless, the antenna shows robustness toward the location in the semi-anatomical model: the peak value of attainable read range varies only ± 10 cm around 1 meter with no shift in the center frequency of the peak value.

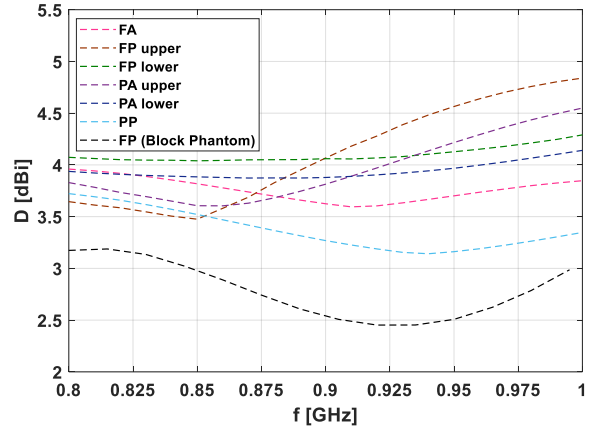


Fig. 5. Simulated antenna directivity in the semi-anatomical head model and the block phantom model.

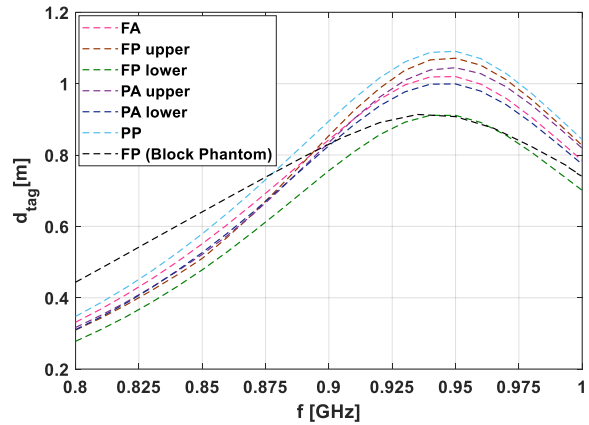


Fig. 6. Simulated maximum attainable read range in the semi-anatomical head model and the block phantom model.

B. Impact of antenna orientation

Due to the structure limitation of the block phantom model, it cannot be expected to predict the correct relationship between the antenna orientation and its electromagnetic performance. This information is valuable for evaluating the antenna feasibility in the real implementation where the orientation of the implant part is difficult to control. Therefore, we modelled the antenna

system in the semi-anatomical model at the previously discussed six locations with a clockwise rotation around the x-axis with a step of 20 degrees at the frequency of 950 MHz. According to the simulated results shown in Fig. 7, the rotation of the antenna introduces a periodically varying fluctuating response in e_r and D

versus the rotation angle, but overall the magnitude of the fluctuation remains below 10 %. Consequently, the attainable read range remains between 0.9 meter and 1.2 meters implying that the impact of the rotation is similar in magnitude as the impact of the location discussed above.

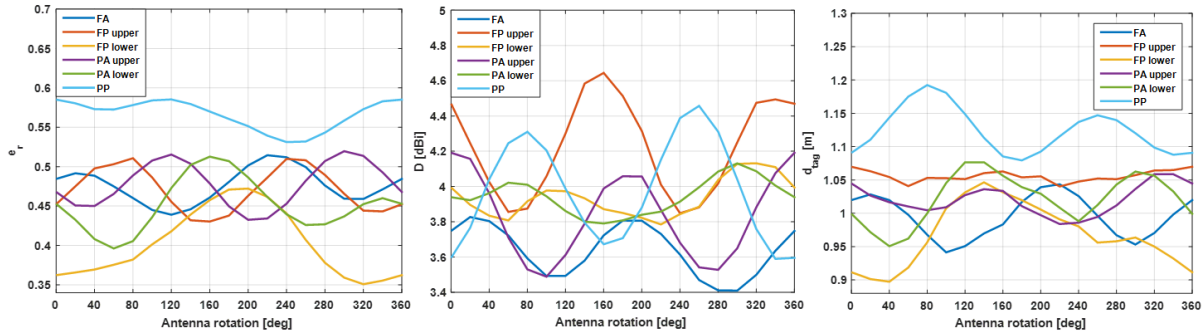


Fig. 7. Simulated results at six implant locations in the antenna rotation test.

C. Impact of variable CSF and skull thickness

To assess the impact of anatomical variability, we changed the thickness of the two most variable tissue layers; skull and CSF stepwise over intervals that cover the ranges shown in Fig. 2 and discussed in Section II.C. First, we set all the layer thickness to the values from the PA lower location (see Table II) and then increased the thickness of the skull from 3 mm to 13 mm with a step of 2 mm. According to the results shown in Fig. 8, D , e_r and d_{tag} decrease notably with the increase in the skull thickness. When the thickness is above 1 cm, the attainable read range drops below 0.5 m. The reason behind this is that the increase in the separation between the implant and wearable part weakens the electromagnetic coupling between the two.

by changing its thickness from 2.5 mm to 12.5 mm with a step of 2 mm while the other layer thicknesses were fixed. Figure 9 presents the simulated results. The decreasing trend in D with increasing layer thickness is similar to that observed in the case of the skull. However, overall the change is smaller. Likewise, the change in e_r versus the layer thickness shows similar character as in the case of skull thickness. However, here the separation (and therefore the coupling) between the implant and wearable parts remains constant and correspondingly the change in e_r is smaller and contributed to the increase in the amount of the high-conductivity CSF in the proximity of the antenna which increases the ohmic loss. Overall, the attainable read range remained at approximately 1 meter as the CSF layer thickness reached 12.5 mm.

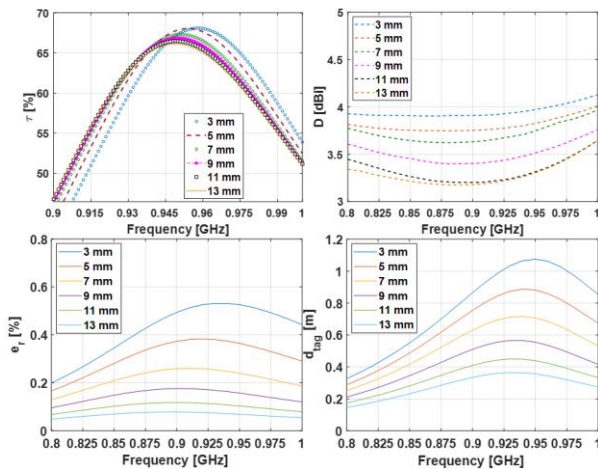


Fig. 8. Simulated results with the continuous change in the thickness of skull layer.

A similar test was conducted for the CSF layer

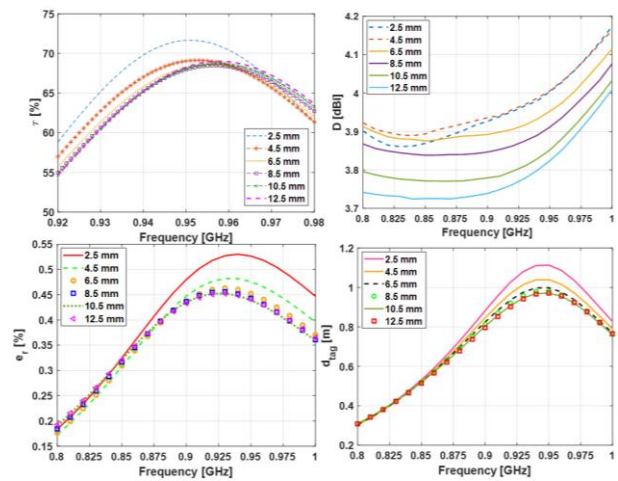


Fig. 9. Simulated results with the continuous change in the thickness of CSF layer.

VI. CONCLUSION

We evaluated the robustness of a spatially distributed implantable antenna system carrying an RFID microsystem toward several sources of variability that are likely to occur in practice. To achieve this, we used a semi-anatomical human head model based on a layered ellipsoid to mimic the human head environment with freely adjustable tissue layer thickness. The antenna system provided approximately consistent performance at six different locations covering most of antenna placements on the head and insensitivity toward antenna orientation with respect to the head. Moreover, the attainable read range of the implanted RFID remained above 0.5 m with the thickness of the skull reaching 1 cm. These results ensure the feasibility of our antenna system as a wireless platform in brain care applications further.

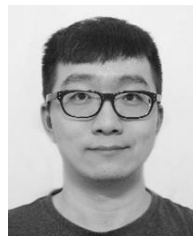
Our ongoing and future work focuses on integrating physiological sensors into the evaluated antenna system and development of a wearable part that provides circular polarization.

ACKNOWLEDGMENT

This research was funded by Academy of Finland, Jane and Aatos Erkkö Foundation.

REFERENCES

- [1] R. M. Neely, D. K. Piech, S. R. Santacruz, M. M. Maharbiz, and J. M. Carmena, "Recent advances in neural dust: Toward a neural interface platform," *Current Opin. Neurobiol.*, vol. 50, pp. 64-71, 2018.
- [2] M. W. A. Khan, L. Sydänheimo, L. Ukkonen, and T. Björninen, "Inductively powered pressure sensing system integrating a far-field data transmitter for monitoring of intracranial pressure," *IEEE Sensors J.*, vol. 17, no. 7, pp. 2191-2197, 2017.
- [3] M. J. Cook, T. J. O'Brien, S. F. Berkovic, et al., "Prediction of seizure likelihood with a long-term, implanted seizure advisory system in patients with drug-resistant epilepsy: A first-in-man study," *Lancet Neurol.*, vol. 12, no. 6, pp. 563-571, 2013.
- [4] E. Kampianakis, A. Sharma, J. Arenas, and M. S. Reynolds, "A dual-band wireless power transfer and backscatter communication approach for implantable neuroprosthetic devices," *2017 IEEE International Conference on RFID (RFID)*, Phoenix, AZ, pp. 67-72, 2017.
- [5] C. W. L. Lee, A. Kiourti, and J. L. Volakis, "Miniaturized fully passive brain implant for wireless neuropotential acquisition," *IEEE Antennas and Wireless Propagation Letters*, vol. 16, pp. 645-648, 2017.
- [6] H. N. Schwerdt, F. A. Miranda, and J. Chae, "Wireless fully passive multichannel recording of neuropotentials using photo-activated RF back-scattering methods," *IEEE Transactions on Microwave Theory and Techniques*, vol. 63, no. 9, pp. 2965-2970, 2015.
- [7] S. Ma, L. Ukkonen, L. Sydänheimo, and T. Björninen, "Split ring resonator antenna system with implantable and wearable parts for far field readable backscattering implants," *Proc. IEEE AP Soc. Intl. Symp. on Antennas and Propag.*, San Diego, CA, USA, pp. 1689-1690, 2017.
- [8] G. A. E. Vandenbosch, "State-of-the-art in antenna software benchmarking: Are we there yet?," *IEEE Antenna and Propagation Magazine*, vol. 56, no. 4, Aug. 2014.
- [9] T. Björninen, L. Sydänheimo, and L. Ukkonen, "Development and validation of an equivalent circuit model for UHF RFID IC based on wireless tag measurements," *AMTA Symp.*, Bellevue, WA, USA, pp. 6, 2012.
- [10] S Gabriel, R W Lau, and C Gabriel, "The dielectric properties of biological tissues: III. Parametric models for the dielectric spectrum of tissues," *Phys. Med. Biol.*, vol. 41, no. 11, pp. 2271-2293, 1996.
- [11] IT'IS Foundation, Tissue Properties [Online]. Available: <https://www.itis.ethz.ch/virtual-population/tissue-properties/downloads>
- [12] A. Drossos, V. Santomaa, and N. Kuster, "The dependence of electromagnetic energy absorption upon human head tissue composition in the frequency range of 300-3000 MHz," *IEEE Trans. Microwave Theory Techn.*, vol. 48, no. 11, pp. 1988-1995, 2000.
- [13] A. Bashkatov, E. Genina, Y. Sinichkin, V. Kochubey, N. Lakodina, and V. Tuchin, "Glucose and mannitol diffusion in human dura Mater," *Biophysical J.*, vol. 85, no. 5, pp. 3310-3318, 2003



Shubin Ma received the B.E. degree in Communication Engineering from Xi'an University of Posts and Telecommunications, China, in 2011 and the M.Sc. (Tech.) degree from Tampere University of Technology,

Finland, in 2017.

He is currently pursuing the Ph.D. degree with the BioMediTech Institute and Faculty of Biomedical Science and Engineering at Tampere University of Technology. His research interests include electromagnetic modelling, antenna designs, and implantable biomedical systems.



Lauri Sydänheimo received the M.Sc. and Ph.D. degrees in Electrical Engineering from the Tampere University of Technology (TUT), Tampere, Finland. He is currently a Professor with the Faculty of Biomedical Sciences and Engineering, TUT.

He has authored more than 200 publications in radio-frequency identification tag and reader antenna design and wireless system performance improvement. His current research interests include wireless data communication and wireless identification and sensing.



Leena Ukkonen received the M.Sc. and Ph.D. degrees in Electrical Engineering from the Tampere University of Technology (TUT), Tampere, Finland, in 2003 and 2006, respectively.

She is currently a Professor and Academy Research Fellow with the Faculty of Biomedical Science and Engineering, TUT, Tampere, where she is leading the Wireless Identification and Sensing Systems Research Group.



Toni Björninen received the M.Sc. and doctoral degrees in Electrical Engineering in 2009 and 2012, respectively, from Tampere University of Technology (TUT), Tampere, Finland.

He is currently an Academy of Finland Research Fellow in Bio-MediTech Institute and Faculty of Biomedical Sciences and Engineering in TUT. He has been a Visiting Postdoctoral Scholar in Berkeley Wireless Research Center in UC Berkeley and in Microwave and Antenna Institute in Electronic Engineering Dept., Tsinghua University, Beijing. His research focuses on technology for wireless health including implantable and wearable antennas and sensors, and RFID-inspired wireless solutions.

Björninen is an author of more than 140 peer-reviewed scientific publications. He is a Senior Member of IEEE and serves as an Associate Editor in IET Electronics Letters and IEEE Journal of Radio Frequency Identification.

Multiple Human Targets Detection and Localization Using Leaky Coaxial Cable Sensing Technique

Qiao Guan^{1,2}, Hongmin Lu^{1,2}, Chongchong Chen¹, and Chuanxia He²

¹ School of Electronic Engineering
Xidian University, Xi'an, Shaanxi 710071, China
guanqiao@stu.xidian.edu.cn, hmlu@mail.xidian.edu.cn, ccchen@stu.xidian.edu.cn

² Key Lab of High-Speed Circuit Design and EMC
Ministry of Education, Xidian University, Xi'an, Shaanxi 710071, China
guanqiao@stu.xidian.edu.cn, hmlu@mail.xidian.edu.cn, hechuanxia@stu.xidian.edu.cn

Abstract — Leaky coaxial cable (LCX) not only widely applies to the wireless communication systems, but also used as a LCX sensor for the intrusion detection systems (IDS). For evaluating the usability of the specialized LCX, the electrical parameters and the radiation pattern of the LCX sensor are measured. Moreover, in order to achieve the multiple targets localization, the novel location algorithm is proposed for the IDS based on the specialized LCX sensor in the VHF band. In this paper, the multiple targets are identified precisely by the synchronous subtraction, the time-domain digital pulse compression and the window function. By emitting a chirp signal into the LCX sensor, the echo signal containing the targets' response is received by the signal receiver (Rx). Then the pulse accumulation can be used for decreasing the noise signal in the digital signal processor (DSP), and the peak characteristics of the targets' echo signal are improved by the pulse compression and the Kaiser window function. Finally, by calculating the delay time of the echo signal after using the synchronous subtraction, the targets locations are obtained. The results show that transmission attenuation of the specialized LCX is 0.75 dB/100m and its coupling Loss is 71.63dB, and S_{11} is -39.9dB when the central frequency is 100MHz. The range resolution of the intruder detection system based on LCX sensor is as small as 3.32m and the positioning accuracy is less than 0.8m, which realizes the multiple targets detection and good localization results.

Index Terms — Aperture and pulse compressing, electromagnetic sensor, multiple targets.

I. INTRODUCTION

Leaky coaxial cable(LCX) is similar to the coaxial cable except the slotted apertures on its outer conductor.

Hence the LCX can achieve the wave radiation through the outer conductor by the aperture antenna theory [1]. Since the LCX has two functions that of the signal transmission and the electromagnetic wave radiation, the LCX has been applied in the perimeter intruder detection system (IDS), train communication and the MIMO application [2,3,4]. A LCX sensor consisting of two LCXs can be used in IDS, and these two specialized LCX are placed parallel. One LCX emits the detection signal, and the other LCX receives the echo signal, so the two LCXs form a detection area in space. By distinguishing the change of the echo signal, it will achieve the purpose of the target localization.

In practice, the modern IDS have higher requirements for the effective distance, the range resolution, the accuracy of measurement and the electronic countermeasures. Meanwhile, little attention has been devoted to the multiple targets localization, and most of IDS based on LCX sensor [5,6] cannot provide the good positioning accuracy and the range resolution.

In this paper, an IDS based on the LCX sensor for multiple targets localization is realized by introducing the synchronous subtraction, the pulse compression [7] and the window function. When the targets enter the LCX sensor detection area, the echo signal is subtracted synchronously, then the process of pulse compression and the Kaiser window function make the subtraction results in a good performance, which provide the good peak characteristics. In addition, the pulse accumulation can be used for decreasing the noise signal, which can improve the anti-interference ability and flexibility. Compared with the common IDS based on LCX sensor, the proposed signal processing algorithm has the advantages of the smaller range resolution and the higher positioning accuracy.

II. DESIGN OF INTRUDER DETECTION SYSTEM BASED ON LCX SENSOR

A. Location method

The structure of the LCX is different from that of the conventional coaxial cable. As shown in Fig. 1, the LCX consisted of the inner conductor, the insulation medium, the outer conductor and the sheath from inside to outside in sequence. The outer conductor is engraved with periodic slots. The coupling loss, the frequency band and the transmission attenuation are its important electrical performance indexes [8,9]. Table 1 shows the detail information of the LCX.

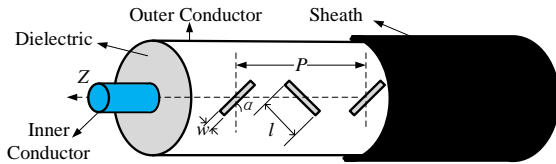


Fig. 1. Configuration of the leaky coaxial cable.

Table 1: The detail information of the LCX

Aperture		LCX	
Patch <i>P</i>	1 meter	Diameter of inner conductor	17.8 mm
Angle	45 deg	Thickness of outer conductor	0.1 mm
Width <i>w</i>	3 mm	Diameter of the insulation medium	42 mm
Length <i>l</i>	130 mm	Thickness of Sheath	8 mm

LCX sensor is composed of two identical LCX. As shown in Fig. 2, a chirp signal is transmitted from the signal source (*Tx*) once the IDS begin to work. When several targets step into the detection field which is established by the LCX sensor, the field will be disturbed and the target can be located by identifying the small disturbance.

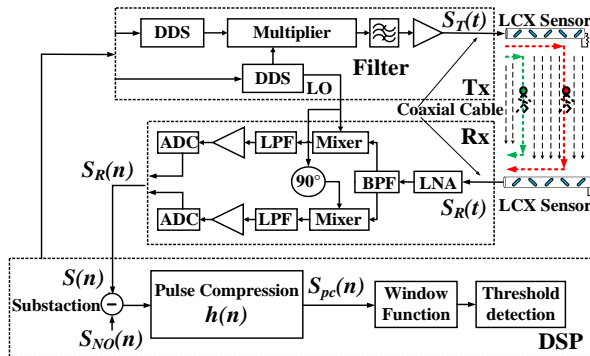


Fig. 2. IDS based on leaky coaxial cable sensor.

The chirp signal is defined in Fig. 3. The pulse width $t_R=100\text{ns}$, the pulse cycle $T_R = 10\mu\text{s}$, the start frequency $f_a = 80\text{MHz}$, the stop frequency $f_b = 120\text{MHz}$, the bandwidth $B = f_b - f_a$, τ_1 and τ_2 are the delay time of echo signal that are reflected by the targets.

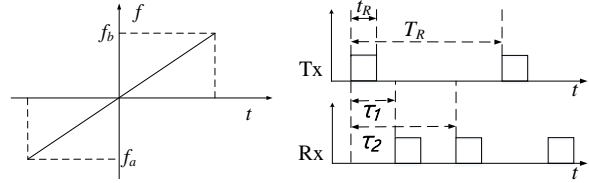


Fig. 3. Frequency and magnitude characteristics of the chirp.

The chirp signal can be written as:

$$s_T(t) = A \cdot \text{rect}\left(\frac{t - t_R/2}{t_R/2}\right) \cos(2\pi f_a t + \pi K t^2), \quad (1)$$

where A is the amplitude of the emitted chirp signal, Rect is a rectangular function, $K=B/t_R$.

When there are N targets entering the detection area at the same time, there will be N echo signals received by the Rx. In this case, these signals will be mixed after the reflections of those N targets. Assuming the delay time of the i -th echo signal is τ_i when chirp signal passes the i -th target. The mixed echo signal can be expressed as:

$$s_R(t) = \sum_{i=1}^N \{A_i \cdot \text{rect}\left(\frac{t - t_R/2 - \tau_i}{t_R/2}\right) \cdot \cos[2\pi f_0(t - \tau_i) + \pi K(t - \tau_i)^2]\} \quad (2)$$

where A_i is the amplitude of the i -th echo signal and A_i is related to coupling loss and transmission attenuation [9,10]. The delay time $\tau_i = 2R/c$, where R is the distance from signal generator to the target, velocity of signal $c = c_0 / \sqrt{\mu_r \epsilon_r} = 0.887 \cdot c_0$, where c_0 is the velocity of electromagnetic in free space [11]. And signal transmitted slower in the LCX because of $\epsilon_r > 1$.

B. Pulse compression and windows function

Multiple targets are usually difficult to be identified precisely. To improve the positioning accuracy and the range resolution, it needs to do further approach of the echo signal. Therefore, the pulse compression need to be taken into consideration. On one hand, the pulse compression approach improves the average power of the detection signal by using a wide pulse width, so that it ensures the sufficient distance, On the other hand, the pulse compression improves the performance of the range resolution by using a narrow pulse width. Therefore, it is a good solution to solve the contradictions between the long detection distance and precise range resolution.

As Fig. 2 shown, assuming the chirp signal [12] is $S_T(t)$, the echo signal is $S_R(t)$, then by the matching filter theory [13], the unit impulse response of the filter $h(n)$ can be calculated by:

$$h(n) = S_T^*(N - n - 1). \quad (3)$$

The echo signal $S_R(n)$ is stored as $S_{NO}(n)$ in the DSP when there are no targets in the detection area. The output signal $S_{PC}(n)$ is the convolution of the subtraction signal $S(n)$ and the unit impulse response $h(n)$, which can be written as:

$$S_{PC}(n) = S(n) * h(n) = \sum_{k=0}^{N-1} S(k)h(n-k), \quad (4)$$

where $S(n) = S_R(n) - S_{NO}(n)$. The amplitude of $S_{PC}(n)$'s peaks suggest the size of the targets, the number of the $S_{PC}(n)$'s peaks suggest the number of the targets, and the delay time t_R of the $S_{PC}(n)$'s peaks provide the information of the targets' positions. Besides, the windows function can be used for optimizing the peak characteristics, which is benefit to judge the targets by considering the threshold for warning alarm.

According to Equation (2), the digital pulse compression process in time-domain is the linear convolution operation of the echo signal $S_R(n)$ and the unit impulse response $h(n)$. When the chirp signal $S_T(n)$ is emitted to detect the target and returns, the echo signal $S_R(n)$ corresponds to a certain distance range. Therefore, the output signal $S_{PC}(n)$ is related to an intrusion location when the echo signal $S_R(n)$ passes through the matched filter, then the position is got by calculating the delay time from the output signal $S_{PC}(n)$.

III. MULTIPLE TARGETS LOCALIZATION WITH THE PROPOSED METHOD

A. Leaky coaxial cable sensor

As shown in Fig. 1, LCX consists of inner conductor, insulation medium, outer conductor, and the sheath. The inner conductor is a cylinder made of copper, and the diameter of the inner conductor is 17.3 mm. The diameter of insulation medium is 43 mm, the degree of foamed PE dielectric is 76%, the dielectric constant is 1.247 and dielectric loss angle tangent is $1.7e-5$. The outer conductor is defined as a PEC in the simulation software. In addition, some apertures are on the outer conductor, whose width $w = 4$ mm, $P = 1000$ mm and angle $a = 45$ deg, the length of the aperture $l = 120$ mm. Table 2 illustrates the experimental and simulation results of LCX.

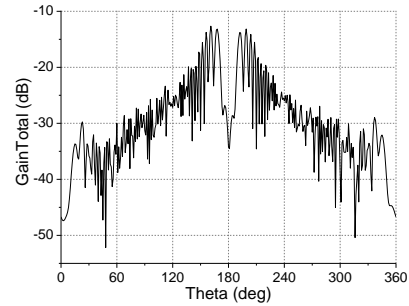
In Table 2, it can be seen that the LCX have a good match with the input port and the terminal port. The low transmission attenuation guarantees a long detection range, meanwhile, the coupling loss meets the requirement of the electromagnetic wave radiation. The

average S_{11} is -39.9dB in the simulation result, which illustrates the low reflection coefficient, therefore the leaky coaxial cable is well matched.

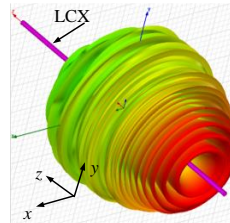
Table 2: Experimental and simulation results of the LCX (100 MHz)

Test Item	Simulation	Experiment
Characteristic impedance	51.3Ω	49.6Ω
Transmission attenuation	0.78dB/100m	0.75 dB/100m
Coupling loss	66dB	71.63dB
S_{11}	39.9dB	/

When the IDS works in the VHF band, the human target has the best response to the detection signal [13], which can avoid the false alarm caused by the small animal targets. Meanwhile, the relatively small transmission attenuation provides longer detection range. The radiation characteristics of the LCX are shown in Fig. 4.



(a) 2-D Radiation pattern



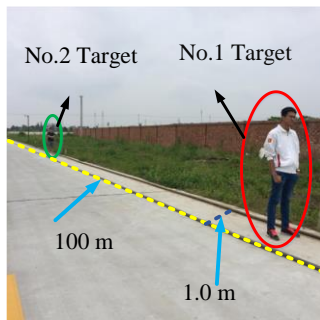
(b) Radiation characteristic in 3-D pattern

Fig. 4. Radiation patterns of the LCX in 2-D and 3-D.

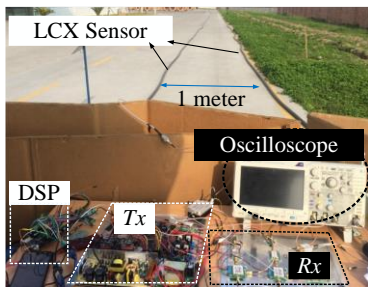
The radiation pattern shows that the LCX sensor has a steady radiation electric field on its axis direction. Compared with the traditional antenna, radiation pattern of the LCX has no main lobe with high radiation ratio and the front-to-rear ratio in Fig. 4, but LCX has an annular main lobe which is called the maximum radiation direction. In this case, the echo signal is possible and easy to be reflected directly by the targets and be transmitted to the Rx. In other words, when the target enters the detection area and disturbs the electromagnetic field, then the parameters of the original environment change, and the change suggests the position information.

B. The IDS based on LCX sensor

The multiple targets intrusion experiments were carried out as shown in Fig. 5 (a). Two stationary targets, namely No.1 target and No.2 target, stand in the axial of LCX sensor with the appointed distance, and there is no Doppler frequency shift and relative motion between the R_x and the targets. Figure 5 (b) is the illustration of the IDS, which consists mainly of T_x , R_x , LCX sensor and DSP .



(a) The multiple targets intrusion experiment



(b) The IDS based on LCX

Fig. 5. Multiple targets localization.

After the chirp signal emits (the pulse period $t_R = 100ns$, the pulse cycle $T=2\mu s$, the start frequency $f_a=80MHz$, the stop frequency $f_b=120MHz$), the echo signal is obtained and shown in Fig. 6.

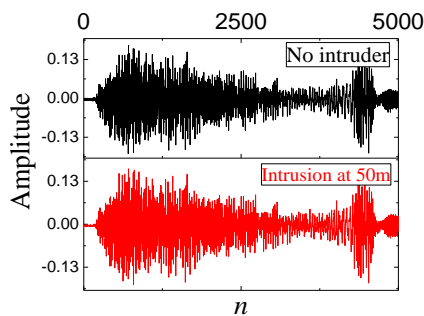


Fig. 6. The echo signal with and without human.

Where n is the sample sequence of the digital echo signal. Obviously, the response of the target information is mixed with the strong background noise.

As Fig. 7 shown, there is almost no difference between the system response and echo signal because the response of the target is too weak to distinguish from the system response, and the intruder information cannot be observed directly on those echo signals.

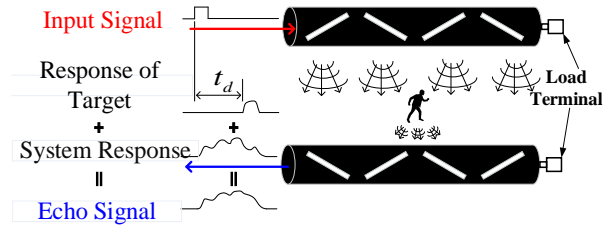


Fig. 7. Signal transmission characteristics.

In the experiments, those five different positions, namely 20m-30m, 10m-30m, 10m-50m, 10m-70m and 10m-90m are conducted respectively. When subtracting the echo signal without people from the normal echo signal with the two people echo signal synchronously after both echo signal is passing through the R_x , then the subtraction signal is obtained in Fig. 8, where there are two targets exist in the subtraction signal.

The pulse accumulation is a radar signal processing method, which can greatly reduce the noise of echo signal and improve the signal noise rate (SNR). Therefore, after the low-pass filter (LPF) and pulse accumulation, as shown in Fig. 8, it is easy to identify two targets by calculating the peaks of the five echo signals mentioned above. According to the radar principle, the range resolution of the IDS based on LCX sensor is $c \cdot t_R = 13.3m$ generally, while the range resolution can reach $c / 2 \cdot B = 3.32m$ after the pulse compression. Therefore, the echo signal will be aliasing and unable to identify multiple targets without the pulse compression when the distance between multiple targets is less than 13.3 meters. However, the multiple targets can be identified easily after the pulse compression as long as the distance between multiple targets is more than 3.32 m in theory.

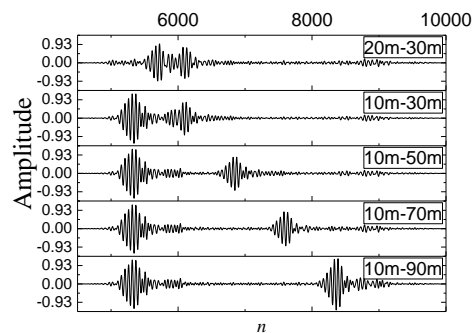


Fig. 8. Pulse compressing approach in 5 cases.

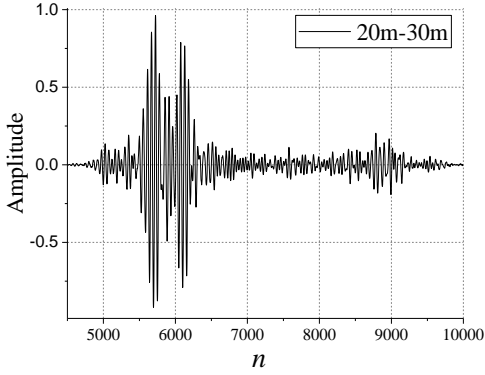


Fig. 9. The 20m-30m case after the pulse compression and the Kaiser window function.

However, the echo signal of two targets is indistinguishable in the 20m-30m case, which suggests a worse range resolution. In Fig. 9, it is easy to notice two peaks obviously by introducing the Kaiser window function after the pulse compression signal for further improvement in 20m-30m case.

Finally, a six-targets experiment is analyzed. The positions of the multiple targets are 10m, 20m, 30m, 50m, 70m and 90m along the axis of the LCX sensor. As Fig. 10 shown, the digital signal processing result of the six targets is obtained by the method including the subtraction synchronously, the pulse compression and the window function processing. Moreover, this method can achieve the high detection rate by identifying multiple targets. Setting the proper alarm threshold can improve the detection probability and reduce the failed detection rate.

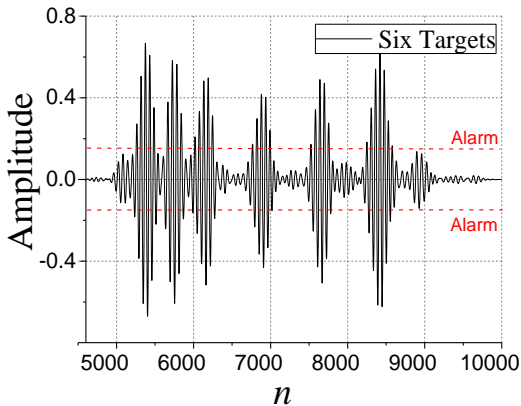


Fig. 10 Multiple targets detection result

The method can achieve high detection rate by identifying multiple targets. Setting the proper alarm threshold can improve the detection probability and reduce the failed detection rate and false alarm rate. The distance between the target and the transmitter can be calculated by the delay time of the chirp signal and the

echo signal. Table 3 is the detail information of the multiple targets localization result. For example, the IDS recognized the sample sequence $n=5348$ when the target is at the 10m (measured position), in this case, the delay time τ can be calculated by n , and the corresponding τ is 75.98ns. Then the calculated position can be obtained by:

$$R = \frac{\tau \cdot 0.887 \cdot c_0}{2} = 10.11 \text{ (m)}. \quad (5)$$

Table 3: The comparison of measured and calculated result of targets position

Sequence n	Delay Time τ_i	Measured Position	Calculated Position
5348	75.98 ns	10 m	10.11 m
5718	149.72ns	20 m	19.92 m
6093	221.17 ns	30 m	29.43 m
6849	378.45 ns	50 m	50.36 m
7609	523.42 ns	70 m	69.65 m
8363	682.51 ns	90 m	90.80 m

According to the difference between the measured positions and calculated positions, the new method reduces the range resolution and realizes the multiple targets localization of the IDS based on LCX sensor, and the positioning accuracy is about 0.8 m. Therefore, the pulse compression of the echo signal and the window function are introduced to optimize its peak characteristics of the targets, which proves to be an effective method for the multiple targets identification and localization.

VI. CONCLUSION

For perimeter intruder detection system based on the specialized LCX sensor, a new method consists of the digital pulse compression and the window function for improving peak characteristics of the target is proposed in this paper. The position of target can be determined by calculating the delay time after the subtraction synchronously, the low pass filtering processing, the pulse compression and the window function processing. The method mentioned above improves the range resolution and positioning accuracy. The multiple targets localization is achieved with the chirp signal (frequency range: 80MHz~120MHz). The range resolution is 3.32m, and the positioning accuracy is below 0.8m. The remote distance target localization and the environmental adaptability will be the next research work.

ACKNOWLEDGMENT

This work was supported by the Fundamental Research Funds for the Central Universities (JB160205).

REFERENCES

[1] J. H. Wang and K. K. Mei, "Design of leaky

- coaxial cables with periodic slots,” *Radio Science*, vol. 37, no. 5, pp. 1-10, 2016.
- [2] Q. Guan, C. C. Chen, and C. X. He, “A novel sensor using VHF zigzag-slotted leaky coaxial cable for intruder localization,” *Microw. and Opti. Tech. Lett.*, no. 60, pp. 634-639, 2018.
- [3] S. Okada, T. Kishimoto, K. Akagawa, et al., “Leaky coaxial cable for communication in high speed railway transportation,” *Radio & Electronic Engineer*, vol. 45, no. 5, pp. 224-228, 2010.
- [4] Y. Wu, G. Zheng, and T. Wang, “Performance analysis of MIMO transmission scheme using single leaky coaxial cable,” *IEEE Anten. & Wirel. Propa. Letters*, no. 16, pp. 298-301, 2017.
- [5] Q. Guan, X. F. Fan, Y. Liu, et al., “Research on VHF buried sensor using leaky coaxial cable techniques,” *Journal of Microw.*, vol. 33, no. 4, pp. 16-20, 2017.
- [6] K. I. Nishikawa, T. Higashino, K. Tsukamoto, et al., “Two dimensional position detection method using bi-directional leaky coaxial cable based on TDOA,” *IEEE Interna. Symp. on Personal, Indoor and Mobile Radio Commu.*, Tokyo, pp. 2167-2170, 2009.
- [7] A. Johnston, “Improvements to a pulse compression radar matched filter,” *Radio & Electronic Engineer*, vol. 53, no. 4, pp. 138-140, 1983.
- [8] C. Zhang, J. Wang, M. Chen, et al., “Radiation characteristic of the leaky circular waveguide with periodic slots,” *IEEE Anten. & Wirel. Propaga. Lett.*, vol. 11, no. 11, pp. 503-506, 2012.
- [9] A. Guan, C. C. Chen, and B. X. Song, “A study of designing circular polarization for leaky coaxial cable at 900 MHz,” *Progr. in Electromag. Research Lett.*, vol. 76, pp. 39-46, 2018.
- [10] J. H. Wang, “Leaky coaxial cable with circular polarization property,” *IEEE Transa. on Anten. and Propag.*, vol. 59, no. 2, pp. 682-685, 2011.
- [11] Y. Du, W. Li, Y. Ge, et al., “A high-frequency signal generator based on direct digital synthesizer and field-programmable gate array,” *Review of Scientific Instruments*, vol. 88, no. 9, pp. 096-103, 2017.
- [12] H. L. Pei, T. D. Abhayapala, and T. A. Lamahewa, “Multiple targets localization using wideband echo chirp signals,” *IEEE Transactions on Signal Processing*, vol. 61, no. 16, pp. 4077-4089, 2013.
- [13] A. Bergman, T. Langer, and M. Tur, “High spatial resolution, low-noise brillouin dynamic gratings reflectometry based on digital pulse compression,” *Optical. Letters*, vol. 41, no. 15, pp. 3643-3646, 2016.



Qiao Guan received the B.S. and M.S. degrees from the School of Electronic Engineering, Xidian University, Xi’an, China, in 2013 and 2015. He is currently pursuing his Ph.D. degree of the Electromagnetic and Microwave Technology in Xidian University. His research interest in the electromagnetic sensor, radar signal detection and estimation, electronics, and RF circuits.



Hongmin Lu, Professor, Ph.D. of Xi’an Jiaotong University, Postdoctoral Dellow of Xidian University of Electronic Science and Technology. Now he is a Professor at Xidian University, Chairman of Telecommunications Engineering Department, a Professor of National Key Laboratory of Antenna and Microwave Technology. His current research interests include the theory of high speed circuit and electromagnetic compatibility.

Conformal Load-Bearing Antenna Structure for MIMO Applications

David L. Zeppettella¹ and Mohammad Ali²

¹ Air Force Research Laboratory, Dayton, OH 45433, USA
david.zeppettella@us.af.mil

² Department of Electrical Engineering, University of South Carolina, Columbia, SC 29208, USA
alimo@enr.sc.edu

Abstract — A broadband, airfoil-integrated, VHF antenna is introduced for conformal load-bearing structures (CLAS) applications. A two-layer antenna is developed and the effects of integration with a composite sandwich structure are investigated. A prototype structure is fabricated that exceeds an octave of measured impedance bandwidth and simulated gain and pattern bandwidth. Envelope correlation coefficient (ECC) and simulated radiation patterns are used to gauge feasibility of the structure for use in a MIMO application on a twin-tail drone.

Index Terms — CLAS, multifunctional structure, structural antenna.

I. INTRODUCTION

While the use of unmanned air vehicles (UAV) has traditionally been restricted to military operations, a number of private sector firms have recently announced plans to provide some type of commercial service that involves the use of a UAV. Applications such as package delivery and providing internet access in remote areas have been proposed. Although the concept of operations and type of service being provided may vary, one requirement common to all applications is the need for wireless communication systems and antennas on-board the aircraft. One specific application that has drawn significant interest is Cognitive Radio [1-2] communication where spectrum allocated for other applications but not in use at a particular instant can be used by another communication system. For example, consider television broadcast channels. If some of the channels are not used, some time-opportunistic sensing and leveraging could allow communication services through those channels. Sensing and reuse is the key, and thus broadband antennas or reconfigurable antennas will play a significant role.

The focus of the present paper is VHF communication, namely 90 MHz and higher. The goal is to obtain as much bandwidth as possible without sacrificing pattern and gain. Traditional broadband

antenna solutions such as resistively matched antennas can provide broad bandwidths but suffer from very low gain [3]. Recent works on broadband matching of electrically small antennas using active circuits include the application of non-Foster active circuits [4-9]. The possibility of using non-Foster circuits to increase the bandwidths of a dipole [4], a monopole [5], a dipole [6], a loop and a broadband planar dipole [7] and a VHF monopole [8] antenna were studied. Although these methods provide useful performance improvements they are typically geared towards receiving application. Furthermore, they are complicated, and costly.

Given that many modern small and mid-sized UAVs are either fully or partially made of dielectric materials such as fiberglass or Kevlar composites, a new class of antennas that are integral to the mechanical structure of the UAV can be realized to provide superior performance characteristics. Such dual purpose structures have been termed generally as multi-function structures, and more specifically as Conformal Load-bearing Antenna Structures (CLAS) [10-13]. The key tenet of the CLAS concept is that a much larger antenna volume can be obtained by leveraging the outer surface area and structure of an air vehicle to implement large antennas or arrays, ultimately leading to increased effective aperture. Thus, from an RF perspective, this approach enables more efficient and broadband antennas. From an aircraft perspective, CLAS technology has minimal impact on vehicle weight and no impact on aerodynamic drag, unlike externally mounted blade antennas and pods that protrude into the airstream. However, CLAS design is a multi-disciplinary undertaking that must consider the desired RF performance, mechanical loading requirements, and properties of structural composite materials. Typically, a subcomponent of the UAV, such as the fuselage or a wing, is selected to be designed as a multi-function structure. To enable operation as an antenna, conductors of the proper thickness must be included with the composite structural materials, and such conductors need to be deposited or bonded to all other materials comprising the structure in a manner that does not

degrade mechanical performance.

As mentioned, the focus of this paper is to design and develop a broadband CLAS VHF antenna structure. The preliminary feasibility study of a VHF antenna for airfoil integration was presented in our conference paper [14] which included the design using copper foil and foam and parametric simulations of the antenna using FEKO. The work presented in this paper goes far beyond that. The objectives are to investigate if a broadband VHF CLAS assembly can be designed with significant bandwidth and nearly omni-directional pattern looking downward, study the effect of structural materials on bandwidth through Characteristic Mode Analysis, and validate simulated results through measurement of prototype structures. Finally, also investigate the potential for such CLAS components to be used in a MIMO configuration on a twin-tail UAV by computing the correlation coefficients and the patterns.

II. ANTENNA CONFIGURATION

As mentioned, the original geometry can be found in our previous paper [14]. The idea is to integrate the antenna into a composite airfoil such as shown in Fig. 1, and a cross-sectional schematic of the initial integration concept can be seen in Fig. 2. As seen, the antenna consists of two traces, Antenna Trace 1 and Antenna Trace 2, that are included at the interfaces of two of the four layers of dielectric materials making up the structure. Antenna Trace 1 is inserted between the lower skin and the first foam layer. Antenna Trace 2 is inserted between the two foam layers in the core of the structure. The Lower and Upper skins are made from dielectric materials commonly used in the fabrication of composite aircraft structures, e.g., fiberglass. In a practical specimen the antenna will be excited using a coaxial cable. For simplicity, the illustration in Fig. 2 shows a sinusoidal excitation as the feed. The separation between the Lower and Upper skins and the thicknesses of the different layers of dielectric materials are variables and depend on both the expected mechanical load and the desired antenna performance.

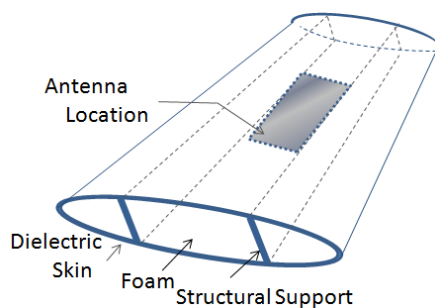


Fig. 1. Airfoil geometry and antenna location.

Initially the antenna design started without the presence of any dielectric materials to understand the

dependency of the antenna performance on conductive material design variables. Subsequently the dielectric materials were added on and adjustments for tuning were made. The design started with two rectangular conducting traces. The size of the larger conducting trace, e.g., Antenna Trace 1 is ultimately constrained by the size of the air foil, with more space being available span-wise than chord-wise, and a limit of 76 cm by 62 cm was considered. The thickness of conductive material considered was 127 μm . The initial length of the smaller conducting trace, e.g., Antenna Trace 2 was determined by assuming that the antenna is a quarter wave monopole sized to operate at the center of the band of interest (150 MHz). Thus the initial length was determined to be 50 cm; however, the structural composite materials into which the antenna will eventually be placed have a dielectric loading effect. To compensate for this, the initial length for the small rectangle was shortened to 40 cm, which corresponds to an operational frequency of 187.5 MHz in free space.

Antenna design was targeted towards obtaining as much bandwidth as possible within these and other dimensional constraints. The height between Antenna Traces 1 and 2 was varied and many other parameters were varied to arrive at an optimum design. These studies were conducted using FEKO. The design progress summary is illustrated in Fig. 3. It was found that a spacing of 3.5 cm resulted in good return loss bandwidth. Detail descriptions on the design evolution are available in [14]. Several key adjustments were made to the initial starting design, namely: (1) Two stubs and a slot were added to Antenna Trace 1, and (2) Antenna Trace 2 was moved slightly towards the slot from the outer edge to create an overhang.

The overhang feature was introduced to improve the impedance match by creating and controlling the equivalent shunt capacitance resulting from Antenna Trace 2. Table 1 shows the final dimensions.

This antenna serves as the baseline antenna for this paper and will provide a basis for comparison during the process of converting the initial concept into a CLAS design. Table 2 lists the antennas that will be discussed and gives a brief description of each. Antenna C indicates the design when integrated within composite materials (details given in Section III. B), while Antennas D and E each represent pairs of antennas for MIMO operation (details given in Section III. E).

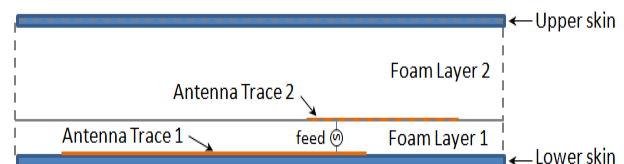


Fig. 2. Antenna and materials layout, cross-sectional view.

Table 1: Dimensions of the proposed antenna

Parameter	cm	Parameter	cm
W	62	g	12
L	76	h	8
c	40	l	14
d	22	w	6
e	3.5	i	8
s	58		

Table 2: List of antennas

Name	Description
Antenna A	Copper sheet and air
Antenna B	Expanded metal and foam
Antenna C	Composite sandwich
Antenna D	Dual parallel tail
Antenna E	Dual canted tail

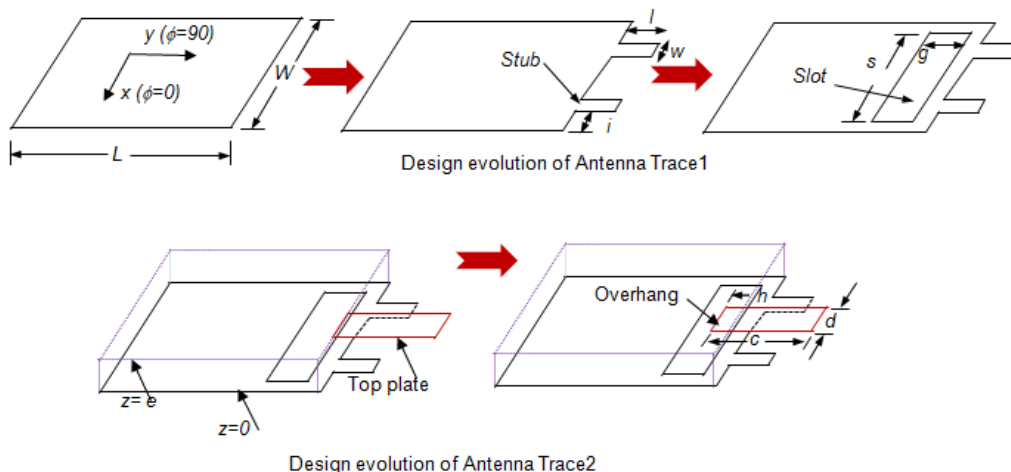


Fig. 3. Antenna design evolution.

III. RESULTS

A. Antenna A – No dielectric materials

Simulation results (bandwidth and pattern)

Simulated S_{11} results of Antenna A, with dimensions noted in Table 1, are shown in Fig. 4. As the plot shows, the S_{11} is below -10 dB from approximately 96 MHz to 241 MHz. Thus a 2.5:1 bandwidth is achieved.

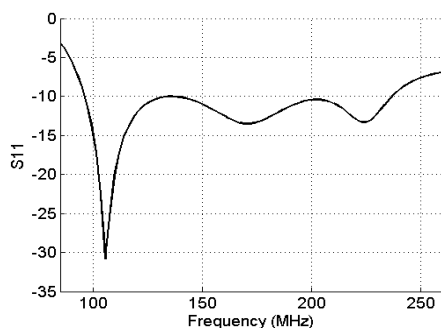


Fig. 4. Simulated S_{11} for Antenna A.

Figure 5 shows simulated radiation patterns for the three principal planes at 97 MHz and 240 MHz. The patterns are consistent over much of the frequency band with some distortion present at the upper end. It should be noted that although the $\theta=90$ degree pattern at 240 MHz shows a null along what would be the azimuth for an aircraft, there are still lobes directed both above and

below this plane. Thus, it is reasonable to expect that RF systems utilizing the antenna would continue to function across the band, albeit with some degradation at the higher frequencies.

Characteristic mode understanding

To understand the return loss bandwidth of the antenna from a Characteristic Mode (CM) theory point of view, CM simulations were conducted using FEKO. The objective was to determine the different modes that may have resulted from the antenna of Fig. 3 and their role in determining the overall antenna operating bandwidth.

CM analysis has been applied by other researchers to understand antenna modes, modal significance, and bandwidths from a CM point of view [15-17].

CM theory was introduced in the late 1960's by Garbacz who proposed that characteristic currents could be determined through analysis of the scattering matrix [18]. These characteristic currents are real surface currents on a conducting body that depend only on the geometry of the body and are independent of any external excitation. Later, Harrington and Mautz expanded upon the theory by proposing that the impedance matrix could also be used for this purpose [19, 20] through solution of the weighted eigenvalue equation:

$$[X] \vec{J}_n = \lambda_n [R] \vec{J}_n, \quad (1)$$

where R and X represent the real and imaginary part of the impedance matrix of the conducting body, λ_n are the

eigenvalues, and \vec{J}_n are the characteristic currents.

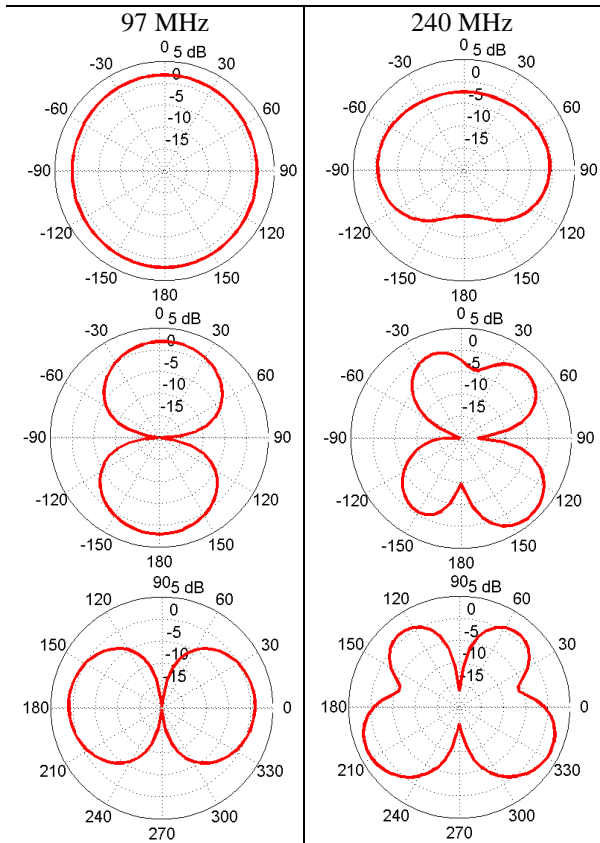


Fig. 5. Radiation patterns at $\phi = 0$, $\phi = 90$, and $\theta = 90$ planes.

In general, the magnitude of the eigenvalue, $|\lambda_n|$, is a figure of merit that indicates how well a given mode radiates. Modes for which $|\lambda_n|$ is small are the most effective radiators, while large values of $|\lambda_n|$ indicate that a mode is a poor radiator [21]. Resonance is indicated when the value of λ_n is zero.

One use of the eigenvalue is to calculate the so-called modal significance, as given by (2):

$$MS = \left| \frac{1}{1 + j\lambda_n} \right|. \quad (2)$$

Modal significance is essentially an alternative representation for eigenvalues and it represents the normalized amplitudes of the eigencurrents [22]. In (2) it is easily observed that modal significance takes on a value of one in the case of resonance ($\lambda_n = 0$), and goes to zero for large values of λ_n [23]. A useful application of modal significance is to determine which characteristic modes are significant in terms of contributing to radiated power. A mode is considered significant when $MS > \frac{1}{\sqrt{2}}$

while the case of $MS < \frac{1}{\sqrt{2}}$ indicates a non-significant mode [24].

A modal significance plot computed using FEKO for Antenna A is shown in Fig. 6. The dashed line in the figure indicates a modal significance of 0.7; thus it is easily seen that modes 1, 2, and 4 are significant while mode 3 is non-resonant and does not contribute to radiated power over the frequency band of interest. Furthermore, considering the modal half-power bandwidth, defined as:

$$BW_n = \frac{f_u - f_l}{f_r}, \quad (3)$$

where f_u and f_l are the upper and lower frequencies at which $MS = 0.7$, f_r is the resonant frequency ($MS = 1$), and the subscript n denotes the n^{th} mode, the bandwidth of mode 2 is found to be 51%, mode 4 has a bandwidth of 29%, and mode 1 has a bandwidth of 19%. One interesting aspect of the modal significance plot is that there are no significant modes between about 115 and 150 MHz (Fig. 6); yet the S_{11} plot shown in Fig. 4 shows the match is good over this frequency band. It would initially seem that there should be another dominant mode over this frequency range. The concept of modal interaction described in [17] can be used to explain this discrepancy which states that modal interactions between the modes essentially create a matching circuit that provides a good S_{11} match even in the absence of $MS \geq 0.7$.

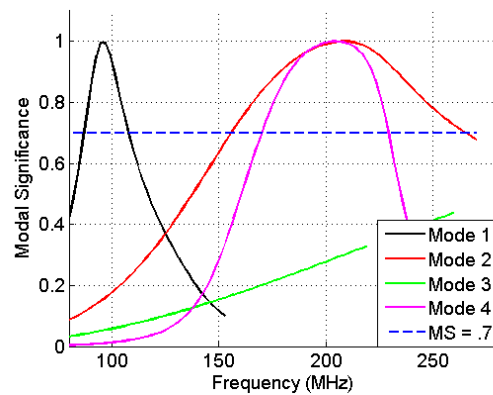


Fig. 6. Modal significance for Antenna A.

The current distribution on the antenna was also studied using FEKO. Figure 7 shows the current distribution at three different points within the frequency band over which S_{11} is below -10 dB. It is apparent that the stubs become more active and the current is more concentrated toward the edges of Antenna Trace 1 at higher frequencies.

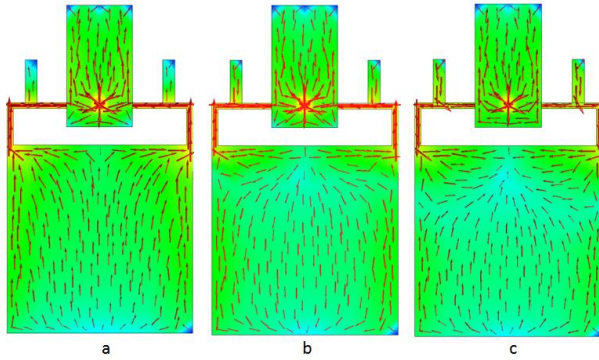


Fig. 7. Current distribution for a) 96 MHz, b) 142 MHz, and c) 238 MHz.

Experimental results

A prototype of Antenna A was fabricated using the dimensions detailed in Table 1. The antenna traces were precision cut from a roll of copper sheeting with a width of 91 cm (3 ft) and a thickness of 127 μm (5 mil) to enable a continuous conductive surface. Two 3.5 cm thick pieces of Rohacell foam were cut from a large block to serve as a spacer between the traces. An L-shaped piece of polyethylene was attached to the sides of the foam sheets with plastic screws to add mechanical stiffness. The antenna traces were then positioned with proper orientation to each other on opposite sides of the foam spacer and secured in place with masking tape. A photo of the prototype with the slotted trace visible is shown in Fig. 8 (a).

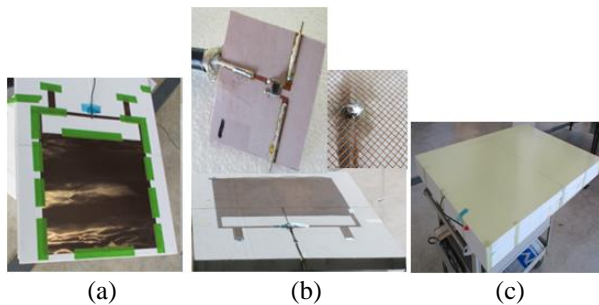


Fig. 8. (a) Antenna A, (b) Antenna B with insets showing feed board and nature of mesh, and (c) Antenna C.

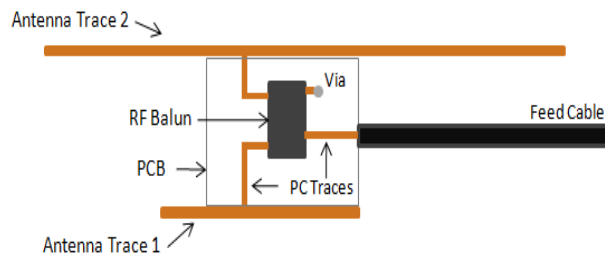


Fig. 9. Cross sectional view of feed showing the orientation of the balun PCB.

At the feed point, a section of foam was removed between the traces, and a PCB containing an RF balun from RF Micro Devices (part no. RFXF9503) was positioned between the upper and lower traces. The PCB, which is shown on the upper right of Fig. 8 (b), had a 50 ohm microstrip line at the input and two traces on the output side to attach wires for connection to the antenna traces. A coaxial cable was soldered directly to the PCB input, and the other end of the cable was terminated with an SMA connector. The PCB is 3.5 cm wide, and is installed vertically between the two copper layers to minimize wire lead length. Wires with a diameter of 0.9 mm were soldered to each PCB output terminal, and the wires were in turn soldered to the copper sheets at the feed point. Figure 9 is an illustration of the feed assembly.

Upon completing assembly of the antenna, S_{11} measurements were taken. Given the VHF operating range of the antenna, the measurement was made in a large aircraft hangar with a ceiling height of approximately 80 feet. The antenna was placed on top of two large foam blocks at a height of approximately 1.5 m above the floor and secured with tape. An Agilent E5071CVNA was placed on a cart and positioned next to the foam blocks with the connection between the VNA cable and antenna feed cable secured to the top of the foam block with tape.

Simulated and measured S_{11} data are compared in Fig. 10. In terms of bandwidth within S_{11} below -10 dB the two results are in good agreement. The measured S_{11} is below -10 dB from 93 MHz to 230 MHz, for a bandwidth ratio of 2.47:1. This agrees well with the simulated -10 dB bandwidth of 96 to 241MHz (2.5:1 ratio). The main discrepancy is at the upper end of the frequency band. This could be due to a slight difference in the feed between the model and the prototype antenna. A larger diameter wire (5 mm) was used in the simulation than was available when the prototype was constructed, and the smaller 0.9 mm wire and thin PCB trace used to feed the prototype could have caused this reduction in the bandwidth.

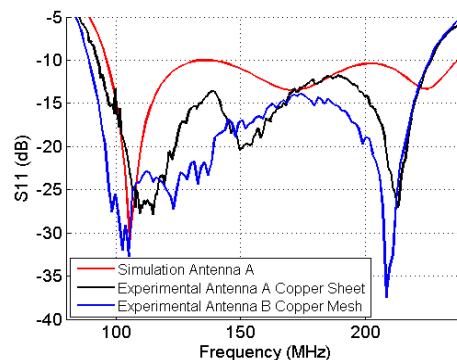


Fig. 10. Comparison of simulated and measured S_{11} of prototype antennas.

To move toward a more structural version of the antenna, Antenna B was constructed using expanded metal instead of the solid copper sheets. Solid copper cannot be used in structural composite applications because it is difficult to bond to a component, and, even if this were possible, it would represent a significant parasitic weight increase for the structure. Expanded metal is commonly used on composite aircraft for lightning strike protection, and it is essentially a metallic mesh that is produced by interweaving small diameter wires or stamping a mesh pattern from a solid conductive sheet. The porous nature of the mesh allows structural epoxy to flow through and bond the mesh to the surface of a composite part during curing. From a mechanical perspective, the mesh is easier to conform to complex shapes and contributes less parasitic weight than a solid sheet. A mesh material from Astroseal Products Mfg. Corp. having grid dimensions of 1 mm by 1.6 mm and a thickness of 130 μ m was used for the prototype antenna. Fig. 8 (b) shows Antenna B with Antenna Trace 1 visible. The nature of the mesh material can be seen in the close-up on the upper left, which shows the area around the feed. The S_{11} measurement was repeated, and the results are shown by the blue line in Fig. 10. It was found that Antenna B had a slightly higher bandwidth ratio (2.5:1) than Antenna A (2.47:1). This came about because Antenna A was inadvertently fabricated with 5 mm less vertical spacing between the upper and lower traces.

B. Structural integration effects

Simulation results (bandwidth and pattern)

As seen in Fig. 2, the proposed antenna would have to be integrated within a structural sandwich containing various dielectric materials. The effects of such integration were studied through simulations in FEKO. Initially the configuration shown in Fig. 11 was simulated. As seen, Antenna Trace 1 is in direct contact with the Lower skin. Antenna Trace 2 is much farther away from the Upper skin. The thickness of the Lower and Upper skins was 5 mm. Although it is recognized that some additional supporting mechanical structure would be required, this was not included in the initial simulations. It was also assumed that the airfoil would have a significant through-thickness dimension because only a large airfoil would be able to accommodate the 1.16 m by 0.62 m antenna.

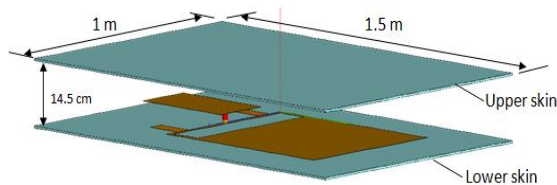


Fig. 11. Addition of dielectric sheets to represent a composite sandwich structure (Antenna C).

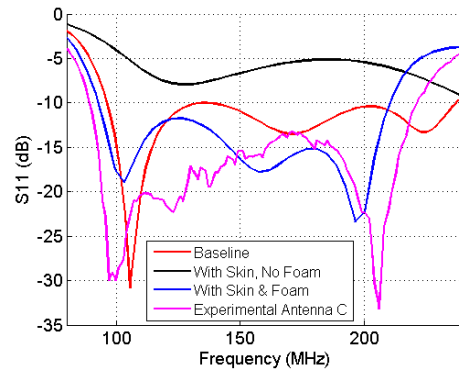


Fig. 12. Simulated S_{11} of antenna in the presence of dielectric skins. Cases with and without foam are shown.

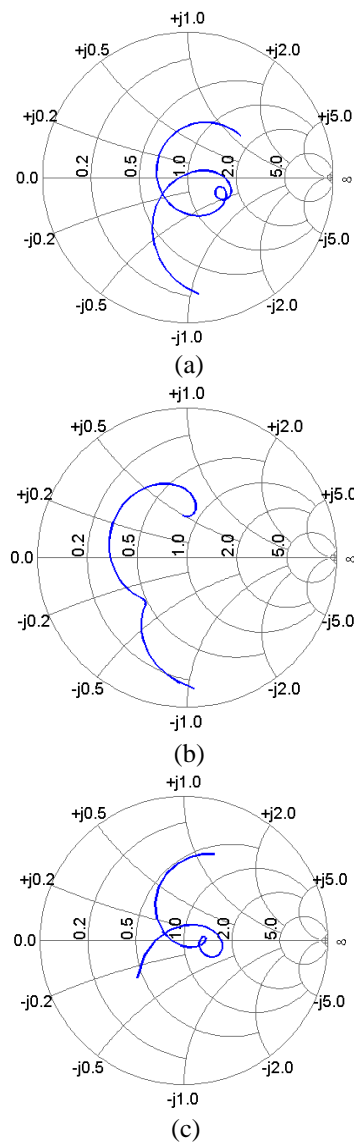


Fig. 13. Smith charts showing simulated data for: (a) baseline antenna (no dielectric), (b) fiberglass skin, no foam buffer, and (c) fiberglass with 5mm foam buffer.

The dielectric skin layers were modeled as 1.5 m by 1 m fiberglass composite sheets with $\epsilon_r = 4.0$ and $\tan \delta = 0.01$. The foam was modeled as air because $\epsilon_r = 1.08$ is typical for foam used in structural composites. Simulated S_{11} results for this pseudo-structural antenna are shown in Fig. 12 (black trace). Comparing that with the S_{11} response of the baseline antenna in free space without any dielectric (red trace), it is obvious that the presence of the dielectric skin materials has significantly degraded the antenna performance. To examine the variability in dielectric constant and its effect on antenna performance, a second simulation was performed by replacing the fiberglass skins with cyanate-ester/quartz ($\epsilon_r = 3.25$, $\tan \delta = 0.006$). Interestingly, the results were the same as for fiberglass, suggesting that the problem was with the integration scheme itself as opposed to arising from material properties.

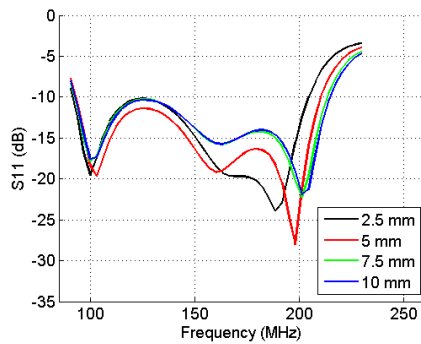


Fig. 14. Effect of foam buffer thickness on S_{11} .

The integration concept was reconsidered, and it was noted that the only major difference between the structural and non-structural antenna was that the lower dielectric sheet was in direct contact with the slotted conductive trace in the structural version. The dielectric sheet was moved down 5 mm (see Fig. 11) in the FEKO model to determine if the mere presence of dielectric material near the feed and slot area was affecting the input impedance of the antenna. This 5 mm of separation could be achieved in a composite structure by adding an additional foam layer between the lower sheet and the slotted trace.

As indicated by the blue line on the S_{11} plot of Fig. 12, a significant portion of the previously observed bandwidth was recovered through the inclusion of the foam buffer. The bandwidth ratio for the structural antenna is 2.26:1 with the reduction occurring at the high end of the operational band. It was also noted that the beginning of the operating band shifted downward slightly from 96 to 93 MHz.

Figure 13 shows the structural interaction discussed above on a Smith chart. Fig. 13 (a) is the baseline antenna in air, and Fig. 13 (b) shows the deleterious effect of the dielectric skin being in direct contact with

Antenna Trace 1. The Smith chart of Fig. 13 (c) shows that the inclusion of the foam buffer results in much improved performance that is similar to that observed for the baseline antenna.

The effect of the foam buffer thickness on S_{11} was investigated through additional simulations, and the resulting data are shown in Fig. 14. It was determined that a foam thickness greater than 5 mm resulted in slightly more bandwidth, while a thickness under 5 mm resulted in less bandwidth. The buffer thickness was ultimately left at 5 mm because it provided a slightly better match over most of the band and facilitated structural fabrication by making the antenna less intrusive into the structure. Simulated radiation pattern plots are shown in Fig. 15. Table 3 shows the peak gain at discrete points in the operating band for each of the dielectric materials that were studied.

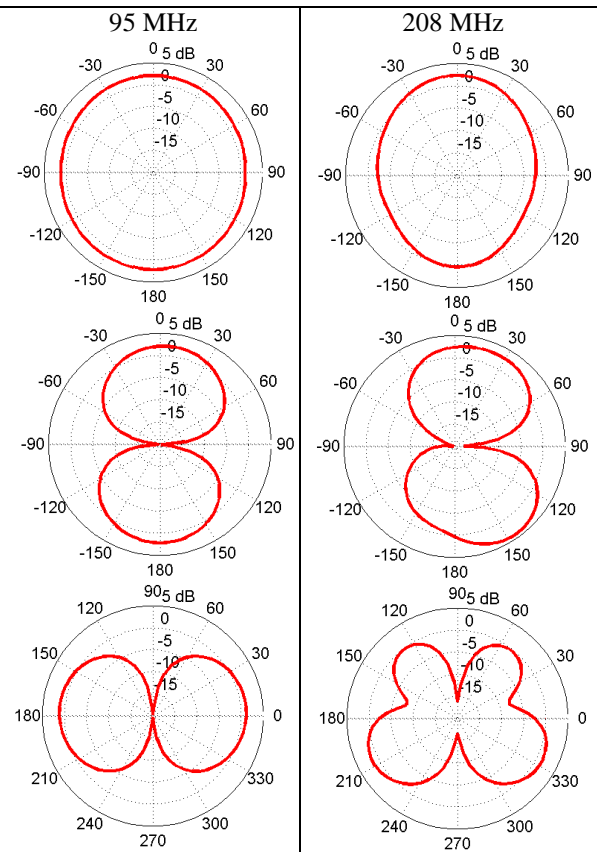


Fig. 15. Radiation patterns at $\phi = 0$, $\phi = 90$, and $\theta = 90$ planes.

Table 3: Comparison of simulated peak gain for different composite materials (dBi)

Dielectric	100 MHz	150 MHz	200 MHz
None	2.2	2.7	2.7
Cyanate-Ester Quartz	2.4	2.7	2.7
Fiberglass	2.3	2.6	2.4

From a comparison of Fig. 15 and Fig. 5, it is evident that the patterns in each of the principal planes at the lower end of the band are similar. Comparing the patterns at the upper end of the band in Fig. 15 to those in Fig. 5, it is seen that there is close agreement in the $\theta = 90$ degree plane, but some variation is found in the other planes. This is because the upper end of the band is 221 MHz in Fig. 15, whereas it is 240 MHz in Fig. 5.

Characteristic mode understanding

The CM analysis was repeated for the antenna integrated with the structural skin and in the presence of the foam. FEKO simulation results generated the modal significance plot shown in Fig. 16. In general, these results agree with the results seen in Fig. 6 for the non-structural antenna. However, two differences are noted. First, for the structural antenna with the skins and foam, all of the frequencies of the resonant modes have shifted lower. Second, modes 1, 2, and 4 have somewhat narrow bandwidths. Table 4 compares modal bandwidths calculated for Antennas A and C.

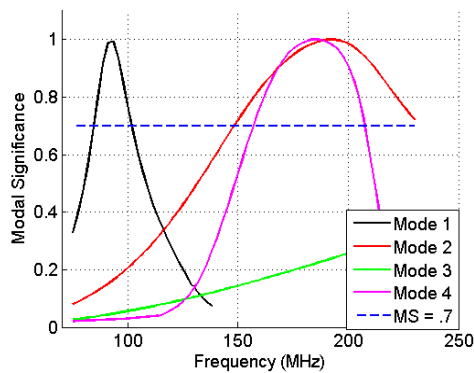


Fig. 16. Modal significance for structural antenna.

Table 4: Comparison of modal bandwidth for Antenna A and Antenna C

Mode	Bandwidth (MHz) (Antenna A)	Bandwidth (MHz) (Antenna C)
1	21.4	18.3
2	106.7	80.8
4	59.5	50.8

Experimental results of structurally integrated antenna

Upon completing the analysis of structural integration effects, Antenna C was constructed (see Fig. 8 (c)) using 2 mm thick fiberglass sheets instead of the 5 mm thick fiberglass and cyanate-ester quartz sheets used in the simulations. The thinner sheets were already on-hand, and this change saved the cost of purchasing commercial composite sheets or the supplies needed to manufacture custom composite panels, not to mention the labor cost and time associated with manufacturing. The expected impact of the thinner material was that

measured performance would be slightly better than for the thicker dielectric used in simulations. The measured S_{11} versus frequency for this antenna are shown in Fig. 12 using the magenta line. As seen, the operating bandwidth within -10 dB S_{11} is from 89 to 221 MHz. As expected, the measured performance of Antenna C was better than the simulation results (2.48:1 bandwidth ratio vs. 2.26:1), but it is evident in Fig. 10 that Antenna C has less bandwidth than Antenna B - which agrees with what was observed in simulations.

C. MIMO application

A common vehicle configuration for UAVs is the inverted V tail, in which the conventional horizontal and vertical stabilizers are replaced by two airfoils that are oriented downward at an angle from the horizontal. Such a structure could be used to implement a structural VHF antenna to enable an airborne MIMO capability. MIMO has been suggested as a means of increasing throughput for communications links [25-27] and improving radar performance [28].

To investigate the feasibility of this concept, two vertically oriented structural antennas (Antenna C) were used to approximate an aircraft having two parallel tails. This physical configuration is designated as Antenna D in Table 2. Because independent antennas are required for MIMO applications, the envelope correlation coefficient (ECC) was used to characterize the relative independence of the antennas. The ECC study was conducted by first using FEKO to calculate the S-parameters with the antennas being separated by distances of 1 m, 1.25 m, and 1.5 m. The resulting data was post-processed using MATLAB to calculate ECC for each case. Simulations indicated that the efficiency of the antenna is on the order of 98%, so accurate results for ECC can be expected through the use of S parameters as given by (4) [29]

$$ECC = \frac{|S_{11}^* S_{12} + S_{21}^* S_{22}|^2}{(1 - |S_{11}|^2 + |S_{21}|^2)(1 - |S_{21}|^2 + |S_{12}|^2)} \quad (4)$$

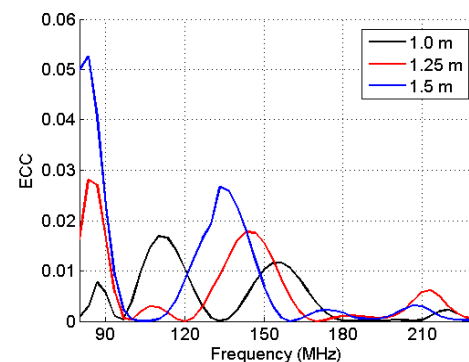


Fig. 17. ECC for vertical tails separated horizontally by 1.0, 1.25, and 1.5 m.

Figure 17 shows plots of ECC versus frequency for each separation distance over the band of interest. The data indicate that not only is ECC low for all separation distances, the case of 1 m separation results in the lowest overall ECC across the band. This result is encouraging because a 1 m separation distance is a reasonable value for tail separation on a twin tail UAV.

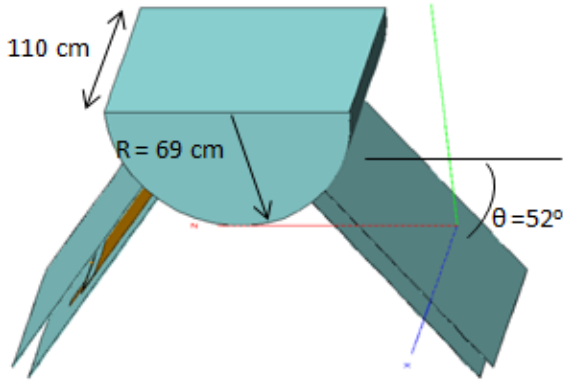


Fig. 18. FEKO model of an inverted V-tail UAV configuration.

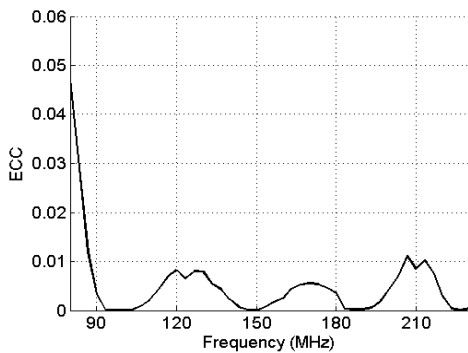


Fig. 19. ECC for the inverted V tail model.

Given the encouraging ECC results obtained with the parallel tail configuration, another study was conducted with the antennas canted at a 52 degree angle from the horizontal to represent antennas being integrated with inverted V tails. This configuration is designated as Antenna E, and is shown as a FEKO model in Fig. 18. The model also includes a section of fuselage with a radius of 69 cm and length of 110 cm. It was assumed that the fuselage is a cyanate-ester quartz composite with a thickness of 5 mm. The forward and aft sections of the fuselage are closed out with a 5 mm thick composite panel representing a bulkhead, although we note that the aft section would be partially open to accommodate a propeller shaft. The tails themselves are represented as Antenna C of Fig. 11 having the same dimensions with the exception that the spacing between the dielectric sheets was reduced to 10 cm.

The previously described process was used to calculate ECC based on (4) for the inverted V tail model, and the results are shown in Fig. 19. A comparison of Figs. 19 and 17, shows that the inverted V tail configuration achieves a lower ECC than was realized with any of the parallel tail configurations previously studied.

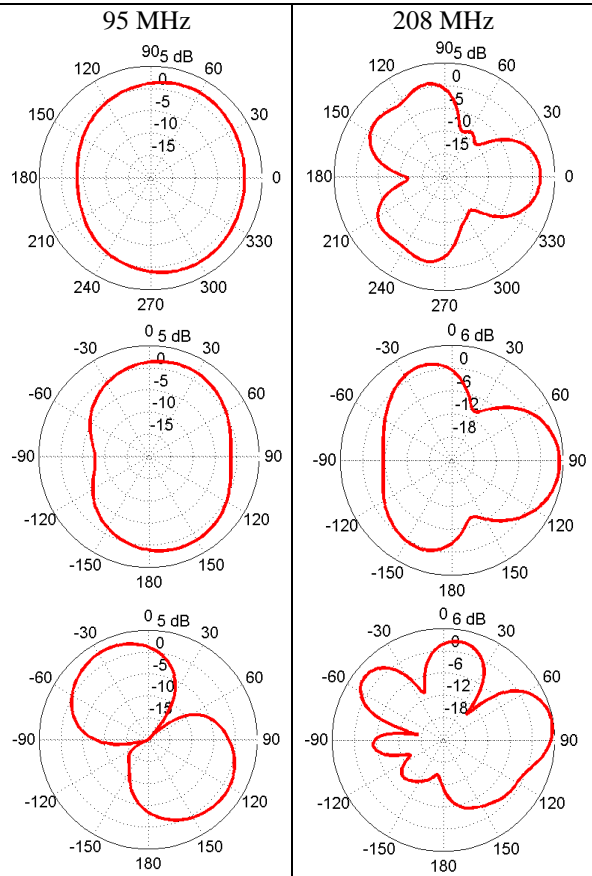


Fig. 20. Simulated radiation patterns for aircraft azimuth, pitch, and roll planes.

Simulated radiation patterns for the inverted V tail concept are shown in Fig. 20. The simulations were conducted with one antenna excited and the other terminated with a 50 ohm load. The patterns of each antenna were found to be nearly identical except for the orientation in the roll plane being canted at +/- 52 degrees as would be expected because this is the orientation of the antenna structure. The plots at the low end of the band in Fig. 20 show good symmetry with slightly more gain in the forward direction than aft (Fig. 20). At the upper end of the band in Figs. 20 (d-f), the patterns become more directional with energy being directed forward and outboard. While the null directed to the aft at the upper end of the frequency band could be undesirable in some applications, the independent

patterns combined with low ECC value across the band indicate the use of tail-integrated antennas for a MIMO is feasible.

IV. CONCLUSION

The study, design, and fabrication of a broadband VHF antenna for integration into a composite airfoil are presented. It is demonstrated that a broadband antenna operating from 89-221 MHz can be incorporated into composite structures. Simulation and experimental results clearly show that such antennas can be built using structural composite materials, such as cyanate-ester/quartz, Rohacell foam and conductive mesh with appropriate thicknesses commensurate with the frequency band of operation. The need for a foam buffer layer in between the antenna trace and the dielectric skin is demonstrated and the thickness of such a layer is optimized through simulations. Characteristic Mode (CM) analyses are performed to further understand and elucidate the bandwidth of the antenna as function of its modes and modal significance. The CM analyses was conducted in two ways with the first being a single sweep from 80 to 235 MHz, and the second being a segmented approach consisting of three separate simulations over subsets of the operational band. The latter approach was adopted because FEKO indicated that tracking errors occurred during the single sweep analysis. The details on the CM simulations of the antenna are available in [30].

The CM analyses for most of the antennas clearly delineate the individual modes and the modal interactions by means of which the antenna achieves broadband performance. The CM simulations also demonstrate the effects of the composite material loading on antenna operating frequency and bandwidth. Multiple antenna prototypes were built and tested. The final one was a sandwich structure consisting of cyanate-ester/quartz skins, Rohacell foam, and copper mesh. Experimental results on this antenna demonstrate antenna bandwidth from 89-221 MHz. Simulated radiation patterns show good coverage with a gain between 2 and 3 dBi across the band. The proposed sandwich structure antenna was also studied for possible MIMO application under an inverted V tail UAV configuration. The two antennas in that configuration clearly show excellent performance based on their ECC and simulated radiation patterns.

ACKNOWLEDGMENT

Funding provided by the Air Force Research Laboratory, Wright-Patterson AFB, OH; cleared for public release - case nos. 88ABW-2017-1874, 88ABW-2018-0542.

The authors would like to thank Todd Bussey, Jason Jewell, Philip Knoth, Jason Miller, and Russ Topp for their assistance in the fabrication of prototype antennas.

REFERENCES

- [1] J. Mitola and G. Q. Maguire, "Cognitive radio: making software radios more personal," *IEEE Personal Communications*, vol. 6, no. 4, pp. 13-18, Aug. 1999.
- [2] Y. Tawk, S. K. Jayaweera, C. G. Christodoulou, and J. Costantine, "A comparison between different cognitive radio antenna systems," *International Symposium on Intelligent Signal Processing and Communication Systems (ISPACS)*, pp. 1-5, Dec. 2011.
- [3] C. J. Leat, "Resistively loaded helical antennas for ground-penetrating radar," *IEE Proc. - Microwaves, Antennas, and Propagation*, pp. 204-210, Jan. 2003.
- [4] S. E. Sussman-Fort and R. M. Rudish, "Non-Foster impedance matching of electrically-small antennas," *IEEE Trans. Antennas Propagat.*, vol. 57, no. 8, pp. 2230-2241, Aug. 2009.
- [5] K. S. Song, *Non-Foster Impedance Matching and Loading Networks for Electrically Small Antennas*, Ph.D. Dissertation, The Ohio State University, 2011.
- [6] M. Hirvonen, A. Hujanen, J. Holmberg, and J. C. E. Sten, "Bandwidth limitations of dipoles matched with non-Foster impedances," *IEEE Antennas Propagat., Soc. Euro. Conf.*, pp. 1-5, Nov. 2007.
- [7] S. Koulouridis and J. L. Volakis, "Non-Foster circuits for small broadband antennas," *IEEE Antennas Propagat. Soc. Intl. Symp.*, Charleston, SC, pp. 1-4, June 2009.
- [8] C. R. White, J. S. Colburn, and R. G. Nagele, "A non-Foster VHF monopole antenna," *IEEE Antennas Wireless Propagat. Lett.*, vol. 11, pp. 584-587, 2012.
- [9] M. N. Alam, R. Dougal, and M. Ali, "Electrically small broadband VHF/UHF planar antenna matched using a non-Foster circuit," *Microwave Optical Technol. Lett.*, vol. 55, pp. 2494-2497, Oct. 2013.
- [10] J. Tuss, A. Lockyer, K. Alt, F. Uldrich, R. Kinslow, J. Kudva, and A. Goetz, "Conformal load bearing antenna structure," in *Proc. 37th AIAA Structural Dynamics and Materials Conf.*, pp. 836-843, 1996.
- [11] P. J. Callus, "Novel Concepts for Conformal Load-bearing Antenna Structure," Defense Technical Information Center, Fort Belvoir, VA, 2007.
- [12] D. Banks, M. Berden. W. Baron, and J. Tenbarge, "Structurally integrated X-band array development," *Multifunctional Structures /Integration of Sensors and Antennas*, Neuilly-sur-Seine, France: RTO, Meeting Proceedings RTO-MP-AVT-141, paper 17, pp. 17-1-17-12, 2006.
- [13] N. Bishop, J. Miller, D. Zeppetella, W. Baron, J. Tuss, and M. Ali, "A broadband high-gain bi-layer

- LPDA for UHF conformal load-bearing antenna structures (CLAS) applications,” *IEEE Trans. Antennas Propagat.*, pp. 2359-2364, May 2015.
- [14] D. Zeppettella and M. Ali, “VHF antenna for airfoil structural integration,” *IEEE Antennas and Propagation Society International Symposium*, June 26 – July 1, 2016. DOI:10.1109/APS.2016.7696637
- [15] B. Strojny and R. Rojas, “Characteristic mode analysis of electrically large conformal bifilar helical antenna,” *Proceedings of the Fourth European Conference on Antennas and Propagation (EuCAP)*, Apr. 2010.
- [16] B. Raines and R. Rojas, “Design of frequency reconfigurable antennas using the theory of network characteristic modes,” *IEEE Trans. Antennas Propagat.*, pp. 3106-3113, Oct. 2010.
- [17] J. Adams and J. Bernhard, “A modal approach to tuning and bandwidth enhancement of an electrically small antenna,” *IEEE Trans. Antennas Propagat.*, pp. 1085-1092, Apr. 2011.
- [18] R. J. Garbacz, *A Generalized Expansion for Radiated and Scattered Fields*, Ph.D. dissertation, Dept. of Electrical Engineering, The Ohio State University, Columbus, OH, 1968.
- [19] R. F. Harrington and J. R. Mautz, “Theory of characteristic modes for conducting bodies,” *IEEE Trans. Antennas Propagat.*, vol. AP-19, no. 5, pp. 622-628, Sept. 1971.
- [20] R. F. Harrington and J. R. Mautz, “Computation of characteristic modes for conducting bodies,” *IEEE Trans. Antennas Propagat.*, vol. AP-19, no. 5, pp. 629-639, Sept. 1971.
- [21] E. Newman, “Small antenna location synthesis using characteristic modes,” *IEEE Trans. Antennas Propagat.*, vol. 27, no. 4, pp. 530-531, July 1979.
- [22] B. A. Austin and K. P. Murray, “The application of characteristic-mode techniques to vehicle-mounted NVIS antennas,” *IEEE Trans. Antennas Propagat.*, vol. 40, no. 1, pp. 7-21, Feb. 1998.
- [23] W. Strydom and M. Botha, “Investigating antenna radiation properties with characteristic mode analysis,” *AFRICON, 2013*, Mar. 6, 2014, DOI:10.1109/AFRICON.2013.6757604
- [24] Y. Chen and C. Wang, *Characteristic Modes: Theory and Applications in Antenna Engineering*. John Wiley & Sons, Inc., Hoboken, New Jersey, 2015.
- [25] D. Reith, C. Heller, D. Blaschke, and G. Aschield, “Line-of-sight MIMO in aircraft-to-aircraft data links,” *IEEE/AIAA 33rd Digital Avionics Systems Conference (DASC)*, Dec. 11, 2014, DOI:10.1109/DASC.2014.6979437
- [26] C. Zhang, K. Pang, and L. Ma, “Interpolated airborne MIMO antenna array,” *IEEE Antennas Wireless Propagat. Lett.*, vol. 14, pp. 72-75, Sep. 4, 2014.
- [27] B. Holter, J. Hakegard, and T. Myrvoll, “On the use of MIMO in aeronautical communications,” *Proc. 2nd ENRI International Workshop on ATM/CNS (EIWAC2010)*, Tokyo, Japan, 2010. SINTEF S17195.
- [28] A. Flattie, “Performance evaluation of MIMO cooperative radar by considering high altitude aeronautical platforms,” *International Conference on challenges in IT, Engineering and Technology (ICCIET2014)*, Phuket (Thailand), July 17-18, 2014. <http://dx.doi.org/10.15242/IEE.E0714069>
- [29] C. Votis, G. Tatsis, and P. Kostarakis, “Envelope correlation parameter measurements in a MIMO antenna array configuration,” *Int. J. Communications, Network and System Sciences*, 3, 350-354, 2010. doi:10.4236/ijcns.2010.34044. Published Online April 2010. <http://www.SciRP.org/journal/ijcns/>
- [30] D. Zeppettella, *Multifunction Radio Frequency Composite Structures*, Ph.D. Dissertation, University of South Carolina, Columbia, SC, 2018.



David Zeppettella is an Electronics Engineer at the Air Force Research Laboratory where he leads research on multifunction structures. His research focuses on dual-purpose composite structures for structural state sensing and RF applications. He received his Ph.D. degree in Electrical Engineering from the University of South Carolina in 2018. Previously he received his M.S. degree in Electrical Engineering from The University of Dayton and his B.E. degree also in Electrical Engineering from Youngstown State University. Zeppettella has 19 years of engineering and R&D experience.



Mohammad Ali (M'93–SM'03) received the B.Sc. degree in Electrical and Electronic Engineering from the Bangladesh University of Engineering and Technology, Dhaka, in 1987 and the M.A.Sc. and Ph.D. degrees, both in Electrical Engineering, from the University of Victoria, Victoria, BC, Canada, in 1994 and 1997, respectively. Since August 2001, he has been with the Department of Electrical Engineering, University of South Carolina at Columbia where currently he is a Professor. He is the author/coauthor of over 180 publications and 9 US patents.

Wideband Dual-polarized Vivaldi Antenna with Gain Enhancement

Huanhuan Lv, Qiulin Huang*, Jianqiang Hou, and Jinlin Liu

National Laboratory of Science and Technology on Antennas and Microwaves
Xidian University, Xi'an, 710071, China

lvhuanhuan4213@126.com, *qiulhuang@mail.xidian.edu.cn, houjq@163.com, xdjinlinliu@126.com

Abstract — A wideband dual-polarized Vivaldi antenna covering 1.85-18.3 GHz band with enhanced gain is presented in this letter. The proposed antenna consists of two Vivaldi antenna elements (VAEs), which are designed based on the conventional Vivaldi antenna. Dual-slot structure is employed to improve the gain of the conventional Vivaldi antenna. As a result, spherical-like waves across the slot aperture of the conventional Vivaldi antenna can be transformed to be plane-like waves and thus gain enhancement can be achieved. In order to extend lower frequency limit of the VAE, elliptical slots are adopted. The proposed dual-polarized Vivaldi antenna is obtained by combining two VAEs in a cross-shaped form. The prototype is simulated, fabricated, and measured. A good agreement between EM simulated and measured results evidently validates the proposed antenna.

Index Terms — Dual-polarized Vivaldi antenna, enhanced radiation characteristics, wideband.

I. INTRODUCTION

Vivaldi antenna has been widely used in the wideband communication system owing to the features of planar structure, low profile, ease of fabrication and compatibility with backend circuits since its appearance in 1979 [1]. Moreover, modern antenna measurement systems such as material testing systems or near-field antenna measurement systems require antennas with the capability of dual-polarization. In recent years, dual-polarized Vivaldi antenna has attracted considerable interests.

A common way to design dual-polarized Vivaldi antennas is to place two Vivaldi antenna elements (VAEs) orthogonally along the edge. Wideband dual-polarized antenna arrays based on this placement method are presented in [2-5]. However, for single dual-polarized antenna, this placement method causes displacement of the phase center between two VAEs. In [6], a dual-polarized cross-shaped Vivaldi antenna covering 0.7 to 7.3 GHz is presented, which obtains good cross-polarization isolation.

One of the challenges in designing the Vivaldi antenna is to improve the gain. In [7-10], corrugated ripples are used to reduce the current distribution along the antenna edge to achieve gain enhancement. In [11], a dual-polarized cross-shaped Vivaldi embedded in a dielectric is presented, which obtains a maximum gain value of 10.5 dBi.

In this letter, a wideband dual-polarized Vivaldi antenna covering 1.85-18.3 GHz band for the antenna measurement system is presented. Two VAEs are placed in a cross-shaped form to achieve dual-polarization. The VAE is modified from the conventional Vivaldi antenna by introducing dual-slot structure, which can improve the gain without increasing size of the antenna. Elliptical slots are adopted to extend lower frequency limit of the Vivaldi antenna and the radiation characteristics at lower frequencies are improved. The proposed dual-polarized Vivaldi antenna is simulated, fabricated, and measured. The measured results show that the proposed antenna features wideband, high gain and good cross-polarization isolation performance.

II. ANTENNA DESIGN

Figure 1 illustrates evolution process of the VAE. Three antennas denoted as Ant I, Ant II and Ant III are designed on the Rogers RO4350 substrate with relative permittivity $\epsilon_r = 3.66$. The radiation surfaces are printed on the top side of the substrate and feedlines are printed on the other side of the substrate. Three antennas have the same size of 145 mm \times 58 mm \times 0.5 mm. Simulated S_{11} and boresight ($\Phi = 0^\circ$, $\Theta = 90^\circ$) gain of Ant I, Ant II and Ant III are shown in Fig. 2. The simulated results are obtained by using High Frequency Structure Simulation (HFSS) software with Finite Element Method (FEM).

Ant I is a conventional Vivaldi antenna, whose lower frequency is set as 2.6 GHz. It is known that lower frequency of a Vivaldi antenna is related to the aperture width, which is denoted as W_1 in Fig. 1. The reason for setting an initial frequency higher than the required lower frequency (1.85 GHz) is to maintain a relatively compact size before the optimization. The aperture width

W_1 is set to be 58 mm based on analysis in [12]. Tapered transmission lines are used to feed the antenna to improve impedance matching. Exponential curves y_{c1} and y_{c2} of Ant I are described by the equations as follows:

$$y_{c1} = 0.00001254e^{0.13x} + 0.6 \quad 0 \leq x \leq L_2, \quad (1)$$

$$y_{c2} = -0.00001254e^{0.13x} - 0.6 \quad 0 \leq x \leq L_2. \quad (2)$$

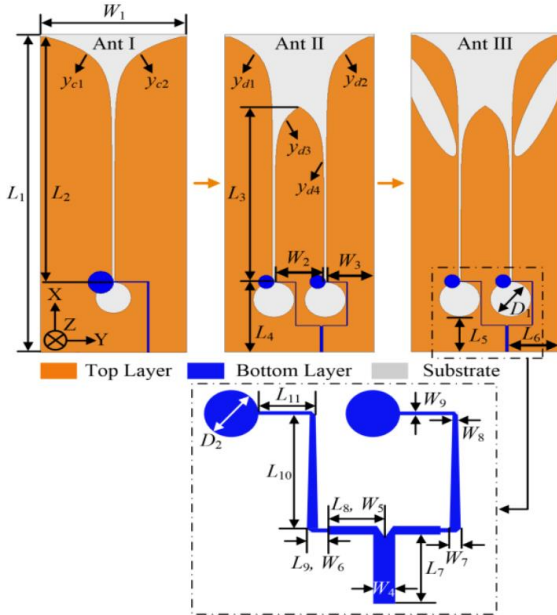


Fig. 1. Evolution process of VAE.

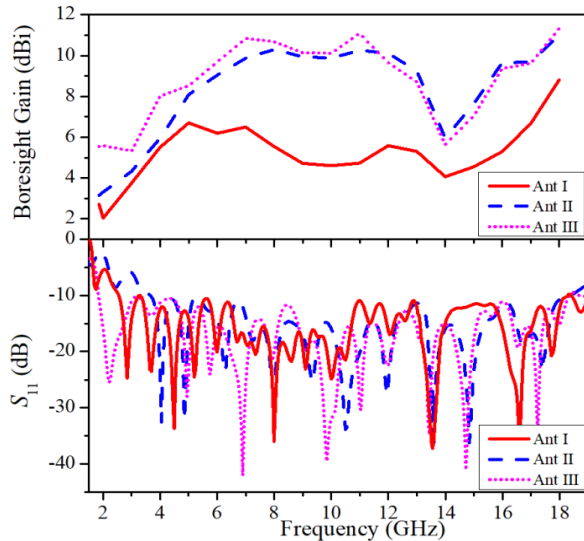


Fig. 2. Simulated S_{11} and boresight ($\Phi = 0^\circ$, $\Theta = 90^\circ$) gain of Ant I, Ant II and Ant III.

It can be seen from Fig. 2 that -10 dB impedance bandwidth of Ant I can cover 2.6-18.3 GHz band with maximum boresight gain of 6.7 dBi. To improve boresight gain without introducing a dimensional increase, dual-

slot structure is used to design Ant II as shown in Fig. 1. Four exponential curves denoted as y_{d1} , y_{d2} , y_{d3} and y_{d4} can be described by the equations as follows:

$$y_{d1} = 0.000007837e^{0.13x} + 10.5 \quad 0 \leq x \leq L_2, \quad (3)$$

$$y_{d2} = -0.000007837e^{0.13x} - 10.5 \quad 0 \leq x \leq L_2, \quad (4)$$

$$y_{d3} = -0.00004324e^{0.15x} + 9.5 \quad 0 \leq x \leq L_3, \quad (5)$$

$$y_{d4} = 0.00004324e^{0.15x} - 9.5 \quad 0 \leq x \leq L_3. \quad (6)$$

Accordingly, the feedline is changed to a T-shaped network. In contrast to traditional Vivaldi antenna, dual-slot structure can generate two columns of in-phase waves with equal amplitudes, which are mutually coupled across the aperture.

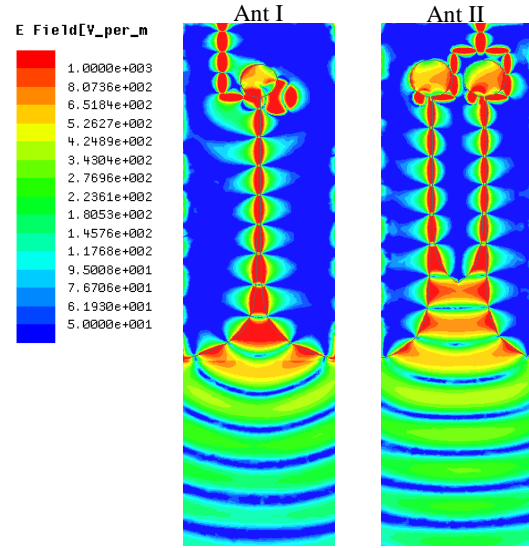


Fig. 3. Simulated electric field distributions of Ant I and Ant II at 10 GHz.

Shown in Fig. 3 are simulated electric field distributions of Ant I and Ant II at 10 GHz. It can be observed that compared with spherical-like waves across the slot aperture of Ant I, waves generated by dual-slot structure are plane-like waves, which can produce high boresight gain. However, the aperture size of each slot in Ant II is actually reduced compared with Ant I and the lower frequency of VAE is increased as shown in Fig. 2. In order to solve this problem to meet the required lower frequency, elliptical slots are etched in Ant III as shown in Fig. 1. Simulated surface current flow of Ant II and Ant III at 1.85 GHz is shown in Fig. 4 to illustrate the operating characteristics of the elliptical slots at lower frequencies. It can be seen that the effective length of the surface current path is visibly lengthened with the utilization of elliptical slots and new resonant mode can be introduced to enhance the radiation characteristics at lower frequencies. It can be observed from Fig. 2 that -10 dB impedance bandwidth of Ant III can cover 1.85 GHz to 18.3 GHz. Thus, Ant III is chosen as the final VAE.

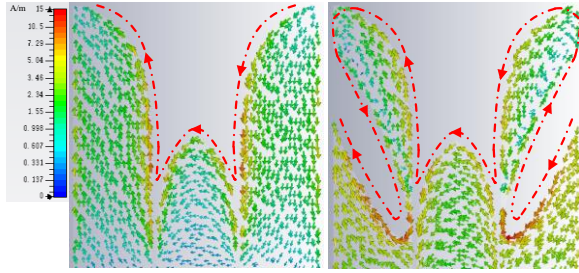


Fig. 4. Simulated surface current flow of Ant II and Ant III at 1.85 GHz.

III. SIMULATION AND TEST OF ANTENNA

HFSS with FEM is used to simulate and optimize the proposed VAE. The numerical analysis procedure is demonstrated as follows. In this paper the parameters under study include the total length of radiation slot line L_2 , the length of middle structure L_3 and the location of elliptical slot L_e . The results are obtained when one single parameter is changed and other parameters are constant.

A. The influence of L_2 on the performance of VAE

The effect of varying the total length of radiation slot line L_2 on S_{11} of VAE is shown in Fig. 5. It can be seen that with increasing L_2 from 112 mm to 132 mm, S_{11} curves in low frequency bands have larger changes and stop-bands occur around 2.6 GHz. And with decreasing L_2 from 112 mm to 102 mm, S_{11} curves also cannot fully cover 1.85-18.3 GHz. Therefore, the optimal value $L_2 = 112$ mm is obtained.

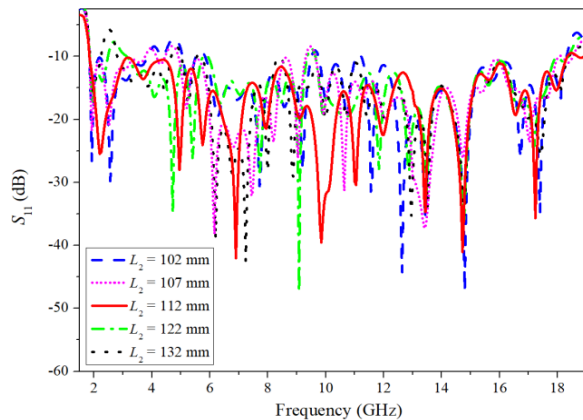


Fig. 5. Simulated S_{11} of VAE under different values of L_2 .

B. The influence of L_3 on the performance of VAE

The initial value of length L_3 is set based on the design rule:

$$L_3 > \max\{0.5\lambda_{\max}, 2\lambda_{\min}\}, \quad (7)$$

where λ_{\min} and λ_{\max} stand for the minimum and maximum

wavelengths in the operation band [13]. The length L_3 has direct influence on the coupling effect between waves generated by dual-slot structure. Thus the length L_3 has significant effect on the bandwidth of VAE. Figure 6 shows simulated S_{11} of VAE under different values of L_3 . It can be seen that when L_3 is equal to 62 mm or 72 mm, lower frequency of VAE cannot cover 1.85 GHz. And a stop-band occurs around 4 GHz when L_3 is increased. Hence, the length L_3 is set to be 82 mm.

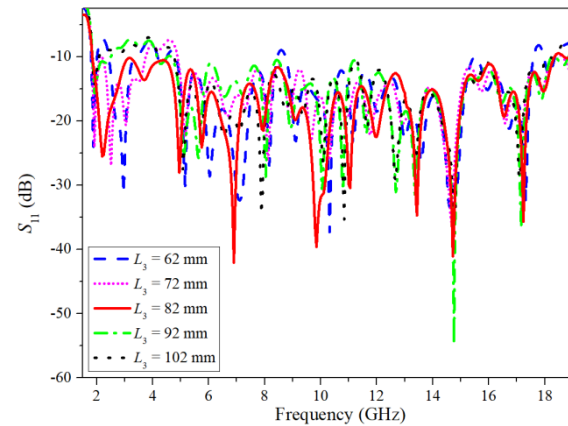


Fig. 6. Simulated S_{11} of VAE under different values of L_3 .

C. The influence of L_e on the performance of VAE

The major axis and minor axis of the elliptical slot are 25 mm and 5 mm. This paper is focused on the location of elliptical slot, which has direct influence on the surface current distribution. Figure 7 shows simulated S_{11} of VAE under different values of L_e . As depicted in Fig. 7, a stop-band is presented around 3 GHz when L_e is equal to 52 mm or 47 mm, and as L_e arrives at 62 mm and 57 mm, two stop-bands are presented around 5 GHz and 9 GHz. To obtain good performance from 1.85 GHz to 18.3 GHz, the position of elliptical slot L_e is optimized to be 57 mm.

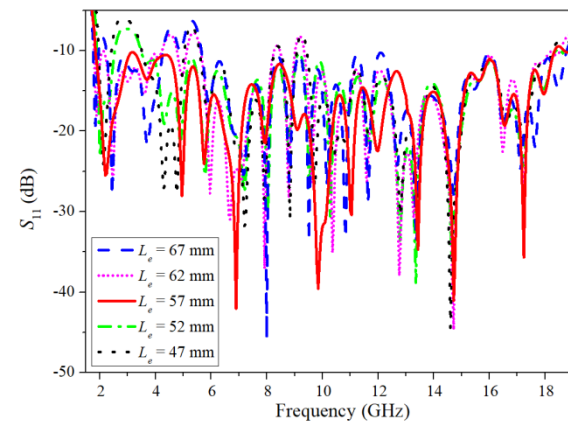


Fig. 7. Simulated S_{11} of VAE under different values of L_e .

D. Configuration of dual-polarized Vivaldi antenna

By combining two VAEs in a cross-shaped form, the proposed dual-polarized Vivaldi antenna is obtained. Figure 8 (a) shows the implementation details of proposed dual-polarized Vivaldi antenna. Two complementary cuboid slots are cut in substrates of VAEs for mounting the VAEs orthogonally. The lengths of two cuboid slots are 133.9 mm and 11.1 mm and the widths of two cuboid slots are 0.5 mm.

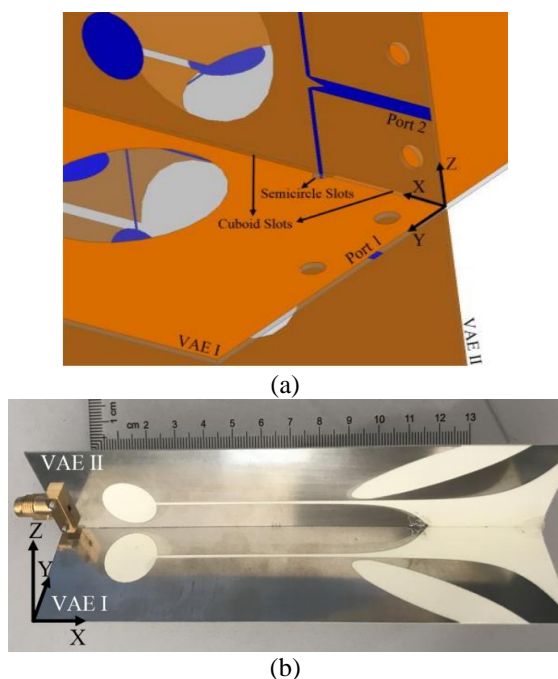


Fig. 8. (a) Implementation details and (b) photograph of the proposed cross-shaped dual-polarized Vivaldi antenna.

In order to avoid feedlines overlapping, feedlines of two VAEs are staggered to each other and that means line L_7 is shortened while L_{10} is lengthened to keep the total length of feedline unchanged. Thus, the phase center of VAE can remain the same. The stagger distance between two feedlines is optimized to be 2 mm. As shown in Fig. 8 (a), two semicircle slots are etched in radiation surfaces of VAEs to avoid galvanic contact between feedlines and radiation surfaces. Besides, mounting holes are cut in substrates for RF connectors. The optimized dimensions of the VAE are given as follows (all in mm): $L_1 = 145$, $L_2 = 112$, $L_3 = 82$, $L_4 = 32$, $L_5 = 16$, $L_6 = 19.91$, $L_7 = 12$, $L_8 = 8.3$, $L_9 = 1.86$, $L_{10} = 19.72$, $L_{11} = 8.58$, $L_e = 57$, $W_1 = 58$, $W_2 = 19$, $W_3 = 18.5$, $W_4 = 1.18$, $W_5 = 0.36$, $W_6 = 0.2$, $W_7 = 0.32$, $W_8 = 0.16$, $W_9 = 0.2$, $D_1 = 16$, $D_2 = 6.1$. A prototype of the proposed dual-polarized Vivaldi antenna is fabricated as shown in Fig. 8 (b).

E. Test of antenna

Simulated and measured S -parameters are shown in Fig. 9. The measurement is performed on an Agilent

8720ES network analyzer. It can be seen that the proposed dual-polarized Vivaldi antenna can cover 1.85-18.3 GHz band with S_{11} better than -10 dB. The measured isolation level between two VAEs across operation band is better than -25 dB. The discrepancies between simulated and measured results may be caused by fabrication errors, the variation of material properties and extra loss of the RF connectors.

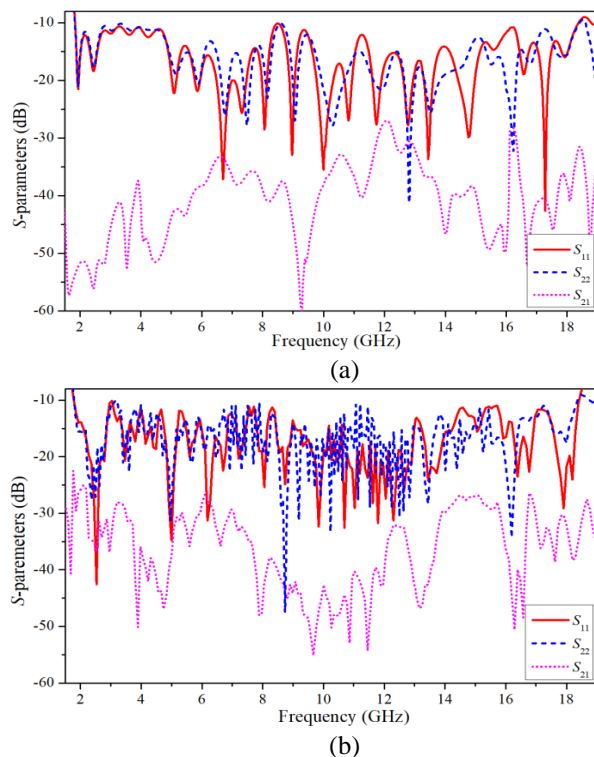


Fig. 9. (a) Simulated and (b) measured S -parameters of the proposed antenna.

Figure 10 presents measured normalized radiation patterns of the proposed antenna prototype at 1.85 GHz, 6 GHz, 13 GHz and 18 GHz. The patterns are presented in xoy and xoz planes with the same coordinate system shown in Fig. 8 and each plane contains both polarization components (co-polarization and cross-polarization). The results are obtained when one VAE is excited and the other one is terminated to a 50Ω load. It can be seen that radiation patterns of VAE I in xoy plane are similar to radiation patterns of VAE II in xoz plane due to the orthogonal orientation of two VAEs.

Figure 11 presents simulated and measured boresight gain of the proposed antenna. The results are obtained when one VAE is excited and the other one is terminated to a 50Ω load. It can be seen that gain values at lower frequencies are higher than 4 dBi and peak gain values of VAE I and VAE II are as high as 11.3 dBi and 11.18 dBi. Figure 12 presents measured cross-polarization isolation as a function of frequency in the boresight direction. It can

be seen that cross-polarization isolation of the proposed antenna is better than 16.5 dB across 1.85-18.3 GHz band, which means that the power ratio of radiated cross-polarized components to the co-polarized components is less than 2.2%. Table 1 shows comparisons between this work and previous research. The proposed antenna obtains good gain performance with compact aperture width in the operation band.

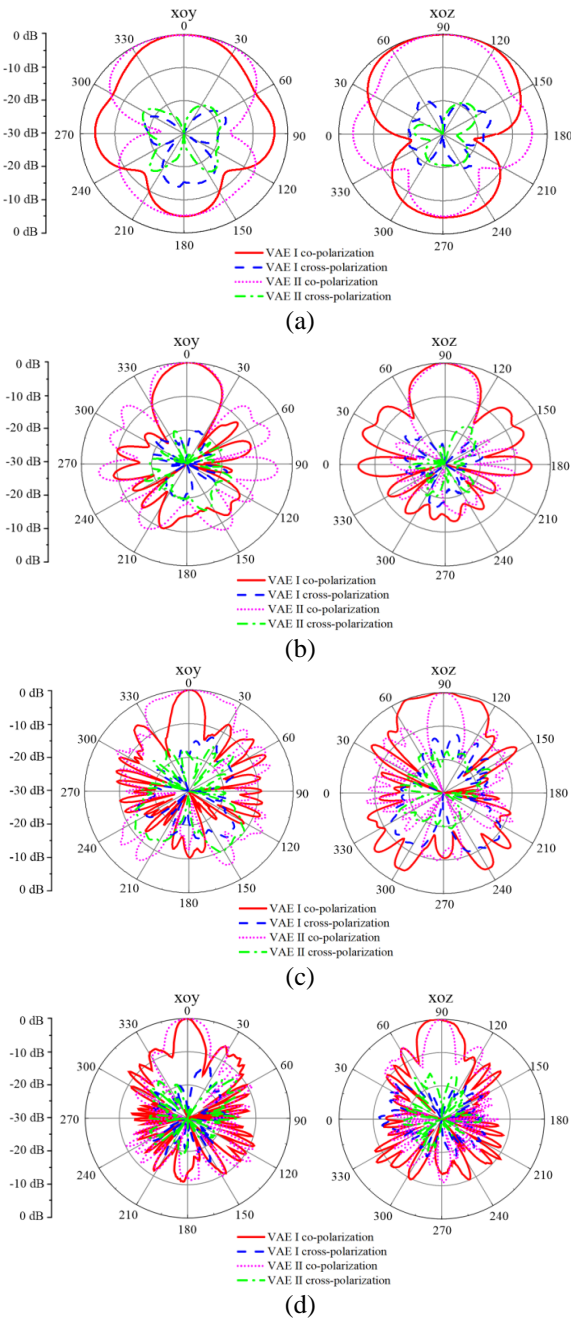


Fig. 10. Measured normalized radiation patterns of the proposed antenna in xoy and xoz planes at: (a) 1.85 GHz, (b) 6 GHz, (c) 13 GHz, and (d) 18 GHz.

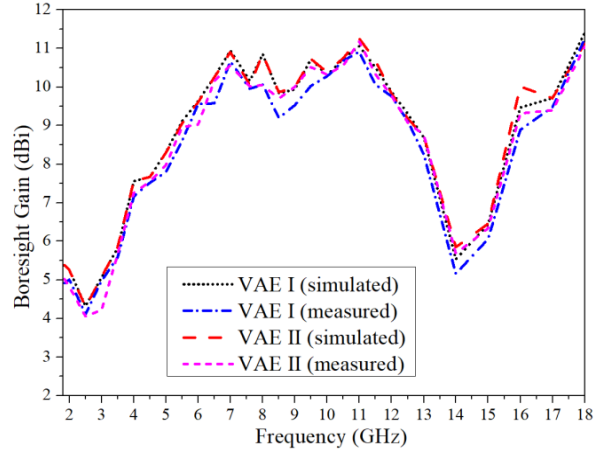


Fig. 11. Simulated and measured boresight gain of the proposed antenna.

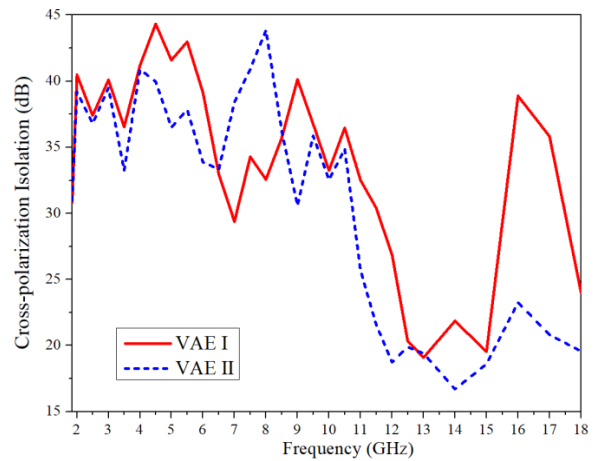


Fig. 12. Measured cross-polarization isolation in the boresight direction of the proposed antenna.

Table 1: Comparisons between this work and previous research

Ref.	Fractional Bandwidth (GHz)	Aperture Width (mm)	Aperture Width/ λ_{max}	Gain (dBi)
6	0.7-7.3	220	0.51	3.8-11.2
8	1.4-12	110	0.51	4-11.3
9	0.8-3.8	150	0.4	2.4-8.1
This work	1.85-18.3	58	0.36	4.06-11.3

Note: λ_{max} stands for maximum wavelength in the operation band.

IV. CONCLUSION

A wideband dual-polarized Vivaldi antenna covering 1.85-18.3 GHz band is presented in this letter. The proposed antenna consists of two VAEs, which are placed in a cross-shaped form to achieve dual-polarization.

Dual-slot structure is utilized and optimized to enhance radiation characteristics. Elliptical slots are used to extend lower frequency limit and enhance the radiation characteristics at lower frequencies. A prototype of the proposed dual-polarized Vivaldi antenna is fabricated and measured. Measured results agree well with simulated ones and the proposed antenna is qualified to be used in modern antenna measurement systems.

REFERENCES

- [1] P. J. Gibson, "The Vivaldi aerial," *1979 9th European Microwave Conference*, pp. 101-105, 1979.
- [2] J. Remez, A. Segal, and R. Shansi, "Dual-polarized wide-band wide scan multi-beam antenna system from tapered slot-line elements array," *IEEE Antennas and Wireless Propagation Letters*, vol. 4, pp. 293-296, 2005.
- [3] M. Elsallal and J. Mather, "An ultra-thin, decade (10:1) bandwidth, modular "BAVA" array with low cross-polarization," *2011 IEEE International Symposium on Antennas and Propagation (APSURSI)*, pp. 1980-1983, July 2011.
- [4] R. W. Kindt and W. R. Pickles, "Ultrawideband all-metal flared-notch array radiator," *IEEE Transactions on Antennas and Propagation*, vol. 58, no. 11, pp. 3568-3575, Nov. 2010.
- [5] J. B. Yan, S. Gogineni, B. Camps-Raga, and J. Brozana, "A dualpolarized 2–18-GHz Vivaldi array for airborne radar measurements of snow," *IEEE Transactions on Antennas and Propagation*, vol. 64, no. 2, pp. 781-785, Feb. 2016.
- [6] M. Sonkki, D. Sanchez, V. Hovinen, E. T. Salonen, and M. Ferrando, "Wideband dual-polarized cross-shaped Vivaldi antenna," *IEEE Transactions on Antennas and Propagation*, vol. 63, no. 6, pp. 2813-2819, June 2015.
- [7] F. B. Zarrabi, N. P. Gandji, R. Ahmadian, H. Kuhistani, and Z. Mansouri, "Modification of Vivaldi antenna for 2-18 GHz UWB application with substrate integration waveguide structure and comb slots," *Applied Computational Electromagnetics Society Journal*, vol. 30, no. 8, pp. 844-849, Aug. 2015.
- [8] H. Xu, J. Lei, C. J. Cui, and L. Yang, "UWB dual-polarized Vivaldi antenna with high gain," *2012 International Conference on Microwave and Millimeter Wave Technology (ICMMT)*, pp. 1-4, May 2012.
- [9] Y. Z. Zhu, D. Y. Su, W. X. Xie, Z. H. Liu, and K. W. Zuo, "Design of a novel miniaturized Vivaldi antenna with loading resistance for ultra wideband (UWB) applications," *Applied Computational Electromagnetics Society Journal*, vol. 32, no. 10, pp. 895-900, Oct. 2017.
- [10] M. A. Ashraf, K. Jamil, A. R. Sebak, M. Shoaib, Z. Alhekail, M. Alkanhal, and S. Alshebeili, "Modified antipodal Vivaldi antenna with shaped Elliptical corrugation for 1-18 GHz UWB application," *Applied Computational Electromagnetics Society Journal*, vol. 30, no. 1, pp. 68-77, Jan. 2015.
- [11] G. Adamiuk, T. Zwick, and W. Wiesbeck, "Compact, dual-polarized UWB-antenna, embedded in a dielectric," *IEEE Transactions on Antennas and Propagation*, vol. 58, no. 2, pp. 279-286, Feb. 2010.
- [12] R. Janaswamy and D. H. Schaubert, "Characteristic impedance of a wide slotline on low-permittivity substrates (short paper)," *IEEE Transactions on Microwave Theory and Techniques*, vol. 34, no. 8, pp. 900-902, Aug. 1986.
- [13] J. Lee, *Antenna Engineering Handbook*. 4th ed., New York: McGraw-Hill, 2007.



Huanhuan Lv received his B.S. and M.S. degrees from Xidian University, Xi'an, Shaanxi, China, in 2013 and 2016, respectively. He is currently working towards the Ph.D. degree in Electromagnetic Field and Microwave Technology at Xi'dian University, Xi'an, Shaanxi, China. His research interests are in wideband antennas, arrays and microwave circuits.



Qiulin Huang received his B.S. and Ph.D. degrees from Xidian University, Xi'an, Shaanxi, China, in 2001 and 2007, respectively. In 2002, he joined the School of Electronic Engineering at Xidian University. His research interests include smart antennas and arrays, and satellite navigation and anti-interference technology.



Jianqiang Hou received his B.S., M.S. and Ph.D. degrees from Xidian University, Xi'an, Shaanxi, China, in 1999, 2004 and 2010, respectively. In 2006, he joined the School of Electronic Engineering at Xidian University. His research interests include microwave circuit and system, antennas, and electromagnetic compatibility.



Jinlin Liu received her M.S. degree in Electromagnetic Field and Microwave Technology from Xidian University, Xi'an, Shaanxi, China, in 2016. She is currently working toward the Ph.D. degree in Electromagnetic Field and Microwave Technology at Xidian University. Her research interests include design of antennas, and microwave circuits.

UWB Gain Enhancement of Horn Antennas Using Miniaturized Frequency Selective Surface

Mehmet A. Belen¹, Filiz Güneş², Peyman Mahouti², and Aysu Belen²

¹ Department of Electric and Electronic Engineering
University of Artvin Çoruh, Artvin, TURKEY
mehmetalibelen@artvin.edu.tr

² Department of Electronics and Communication Engineering
University of Yıldız Technical, Istanbul, TURKEY
gunes@yildiz.edu.tr, pmahouti@yildiz.edu.tr, aysuyldrm07@gmail.com

Abstract — In this work, enhancement of the radiation performances of horn antennas are worked out within their operation bandwidth by placing the miniaturized Frequency Selective Surface (FSS)s perpendicularly into the inner part of their flares. Here each FSS consists of only a single miniaturized double-sided inverted T-shaped square unit cell designed on the low-cost FR4 with relative permittivity 4.4, loss tangent 0.0035 and thickness 1.58 mm in 3D CST environment so that it is able to focus the propagating electromagnetic waves to increase the directivity properties like a dielectric lens, while keeping the mismatching characteristics with less size and low manufacturing cost compared to its counter parts. Herein an exponentially tapered TEM horn with the operation bandwidth of 5-13 GHz is taken as an example horn antenna for measurements. From the measured results of the prototyped module, it can be observed that the proposed module keep mismatching characteristics of the horn antenna, meanwhile the gain and beam widths are enhanced to amplify the signal in the operation band without any increase in the total volume of the module or making the design bulky. Thus, it is expected that this methodology can be implemented to horn antennas effectively reducing volume and cost of communication systems.

Index Terms — Enhancement, FSS, gain, horn antenna, TEM horn, UWB.

I. INTRODUCTION

Frequency Selective Surfaces (FSSs are typically designed on planar periodic arrays of metal patches or slots with filtering characteristics of electromagnetic waves aimed at certain frequencies that could be tuned with change at the geometrical parameters of the unit element and dielectric shape [1-5]. In fact, because of this band stop feature, FSSs become very important and widely used for antennas and radars' cross-section reduction in

modern military platforms such as ships, aircrafts, and missiles. Communication systems in these platforms are always enclosed with FSSs. As electronic devices can be destroyed by strong electromagnetic interference (EMI), the anti-interference capability of communication systems in these platforms is urgently required. Thus, these make it required to design antenna and FSS as an integrated module called the filtering antenna with the typical works [3-5]. In the recent work [5], a Modified Double Square Loop (MDSL) unit element is designed to build a dual-band FSSs to be placed perpendicularly the aperture of a horn antenna as a band-stop prefilter for mobile communication (GSM) frequency bands operating at 900 and 1800 MHz simultaneously. Also FSS design can be used for absorbers by coatings their surfaces to selectively allow certain frequencies to pass through [6-7]. Aim of this work is to design miniaturized FSSs for enhancement of gain and beamwidths of the horn antennas by inserting perpendicularly into the bottom of their apertures while keeping their mismatching characteristics in their operation bandwidths. For this purpose, double-sided inverted T-shaped square is designed in 3D CST environment as a unit cell subject to the 5-13 GHz bandwidth of the exponentially tapered horn antenna available in our laboratory. Three unit cells are found to be sufficient to be placed to the bottom of its aperture for the enhancement of gain and beamwidth. In the next section, design and fabrication of the FSS loaded horn antenna will be given. Measurements will be followed in the third section, and finally the paper ends conclusion section.

II. DESIGN CONSIDERATIONS AND SIMULATIONS

A. TEM horn antenna

An exponentially tapered TEM horn with the operation bandwidth of 5–13 GHz is considered as a

prototype antenna for the gain and beamwidth enhancement (Fig. 1). The geometrical dimensions of the horn antenna are given in Table 1.

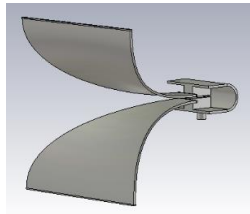


Fig. 1. 3-D view of an exponentially tapered TEM.

Table 1: Geometrical parameters of TEM horn antenna in mm

TEM Horn	Aperture Width	Aperture Height	Length
	74	73.5	60

B. FSS unit element: Double-sided inverted T-shaped square

Herein it is aimed to design FSSs for the horn antennas functioning as a dielectric lens in the requested frequency band so that they can be fixed in the inner parts of their flares, simply using foams or the equivalent materials with the unit relative dielectric constant. For this mean, a double sided inverted T-shape is selected as a suitable geometry design to be prototyped on low cost dielectric substrate FR4 (relative permittivity 4.4, loss tangent 0.0035, thickness 1.58 mm) given in Fig. 2 and its design schematic in Fig. 3.

Design and optimization process of the FSS model is carried out in CST environment with respect to the design goals of enhanced horn antenna design so that the unit element of FSS design would act as a band pass filter with the requested operation band of 5-13 GHz and increase the directive of the horn antenna. The simulated scattering parameters of the optimized unit FSS design are given in Fig. 4 alongside of its parametric values in Table 2. As it can be seen from Table 2, the size of designed FSS model is suitable to be used as FSS array and can easily be fitted to the inner part of the horn antenna. In Fig. 5 the antenna module itself is presented, alongside of the antennas simulated return loss and gain characteristics in Figs. 6-7, where Z and the gap are taken as parameters, defined as the distances of the FSS unit from the aperture and between its elements. The optimal values for gap and Z are taken as 8 mm and 5 mm. Furthermore, the surface current and H-field distributions of the antenna are given, respectively in Figs. 8-9. As can be observed from these figures, FSS unit causes the current and H-field to be intensified in the inner part of the flare as can be expected which result in enhancement of the gain within the operation band. In the next section of the work the experimental results of prototyped FSS design will be given.

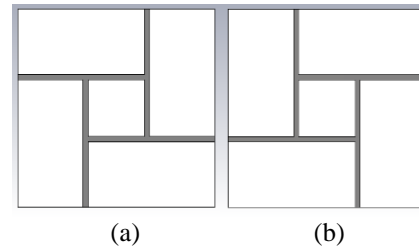


Fig. 2. Double-sided inverted T-shaped square: (a) top view, and (b) identical mirrored bottom view.

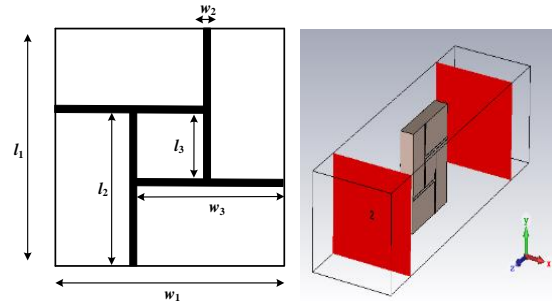


Fig. 3. Design schematic of double-sided inverted T-shaped square microstrip patch.

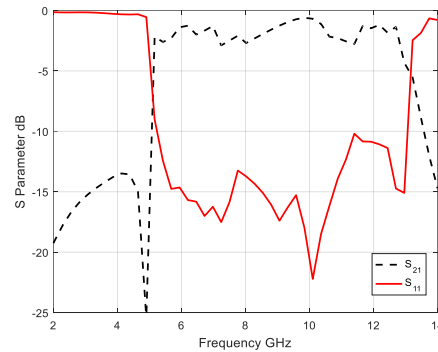


Fig. 4. Scattering characteristics of the FSS unit cell.

Table 2: Geometrical parameters of optimally designed double-sided inverted T-shaped square unit cell in mm

W_1	W_2	W_3
8	0.2	5.2
L_1	L_2	L_3
8	5.2	2.6

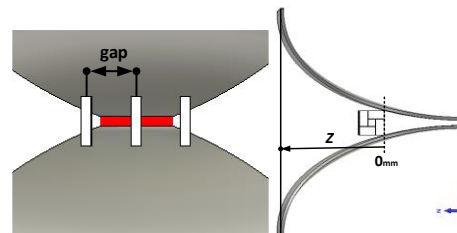


Fig. 5. Complete module.

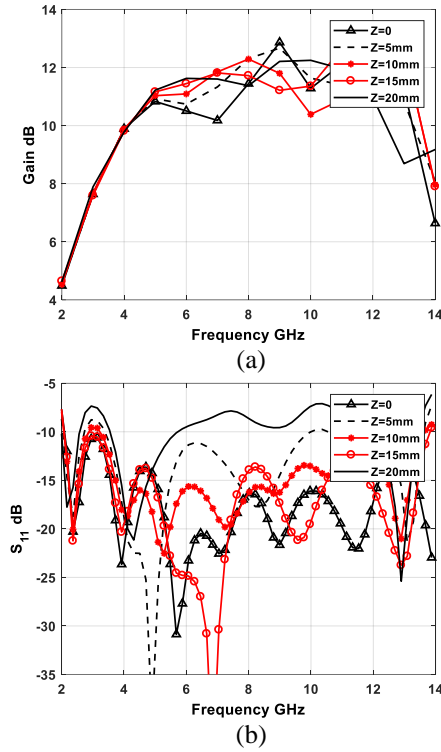


Fig. 6. Simulated: (a) maximum gain, and (b) S₁₁ with respect to the FSS's distance from the antenna; gap=5mm.

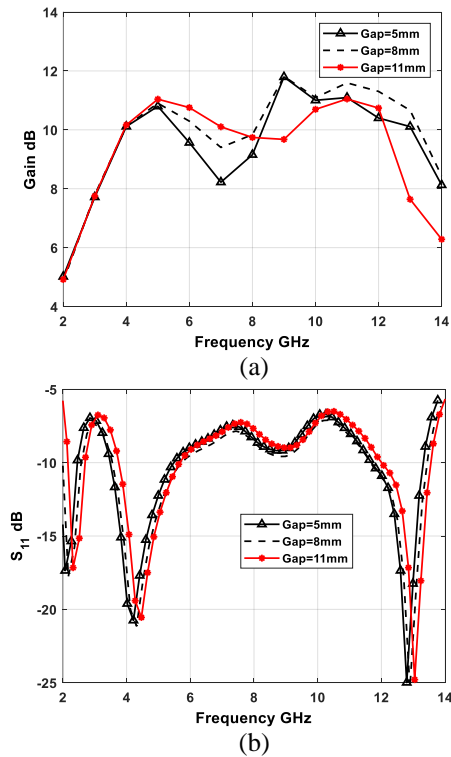


Fig. 7. Simulated: (a) maximum gain, and (b) S₁₁ with respect to the FSS's; gap Z=0.

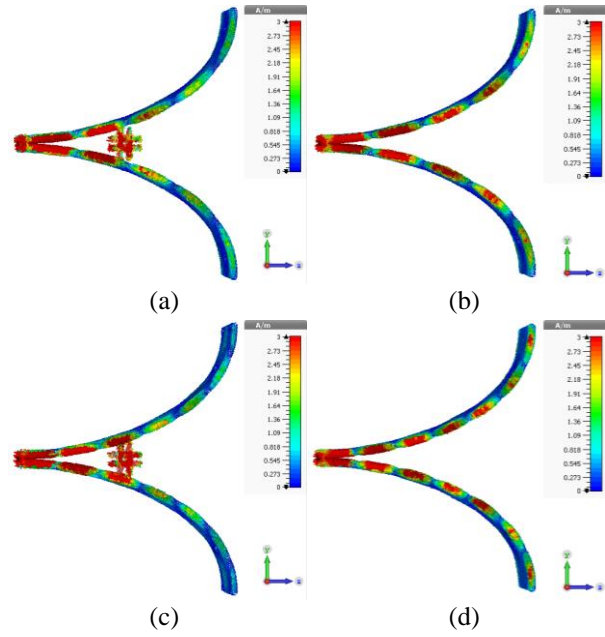


Fig. 8. Surface current distribution for 9 GHz: (a) with FSS and (b) without FSS; 12 GHz: (c) with FSS and (d) without FSS.

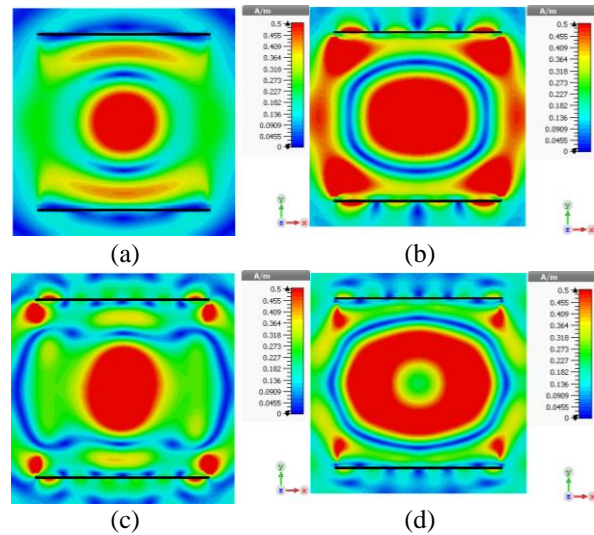


Fig. 9. H-Field distribution for 8 GHz: (a) with FSS and (b) without FSS; for 12 GHz: (c) with FSS and (d) without FSS.

III. MEASUREMENT

In this section the measurement results of the prototype module are presented. The return loss, transmission characteristic, maximum far field gain and radiation pattern of the proposed module are measured using two identical antennas in [8] as a reference antenna, the measurement setup is presented in Fig. 10 and the measurement results are given in the Figs. 11-13.

In Fig. 11, the measured return losses of the module are given. As seen from the Fig. 11, placing FSS unit into the inner part of antenna aperture does not cause any disruptive effect on the return loss performance of the antenna in the operation band. Figures 12 and 13 present the measured transmission and radiation pattern characteristics of antennas and modules at maximum gain direction $\phi=90^0$, $\theta=90^0$, respectively. As it can be seen from these characteristics, the proposed FSS unit increases the gain in the desired bandwidth 6–13 GHz, while keeping the return loss characteristics.

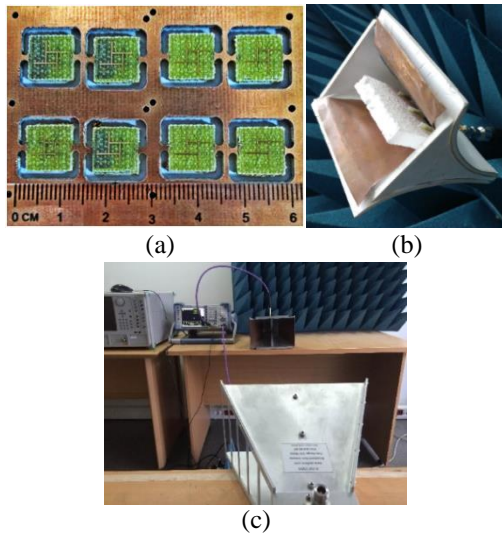


Fig. 10. Fabricated (a) unit double-sided inverted T-shaped square FSSs, (b) completed module, and (c) measurement setup.

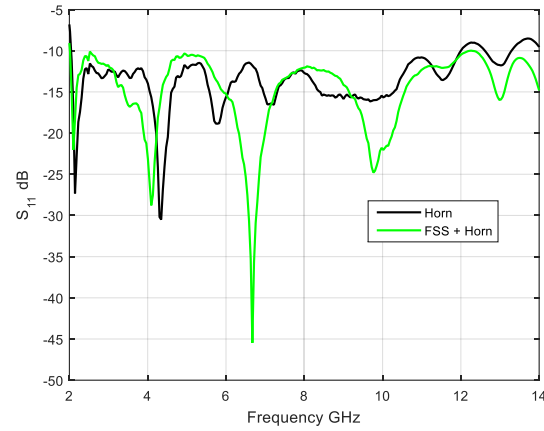


Fig. 11. Measured return loss characteristics.

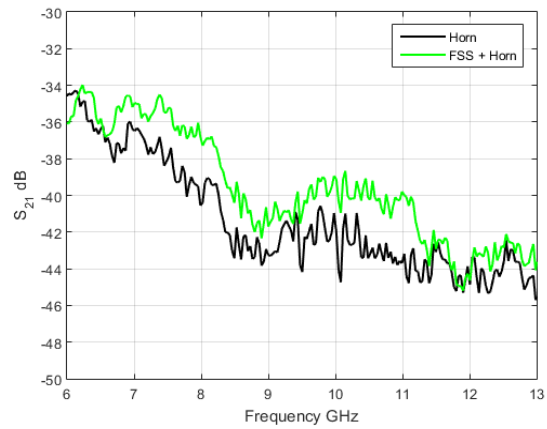


Fig. 12. Measured transmission characteristics.

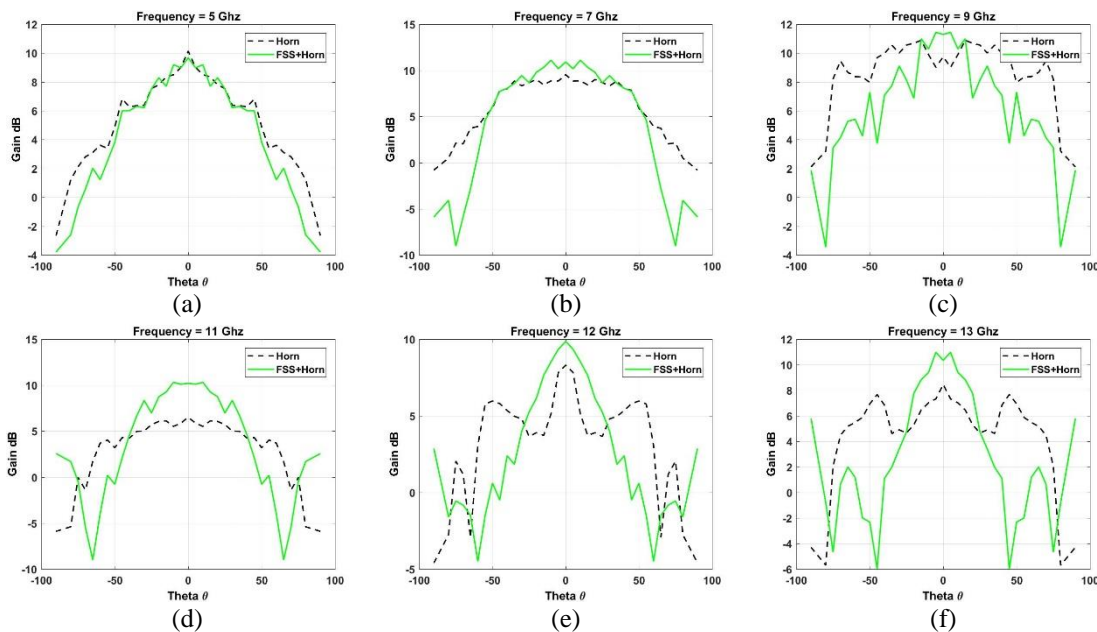


Fig. 13. Measured radiation patterns of the horn and FSS loaded horn antenna.

In Fig. 13, the measured radiation patterns of the antennas are presented. Furthermore the gains and 3 dB beam widths are also given in Table 3, respectively. From the characteristics in Figs. 13 (a)-(f), Tables 2 and 3, one can see the directivities of the horn are significantly increased after the implementations of FSS structures.

Table 3: Measured gain (dB) at $\phi=90^\circ$, $\theta=90^\circ$ and 3dB beamwidth (degree) measurement results

Frequency (GHz)	Gains at $\phi=90^\circ$		3dB Beamwidth	
	No FSS	FSS	No FSS	FSS
5	10.1	9.7	60	60
6	12.4	10.9	90	100
7	9.5	10.9	94	80
8	7.5	10.7	110	80
9	9.7	11.3	100	20
10	6.4	8.2	90	60
11	6.5	10.2	120	50
12	8.3	9.8	20	30
13	7.4	10.3	40	40

Table 4: Comparison of gain enhancements of typical horn modules in the similar bandwidth

	Frequency (GHz)	Dielectric Size (mm)	Gain Enhancement (dB) Over Operation Band (GHz)				
			5	7	9	11	13
			Here	5-13	8x8	0	1.4
[9]	5-15	16x16	2	0	0.5	0.2	1
[10]	1-15	60x100	4	3	5	0	0

Table 5: Comparison of mismatching S_{11} (dB)s of typical horn modules in the similar bandwidth

f (GHz)	Here		[9]	[10]	
	No FSS	With FSS		No Lens	With Lens
5	-13	-11	-12	-10	-15
7	-17	-20	-8	-14	-17
9	-16	-16	-20	-26	-15
11	-13	-13	-17	-9	-9
13	-12	-16	-25	-17	-7

Furthermore comparisons of the gain enhancements and mismatching S_{11} (dB)s among the typical macro - designed horn modules loaded dielectric lens [9] or dielectric [10] are given in Tables 4 and 5, respectively. From these tables, one can infer that our proposed horn module using the miniaturized FSSs can work much more effectively than the counterparts within the planned operation bandwidth with low-cost and very small size loading.

VI. CONCLUSION

In this work, design of miniaturized FSS are carried out for gain enhancement of Horn Antennas to be placed

to the inner part of horns flares. As it can be seen from the measurement results, the proposed module functions similar performance with the traditionally dielectric lens loaded horn antennas with less size and low manufacturing cost. The prototyped module keeps mismatching characteristics of the horn antennas, meanwhile the gain and beam-widths are enhanced to amplify the signal in the desired band without any increase in the total volume of the module or made the design bulky. Thus, it is expected that this methodology can be implemented to effectively reduce volume and cost of communication systems. This novel design methodology can easily be implemented in the communication systems where manufacturing cost, volume and weight of the module are at most importance needed for structural constraints.

REFERENCES

- [1] B. A. Munk, *Frequency Selective Surfaces: Theory and Design*. John Wiley & Sons, NY USA ISBN: 0-471-37047-9, 2000.
- [2] F. C. Seman and N. K. Khalid, "Double square loop FSS with slots for closer band spacing at oblique incidence," *In Proc. IEEE Asia-Pac. Conf. Appl. Electromagn.*, pp. 195,198, Dec. 8-10, 2014.
- [3] P. Mahouti, F. Güneş, M. A. Belen, A. Çalışkan, S. Demirel, and Z. Sharipov, "Horn antennas with enhanced functionalities through the use of frequency selective surfaces," *Int. J. RF Microwave Comp. Aid Eng.*, 26: 287-293, 2016. doi:10.1002/mmce.209
- [4] P. Mahouti, F. Güneş, M. A. Belen, Z. Sharipov, and S. Demirel, "TEM horn antennas with enhanced functionalities through the use of frequency selective surfaces," *The 3rd EMC Turkiye Conference*, Isik University, Maslak/Istanbul, Sep. 2-4, 2015.
- [5] F. Güneş, Z. Sharipov, M. A. Belen, and P. Mahouti, "GSM filtering of horn antennas using modified double square frequency selective surface," *Int. J. RF Microwave Comp. Aid Eng.*, 27, 2017. doi: 10.1002/mmce.2114
- [6] J. A. Miller, J. C. Batchelor, and A. P. Edward, "FSS printed using conducting ink," *In Proc. IEEE Antennas Propag. Soc. Int. Symp.*, pp. 1-4, 2010.
- [7] R. D. Seager, A. Chauraya, J. Bowman, M. Broughton, R. Philpott, and N. Nimkulrat, "Fabric based frequency selective surfaces using weaving and screen printing," *Electron. Lett.*, vol. 49, no. 24, pp. 1507-1509, 2013.
- [8] A-info, LB8180, 0.8-18 GHz Broadband Horn Antenna. Available at: http://www.ainfoinc.com/en/p_ant_h_brd.asp, Accessed on August 15, 2017.
- [9] R. J. Bauerle, R. Schrimpf, E. Gyorko, and J. Henderson, "The use of a dielectric lens to improve the efficiency of a dual-polarized quad-ridge horn from 5 to 15 GHz," *IEEE Transactions on Antennas*

- and Propagation*, vol. 57, no. 6, June 2009.
- [10] A. S. Türk, A. K. Keskin, and M. D. Şentürk, "Dielectric loaded TEM horn-fed ridged horn antenna design for ultrawideband ground-penetrating impulse radar," *Turkish J. Elec. Eng. & Comp. Sci.*, 23: 1479-1488, 2015.

A Low-Profile Miniaturized Frequency Selective Surface with Insensitive Polarization

Meiyu Wang¹, Lei Zhao^{2*}, Jun Wang², Xinhua Liang³, Shengjun Zhang⁴, Yingsong Li¹, and Wenhua Yu²

¹ College of Information and Communication Engineering
Harbin Engineering University, Harbin, 150001, China

² Center for Computational Science and Engineering, School of Mathematics and Statistics
Jiangsu Normal University, Xuzhou, China

*leizhao@jsnu.edu.cn

³ School of Physics Electronic Engineering, Jiangsu Normal University, Xuzhou, China

⁴ National Key Laboratory of Science and Technology on Test Physics & Numerical Mathematical, Beijing, China

Abstract — In this letter, a low-profile miniaturized broadband bandpass frequency selective surface (FSS) is proposed. The proposed structure consists of a convoluted dipole metal layer and its complementary pattern, which are separated by a dielectric substrate with a thickness of $0.003\lambda_0$, where λ_0 is the resonant wavelength in free space. The cell size of the proposed FSS is only $0.03\lambda_0 \times 0.03\lambda_0$. Furthermore, 3 dB bandwidth of the proposed FSS is approximately 50% for the normal incidence. Low profile and miniaturization of the structure element contribute to the great stability of frequency response under the incident waves with different incident angles and polarizations. To better understand the operational principle of the proposed FSS, the equivalent circuit model is presented. The proposed FSS prototype was fabricated and measured to validate the design.

Index Terms — Angular stability, frequency selective surface, miniaturization, wideband

I. INTRODUCTION

Frequency selective surfaces (FSSs) as spatial filters have been extensively studied in the past decades, and they have been widely used for antennas, radomes, satellite communications, electromagnetic interference (EMI) shielding and other microwave and millimeter wave applications [1-3]. Due to the space constraints in practical applications, it is necessary to include enough number of unit cells in a finite space to achieve the similar performance as in an infinite space. In addition, reducing cell size cannot only delay the generation of grating lobes, but also reduce the distortion in conformal surfaces. Recently, a large number of studies have been

focusing on miniaturization of the unit cell, and many techniques are proposed to achieve miniaturization. The miniaturization of the unit cell can be expressed as reducing the resonance frequency without changing the unit size.

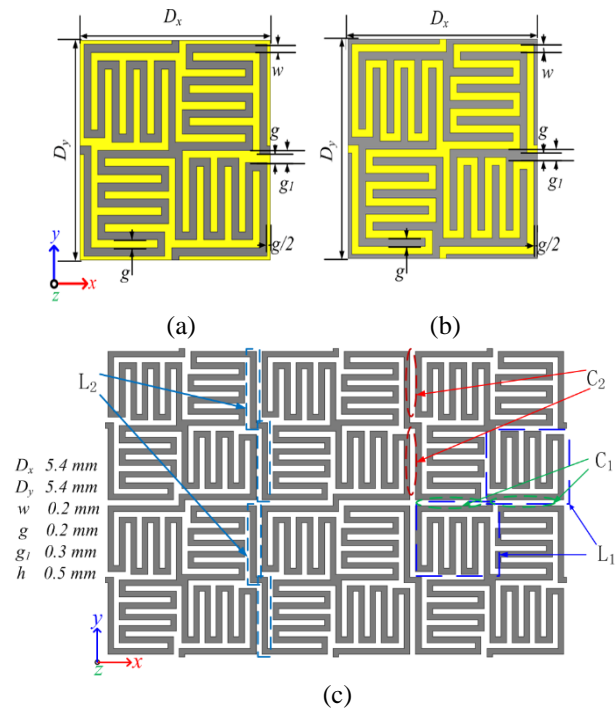


Fig. 1. Geometry of the proposed FSS. (a) Top layer element. (b) Bottom layer element. (c) Top layer structure and parameter description.

It is well known that the resonant frequency reduction needs to increase the inductance and capacitance values of the equivalent circuit. In [4], a class of bandpass FSSs were proposed, which were made up of metallic patches separated by a thin substrate backed by a wire mesh with the same periodicity. The unit size of the structure does not depend on a half resonant wavelength. By minimizing the line width and gap, the cell size can be greatly reduced. With the interweaving technique proposed in [5], the convoluted cross dipole is modified to interweaved with its neighbors to reduce resonant frequency. The miniaturized FSS using 2.5D closed loop connected in series by four vias is provided in [6]. The miniaturization of the 2.5D structure is achieved by expanding the 2D structure to 2.5D in space, increasing inductances in the unit cell and capacitance between the adjacent cells through vias. Another alternative method is to add lumped elements directly between the gaps in the structures [7]. Because the lumped components require soldering and their own stability requirements, this method can only be used in particular environments.

In addition, multilayer [8] and convoluted structures [9] are also provided for miniaturization. In [10], two layers on two sides of a substrate are arranged orthogonal to each other for generating a very strong cross-layer capacitance to achieve miniaturization that can miniaturize the element size much further. An ultra-thin single-layer miniaturized-element FSS based on meander line approach is shown in [11]. Being asymmetric in nature, the structure is sensitive to polarization.

In this letter, a new miniaturized low profile bandpass FSS is proposed. Since the bandpass FSS is usually modeled as a parallel LC circuit. By using the meander line to increase the strip length, the equivalent inductance is greatly increased. The larger inductance values result in smaller resonant frequencies and wider bandwidth as resonant frequency $f_0 = 1/2\pi\sqrt{LC}$ and bandwidth $W \propto \sqrt{L/C}$. Compared to the structures mentioned above, the proposed FSS has the following advantages: 1) The unit cell size is compact, which only has $0.03\lambda_0 \times 0.03\lambda_0$; 2) The symmetry and miniaturization of the cell size as well as the thin dielectric layer together lead to more stable characteristics.

II. GEOMETRY AND EQUIVALENT CIRCUITS MODEL

Figure 1 shows the geometry of the proposed FSS, which consists of a convoluted line metallic layer etched on the top of the substrate, while its complementary pattern is laid on the back of the substrate. The gray area represents the metal layer and the yellow area represents the dielectric substrate. The element of the structure exhibits 90° of rotational symmetry, a quarter of which is made up of a section of meander line and a metallic

strip connecting adjacent cells. The proposed FSS is etched on a 0.5mm-thick F4B substrate with a relative dielectric constant of 2.65 and a loss tangent of 0.0015. The other design parameters of the proposed structure are given in Fig. 1.

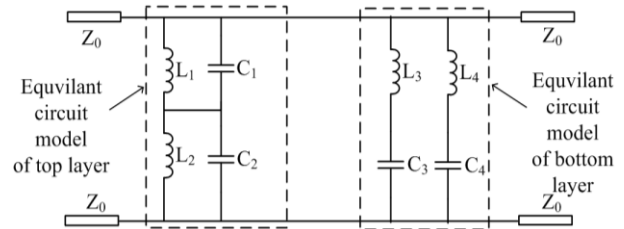


Fig. 2. Equivalent circuit model (ECM) of the proposed FSS.

The equivalent circuit model of the proposed FSS is demonstrated in Fig. 2. The effects of the top layer on total inductance and capacitance are described on the left side of Fig. 2. The equivalent circuit of the bottom layer resonator can be described as the dual form of the top layer, which is shown on the right side of Fig. 2. Under vertical polarization, the direction of the electric field is in the y -axis. The circuit of the top layer resonator without patterns on the back side describes as series of two parallel LC resonators. In the parallel resonator composed of L_1 and C_1 , L_1 corresponds to the strips paralleling to the y -axis, while C_1 is generated by the cell gap perpendicular to the y -axis. L_2 and C_2 respectively represent the mutual inductance and capacitance introduced by the metallic strip between adjacent cells, which work together as a parallel resonator. The meander line increases inductance of the equivalent circuit, while the metallic strip connecting adjacent cells introducing extra inductance and capacitance, which together contribute to the miniaturized unit cell. The corresponding structural parts of the circuit parameters are shown in Fig. 1 (c).

$Z_0 = 377\Omega$ is the free space impedance. The influence of the dielectric layer has been considered for obtaining the circuit parameters of the equivalent circuit. We use the curving fitting method proposed in [13] to get the parameter values of the equivalent circuit model. The top layer resonator is used as an example to discuss the curve fitting.

Firstly, the transmission coefficient $T(\omega)$ of the FSS is obtained by using the full-wave simulation, where the impedance Z_{FSS}^s is calculated by using the following formula:

$$Z_{FSS}^s = \frac{T(\omega) \cdot Z_0}{2[1 - T(\omega)]}. \quad (1)$$

Then, the impedance of the top layer resonator can be expressed as:

$$Z_{FSS}^s = \frac{j\omega(L_1 + L_2 - \omega^2 L_1 L_2 (C_1 + C_2))}{(1 - \omega^2 L_1 C_1)(1 - \omega^2 L_2 C_2)}. \quad (2)$$

Next, we minimize the Euclidean distance between Z_{FSS}^s and Z_{FSS} to obtain the parameters of the equivalent circuit. Finally, the ECM is achieved by using the equivalent circuit parameters. The ECM results of the designed FSS are gotten by the same method used for getting the top layer resonator, where the effects of the dielectric layer are included in the calculation results.

From the curve fitting, the parameters are gotten and listed as follows: $L_1 = 8.65$ nH, $C_1 = 0.13$ pF, $L_2 = 0.79$ nH, and $C_2 = 0.20$ pF are obtained for the top layer resonator; while $L_1 = 9.75$ nH, $C_1 = 0.12$ pF, $L_2 = 0.90$ nH, $C_2 = 0.17$ pF, $L_3 = 2.37$ nH, $C_3 = 0.62$ pF, $L_4 = 3.41$ nH, and $C_4 = 50.21$ fF are achieved for the designed FSS. From the fitting results in Fig. 3, we can observe that the equivalent circuit results for two different cases agree with the full wave simulation results.

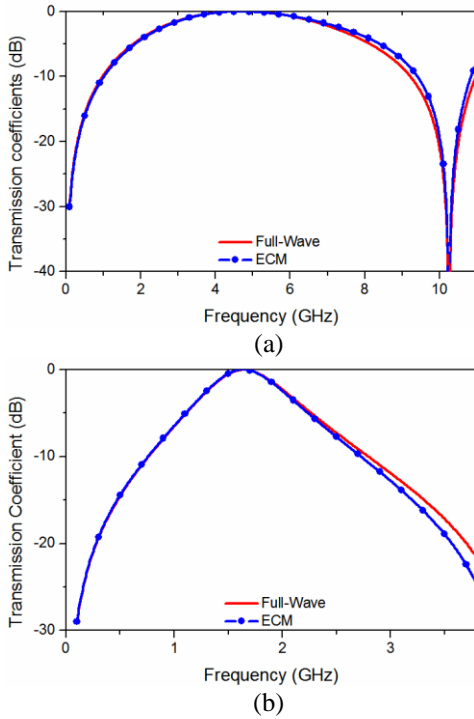


Fig. 3. Simulation and equivalent circuit results of the proposed FSS. (a) Top layer resonator without patterns on the back side. (b) Complementary FSS.

According to the description in [14], if the patch-type and slot-type FSSs (complementary structure of patch-type FSS) have the same size and are illuminated by a plane wave, the resonant frequencies of the patch elements are approximately same. If the complementary arrays are printed on both sides of a substrate, a passband with lower resonant frequency will be generated. In

this letter, the proposed CFSS is used to achieve further miniaturization. Together with the ultra-wide band characters of the original slot-type resonator (top layer resonator), the proposed CFSS eventually achieved miniaturization and wideband characteristics.

III. SIMULATION AND ANALYSIS RESULTS

Full wave simulation is performed by using HFSS with the Master/Slave boundary conditions in the x - and y -directions to achieve periodicity. Floquet modes are used to excite the proposed FSS. Simulated results with different dielectric constants are shown in Table 1. The comparison of the simulation results of FSS and literature is also presented in Table 1. From Table 1, we can see that the proposed FSS has smaller unit cell and larger bandwidth than the previous results. In Table 1, FBW is 3 dB transmission bandwidth.

Table 1: Compare proposed FSS with Literature

Reference	ϵ_r	Unit Cell Size λ_0	f_0	FBW at Normal Incidence (%)
[8]	2.65	0.050	2.16	18.75
[9]	3	0.046	2.5	36
[4]	3.4	0.234	14	30.78
[10]	4.3	0.045	1.35	7.5
[12]	5	0.055	3.82	10.5
Proposed FSS	2.65	0.030	1.64	50.6
	3	0.028	1.57	46.5
	3.4	0.027	1.5	44.7
	4.4	0.024	1.35	40
	5	0.023	1.28	34.4

To illustrate the transmission coefficients of the proposed structure, we only take the relative dielectric constant to be 2.65 as an example. Figure 6 shows the frequency response of the proposed FSS. The detailed TE and TM transmission characteristics under oblique incidences are shown in Tables 2 and 3, respectively. From Tables 2 and 3, we can see that the maximum transmission values both appear at 1.64 GHz for TE and TM wave under the normal incidence.

Table 2: Detailed transmission characteristics of the proposed FSS for TE wave

Incident Angle (degree)	TE				
	0	15	30	45	60
Resonant Frequency (GHz)	1.64	1.63	1.64	1.64	1.64
-3dB Bandwidth (MHz)	830	790	720	600	430

Table 3: Detailed transmission characteristics of the proposed FSS for TM wave

TM					
Incident Angle (degree)	0	15	30	45	60
Resonant Frequency (GHz)	1.64	1.64	1.64	1.65	1.66
-3dB Bandwidth (MHz)	830	840	950	1130	1520

Compared with the normal incidence, when the incidence angle increases to 60° , the maximum shift of the resonant frequency is 0.6% for the TE wave, while the bandwidth is reduced from 830 MHz to 430 MHz. The maximum shift of the resonant frequency is 1.2% for the TM polarization, while its bandwidth is increased from 830 MHz to 1520MHz. It is shown that for the TE wave, the bandwidth decreases as the incident angle increases; for the TM wave, the bandwidth decreases as the incident angle increases. This is because that as the angle of incidence θ varies, for the TE wave, the impedance changes as $Z_0/\cos\theta$, and thus results in a higher loading quality factor of the resonator. For the TM wave, the impedance changes as $Z_0 \cos\theta$, leading to a lower loader quality factor. Higher loading quality factor results in a narrower bandwidth, and vice versa [1, 15].

Figure 4 shows the transmission coefficients under various incident angles and polarization angles. From the figure we can see that the transmission coefficients are basically unchanged for specific incidence angle under different polarizations.

IV. EXPERIMENTAL RESULTS

In order to verify the design, the proposed FSS prototype was fabricated and measured. The fabricated FSS was printed on an F4B dielectric substrate with a relative permittivity of 2.65, which consists of 75×75 cells on both sides of the dielectric layer in an area of $405 \text{ mm} \times 405 \text{ mm}$. Figure 5 shows the photograph of the FSS measurement setup. Measurement is performed using two horn antennas (1~18 GHz) and a vector network analyzer. The FSS located between the two horn antennas that are used as the transmitting and receiving antennas. The center of the FSS is aligned with the centerline of the measurement antenna. Two measurement antennas are aligned to ensure uniform plane wave illumination on the FSS structure. In order to ensure measurement accuracy, the measurement setup is calibrated by measuring data without FSS present. Measurements with different polarizations and incidence angles are achieved by rotating the antennas and FSS structures while keeping the alignment of the central line. The measured results for oblique incident angles and different polarizations are shown in Fig. 6. It can be observed that there are some differences between the

measurement results and the simulation ones, which are mainly caused by manufacturing tolerance and measurement errors, as the measurement conditions are limited.

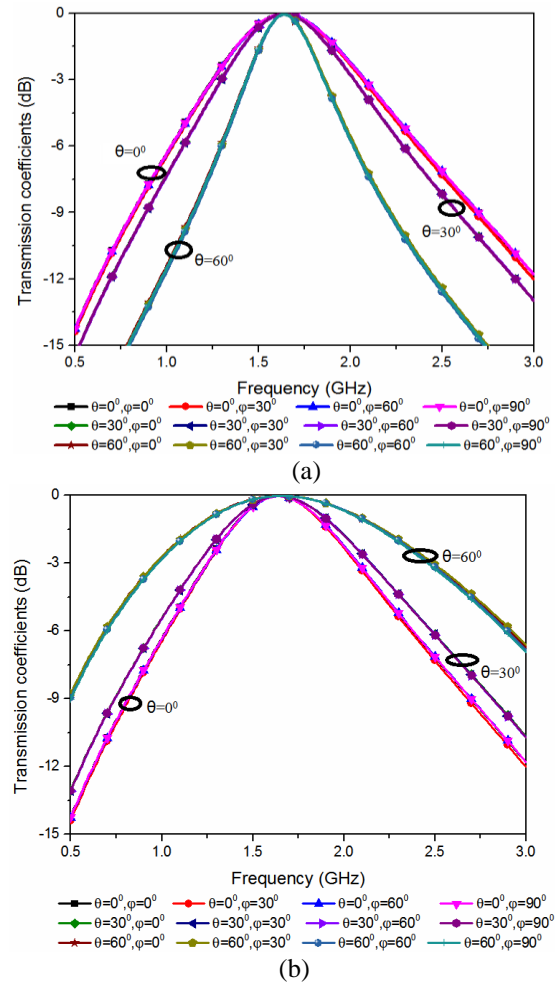


Fig. 4. Transmission coefficients under various incident angles and polarization angles. (a) TE wave incidence, and (b) TM wave incidence.

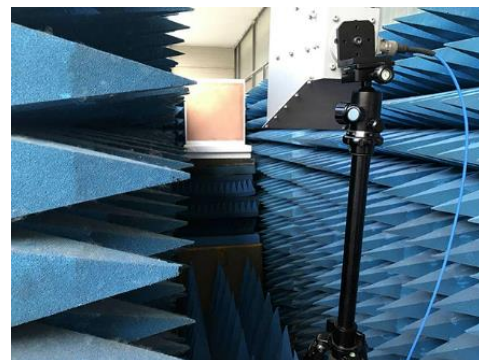


Fig. 5. Measurement setup.

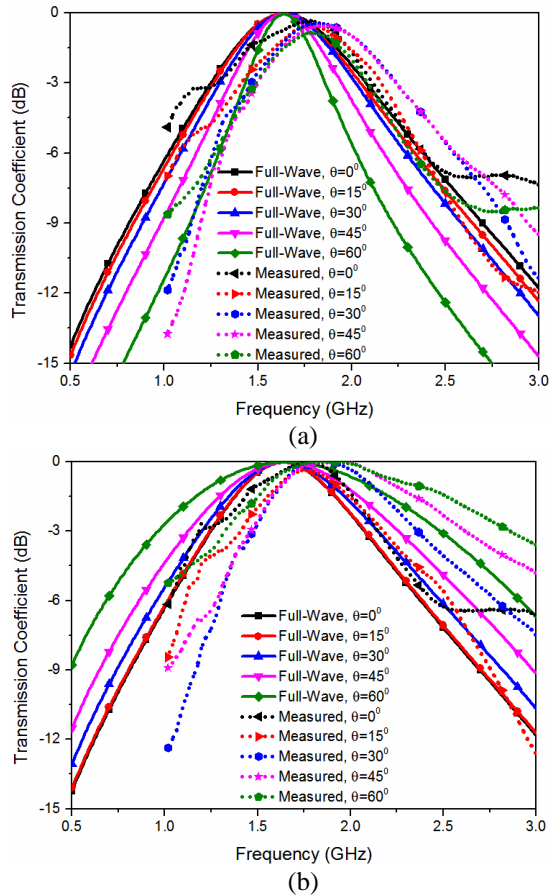


Fig. 6. Simulated and measured transmission coefficients of the proposed FSS. (a) TE wave and (b) TM wave.

V. CONCLUSION

In this letter, a new low-profile FSS based on the meander line and its complementary pattern is proposed to achieve miniaturization, wide bandwidth and polarization insensitive. The unit cell size of the proposed FSS structure can be reduced to $0.03\lambda_0 \times 0.03\lambda_0$. A simple equivalent circuit model is demonstrated to illustrate the working principle of the proposed FSS.

ACKNOWLEDGMENT

This work was supported in part by the National Science Foundation of China under Grant 61771226, 61671223 and 61571031, and in part by the Natural Science Foundation of the Jiangsu Higher Education Institutions of China under Grant no.18KJA110001.

REFERENCES

- [1] B. A. Munk, *Frequency Selective Surfaces: Theory and Design*. New York, NY, USA: Wiley, 2000.
- [2] S. Yang, J. Zhang, Y. Pang, M. Feng, and S. Qu, "Water-based metamaterial absorber for broadband electromagnetic wave absorption," *International Applied Computational Electromagnetics Society Symposium*, pp. 1-2, 2017.
- [3] M. A. A. Abessolo, Y. Diallo, A. Jaoujal, A. El Moussaoui, and N. Aknin, "Stop-band filter using a new metamaterial complementary split triangle resonators (CSTRs)," *Applied Computational Electromagnetics Society Journal*, vol. 28, no. 4, pp. 353-358, 2013.
- [4] K. Sarabandi and N. Behdad, "A frequency selective surface with miniaturized elements," *IEEE Trans. Antennas Propag.*, vol. 55, no. 5, pp. 1239-1245, 2007.
- [5] F. Huang, J. C. Batchelor, and E. A. Parker, "Interwoven convoluted element frequency selective services with wide bandwidths," *Electron. Lett.*, vol. 42, no. 14, pp. 788-790, 2006.
- [6] Y. R. Shi, W. Zhuang, W. C. Tang, C. Wang, and S. Liu, "Modeling and analysis of miniaturized frequency-selective surface based on 2.5-dimensional closed loop with additional transmission pole," *IEEE Trans. Antennas Propag.*, vol. 64, no. 1, pp. 346-351, 2016.
- [7] H. L. Liu, K. L. Ford, and R. J. Langley, "Design methodology for a miniaturized frequency selective surface using lumped reactive components," *IEEE Trans. Antennas Propag.*, vol. 57, no. 9, pp. 2732-2738, 2009.
- [8] H. Li, C. Yang, Q. Cao, and Y. Wang, "An ultrathin bandpass frequency selective surface with miniaturized element," *IEEE Antennas Wireless Propag. Lett.*, vol. 16, pp. 341-344, 2016.
- [9] P. C. Zhao, Z. Y. Zong, W. Wu, and D. G. Fang, "A convoluted structure for miniaturized frequency selective surface and its equivalent circuit for optimization design," *IEEE Trans. Antennas Propag.*, vol. 64, no. 7, pp. 2963-2970, 2016.
- [10] M. N. Hussein, J. F. Zhou, Y. Huang, M. Kod, and A. P. Sohrab, "Frequency selective surface structure miniaturization using interconnected array elements on orthogonal layers," *IEEE Trans. Antennas Propag.*, vol. 65, no. 5, pp. 2376-2385, 2017.
- [11] A. B. Varuna, S. Ghosh, and K. V. Srivastava, "A miniaturized-element bandpass frequency selective surface using meander line geometry," *Microw. Opt. Techn. Lett.*, vol. 59, no. 10, pp. 2484-2489, 2017.
- [12] G. Yang, T. Zhang, W. Li, and Q. Wu, "A novel stable miniaturized frequency selective surface," *IEEE Antennas Wireless Propag. Lett.*, vol. 9, pp. 1018-1021, 2010.
- [13] F. Costa, A. Monorchio, and G. Manara, "Efficient analysis of frequency selective surfaces by a simple equivalent circuit approach," *IEEE Antennas Propag. Mag.*, vol. 54, no. 4, pp. 35-48, 2012.
- [14] D. S. Lockyer, J. C. Vardaxoglou, and R. A. Simpin, "Complementary frequency selective

- surfaces,” *IEE Proc. Microw., Antennas Propag.*, vol. 147, no. 6, pp. 501-507, 2000.
- [15] M. Al-Joumayly and N. Behdad, “A new technique for design of low-profile second-order bandpass frequency selective surfaces,” *IEEE Trans. Antennas Propag.*, vol. 57, no. 2, pp. 452-459, 2009.

The Design of a High Gain Dual-Polarized Quad-Ridged Circular Horn Antenna for Wideband EMC Test Applications

Bekir Solak^{1,3}, Mustafa Secmen², and Ahmet Tekin³

¹ TUBITAK Space Technologies Research Institute
Microwave and Antenna Systems Group, Ankara, Turkey
bekir.solak@tubitak.gov.tr

² Department of Electrical and Electronics Engineering
Yasar University, Bornova, Izmir, 35100, Turkey
mustafa.secmen@yasar.edu.tr

³ Department of Electrical and Electronics Engineering
Ozyegin University, Cekmekoy, Istanbul, 34794, Turkey
ahmet.tekin@ozyegin.edu.tr

Abstract — This paper presents the design of a high gain broadband quadruple-ridged circular horn antenna for Electromagnetic Compatibility (EMC) testing. The proposed antenna contains a wideband feed structure as a transition between coaxial line and quad-ridged circular waveguide behind the conical horn antenna. The wideband matching between impedances at the apertures of the feed and the horn is achieved with a tapering at the flare section along the horn length, which is obtained after a detailed investigation of various tapering profiles. The antenna is designed to operate in horizontal and vertical polarizations (dual linear polarization) simultaneously in EMC tests. This implementation is found to present a return loss greater than 10 dB, isolation level higher than 28 dB, high-gain (minimum 13.6 dBi) and low-gain variation of 4.5 dBi within the frequency range of 1-6.75 GHz (6.75:1 bandwidth) at both polarizations, which is a desired feature in radiated emission and immunity tests.

Index Terms — Circular horn antenna, dual polarization, Electromagnetic Compatibility (EMC), quad-ridged circular waveguide, wideband antenna.

I. INTRODUCTION

Electromagnetic Compatibility (EMC) can simply be explained as how well a device or system is able to operate in an electromagnetic environment without introducing electromagnetic disturbances, which can interfere with the operation of the other electrical products. The EMC standards contain the requirements for the qualification of a particular electronic product that depends on application area in which the product is to be used. EMC studies the unintentional generation,

propagation, and reception of electromagnetic energy [1]. EMC issues can be investigated in two main categories. Radiated emission is related to the unwanted generation of the electromagnetic signal from the product which can spoil the proper operation of the other products. Immunity or susceptibility on the other hand can be considered to be reverse process of the radiated emission where the proper operation of the equipment under test (EUT) exposed to an electromagnetic field is investigated [2]. Tests of both radiated emission and immunity are carried out for a wide frequency bandwidth such as 1-6 GHz with respect to the EMC standards [3]; and hence, wideband antennas should be used for this purpose.

Horn antennas are commonly used for many applications such as radar, radio astronomy, electronic warfare and tests/measurements such as EMC tests. Broadband horn antennas have received more attention in EMC test applications in comparison to other wideband antenna candidates such as biconical and log-period antennas since the horn antennas can provide higher gain, better return loss and more compact structures [4]. Besides, as an important issue in the EMC measurement to save a significant amount of time in the tests, the horn antennas can be used in dual linear polarization simultaneously, which is not easily possible with a single biconical and log-periodic antennas of broadband applications. The traditional horn antennas (pyramidal or conical); however, are originally narrow band where the feed standard rectangular or circular waveguides behind them limits the operation frequency bandwidth [5,6].

The usage of ridges in the rectangular or circular waveguide was shown to give a single mode operation for a substantially wider bandwidth by decreasing the

cutoff frequency of the dominant mode [7-10]. The ridge waveguides, which also become the solution of limited bandwidth problem of the horn antennas, are frequently used for the excitation of wideband horn antennas. In order to give proper matching in the broadband, the ridges should be also used in the flare section of the horn antennas.

The double ridge horn antennas with the double ridged waveguides behind can give single linear polarization [11]. It is shown with the relevant studies that extremely wideband operation can be satisfied for the frequency band of 2-18 GHz (9:1 bandwidth) [12], 1-18 GHz (18:1 bandwidth) [13,14] and even for 2-40 GHz (20:1 bandwidth) [15] by providing $VSWR \leq 2$ or $S_{11} \leq -9.5$ dB (return loss ≥ 9.5 dB). The bands of these single linear polarized antennas are sufficiently enough for EMC tests covering radiation emission and immunity measurements with the frequency bandwidth of 6:1.

In radiated emission and immunity tests, the measurements are generally acquired for both two orthogonal linear polarizations (vertical and horizontal). For this purpose, the EMC tests done with single linear polarized (double-ridged) antennas should be realigned for each polarization case (single vertical and single horizontal), which increases the measurement time significantly. Therefore, recently, dual linear polarized antennas, which are able to take the measurements of both polarizations at once, are becoming more popular. The dual polarization in the horn antennas can be realized by using quadruple ridges both in the waveguide behind horn and in the flare of the horn along axial direction. However, the usage of quad-ridged structure reduces the bandwidth significantly due to excitation of additional higher-order modes as compared to double-ridged case such that the ultra-wideband operations such as 9:1, 18:1 or 20:1 bandwidth cannot be obtained easily. For broadband applications, the square and circular cross-sections are used. However, when the studies with square horn in [16] and circular horn in [17], which give $VSWR \leq 2.6$ and $VSWR \leq 2.2$ for 8-18 GHz, respectively; and the square and circular structures giving 4:1 and 6:1 bandwidth, respectively in [18] are investigated, the circular (conical) horn antennas can be stated to give better performance. This has led to the choice of circular cross-section in the proposed study.

The antennas used in EMC radiated emission and immunity test are desired to have high gain and low gain variation (almost constant gain) as well as low VSWR and dual linear polarization characteristics. When most of the reported studies with circular or square quad-ridged horn antennas for wideband applications were investigated [17,19-21], it was noticed that none could provide return loss higher than 10 dB (or $VSWR \leq 1.925$) for 6:1 frequency bandwidth, which is very much needed for radiated emission and immunity tests at 1-6 GHz. Two recent designs [22, 23] among these studies have

improved results by giving return losses higher than 10 dB at both ports, i.e. $S_{11} \leq -10$ dB and $S_{22} \leq -10$ dB, within almost 6:1 bandwidth (1.66-10 GHz in [22] and 2-12 GHz) in [23]). However, the performances of minimum gain and gain variation within the frequency band are not so satisfactory such that the work in [22] approximately reports minimum 8 dBi gain at the lower part of the frequency band, and a gain variation of 10 dB within the band; while the design in [23] has about 10 dBi minimum gain, and 8 dB variation.

In this paper, a circular horn antenna with quadruple ridges in the flare of the horn and in the circular waveguide behind the antenna is designed. The proposed antenna works at the EMI test frequency band of 1-6.75 GHz (6.75:1 bandwidth) by yielding a reflection coefficient below -10 dB ($VSWR \leq 1.925$), minimum 13.6 dBi gain and about 4.5 dB gain variation within the band with dual polarization feature. This special antenna, which is designed to cover the frequency bands of EMC radiated emission and immunity tests, has also minimum isolation of 28 dB between ports. The antenna achieves the mentioned performance metrics with a quad-ridged circular waveguide including a specially designed back cavity to make a proper transition from coaxial feed to the quadruple circular waveguide, and a conical horn with a x^p tapered ridge profile, which is obtained as a result of a detailed profile and parametric investigations.

The rest of the paper is organized as follows: Section II includes the design and results for the transition from coaxial to quad-ridged circular waveguide, which consists of a special back cavity to suppress the effects of undesired higher order modes inside the circular waveguide. As to the design part of circular horn, the investigation of possible ridge profiles inside the conical horn and the parameter study of the ratio of aperture radius to circular waveguide radius (the radius of the beginning of the flare) are given in Section III. Finally, CST Microwave Studio simulation results of the overall antenna are presented in Section IV, followed by the conclusion in Section V.

II. THE DESIGN OF COAXIAL TO QUAD-RIDGED CIRCULAR WAVEGUIDE AS THE FEED OF CIRCULAR HORN ANTENNA

As stated in Section I, the ridged waveguides can supply wider bandwidth in comparison to hollow waveguides by decreasing the cutoff frequency of the dominant mode and increasing the frequency bandwidth between the dominant mode and the second lowest mode (second higher order mode). However, as described in [8] and [10], in the case of quadruple ridged waveguide, although the insertion of ridges decreases the cutoff frequency of the fundamental mode would also reduce the cutoff frequency second lowest mode. The cutoff frequency of second lowest mode becomes very close to that of the fundamental mode when the ridge is heavily

loaded, i.e., the gap between the ridges are so small. Therefore, if a single mode operation is desired, the effect of the second lowest mode should be suppressed. In the circular quad-ridge waveguide case, the dominant mode is TE_{11} mode and the second lowest one is TE_{21L} , which arises from the splitting of TE_{21} mode into TE_{21L} and TE_{21U} . Besides, if a wideband operation with about 6:1 bandwidth is desired, other higher modes such as TE_{21U} , TE_{01} , TE_{31} and TM_{01} modes of circular quad-ridged waveguide should be also taken into account that the cutoff frequencies of these modes probably fall into the frequency region of interest. Therefore, the transition from coaxial to quad-ridged waveguide should be carefully designed to annihilate the effects of these higher order modes. The design of the mentioned transition is critical in terms of return loss and isolation performances of the overall antenna structure. The circular horn part of the overall antenna design does not significantly deteriorate the reflection and isolation performance of the overall antenna structure when a smooth tapering is used for the ridges inside the flared circular horn. Therefore, the return loss and isolation performances are mainly determined with the feed waveguide part of the overall design.

The suppression of these higher order modes and especially for the most crucial higher order mode of TE_{21L} cannot be achieved successfully by just arranging the probe of SMA connector inserted into the standard circular quad-ridged waveguide whose one side is back shorted with a metallic plate along the propagation axis without the addition of any cavity. This is because the suppression of TE_{21L} mode also makes a reduction in the effect of TE_{11} mode since the cutoff frequencies of both modes are close to each other. Therefore, in order to provide a wider bandwidth, a back cavity structure behind the feeding pins is generally used.

In [17] and [18], the cylindrical and conical back cavities are implemented; however, the overall most of these structures were reported to yield no more than 3:1 bandwidth which is not sufficient for EMC emission and immunity tests. In this study, a transition depicted in Fig. 1 is designed to acquire satisfactory reflection and isolation performance. When the structure in Fig. 1 is investigated, there is a back-shortened part behind feed probes, which has the cross section of a quadruple circular waveguide with different ridge dimensions than feed quadruple circular waveguide. Therefore, hollow circular waveguide cavity used in [17] is replaced with a quadruple circular waveguide.

In the design of this study, it is targeted to obtain reflection coefficient lower than -10 dB for both ports ($S_{11} \leq -10$ dB and $S_{22} \leq -10$ dB), isolation greater than 30 dB, and the transmission coefficients of all possible and effective higher order modes such as TE_{21U} , TE_{01} , TE_{31} and TM_{01} modes lower than -10 dB for an effective

suppression of these undesired modes. The dimensions of the designed transition structure are obtained after performing an optimization process in CST Microwave Studio. The corresponding dimensions are given in Fig. 2 along with relevant cut views of the structure where the optimum radius of circular waveguide is found to be about $r_i = 57.12$ mm. For the given radius of circular waveguide, the corresponding cutoff frequencies of TE_{11} , TM_{01} , TE_{21} , TE_{01} and TE_{31} modes can be calculated approximately as 1.54 GHz, 2.01 GHz, 2.56 GHz, 3.21 GHz and 3.52 GHz, respectively, for a standard hollow circular waveguide [24]. Therefore, this standard hollow circular waveguide without any ridges inside can only operate within 1.5-2 GHz for a single mode operation, and even TM_{01} mode is suppressed, its bandwidth is not more than 1.66:1. If a frequency band of 1-6.75 GHz is desired, the cutoff frequency of fundamental TE_{11} mode should be decreased to below 1 GHz.

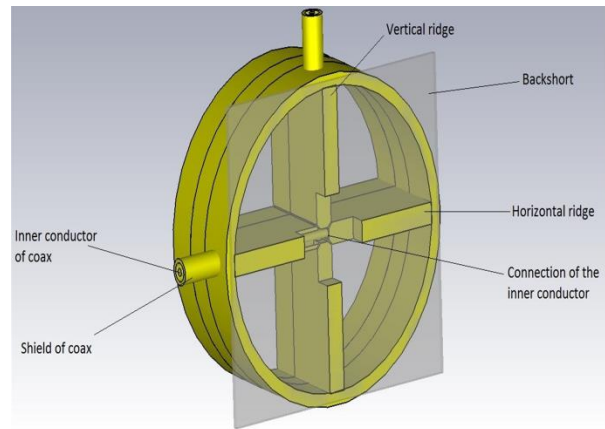


Fig. 1. The designed structure for the transition from coaxial feeds to circular quad-ridged waveguide where back-short metallic wall is deliberately shown as transparent.

When the quad-ridged dimensions given in Fig. 2 is used following the optimization process, it is verified in CST Microwave Studio that the cutoff frequencies of TE_{11} , TE_{21L} , TE_{21U} , TE_{01} , TE_{31} and TM_{01} are 0.346 GHz, 0.352 GHz, 2.767 GHz, 3.472 GHz, 3.634 GHz and 4.766 GHz. So, the cutoff frequency of TE_{11} mode is pushed below 1 GHz, and that of TM_{01} mode increases significantly as expected. However, again as expected, the cutoff frequency of the second lowest mode of TE_{21L} becomes quite close to TE_{11} mode. Since the desired frequency band is between 1 GHz and 6.75 GHz, the higher modes of TE_{21L} , TE_{21U} , TE_{01} , TE_{31} and TM_{01} whose cutoff frequencies are below 6.75 GHz should be suppressed as much as possible. This suppression is achieved by using a modified back cavity whose dimensions are given in Fig. 2 (b).

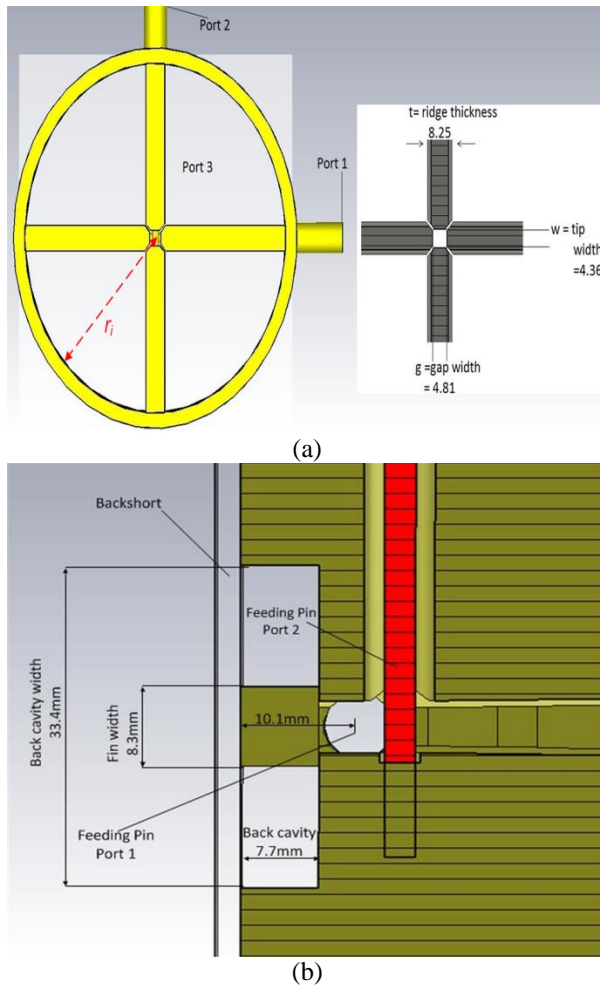


Fig. 2. (a) The front view of the designed transition structure and the relevant dimensions in mm, and (b) the side view of the designed transition structure and the relevant dimensions in mm.

The results corresponding to suppression of these modes are shown in Fig 3 (a) and 3(b) for the excitation from port 1 and port 2, respectively where the values below -40 dB are not presented for a better view. The reflection coefficients (S_{11} and S_{22}) and isolation between ports (S_{12} and S_{21}) are also given in addition to transmission coefficients (S_{31} for port 1 and S_{32} for port 2) of undesired modes. As it can be observed from the results in Fig. 3, all of the undesired higher order modes taken into account are suppressed more than 10 dB within the frequency band of 1-6.75 GHz for each port such that most of these modes are reduced by 15 dB within the given frequency band. Besides, the isolation is found to be more than 30 dB throughout the given band as desired. Finally, the reflection is below -10 dB for 1-6.75 GHz for the excitation of port 1, and 1-6.5 GHz for the excitation of port 2.

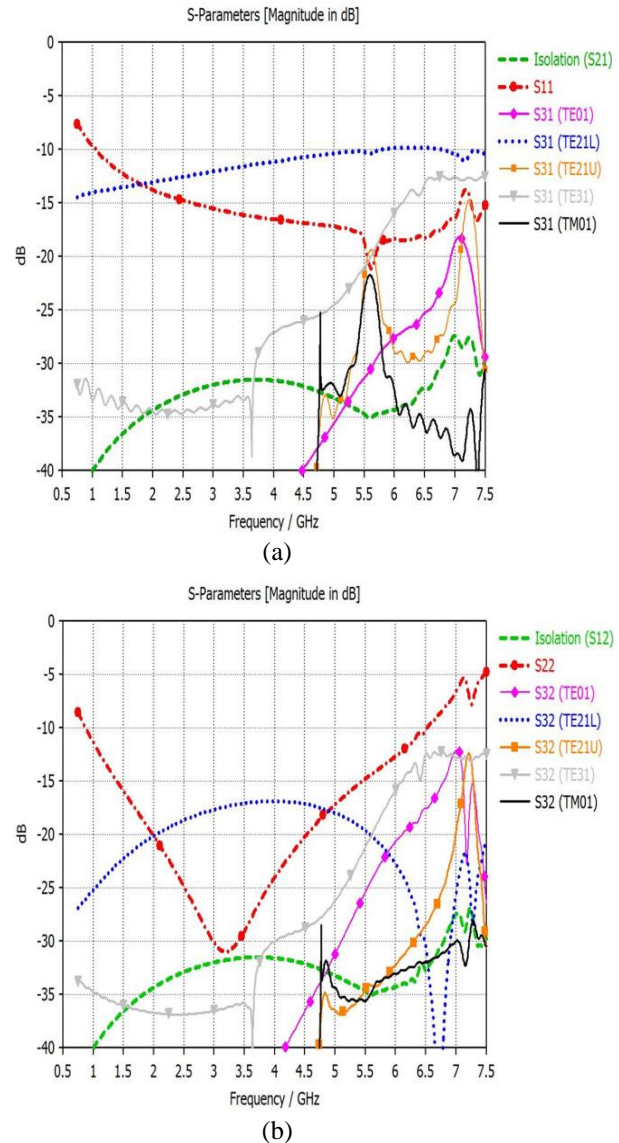


Fig. 3. (a) The reflection coefficient (S_{11}), isolation and transmission values (S_{31}) of undesired modes for port 1, and (b) the reflection coefficient (S_{22}), isolation and transmission values (S_{32}) of undesired modes for port 2.

III. QUAD-RIDGED CIRCULAR HORN ANTENNA STRUCTURE

After the determination of the transition from SMA feed connectors to quad-ridged circular waveguide, the design details of a circular horn section having quadruple ridges at the flare extension are presented. The quad-ridge circular waveguide structure of the previous section is arranged to match the mentioned flare extensions of the horn part. Due to the strict requirements of the application itself, the final antenna structure is expected to maintain about 13 dBi gain for 1-6.75 GHz

full-band in order to attain high gain characteristics for the antenna. In the aperture antennas including horn antennas, the minimum gain is usually achieved at the lowest frequency. Therefore, it is aimed to get minimum 13.75 dBi gain at 1 GHz for the design in consideration. The approximate and classical gain formula for circular horn antenna is given as [5]:

$$G(\text{dBi}) = 10 \log_{10} \left[\varepsilon_{ap} \frac{4\pi}{\lambda^2} (\pi a_{horn}^2) \right], \quad (1)$$

where ε_{ap} is the aperture efficiency, λ is the wavelength and a_{horn} is the radius at horn aperture. By taking maximum wavelength as $\lambda = 30$ cm (wavelength at $f = 1$ GHz) and ε_{ap} about 0.51 according to [5], the aperture radius of horn is approximately calculated to be $a_{horn} = 32.7$ cm for the desired minimum gain of 13 dBi. Then, the axial length (AL) of the horn is evaluated by using the curves given in [25], which relates the gain, diameter of the circular horn and axial length. The axial length of the designed horn is calculated as approximately $AL = 2.1\lambda$, which corresponds to about $AL = 63$ cm. The patterns of the ridges and sidewall of double or quadruple ridged circular horn antennas are usually determined with some special profile functions for a smooth taper between feed waveguide and horn aperture. All profiles, which are described as a radius value any z point at axial direction in [26], contain the parameters of L (length along axial direction), a_i (the radius at the feed point when $z = 0$) and a_o (the radius at the aperture point when $z = L$). For instance, the profile selected in this study, which is x^p profile, has the function of:

$$a(z) = a_i + (a_o - a_i) \left[(1-A) + A \left(\frac{z}{L} \right)^p \right], \quad (2)$$

where p is exponent parameter, and A is the linearity parameter. The ridge shape inside the circular horn can be categorized as un-truncated and truncated where a sample view of truncated ridge shape is depicted in Fig. 4. This particular design choice was preferred in this study. In the un-truncated ridge shape, the length parameter in (2) is selected as axial length (AL); consequently, taper length becomes equal to AL in Fig. 4. Besides, the radii at the aperture point parameter a_o are selected $a_{horn} = a_{side} = a_{ridge}$. Consequently, the curves for ridge and sidewall tapers approach to a point at $z = AL$ to form a tip at the end side of the ridge. In other words, the part without ridge in Fig. 4 is filled by a ridge structure giving a ridge shape with one side is a tip point and another side an edge.

In the truncated ridge shape, the length parameter in (2) is selected as taper length (TL) in Fig. 4, which was smaller than AL. Besides, $a_{horn} > a_{side} > a_{ridge}$ should be satisfied as given in Fig. 4. By satisfying these conditions, a ridge shape having edges at the both sides as shown in Fig. 4 was attained. The truncated ridge

structure has more flexibility and more design parameters with additional degrees of freedom in comparison to un-truncated one. Actually, when the studies in [17] and [18] utilizing from un-truncated ridges and the one in [23] using truncated ridges are compared, the superiority of the truncated ridges can be observed since it clearly yields a wider bandwidth. Therefore, the truncated ridge profiles rather were considered in the design. A thorough examination is carried out for several different profile functions (exponential, polynomial, x^p , etc.), taper length values (L value in profile functions) and radii at the ridge and sidewall aperture points (a_o values in profile functions). During this optimization process with advanced EM tools, the radii at the feed waveguide point (a_i values in profile functions) were kept as $a_{i,ridge} = 2.4$ mm and $a_{i,side} = 57.12$ mm, which corresponds to half of the gap width in Fig. 2 (b) and radius of the feed quadruple circular waveguide, respectively. Besides, the axial length was fixated at $AL = 63$ cm. The conditions of $L = TL < AL$ and $a_{horn} > a_{side} > a_{ridge}$ were found to be appropriate design parameters. The same profile functions were applied for both ridge and sidewall tapering during the design work. The optimization was strictly aimed to yield the minimum 13 dBi flat gain within 1-6.75 GHz with minimal fluctuations. As a result of the profile study, the x^p tapering is found to give best results with the parameters of $p = 2.15$, $A = 1$, $TL = 56.4$ cm and $a_{o,ridge} = 26.2$ mm for ridge taper and $p = 2.4$, $A = 1$, $TL = 60.3$ cm and $a_{o,ridge} = 28.15$ mm for sidewall taper in (2).

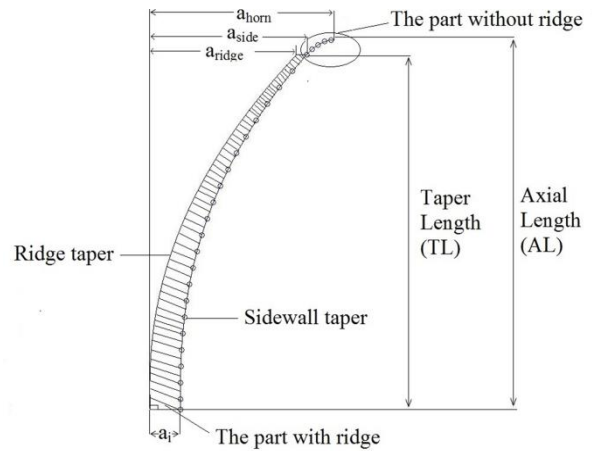


Fig. 4. The geometry of a truncated ridge in a circular horn antenna used in this study.

Among several simulations that were carried out, one crucial result is the comparison of possible profile functions. The corresponding results are depicted in Fig. 5 at which the gain values of the antennas' designs with different profiles for port 1 are given (where the results for port 2 are also similar). From the results in Fig. 5, the

x^p function has the gain between 13.7 dBi and 18.1 dBi in the frequency band of 1-6.75 GHz. The resultant gain variation is only about 4.4 dBi, which is lowest among all possible profiles.

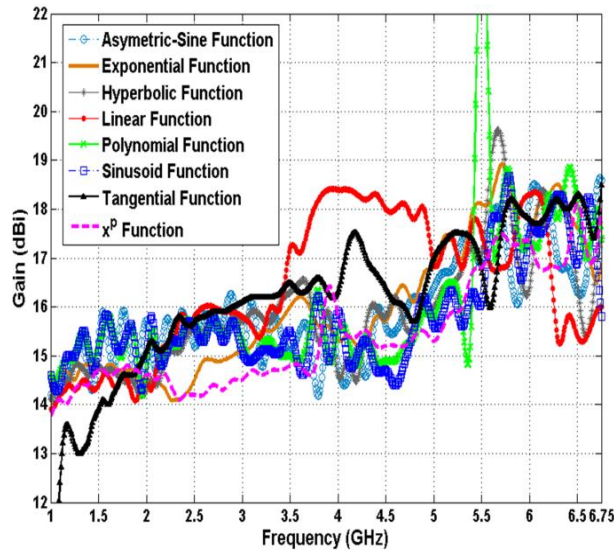


Fig. 5. The gain of the designed antenna for different profile functions when port 1 is excited.

After the reveal of the necessary parameters for the design of the ridges and circular horn antenna, an additional parameter about the feed waveguide dimension was explored. The aim of this analysis was to observe whether a modification in the feed waveguide structure improved the performance of the overall antenna or not. For this purpose, since $a_{i, \text{sidewall}} = 57.12$ mm is also equal to radius of feed quad-ridged circular waveguide behind the antenna, the value of $a_{i, \text{sidewall}}$ is varied by keeping all the parameters in the horn antenna part constant including $a_{o, \text{sidewall}} = 28.15$ cm. Since the radius of the circular waveguide has changed, all the dimensions of the transition including back cavity described in Section II were rearranged accordingly. The ratio of a_o/a_i is equal to $281.5 \text{ mm}/57.12 \text{ mm} = 4.93$ for the sidewall tapering of the original antenna, and this ratio is varied (increased and decreased) by keeping a_o value constant as 28.15 cm. The corresponding results for different a_o/a_i values are demonstrated in Fig. 6. According to results in Fig. 6, the original antenna with $a_o/a_i = 4.93$ still has minimum gain variation with 13.7 dBi minimum gain within the frequency band as compared to other ratio values. The ratio of $a_o/a_i = 5.22$ possesses very close results to those of $a_o/a_i = 4.93$; however, the original antenna gives slightly better results. Thus, this analysis also validates the transition structure.

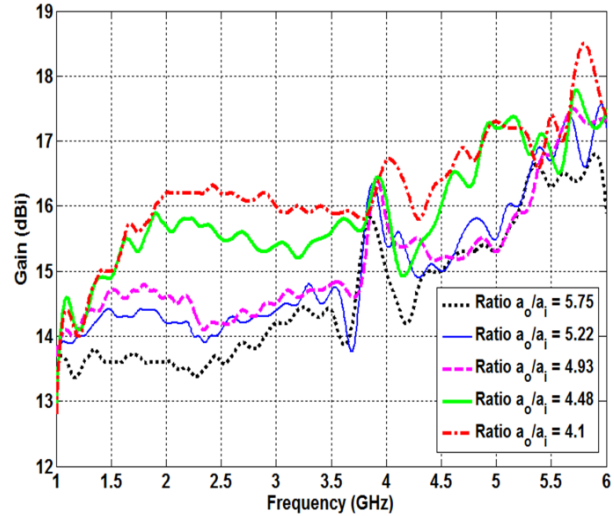


Fig. 6. The gain of the designed antenna for different a_o/a_i ratio values when port 1 is excited.

IV. THE RESULTS OF THE OVERALL ANTENNA

After the reveal of the necessary parameters for the design of the ridges and circular horn antenna with x^p profile ridges are completed, the final minor modifications on the overall antenna structure were done to acquire the concluding results of the antenna. The first slight modification realized on the resulting antenna is the addition of traditional curved-surface sections to the outside of the aperture edges of the circular horn antenna [5]. This insertion generally reduces the undesired diffraction from the edge of the aperture of the horn, which prevents the spoil of this diffraction on the radiation pattern. It also results in a slight improvement on the return loss performance of the antenna. The second modification is the realization of all final simulations with aluminum material for all parts of the designed antenna. The simulations realized in Section III are carried out with perfect electric conductor (PEC) in order to obtain the results more quickly. However, after the final design of the overall antenna was ensured, the simulations were repeated with aluminum to be more suitable for the practical low cost implementation. The simulation view of the final antenna design is depicted in Fig. 7, and the results are collected by exciting each horizontal and vertical polarization port one by one.

First, the reflection coefficient (return loss) and isolation performances of the final structure are examined. The results are shown in Fig. 8 such that the reflection coefficients are below -10 dB ($\text{VSWR} \leq 1.925$) for the desired frequency band of 1-6.75 GHz. The connection of the designed circular horn antenna to the output of

the transition described in Section II and the final modifications on the antenna do also improve overall return loss performance of the transition. When the reflection coefficient results of the transition for port 2 given in Fig. 3 (b) is examined, the values are higher than -10 dB especially for the problematic frequency region of 6.5-6.75 GHz. However, the values came out below -10 dB in the final antenna design as shown in Fig. 8 for this troubling region of port 2. The isolation performance of the overall antenna is found to be better than 28 dB for the whole frequency band. In comparison to the isolation results of the transition, which is higher than 30 dB, the antenna shows a small drop of about 2 dB in the isolation performance value; however, the isolation value of minimum 28 dB over the total frequency band can be still considered as sufficient for the target EMC application.

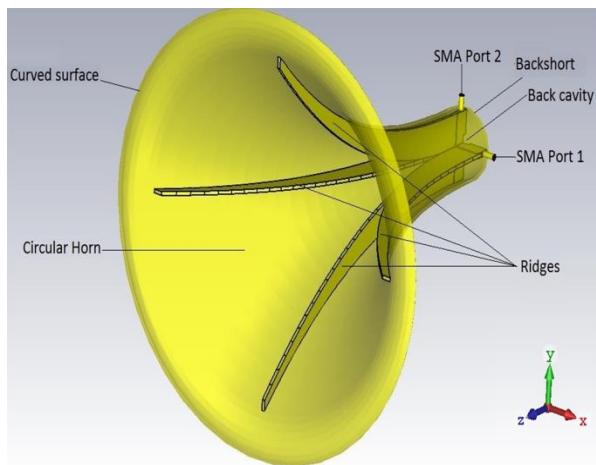


Fig. 7. The simulation view of the designed quad-ridged circular horn antenna.

The next performance parameter investigated was the gain values of the designed antenna at each polarization and gain variation within the frequency band of 1-6.75 GHz. The corresponding simulation results are shown in Fig. 9.

According to the gain results in Fig. 9, the minimum gain is found to be 13.6 dBi for both polarizations and almost 4.5 dBi (between 13.6 dBi and 18.1 dBi) gain variation was observed. This gain variation is lower than the other similar studies in the literature hence the antenna in this work can be regarded to have almost constant gain as well.

As the final analysis in this section, the radiation patterns of the proposed antenna are investigated. The radiation patterns are given for only port 1 in Fig. 10 at some sample frequencies (at the center and edge

frequencies). According to these patterns in Fig. 10, the antenna is directed towards to broadside direction without any significant shift in the beam for both E- and H-planes. Moreover, the cross-polar levels are found to be low such that the lowest co-polar to cross-polar ratio (XPD) within 3 dB beamwidth of co-polar patterns is found to be 22.5 dB and 13 dB for E- and H-planes, respectively at the frequency band of 1-6.75 GHz.

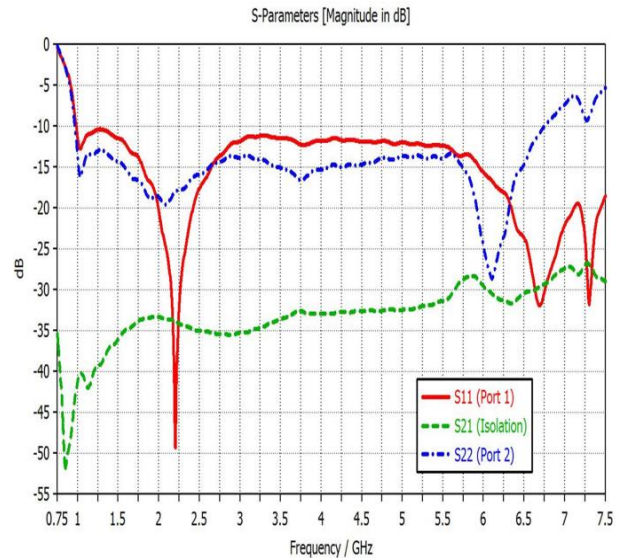


Fig. 8. The reflection coefficients of each port and isolation between ports of the proposed antenna.

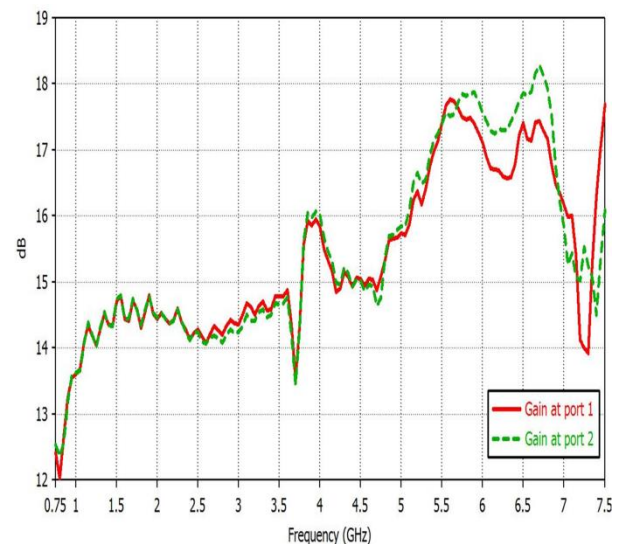


Fig. 9. The gain versus frequency of the proposed antenna for each port (linear polarization).

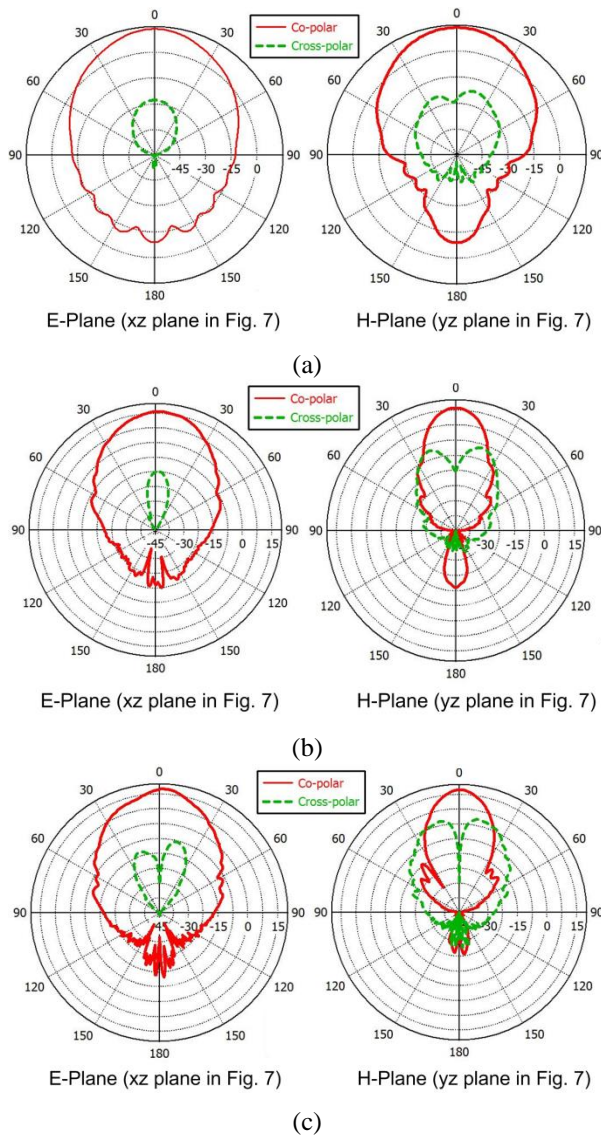


Fig. 10. The E-plane and H-plane radiation patterns of the proposed antenna for port 1 at: (a) 1 GHz, (b) 4 GHz, and (c) 6.75 GHz.

V. CONCLUSION

In this paper, the quad-ridged horn antenna is designed based on detailed profile examinations and the parametric studies. A dual-polarized quad-ridged horn is presented that achieves 6.75:1 frequency bandwidth for the both polarization cases. Moreover, the simulation results of the designed antenna has shown low return loss (>10 dB), low VSWR (<1.925), high isolation (>28 dB), high gain (minimum 13.6 dBi) and reasonable radiation patterns with low cross-polarization level over the operation frequency range 1-6.75 GHz. The antenna is designed to operate in the horizontal and vertical polarizations (dual linear polarization) simultaneously for EMC testing applications (radiated emission and

radiated immunity tests). Compared with the conventional circular quad-ridge horn antennas and other similar studies, the designed antenna achieves better gain at lower frequencies, almost constant gain (a variation of 4.5 dBi) and wider frequency bandwidth.

REFERENCES

- [1] D. G. Baker, *Electromagnetic Compatibility: Analysis and Case Studies in Transportation*. John Wiley & Sons Inc., Hoboken, NJ, USA, 2016.
- [2] T. Williams, *EMC for Product Designers: Meeting the European EMC Directive*. Newnes, Oxford, UK, 2014.
- [3] ETSI EN 301 489-17, Electromagnetic Compatibility and Radio Spectrum Matters (ERM); Electromagnetic Compatibility (EMC) Standard for Radio Equipment; Part 17: Specific Conditions for Broadband Data Transmission Systems, 2016.
- [4] M. Abbas-Azimi, F. Arzam, J. R. Mohassel, and R. Faraji-Dana, "Design and optimization of a new 1-18 GHz double ridged horn antenna," *Journal of Electromagnetic Wave Appl.*, vol. 21, no. 4, pp. 501-506, Apr. 2007.
- [5] C. A. Balanis, *Antenna Theory: Analysis and Design*. 3rd ed., John Wiley & Sons Inc., Hoboken, NJ, USA, 2005.
- [6] T. A. Milligan, *Modern Antenna Design*. 2nd ed., John Wiley & Sons Inc., Hoboken, NJ, USA, 2005.
- [7] S. B. Cohn, "Properties of ridged waveguide," *Proc. IRE*, vol. 35, no. 8, pp. 783-788, Aug. 1947.
- [8] M. H. Chen, G. N. Tsandoulas, and F. G. Willwerth, "Modal characteristics of quadruple-ridged circular and square waveguides," *IEEE Trans. Microwave Theory and Tech.*, vol. 22, no. 8, pp. 801-804, Aug. 1974.
- [9] W. Sun and C. A. Balanis, "MFIE analysis and design of ridged waveguides," *IEEE Trans. Microwave Theory and Tech.*, vol. 41, no. 11, pp. 1965-1971, Nov. 1993.
- [10] W. Sun and C. A. Balanis, "Analysis and design of quadruple-ridged waveguides," *IEEE Trans. Microwave Theory and Tech.*, vol. 42, no. 12, pp. 2201-2207, Dec. 1994.
- [11] A. Mallahzadeh and H. Ahmadabadi, "Design of N-channel rotary joint using curved double-ridged waveguide and concentric coaxial lines," *Applied Computational Electromagnetics Society (ACES) Journal*, vol. 27, no. 1, pp. 50-58, Jan. 2012.
- [12] A. Mallahzadeh and A. Imani, "Modified double ridged antenna for 2-18 GHz," *Applied Computational Electromagnetics Society (ACES) Journal*, vol. 25, no. 2, pp. 137-143, Feb. 2010.
- [13] C. Burns, P. Leuchtman, and R. Vahldieck, "Analysis and simulation of a 1-18 GHz broadband double-ridged horn antenna," *IEEE Trans. Electromagn. Compat.*, vol. 45, no. 1, pp. 55-60, Feb.

- 2003.
- [14] M. Abbas-Azimi, F. Arazm, and R. Faraji-Dana, "Design and optimisation of a high-frequency EMC wideband horn antenna," *IET Microw. Antennas and Propag.*, vol. 1, no. 3, pp. 580-585, June 2007.
- [15] N. Z. Tenigeer, Q. Jinghui, Z. Pengyu, and Z. Yang, "Design of a novel broadband EMC double ridged guide horn antenna," *Progress in Elec. Res. C*, vol. 39, pp. 225-236, 2013.
- [16] R. Dehdasht-Heydari, H. R. Hassani, and A. R. Mallahzadeh, "Quad ridged horn antenna for UWB applications," *Progress in Elec. Res.*, vol. 79, pp. 23-38, 2008.
- [17] A. R. Mallahzadeh, A. A. Dastanj, and S. Akhlaghi, "Quad-ridged conical horn antenna for wideband applications," *International Journal of RF Microwave CAE.*, vol. 19, no. 5, pp. 519-528, Sept. 2009.
- [18] A. Akgiray and S. Weinreb, "Ultrawideband square and circular quad-ridge horns with near-constant beamwidth," *IEEE ICUWB Ultrawideband Conference*, Syracuse, NY, USA, pp. 518-522, Sept. 2012.
- [19] Z. Shen and C. Feng, "A new dual-polarized broadband horn antenna," *IEEE Antennas and Wireless Propagation Letters*, vol. 4, no. 1, pp. 270-273, 2005.
- [20] R. Dehdasht-Heydari, H. R. Hassani, and A. R. Mallahzadeh, "A new 2-18 GHz quad-ridged horn antenna," *Progress in Elec. Res.*, vol. 81, pp. 183-195, 2008.
- [21] J. Liu, Y. Zhou, and J. Zhu, "Research and design of quadruple-ridged horn antenna," *Progress in Elec. Res. Lett.*, vol. 37, pp. 21-28, 2013.
- [22] P. H. Van der Merwe, J. W. Odendaal, and J. Joubert, "An optimized quad-ridged horn antenna with pyramidal sidewalls," *Journal of Elec. Waves and Appl.*, vol. 27, no. 17, pp. 2263-2273, Sept. 2013.
- [23] A. Akgiray, S. Weinreb, W. A. Imbriale, and C. Beaudoin, "Circular quadruple-ridged flared horn achieving near-constant beamwidth over multi-octave bandwidth: Design and measurements," *IEEE Trans. Antennas Propagat.*, vol. 61, no. 3, pp. 1099-1108, Mar. 2013.
- [24] D. M. Pozar, *Microwave Engineering*. 4rd ed., John Wiley & Sons Inc., Hoboken, NJ, USA, 2012.
- [25] A. P. King, "The radiation characteristics of conical horn antennas," *Proc. IRE*, vol. 38, no. 3, pp. 249-251, Mar. 1950.
- [26] C. Granet, "Profile options for feed horn design," *Asia-Pacific Microwave Conference*, Sydney, Australia, pp. 518-522, Dec. 2000.



Bekir Solak was born in Denizli, Turkey in 1988. He received the B.S. degree from Department of Electronics and Communication Engineering, Izmir Institute of Technology, Izmir, Turkey in 2012. Then, he has received his M.Sc. from Department of Electrical and Electronics Engineering, Ozyegin University, Istanbul in 2017. He has been an EMC Engineer in Tubitak Space Technologies Research Institute, Ankara since 2018. His current research interests are the analysis and design of horn antennas for EMC applications.



Mustafa Secmen was born in Izmir, Turkey in 1980. He received the B.S. and Ph.D. degrees from the Department of Electrical and Electronics Engineering, Middle East Technical University, Ankara, Turkey, in 2002 and 2008, respectively. He has been a Professor with Department of Electrical and Electronics Engineering, Yasar University, Izmir since 2010. His current research interests include radar signal processing, microwave component and antenna design for satellite/mobile communications, horn and smart antennas.



Ahmet Tekin has received his EE Ph.D. degree from University of California Santa Cruz, CA, EE MS degree from North Carolina A&T State University, Greensboro, NC and EE BS degree from Bogazici University, Istanbul, Turkey in 2008, 2004, and 2002, respectively. In addition to academic research, he worked for many innovative semiconductor design companies such as; Multigig, Inc., Newport Media, Aydeekay LLC, Broadcom corp., Semtech Corp., Nuvoton Technology Corp., Qualcomm and Waveworks Inc., leading microelectronic designs for communications, consumer and medical markets. His main focus area is analog/RF/mixed-signal integrated circuit design for communication and biomedical applications. He is currently a Faculty Member at Ozyegin University Electrical and Electronics Engineering Department and a Cofounder at Waveworks Inc.

Air Gap Effect on Antenna Characteristics of Slitline and Stripline Dipoles on an Extended Hemispherical Lens Substrate

Truong Khang Nguyen^{1,2} and Huy Hung Tran^{1,2,*}

¹Division of Computational Physics, Institute for Computational Science,
Ton Duc Thang University, Ho Chi Minh City, Vietnam

²Faculty of Electrical and Electronics Engineering, Ton Duc Thang University, Ho Chi Minh City, Vietnam
nguyentruongkhang@tdtu.edu.vn, *tranhuyhung@tdtu.edu.vn

Abstract — This paper presents the effect of an air gap introduced between a planar feed and an extended hemispherical lens on the antenna's impedance, current distribution and radiation characteristics. Two selected planar feeds for study are slitline dipole and stripline dipole. The results showed that as a small gap is introduced, the input impedance of the slitline dipole was almost remained unchanged while that of the stripline dipole was changed remarkably. More importantly, the boresight gain and radiation efficiency of the slitline dipole was improved whereas those of the stripline dipole were degraded with the presence of this air gap. An overall performance comparison for these two designs will be detailed in the paper. This study provides useful guidelines of choosing the proper feed for THz integrated lens antenna applications, especially for indoor THz communication applications such as wireless local area networks and wireless personal area networks in the 300 GHz band.

Index Terms — Air gap, extended hemispherical lens, leaky lens, slitline dipole, stripline dipole.

I. INTRODUCTION

Slot or dipoles feed used in combination with elliptical dielectric lens have been studied intensely for decades in harmonic or pulse systems [1-7]. Such integrated antenna is one of the key parts in high frequency sensing systems such as terahertz-time domain spectroscopy (THz-TDS), i.e., sub-mm waves, that couples the incoming radiation into the receiver [8, 9]. The reason for their important role is that antennas operating in the presence of dielectric lens have significantly improved the front to back ratios and increased the Gaussian coupling efficiency (Gaussicity), while eliminating substrate modes. In addition, as the antenna is printed directly on the top of the substrate lens, its fabrication offers greater dimensional accuracy and durability, and reduced cost than waveguide or waffled structures [10, 11]. More importantly, a planar

integrated lens antenna with an optimum lens substrate and antenna structure plays a critical role in optimizing output power design for particular applications [12-16]. In other words, by choosing the proper feed and optimizing the lens substrate, the impedance and radiation characteristics of a planar integrated lens antenna can be significantly improved, which is essential to the output power of a system.

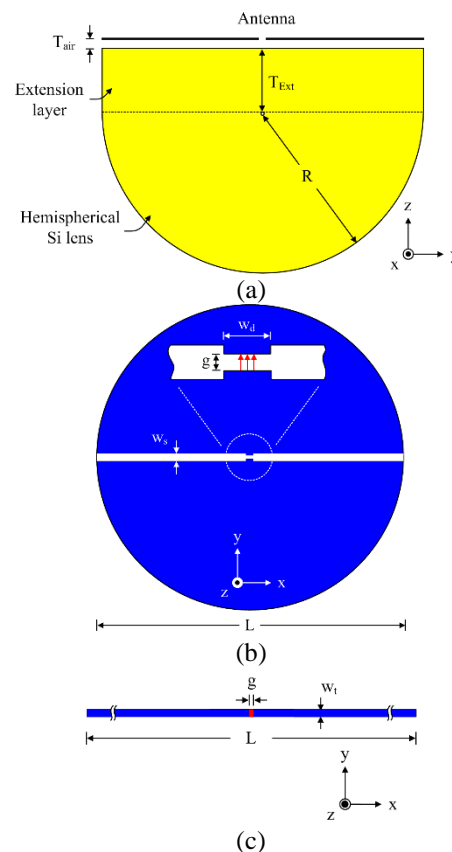


Fig. 1. Geometry of the antenna with an introduced air gap: (a) side view, (b) top view of the slitline dipole, and (c) top view of the stripline dipole.

The effect of an air gap between a leaky-wave slit and a high-permittivity substrate, i.e., semi-infinite or lens, has been studied theoretically and demonstrated experimentally [17-22]. It was found that a very small gap separation distance in terms of wavelength improved coupling efficiency and changed the propagation characteristics along the slit while simultaneously maintaining the directive radiation characteristics. However, a detailed study about this air gap effect on the overall performance of the integrated lens antenna with different planar feeds has received somewhat less attention, particularly at high frequency.

In this paper, we study in detail about this air gap effect on the input impedance, current distribution and radiation characteristics of integrated dielectric lens antennas with different planar feed, that are slitline dipole, i.e., slotline with open ends, and stripline dipole. Numerical results showed that the input impedance of the slitline dipole remained almost unchanged with the presence of such air gap while that of the stripline dipole have changed significantly. The radiation characteristic of the slitline dipole was improved for introducing such small air gap whereas that of the stripline dipole was somehow degraded. These observations provide guidelines in choosing a proper planar feed and an optimum air gap in such leaky lens design for particular application purposes.

II. ANTENNA GEOMETRIES

Figure 1 (a) shows the prototype of an antenna on an extended hemispherical lens fully made of silicon (lossless, $\epsilon_r = 11.9$). The extension layer and radius of the lens are denoted by T_{Ext} and R , respectively. The thickness of the extension layer and the radius of the Si lens are 1.8 mm and 5.0 mm, respectively, which corresponding to a ratio $T_{Ext}/R = 0.36$ for the best possible gain performance [12]. An air gap is introduced between the feed and the leaky lens and is designated as T_{air} . Figures 1 (b) and (c) shows the geometries of the two selected planar feeds that are slitline dipole and stripline dipole. The metal layer for the ground of the slitline dipole and for the stripline dipole had a conductivity of 1.6×10^7 S/m and a thickness of 0.35 mm. The widths of the slitline dipole and the stripline dipole are denoted as w_s and w_t , respectively. Both the slitline dipole and the stripline dipole have a same total length of L which equals to the diameter of the leaky lens. A short dipole was modeled at the slitline center to drive a current source through the slit. The feeding gap for both the slitline dipole and the stripline dipole are designated as g . Design parameters are fixed throughout the study as follows: $w_s = w_t = w_d = 10 \mu\text{m}$, $g = 5 \mu\text{m}$, and $L = 10$ mm. The full-wave simulator Microwave Studio by CST based on the finite-integration time-domain (FIT) technique was used to investigate the antenna characteristics [23]. In the simulation, the antenna was excited by the discrete port feeding with an ‘‘S-parameter’’ source, i.e., a current source

with the reference impedance of 50Ω . This model allows excitation of the entire gap with the S-parameter model to compute the S- and Z-parameters. For the radiation characteristics, principally open boundaries, but with some added space boundaries, were used to accurately calculate the antenna radiation patterns. Accordingly, all the gains and radiation efficiencies shown in the following results are deduced from the radiation patterns of the antenna at the frequencies of interest.

III. ANTENNA CHARACTERISTICS

A. Impedance characteristics

We first studied the air gap effect on the impedance characteristics of the slitline and stripline dipoles. Then, we studied the behavior of impedance characteristics with respect to frequency variation. Figure 2 shows the real and imaginary parts of input impedance with respect to air gap range of 0~50 μm with an increment of 5 μm at the fixed frequency of 300 GHz. Input resistance of slitline dipole increased linearly from 48 Ω to 50 Ω with an increase in air gap from 0~10 μm . From 10~40 μm , it showed a smooth increment of 10 Ω from 50 Ω to 60 Ω . After 40 μm , it became stable and reached a saturation value of 62.5 Ω , as illustrated in Fig. 2 (a). However, the stripline dipole showed completely different behavior, input resistance significantly increased from 75 Ω to 225 Ω with an increase in air gap from 0~20 μm . After 20 μm , input resistance reached the saturation value of 275 Ω . The imaginary part of the input impedance of slitline dipole and stripline dipole showed the inductive and capacitive behavior, respectively, as illustrated in Fig. 2 (b). Input reactance of slitline dipole slightly increased from 12.5 Ω to 25 Ω with an increase in air gap from 0~5 μm . After 5 μm , it reached the saturation value of 30 Ω . Input reactance of stripline dipole decreased from 120 Ω to 100 Ω with an increase in air gap from 0~5 μm . From 5~40 μm , input reactance showed an increment of 70 Ω , so the value varied from 100 Ω to 170 Ω . After 40 μm , it reached the saturation value of 170 Ω . From simulation results, we observed that the input impedance of the stripline dipole had a higher value as compared to the slitline dipole. When, we introduced the air gap between the feed and leaky lens, in case of stripline dipole effective permittivity seen by dipole towards the substrate side reduced, as a result, impedance increased with an increase in the air gap. However, in case of slitline dipole due to the presence of long ground plane, the effective permittivity seen by dipole towards substrate side remained same, as a result, the impedance characteristics remained stable and smooth with or without the air gap. This is the reason that the input impedance of slitline dipole remains the same, while for stripline dipole it significantly increased with air gap variation. From these results, it can be concluded that the slitline dipole supported wideband impedance bandwidth and its input impedance was very slightly

affected by the presence of the air gap. In contrast, the stripline dipole showed a possibility in increasing its input impedance by introducing the air gap and thus would be appropriate for a design with a high input impedance requirement.

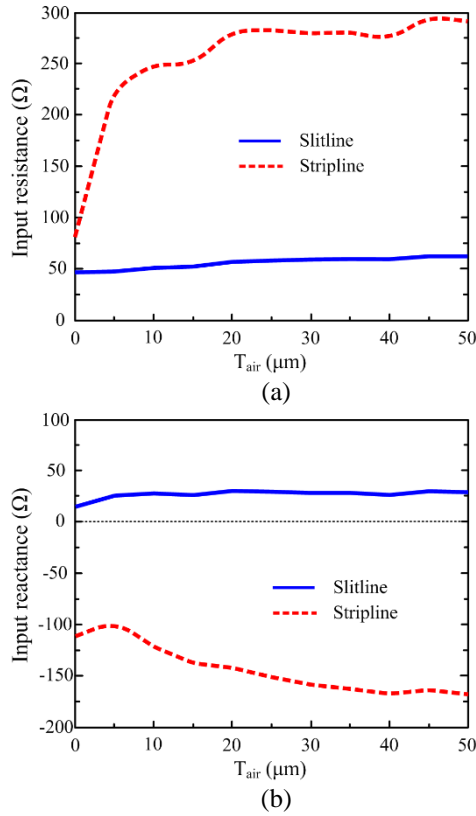


Fig. 2. (a) Input resistance and (b) input reactance (at 300 GHz) as a function of the air gap, T_{air} , in a comparison between slitline and stripline dipoles.

Figure 3 showed the impedance behavior of slitline and stripline dipoles over a broad frequency range of 100–500 GHz at three selected air gaps of 0 μm , 5 μm , and 10 μm . Generally, the input resistance of the slitline dipole slightly increased whereas that of the stripline dipole significantly decreased with the increase in frequency from 100 GHz to 500 GHz. The input resistance of the slitline dipole without air gap ($T_{air} = 0 \mu\text{m}$) remained stable around 25 Ω and exhibited a slight average increment of 5 Ω as we introduced the air gap of 5 μm . However, as we further increased the air gap from 5 μm to 10 μm , the input resistance remained the same as that of the 5 μm case. In contrast, the input resistance of the stripline dipole showed a remarkable variation, i.e., gradually decreased with an amplitude of about 75 Ω , as the frequency increased from 100 GHz to 500 GHz. It can be seen that the presence of the air gap maintained the impedance trend but significantly increased the impedance level of the stripline dipole, observed in Fig.

3 (a) as T_{air} varied from 0 μm to 5 μm . However, as the air gap was further increased from 5 μm to 10 μm , the impedance level only showed a slight increase.

The input impedance behavior of the slitline and stripline dipoles in a function of frequency is illustrated in Fig. 3 (b). The input reactance of the slitline dipole was stable and showed small variation within the frequency of interest either for introducing a small air gap of 5 μm or further increasing this air gap from 5 μm to 10 μm which is similar with its input resistance behavior. However, the input reactance of the stripline dipole exhibited differently with its input resistance. The input reactance of the stripline dipole was gradually decreased with the increase of frequency for the case of without air gap $T_{air} = 0 \mu\text{m}$. However, as a small air gap introduced, its input reactance was gradually increased with the increase of the frequency, as seen for $T_{air} = 5 \mu\text{m}$ and $T_{air} = 10 \mu\text{m}$. From these results, we can conclude that the air gap has significantly influenced the impedance profile of the stripline dipole but only has slightly impacted the impedance profile of the slitline dipole. In addition, the impact level was remarkable for a state change from without ($T_{air} = 0 \mu\text{m}$) to with ($T_{air} = 5 \mu\text{m}$) and was insignificant for further increasing this air gap.

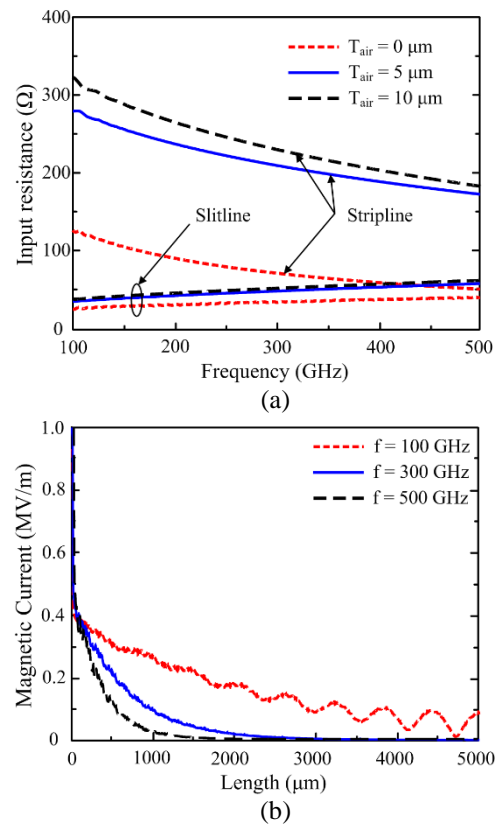


Fig. 3. (a) Input resistance and (b) input reactance as a function of frequency in a comparison between the slitline and stripline dipoles for different air gaps.

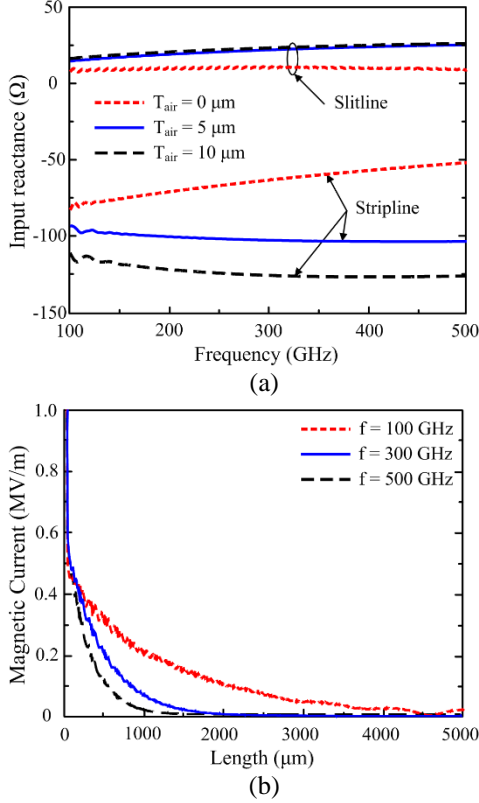


Fig. 4. Magnetic current distribution along the slitline dipole at different frequencies: (a) without air gap ($T_{air} = 0 \mu\text{m}$), and (b) with air gap ($T_{air} = 5 \mu\text{m}$).

B. Current distribution

Figures 4 and 5 show the distributions of surface current over half of the length of the slitline and stripline dipoles, respectively. We considered the two cases of the air gap, i.e., without air gap ($T_{air} = 0 \mu\text{m}$) and with air gap ($T_{air} = 5 \mu\text{m}$), at three different selected frequency values of 100 GHz, 300 GHz, and 500 GHz. A general trend was observed in both stripline and slitline dipoles that the current attenuation increased with increasing the frequency [17]. At a very low frequency of 100 GHz, both the stripline and slitline dipoles exhibited a surface current with standing-wave behavior characterized by the reflection at their terminations. At higher frequencies of 300 GHz and 500 GHz, the surface currents were attenuated more rapidly and consequently left behind no current to be reflected back. From the magnetic current of the slitline dipole illustrated in Fig. 4, we observed that the current attenuated more rapidly for the air gap case in comparison with the without air gap case. In addition, the current distribution in the feeding area, i.e., near the 0-value of length, of the slitline dipole with the air gap was higher than that of the slitline dipole without the air gap. Figure 5 also presented that the current along the stripline dipole attenuated more rapidly for the air gap case in comparison with the without air gap case.

However, in contrast with the slitline dipole, the current distribution in the feeding area of the stripline dipole with the air gap was lower than that of the stripline dipole without the air gap. These results indicate that the presence of the air gap yielded a positive effect of increasing the current distribution localized at the feeding area of the slitline dipole whereas exhibiting a negative effect of decreasing the current distribution localized at the feeding area of the stripline dipole.

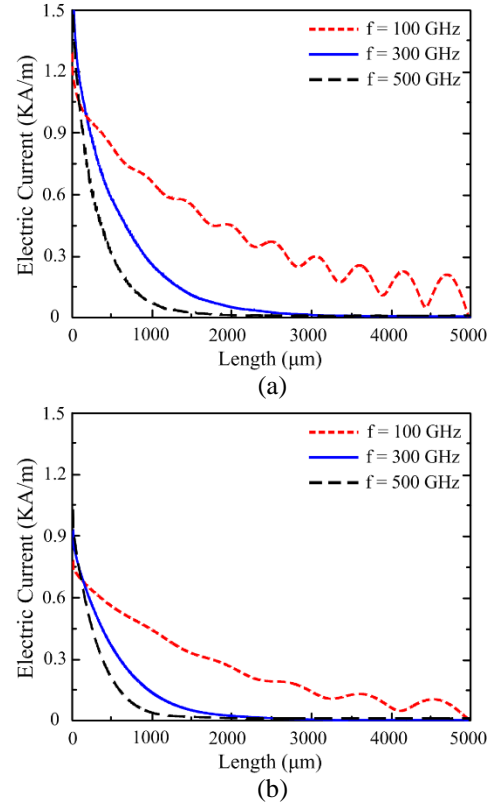


Fig. 5. Electric current distribution along the stripline dipole at different frequencies: (a) without air gap ($T_{air} = 0 \mu\text{m}$), and (b) with air gap ($T_{air} = 5 \mu\text{m}$).

C. Radiation characteristics

To study the radiation characteristics, we first investigated the boresight gain (at $\theta = 180^\circ$) and radiation efficiency of the stripline and slitline dipoles with respect to air gap at a fixed frequency of 300 GHz, as illustrated in Figs. 6 (a) and 6 (b), respectively. The boresight gain of slitline dipole exponentially increased from 21 dBi to 25 dBi as the air gap increased from $0 \mu\text{m}$ to $5 \mu\text{m}$, then slightly decreased from 25 dBi to 23 dBi as the air gap increased from $5 \mu\text{m}$ to $20 \mu\text{m}$, and then linearly decreased from 23 dBi to 19 dBi as the air gap increased from $20 \mu\text{m}$ to $50 \mu\text{m}$. The boresight gain of the stripline dipole, however, gradually decreased with an increase of the air gap from $0 \mu\text{m}$ to $50 \mu\text{m}$. These behaviors can be explained from the current distributions at the feeding

area of the slitline and stripline dipoles as observed in Figs. 4 and 5. The radiation efficiency of the slitline and stripline dipoles followed the similar trend like that of boresight gain up to $20\ \mu\text{m}$, but after $20\ \mu\text{m}$, they became stable with an increase in the air gap. The simulation results indicate that the small air gap has improved the radiation characteristics in term of boresight gain and radiation efficiency of the slitline dipole. The gain and radiation efficiency of the slitline dipole at this optimized air gap, i.e., 25 dBi and 82%, were slightly improved in comparison with the stripline dipole without the air gap, i.e., 24 dBi and 80%. In addition, the slitline dipole with the air gap ($T_{air} = 5\ \mu\text{m}$) would be appropriate choice to select because of its large ground plane that allows the active devices to be easily integrated.

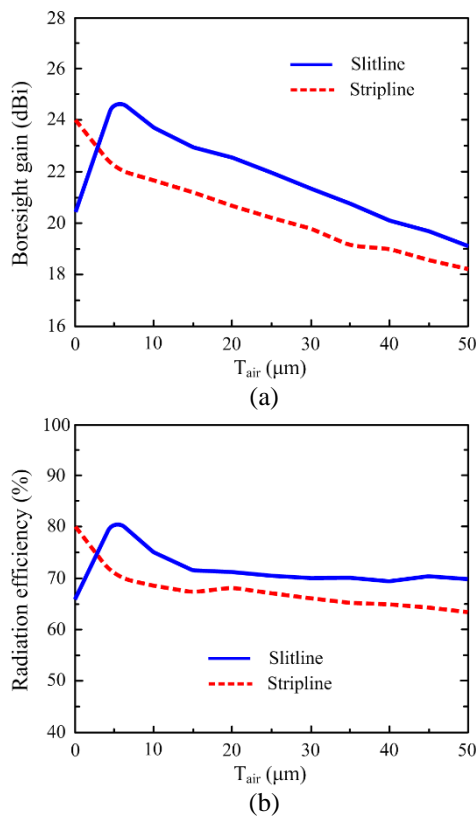


Fig. 6. (a) Boresight gain and (b) radiation efficiency at 300 GHz as a function of the air gap, T_{air} , in a comparison between slitline and stripline dipoles.

Secondly, we investigated the boresight gain (at $\theta = 180^\circ$) and radiation efficiency of slitline dipole and stripline dipole as a function of frequency, i.e., from 100 GHz to 500 GHz, with three selected air gap values of $0\ \mu\text{m}$, $5\ \mu\text{m}$, and $10\ \mu\text{m}$, as shown in Fig. 7 and Fig. 8, respectively. Generally, the boresight gain of slitline dipole and stripline dipole increased with increase in frequency. The boresight gain of the slitline dipole without air gap increased from 12.5 dBi to 23 dBi as

frequency increased from 100 GHz to 500 GHz, however, it contained two peaks and one dip. The first and second peaks occurred at frequency values of 200 GHz and 415 GHz with the magnitudes of 22.5 dBi and 27 dBi, respectively. The dip occurred at 300 GHz with the magnitude of 20 dBi. When we introduced the air gap of $5\ \mu\text{m}$ and $10\ \mu\text{m}$, the boresight gain became smooth and stable and in addition, linearly increased and reached a saturation at a frequency around 300 GHz. The boresight gain versus frequency of the stripline dipole behaved differently. The boresight gain of the stripline dipole had peaks and dips for all three cases of the air gap over the whole frequency range of interest. The introduced air gap did not modify the boresight gain profile of the stripline dipole as the slitline dipole did. The radiation efficiency of the slitline and stripline dipoles behaved similarly with the gain. The stripline dipole without air gap even presented its radiation efficiency with smaller variation than that of the slitline dipole within the frequency range of interest.

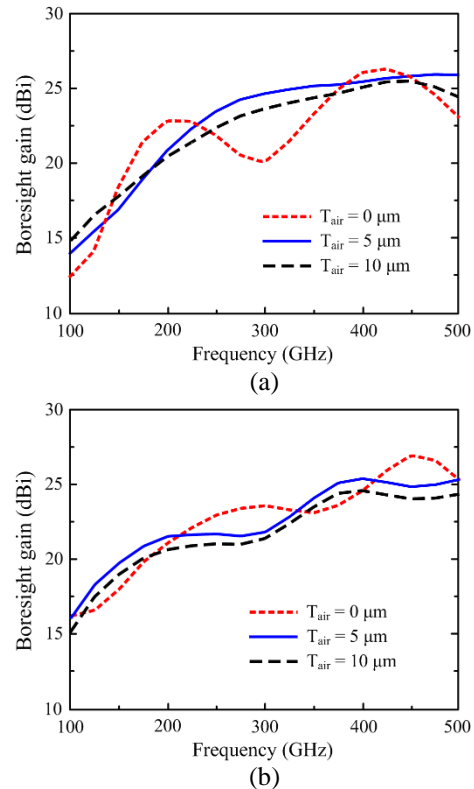


Fig. 7. Boresight gain versus frequency with respect to the air gap variation: (a) slitline dipole and (b) stripline dipole.

Lastly, we checked and compared the radiation patterns of the slitline dipole and stripline dipole at 300 GHz in E -plane and H -plane with two cases of air gap, i.e., without air gap ($T_{air} = 0\ \mu\text{m}$) and with air gap ($T_{air} = 5\ \mu\text{m}$), as shown in Fig. 9 and Fig. 10, respectively. From

Fig. 9, we observed that the radiation pattern of the slitline dipole with an air gap of $5\ \mu\text{m}$ in both E - and H -planes had higher boresight gain than the case of without air gap. As introducing an air gap of $5\ \mu\text{m}$, the width of the main beam in the E -plane remained whereas that in the H -plane became broader because the side lobes merged together. From Fig. 10, we observed that the radiation pattern of stripline dipole without air gap in both E - and H -planes had higher boresight gain than the case of with air gap. In addition, the back radiations of stripline dipole also reduced both in number and magnitude with increase in the air gap, and beamwidths remained the same for both cases. These observed gain behaviors result from the changes of the relative refractive indices of the lower space, which determines the distribution of the radiation of the dipole [24]. While the relative refractive index was reduced by introducing the small air gap under the stripline dipole, that of the slitline dipole case was increased thanks to the resonant cavity effect [17]. It can be seen that the air gap of $10\ \mu\text{m}$, corresponding to $0.01\lambda_0$ at the frequency of 300 GHz, can be used to enhance the antenna gain, which relatively agrees with the experimental results of others [20, 25]. However, the air gap should be smaller and optimized carefully to maximize the gain enhancement of the antenna at the frequency range of interest.

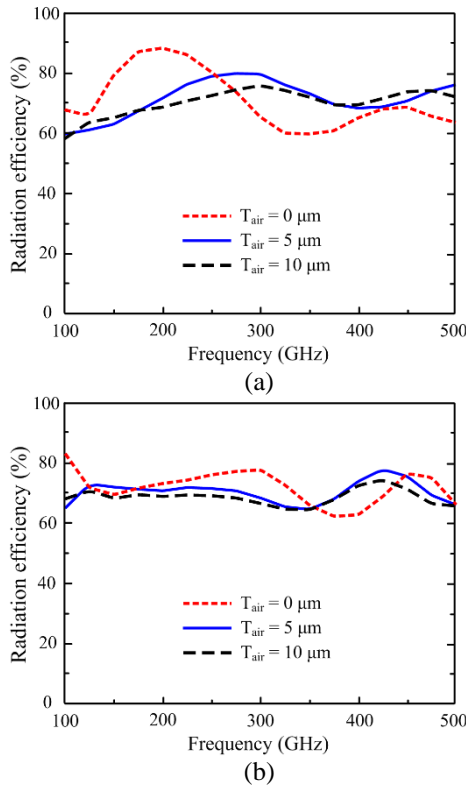


Fig. 8. Radiation efficiency versus frequency with respect to the air gap variation: (a) slitline dipole and (b) stripline dipole.

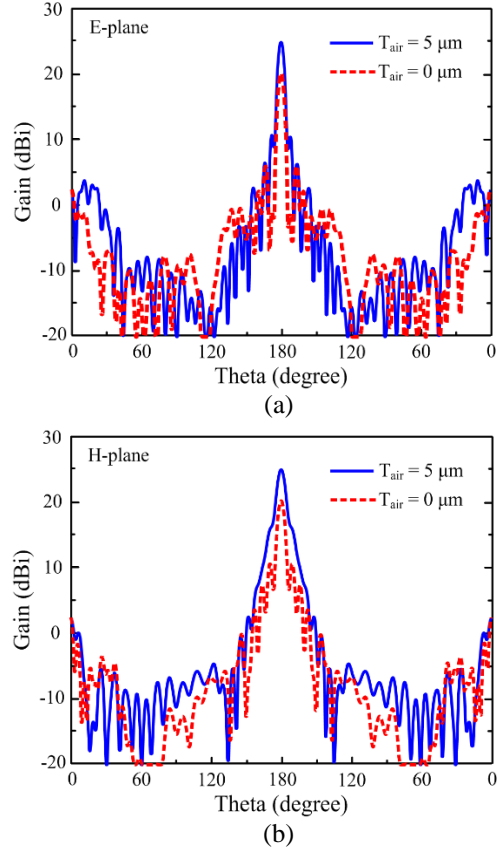


Fig. 9. Radiation patterns at 300 GHz of the slitline dipole with and without the air gap: (a) E-plane and (b) H-plane.

VI. CONCLUSION

A leaky-wave slitline dipole antenna and a traveling wave stripline dipole antenna designed on extended hemisphere Silicon lens were numerically evaluated by introducing the air gap between the lens and the antenna. The influence of the air gap on the antennas' impedance, current distribution and radiation characteristics is studied. The input impedance of stripline dipole showed a remarkable change with introducing a small air gap while it remained almost the same in case of the slitline dipole. The current distribution at the low frequency of the slitline dipole with the presence of the air gap was more stable and smooth than that of the stripline dipole. In the radiation characteristic consideration, the boresight gain and radiation efficiency of the slitline dipole with the presence of air gap was more likely improved while that of stripline it showed degradation. This study provides useful guidelines of choosing the proper feed for THz integrated lens antenna applications, especially for indoor THz communication applications such as wireless local area networks and wireless personal area networks in the 300 GHz band.

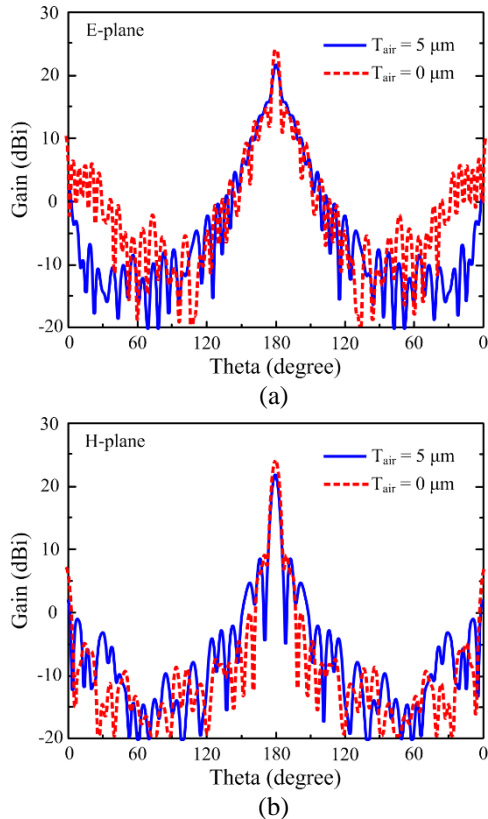


Fig. 10. Radiation patterns at 300 GHz of the stripline dipole with and without the air gap: (a) E-plane and (b) H-plane.

ACKNOWLEDGMENT

T. K. Nguyen would like to thank TWAS (16-184 RG/PHYS/AS_I-FR3240293349).

REFERENCES

- [1] D. F. Filippovic, S. S. Gearhart, and G. M. Rebeiz, "Double slot on extended hemispherical and elliptical silicon dielectric lenses," *IEEE Trans. Microw. Theory Techn.*, vol. 41, no. 10, pp. 1738-1749, Oct. 1993.
- [2] A. Neto, D. Pasqualini, A. Toccafondi, and S. Maci, "Mutual coupling between slots under an elliptical dielectric lens," *IEEE Trans. Antenn. Propag.*, vol. 47, no. 10, pp. 647-650, Oct. 1999.
- [3] M. J.M. van der Vorst, P. J. I. de Maagt, A. Neto, A. L. Reynolds, R. M. Heeres, W. Luinge, and M. H. A. J. Herben, "Effect of internal reflections on the radiation properties and input impedance of integrated lens antennas-comparison between theory and measurements," *IEEE Trans. Microw. Theory Techn.*, vol. 49, no. 6, pt. 1, pp. 1118-1125, June 2001.
- [4] X. Wu, G. Eleftheriades, and T. E. van Deventer-Perkins, "Design and characterization of single and multiple beam MM-wave circularly polarized substrate lens antennas for wireless communications," *IEEE Trans. Microw. Theory Techn.*, vol. 49, no. 3, Mar. 2001.
- [5] A. D. Semenov, H. Richter, H.-W. Hubers, B. Gunther, A. Smirnov, K. S. Il'in, M. Siegel, and J. P. Karamarkovic, "Terahertz performance of integrated lens antennas with a hot-electron bolometer," *IEEE Trans. Microw. Theory Techn.*, vol. 55, no. 2, pt. 1, pp. 239-247, Feb. 2007.
- [6] A. V. Boriskin, G. Godi, R. Sauleau, and A. I. Nosich, "Small hemielliptic dielectric lens antenna analysis in 2-D: Boundary integral equations versus geometrical and physical optics," *IEEE Trans. Antennas Propag.*, vol. 56, no. 2, pp. 485-492, Feb. 2008.
- [7] A. V. Boriskin, R. Sauleau, and A. I. Nosich, "Performance of hemielliptic dielectric lens antennas with optimal edge illumination," *IEEE Trans. Antenn Propag.*, vol. 57, no. 7, pp. 2193-2198, July 2009.
- [8] G. Chattopadhyay, M. Alonso-delPino, N. Chahat, D. González-Ovejero, C. Lee, and T. Reck, "Terahertz antennas and feed," In: Boriskin A., Sauleau R. (eds), *Aperture Antennas for Millimeter and Sub-Millimeter Wave Applications. Signals and Communication Technology*, Springer, Cham, 2018.
- [9] C. Caglayan, G. C. Trichopoulos, and K. Sertel, "Hybrid electromagnetic modeling of lens-integrated antennas for noncontact on-wafer characterization of THz devices and integrated circuits," *ACES Express Journal*, vol. 1, no. 2, pp. 72-75, 2016.
- [10] H. Hashiguchi, K. Kondo, T. Baba, and H. Arai, "An optical leaky wave antenna by a waffled structure," *J. Lightwave Technol.*, vol. 35, no. 11, pp. 2273-2279, 2017.
- [11] K. Konstantinidis, A. P. Feresidis, C. C. Constantinou, E. Hoare, M. Gashinova, M. J. Lancaster, and P. Gardner, "Low-THz dielectric lens antenna with integrated waveguide feed," *IEEE Trans. Terahertz Sci. Technol.*, vol. 7, no. 5, pp. 572-581, 2017.
- [12] I. Woo, T. K. Nguyen, H. Han, H. Lim, and I. Park, "Four-leaf-clover-shaped antenna for a THz photomixer," *Opt. Express*, vol. 18, no. 18, 18532-18542, Aug. 2010.
- [13] T. K. Nguyen, S. Kim, F. Rotermund, and I. Park, "Design of a wideband continuous-wave photomixer antenna for terahertz wireless communication systems," *J. Electromagn. Waves Appl.*, vol. 28, no. 8, pp. 976-988, Apr. 2014.
- [14] T. K. Nguyen, F. Rotermund, and I. Park, "A traveling-wave stripline dipole antenna on a substrate lens at terahertz frequency," *Curr. Appl.*

- Phys.*, vol. 14, pp. 998-1004, May 2014.
- [15] T. K. Nguyen, S. Kim, and I. Park, "Impact of varying the DC bias stripline connection angle on terahertz coplanar stripline dipole antenna characteristics," *J. Electromagn. Waves Appl.*, vol. 27, no. 14, pp. 1725-1734, 2013.
- [16] A. Neto, "UWB, non-dispersive radiation from the planarly fed leaky lens antenna—Part 1 theory and design," *IEEE Trans. Antenn. Propag.*, vol. 58, no. 7, pp. 2238-2247, 2010.
- [17] N. Llombart, G. Chattopadhyay, A. Skalare, and I. Mehdi, "Novel terahertz antenna based on a silicon lens fed by a leaky wave enhanced waveguide," *IEEE Trans. Antenn. Propag.*, vol. 59, no. 6, pp. 2160-2168, 2011.
- [18] N. Llombart and A. Neto, "THz time-domain sensing: the antenna dispersion problem and a possible solution," *IEEE Trans. Terahertz Sci. Technol.*, vol. 2, no. 4, pp. 416-423, 2012.
- [19] D. Cavallo and A. Neto, "A connected array of slots supporting broadband leaky waves," *IEEE Trans. Antennas Propag.*, vol. 61, no. 4, pp. 1986-1994, 2013.
- [20] A. Neto, N. Llombart, J. Baselmans, A. Baryshev, and S. J. C. Yates, "Demonstration of the leaky lens antenna at sub-millimeter wavelengths," *IEEE Trans. Terahertz Sci. Technol.*, vol. 4, no. 1, pp. 26-32, 2014.
- [21] Y. Wang, A. S. Helmy, and G. V. Eleftheriades, "Ultra-optical leaky-wave slot antennas," *Opt. Exp.*, vol. 19, no. 13, pp.12392-12401, 2011.
- [22] F. Tokan, "Optimization-based matching layer design for broadband dielectric lens antennas," *Applied Computational Electromagnetics Society Journal*, vol. 29, no. 6, pp. 499-507, 2014.
- [23] CST Microwave Studio, CST GmbH, 2016. <http://www.cst.com>
- [24] L. Luan, P. R. Sievert, and J. B. Ketterson, "Near-field and far-field electric dipole radiation in the vicinity of a planar dielectric half space," *New Journal of Physics*, vol. 8, pp. 1-11, 2006.
- [25] O. Yurduseven, N. L. Juan, and A. Neto, "A dual-polarized leaky lens antenna for wideband focal plane arrays," *IEEE Trans. Antenn. Propag.*, vol. 64, no. 8, pp. 3330-3337, 2016.



Truong Khang Nguyen received the B.S. degree in Computational Physics from the University of Science, Vietnam National University, Ho Chi Minh City in 2006, and the M.S. and Ph.D. degrees in Electrical and Computer Engineering from Ajou University in Suwon, Korea in 2013. From Oct. 2013 to Dec. 2014, he worked at Division of Energy Systems Research, Ajou University, Korea as a Postdoctoral Fellow. He is currently Head of Division of Computational Physics at Institute for Computational Science, Ton Duc Thang University in Ho Chi Minh City, Vietnam. His current research interests include the design and analysis of microwave, millimeter-wave, terahertz wave, and nano-structured antennas.

Huy Hung Tran received the B.S. degree in Electronics and Telecommunications from Hanoi University of Science and Technology, Hanoi, Vietnam in 2013, and the M.S. degree in the Department of Electrical and Computer Engineering, Ajou University, Suwon, Korea in 2015. His research is focused on wideband circularly polarized, and metamaterial for next generation wireless communication systems.

Optimization and Design of Multi-ring Pole Pieces for Small-sized Permanent Magnetic Resonance Imaging Magnet

Yi-Yuan Cheng¹, Tao Hai¹, Yang-Bing Zheng¹, Bao-Lei Li², and Ling Xia³

¹Department of Mechanical and Electrical Engineering
Nanyang Normal University, Nanyang, 473061, China
chengyy850@gmail.com, nytcht@163.com, zhengyb505@163.com

²Department of Physics and Electrical Engineering
Nanyang Normal University, Nanyang, 473061, China
bl_li@qq.com

³Department of Biomedical Engineering
Zhejiang University, Hangzhou, 310027, China
xialing@zju.edu.cn

Abstract — In magnetic resonance imaging (MRI) system, the main magnet creates a static magnetic field, which largely determines the final imaging quality. Pole pieces of pure-iron are commonly used to improve the field homogeneity in the imaging region. In this work, we attempt to design a novel configuration of multi-ring pole pieces for a small animal MRI system. Based on the model of a small H-type permanent magnet, the magnetic field is calculated using the finite element method, which considers the nonlinearity of the ferromagnetic materials. The pole piece was designed with the particle swarm optimization (PSO) algorithm. The results show that, the optimal multi-ring pole pieces can effectively reduce the uniformity about 10-20 ppm (10^{-6}), with a better performance compared with the flat and traditional one-ring pole piece configuration.

Index Terms — Multi-ring pole pieces, nonlinear optimization, particle swarm optimization, permanent MRI magnet.

I. INTRODUCTION

Nowadays, magnetic resonance imaging (MRI) has become one of the most powerful and important noninvasive diagnostic tools for medical imaging. MRI requires a strong and uniform magnetic field in the imaging region [1-2] which is generated by permanent, resistive or superconducting magnets. Recently, permanent magnets have gained widespread popularity in both clinical applications and biomedical research studies, especially for small animal MRI researches [3-4], due to the low weight, cost and less consumption of electricity, coolant water, and no expensive liquid Helium [5-6].

In a permanent MRI system, the static magnetic

field is generated by permanent ferromagnetic materials, and the well-known widespread end-effect can cause a non-uniform magnetic field distribution and therefore affects the imaging quality [7-8]. Shimming is used prior to the operation of the magnet to improve the homogeneity of the magnetic field. The pole piece made of pure iron can be used to adjust the uniformity of the magnetization characteristic of the permanent material blocks, and special design of shapes of the pole piece can help to improve the field homogeneity in the imaging volume [9]. Previously, several studies have discussed the design and optimization of the shape of the pole piece [10-15] in the standard MRI systems. In these designs, the final pole piece geometry is usually with one shimming ring or curved surface. The pole piece with one shimming ring may offer limited capability in improving the field homogeneity. And in paper [12], regular pole pieces with a smoothly-varying radial profile curved surface offer much better performance in shimming the magnetic field. However, these types of configurations with curved surface are usually difficult to manufacture. In this work, we proposed to design simple, novel configurations with multi-ring pole pieces to improve the uniformity of the magnetic field, and applied in a small-sized permanent MRI system.

The design of pole piece in the MRI magnet involves a nonlinear optimization procedure due to the nonlinear characteristic of the ferromagnetic materials, which is the non-convex problem with multi-pole points. In previous studies [12-14], conventional optimization methods such as the steepest descent method were used. These methods have advantages in efficiency, but it searches for the optimal solution along the direction of the gradient and the solution has a great relationship

with the choice of initial value, that might be just local minimums and it is suitable for convex problems. Particle swarm optimization (PSO) [16] algorithm is one of the latest developed intelligence and global optimization methods, which is used in this paper. It has a number of advantages [17-18] including its relatively simple algorithm structure, easy implementation, computational efficiency and immediate applicability to practical problems.

In this work, we take a small H-type permanent magnet for small animal MRI researches as our model; during the design of pole pieces, the magnetic field analysis is performed by the commercial finite element method (FEM) package ANSYS 14.0. Using the developed nonlinear optimization schemes, a number of novel designs of the multi-ring pole pieces have been proposed and discussed.

II. MODEL AND METHOD

A. Permanent magnet model

As shown in Fig. 1, a small H-type permanent magnet with static magnetic flux density of 0.5 T, and the homogeneous region of a 60 mm diameter sphere volume (DSV) in the center is considered here, which is the effective imaging region.

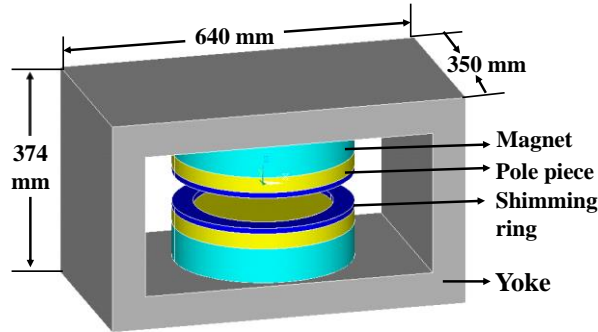


Fig. 1. Construction of the H-type MRI magnet.

The construction of the permanent magnet consists of magnets, pole pieces, shimming rings and the yoke. The single magnet pole made of Nd-Fe-B material (N40) is with 320 mm diameter and 62 mm height, and the air gap between two pole pieces is 75 mm for small animal MRI experiments. The yoke of A3 steel is with 60 mm thickness, and the dimensions have been shown in Fig. 1. The pole pieces with 27.5 mm height and shimming rings made of DT4 pure iron on the surface of magnets are used to improve the uniformity of the magnetic field.

B. The design of multi-ring pole piece

The pole piece is made of pure iron on the surface of the magnet. When the surface of the pole piece is flat and the magnetic flux in the air gap is uneven like the drum; this effect, called the end-effect, is shown in Fig.

2 (a). If the shape of the pole piece is designed properly, then the flux in the air gap is no longer outside the drum, accordingly, the central magnetic field becomes uniform, as shown in Fig. 2 (b). In a small permanent magnet, the effect is more serious because a relatively larger imaging area will be formed for such a small sized magnet. The shape of the pole piece plays an important role in improving the field homogeneity in the imaging volume, which is technically more challenging to design.

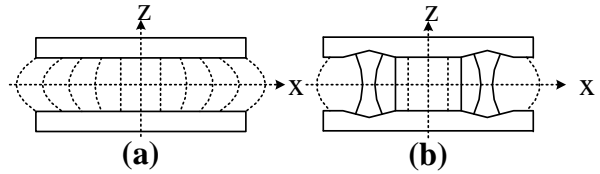


Fig. 2. Magnetic flux distribution. (a) The end-effect; (b) change the shape of pole piece.

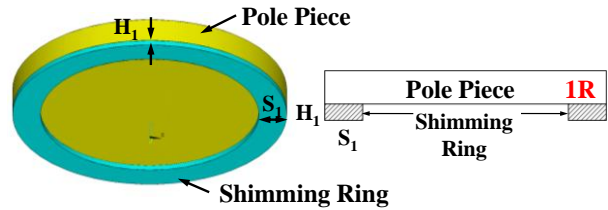


Fig. 3. The pole piece model with a shimming ring and the cross-section.

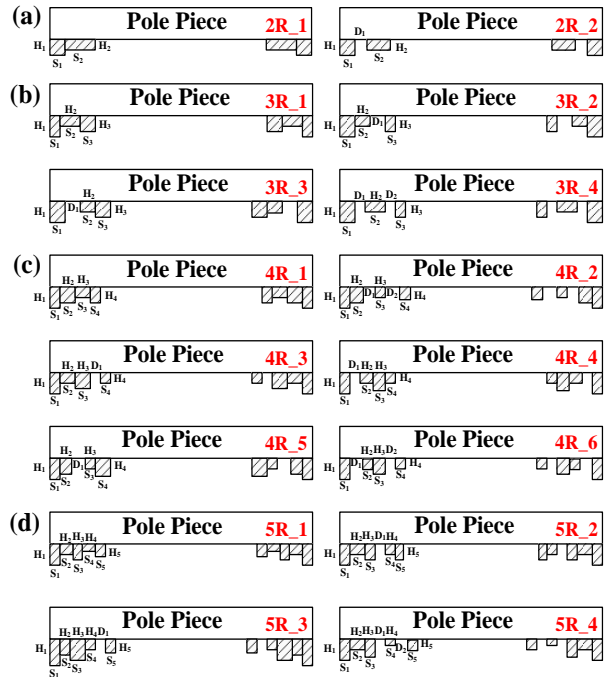


Fig. 4. The cross-section of multi-ring. (a) Two rings; (b) three rings; (c) four rings; (d) five rings.

A shimming ring of the rectangular cross-section is commonly used to adjust the field uniformity in the imaging area, as shown in Fig. 3. A series of rings will be taken into consideration in our work; here, the maximum number of rings we considered is five, because too many rings can make the structure complicated, and difficult to model and manufacture. The cross-sections of rings to be designed in this paper are shown in Fig. 3 and Fig. 4, and each structure is named as the figures, such as 1R, 2R, 3R meaning the number of the rings used in the design and the suffix '_1', '_2'... meaning the different arrangement of the rings and the gap. Meanwhile, the flat pole piece without a shimming ring is named NR.

C. Magnetic field calculation

The finite element method (FEM) is widely used for the calculation of the magnetic fields. In the analysis of the static magnetic field, the finite element equation is described by the vector magnetic potential A as:

$$B = \nabla \times A. \quad (1)$$

Under the constraint conditions of $\nabla \cdot A = 0$, A satisfies the boundary value problem, that is:

$$\begin{cases} \nabla^2 A = -\mu J & \text{in the field of } V \\ A|_S = C & \text{on the boundary of } S \end{cases}, \quad (2)$$

where μ is the permeability, J is the incentive current density and C is the boundary condition.

In this paper, the 3D FEM analysis of the permanent magnet has been carried out by using the commercial general software ANSYS (version 14.0, www.ansys.com). Due to symmetry of the magnet model, a half model is considered. Because the plane of symmetry is perpendicular to the magnetic field lines of the model, the boundary conditions in the plane of symmetry don't need to be handled in ANSYS. The conditions of air field boundary in a long distance are set to zero flux, which is 5 times as the height, the length and width of the whole magnet model respectively. The ferromagnetic material and the air gap are both calculated in the magnet model, so we choose solid 117 type element in ANSYS which adopt the edge-based FEM. The model is divided by free tetrahedral mesh. According to the practical experience of meshing, the components we concern about or the components with the larger changed magnetic fields need be divided into smaller grids, so a fine mesh is used in the DSV region, the pole piece and shimming rings. In addition, the relatively unconcerned components, such as the magnet, the yoke and the outside air part with the relatively small changed magnetic fields, are meshed by a slightly coarse grid.

The model is partitioned into approximately 55000 tetrahedron elements, as shown in Fig. 5 (a), with a maximum element size of 10 mm specified over a 60 mm DSV. There are 348 volume elements and 278 nodes in the DSV as shown in Fig. 5 (b), and the magnetic

flux density of each element is used to calculate the uniformity of DSV. The magnet pole is partitioned into 459 elements with 347 nodes, and the pole piece has 2501 elements and 1506 nodes. The yoke are meshed by a slightly coarse grid with 475 elements and 280 nodes.

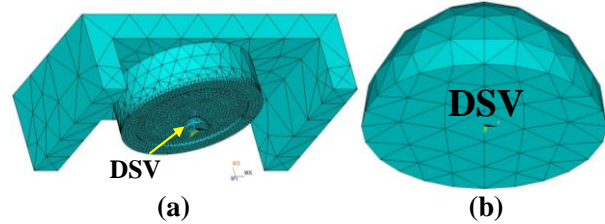


Fig. 5. 3D meshes of the model. (a) Magnet; (b) 60 mm DSV.

The FEM calculation takes into account the nonlinearity of the A3 steel yoke and the DT4 pure iron pole piece, the nonlinear relationships between B and H are shown in Fig. 6. Additionally, the relative permeability of the Nd-Fe-B (N40) permanent magnet is 1.085, and assumed a linear B vs. H dependence. This nonlinear electromagnetic problem is solved by the PSO algorithm (see the next section).

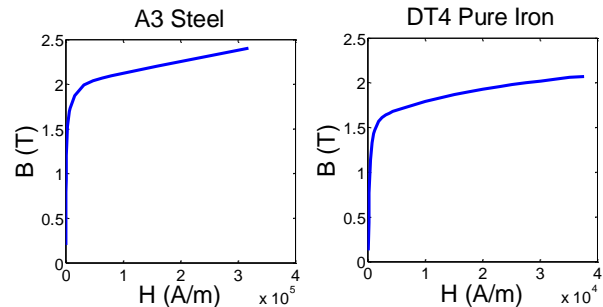


Fig. 6. Nonlinear magnetization curve of ferromagnetic materials used in the design: A3 steel and DT4 pure iron.

D. Nonlinear optimization algorithm for the design of multi-ring pole pieces

The algorithm is programmed through MATLAB R2009b (Math Works, Natick, MA) and worked with ANSYS 14.0 for the magnetic field analysis. All the simulations were performed on a Dell computer with an Intel Core i7 CPU with 10 GB RAMS.

The flow of the optimization is shown in Fig. 7. Mathematically, the optimization can be expressed as:

$$\text{Minimize } y = f(H_i, S_i, D_j). \quad (3)$$

Subject to $H_{min} \leq H_i \leq H_{max}$, $S_{min} \leq S_i \leq S_{max}$, and $D_{min} \leq D_j \leq D_{max}$, for $i=1, \dots, 5$ and $j=1, 2$.

Where Ψ is the objective function; H_i is the height of the i th ring; S_i is the cross section width of the i th ring;

D_j is the distance between two adjacent rings; H_i , S_i and D_j are the design parameters whose elements are subject to the lower and upper limitations, respectively. The maximum number of rings we considered in our work is 5, meanwhile only these 16 kinds of multi-ring models shown in Fig. 4 are taken into consideration, so the value of i is 1,...,5, and the value of j is 1,2. We choose the uniformity of DSV as the objective function and the fitness of PSO defined by the formula:

$$\psi = \frac{B_{\max}(H_i, S_i, D_j) - B_{\min}(H_i, S_i, D_j)}{B_{\text{avg}}(H_i, S_i, D_j)} \times 10^6, \quad (4)$$

where B_{\min} , B_{\max} are the maximum and the minimum nodal value for the magnetic flux density magnitude in the volume of 60 mm DSV, respectively, and B_{avg} is the average magnitude of the magnetic field flux density of the whole DSV.

Meanwhile, we take the magnitude of the magnetic field within the DSV into account, and a constraint should be added, that is, $B_{\text{avg}} \geq 0.5$ T must be satisfied. Because the magnetic flux density of the magnet we design is 0.5T, which is mainly used for small animal imaging, meanwhile, the higher the magnetic flux density, the higher the image quality, and we set 0.5 T as the minimum requirement of the magnetic flux density.

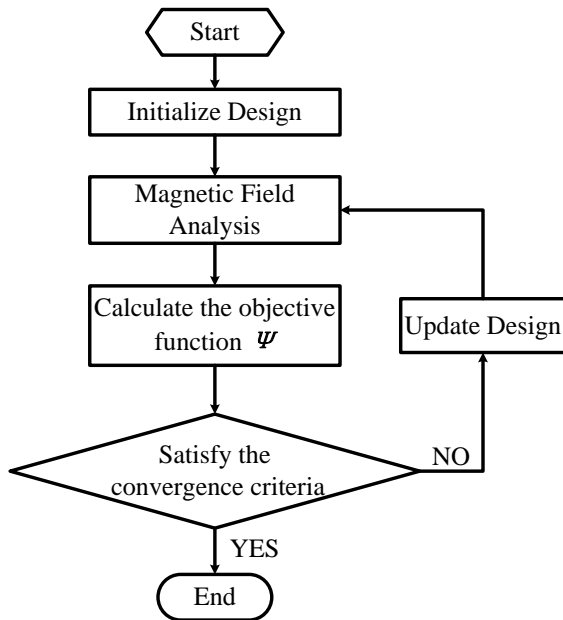


Fig. 7. The flow of the iterative optimization.

The design parameters are updated in the PSO based optimization procedure. Recent advances in the development of the PSO algorithm have elevated its capabilities in handling a wide class of complex engineering and science optimization problems [19-20].

Just as other evolutionary algorithms, the PSO algorithm searches solution using a swarm of particles that are updated from iteration to iteration. The flow of PSO is shown in Fig. 8. To find the best solution in the standard PSO algorithm, each particle changes its searching direction and position according to two factors, that is, its own best previous experience ($pbest$) and the best experience of all other members ($gbest$) according to the following equations which are proposed by Dr. Eberhart and Dr. Kennedy in 1995 [16]:

$$v_m^{k+1} = w_m^k + c_1 \text{rand}() (pbest_m^k - x_m^k) + c_2 \text{rand}() (gbest^k - x_m^k), \quad (5)$$

$$x_m^{k+1} = x_m^k + v_m^{k+1}, \quad (6)$$

where k is the iteration index; v_m^k is the velocity of particle m at iteration k and x_m^k ($x=H_i$, S_i and D_j) is the current position of agent m at iteration k ; $pbest_m^k$ is the best position of the particle m achieved based on its own experience and $gbest^k$ is the best particle position based on overall swarm's experience; c_1 , c_2 are two positive constants, and they are traditionally fixed to be 2; w is the inertial weight, which is between 0.5 and 1 [21] in this paper. After iterative updating by Equations (5) and (6), the global optimum can be found.

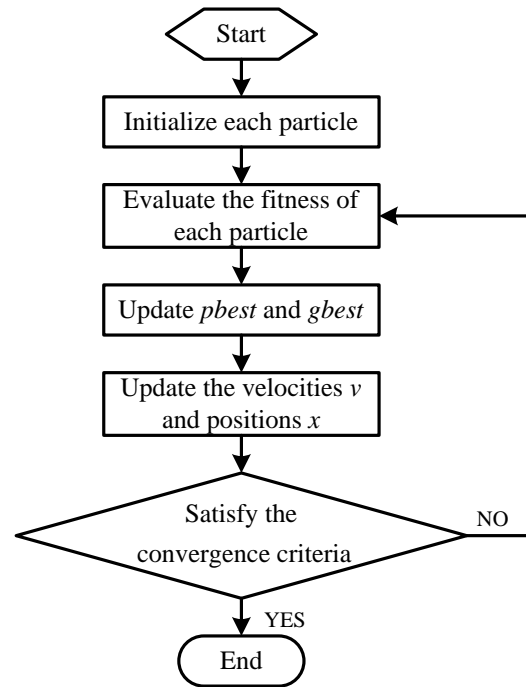


Fig. 8. The flow of PSO.

The iterative optimization process is repeated until a fixed number of iterations have been executed.

III. RESULTS

After iterations of the nonlinear algorithm, the shapes of the pole piece are obtained through the

optimization of permutation and combination with several rings. The comparison of the flat pole piece, one shimming ring pole piece and the multi-ring pole pieces are tabulated in Table 1.

Table 1: Comparison of the magnetic field properties

Type	ID_Name	Magnetic Flux Density (T)	Uniformity (ppm)
No ring	NR	0.5815	609.51
One ring	1R	0.5270	51.28
Two ring	2R_1	0.5131	40.78
	2R_2	0.5312	35.72
Three ring	3R_1	0.5195	39.95
	3R_2	0.5130	34.82
	3R_3	0.5318	45.32
	3R_4	0.5308	40.17
Four ring	4R_1	0.5061	48.28
	4R_2	0.5195	44.55
	4R_3	0.5152	42.53
	4R_4	0.5139	43.06
	4R_5	0.5242	37.62
	4R_6	0.5327	48.53
Five ring	5R_1	0.5059	44.01
	5R_2	0.5103	49.94
	5R_3	0.5085	46.72
	5R_4	0.5235	42.16

Although the magnets with the optimized pole pieces, both one ring and multi-ring, weaken the magnetic flux density compared with the flat pole piece, they are all stronger than 0.5 T which satisfy the design requirement. Meanwhile, they all can significantly improve the magnetic field uniformity. Moreover, all multi-ring pole pieces we have designed in this paper produced the magnetic field uniformity better than the traditional one-ring pole piece named 1R. In all of the attempts, more rings with a little more complex structure can't make much better uniform magnetic field such as all five-ring cases which are inadvisable. But some of two and three-ring cases, such as 2R_2 and 3R_2, show an obvious improvement in terms of the uniformity of the magnetic field.

We chose the best three cases: 3R_2, 2R_2 and 4R_5, which offered better field uniformities. The optimized parameters of the rings are displayed in Table 2. The cross-section and the 3D models of the three cases are compared to the traditional one-ring pole piece in Fig. 9.

The magnets with the optimized pole pieces maintain better density and uniformity of the magnetic field in different DSVs (diameters varied from 10mm-70mm) than the flat pole piece as shown in Fig. 10. These results can be used to estimate the magnetic flux density and uniformity inside the DSV.

From Table 1, we can see that the case of 3R_2 has the minimum uniformity in a 60 mm DSV; however its magnetic flux density is the weakest among the best three cases, meanwhile, and it is also weaker than the traditional one-ring pole piece 1R, so it is inadvisable. The case of 4R_5 can be taken into consideration, because it has a similar field density and a better field uniformity than the traditional one-ring pole piece 1R. The case 2R_2 with a simple structure is acceptable, since its magnetic field is quite good in both the field density and uniformity.

Table 2: Optimized parameters of the best three cases

ID_Name	H _i (mm)	S _i (mm)	D _j (mm)
3R_2	H ₁ =14.23	S ₁ =5.01	D ₁ =9.53
	H ₂ =6.74	S ₂ =5.81	
	H ₃ =10.49	S ₃ =5.67	
2R_2	H ₁ =9.90	S ₁ =9.60,	D ₁ =15.24
	H ₂ =6.93	S ₂ =6.74	
4R_5	H ₁ =5.85	S ₁ =4.58	D ₁ =6.56
	H ₂ =7.94	S ₂ =5.49	
	H ₃ =4.72	S ₃ =5.97	
	H ₄ =8.19	S ₄ =5.78	

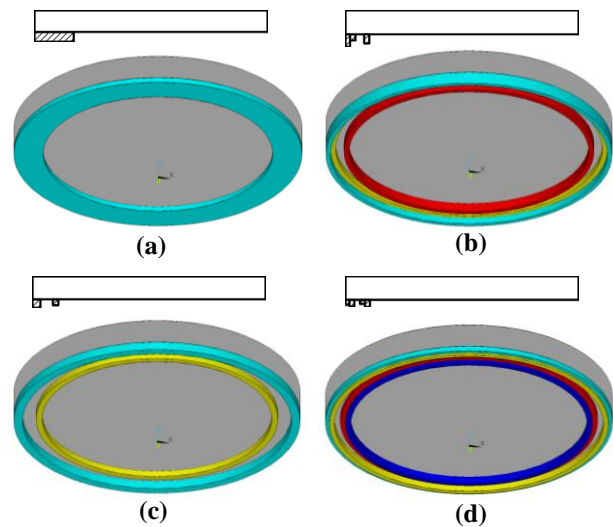


Fig. 9. The cross-section and 3D visualizations of the model. (a) 1R; (b) 3R_2; (c) 2R_2; (d) 4R_5.

For the comparison of the traditional one-ring pole piece 1R and the case 2R_2, the distributions of magnetic field of DSV are shown in Fig. 11. Figures 11 (a)-(b) represent the 1R case, and the scale of color bar is [0.526987 T, 0.527014 T] that the difference of the maximum and minimum is 2.7×10^{-5} T. Figures 11 (c)-(d) represent the case of 2R_2, and the difference of the maximum and minimum is 2.0×10^{-5} T with the scale of color bar of [0.531162 T, 0.531182 T], which is smaller than the 1R case. The case 2R_2 with a simple structure can provide a more uniform distribution of magnetic

field than the traditional one-ring pole piece.

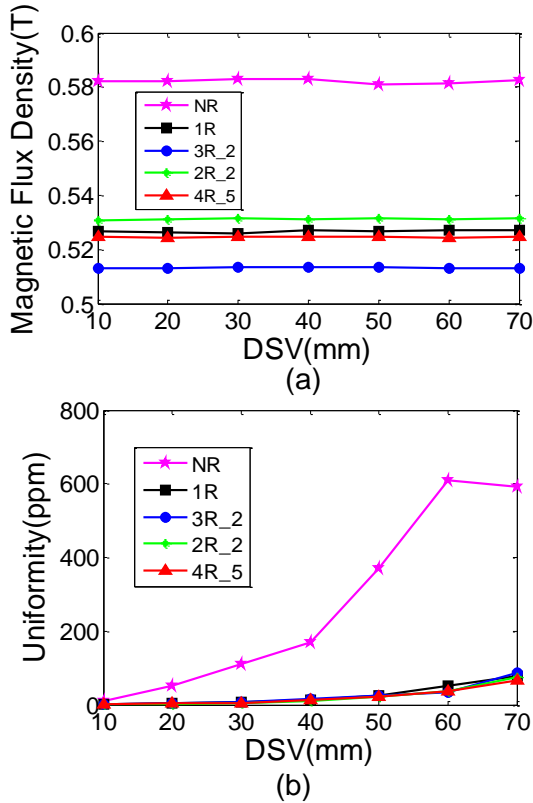


Fig. 10. Magnetic field with respect to the variation 10-70 mm of DSV. (a) Magnetic flux density; (b) uniformity.

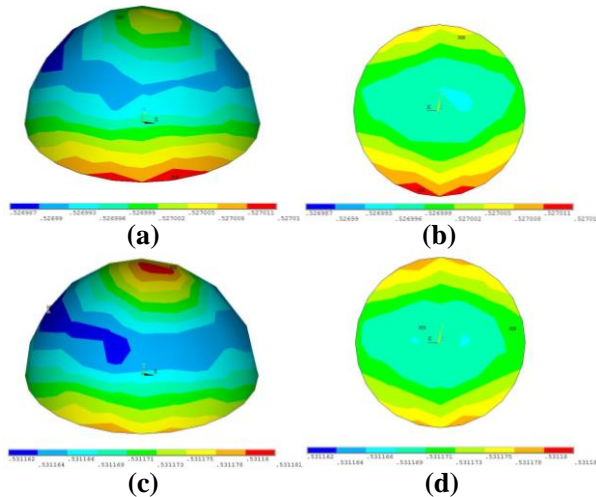


Fig. 11. Magnetic field distribution of DSV. (a) 1R: half DSV; (b) 1R: $z=0$, xy plane; (c) 2R_2: half DSV; (d) 2R_2: $z=0$, xy plane.

IV. CONCLUSION

In this paper, a nonlinear optimization and design of multi-ring pole pieces for a small-sized permanent MRI

magnet have been studied. A number of multi-ring pole piece configurations have been attempted, and the 3D FEM based simulation results demonstrate that, the proposed multi-ring pole piece can effectively improve the magnetic field uniformity. Compared with the traditional one-ring pole piece, the cases 2R_2 and 4R_5 both offer much better shimming solutions when there is no additional passive shim. Although larger number of rings such as five rings has a slightly better field uniformity than the one-ring pole piece, they are not desirable in practice, because it will increase the complexity of the shimming structure. The proposed shimming method can be effectively performed for various permanent MRI magnet systems. The scope of the theoretical work presented here can provide a reference to the actual magnet design and manufacture.

ACKNOWLEDGMENT

This work was supported in part by the National Natural Science Foundation of China under Grant No. 61701262, the scientific and technological project of Henan Province in China under Grant No. 182102310610, the key scientific research project in colleges of Henan Province in China under Grant No. 17A416005 & No. 17A510016 and the special project of Nanyang Normal University in China under Grant No. ZX2016011.

REFERENCES

- [1] Y. Zhang, D. Xie, B. Bai, H. S. Yoon, and C. S. Koh, "A novel optimal design method of passive shimming for permanent MRI magnet," *IEEE Trans. Magnetics*, vol. 44, pp. 1058-1061, 2008.
- [2] H. Sanchez Lopez, F. Liu, E. Weber, and S. Crozier, "Passive shim design and a shimming approach for biplanar permanent magnetic resonance imaging magnets," *IEEE Trans. Magnetics*, vol. 44, pp. 394-402, 2008.
- [3] J. Goebel, A. Pinzano, D. Grenier, A. Perrier, C. Henrionnet, L. Galois, P. Gillet, and O. Beuf, "New trends in MRI of cartilage: Advances and limitations in small animal studies," *Bio-medical Materials and Engineering*, vol. 20, pp. 189-194, 2010.
- [4] A. Schmid, J. Schmitz, J. Mannheim, F. Maier, K. Fuchs, H. Wehrl, and B. Pichler, "Feasibility of sequential PET/MRI using a state-of-the-art small animal PET and a 1 T benchtop MRI," *Molecular Imaging and Biology*, pp. 1-11, 2013.
- [5] T. Miyamoto, H. Sakurai, H. Takabayashi, and M. Aoki, "A development of a permanent magnet assembly for MRI devices using Nd-Fe-B material," *IEEE Trans. Magnetics*, vol. 25, pp. 3907-3909, 1989.
- [6] A. Momy and J. Taquin, "Low-leakage wide-access magnet for MRI," *IEEE Trans. Magnetics*, vol. 33, pp. 4572-4574, 1997.

- [7] C. Juchem, B. Muller-Bierl, F. Schick, N. Logothetis, and J. Pfeuffer, "Combined passive and active shimming for in vivo MR spectroscopy at high magnetic fields," *Journal of Magnetic Resonance*, vol. 183, pp. 278-289, 2006.
- [8] G. Sinha, R. Sundararaman, and G. Singh, "Design concepts of optimized MRI magnet," *IEEE Trans. Magnetics*, vol. 44, pp. 2351-2360, 2008.
- [9] X. Jiang, G. Shen, Y. Lai, and J. Tian, "Development of an open 0.3 T NdFeB MRI magnet," *IEEE Trans. Applied Superconductivity*, vol. 14, pp. 1621-1623, 2004.
- [10] A. Podol'skii, "Design procedure for permanent magnet assemblies with uniform magnetic fields for MRI devices," *IEEE Trans. Magnetics*, vol. 36, pp. 484-490, 2000.
- [11] A. Podol'skii, "Development of permanent magnet assembly for MRI devices," *IEEE Trans. Magnetics*, vol. 34, pp. 248-252, 1998.
- [12] D. Kim, B. Kim, J. Lee, W. Nah, and I. Park, "3-D optimal shape design of ferromagnetic pole in MRI magnet of open permanent-magnet type," *IEEE Trans. Applied Superconductivity*, vol. 12, pp. 1467-1470, 2002.
- [13] T. Tadic and B. G. Fallone, "Three-dimensional nonaxisymmetric pole piece shape optimization for biplanar permanent-magnet MRI systems," *IEEE Trans. Magnetics*, vol. 47, pp. 231-238, 2011.
- [14] T. Tadic and B. Fallone, "Design and optimization of a novel bored biplanar permanent-magnet assembly for hybrid magnetic resonance imaging systems," *IEEE Trans. Magnetics*, vol. 46, pp. 4052-4058, 2010.
- [15] J. Lee and J. Yoo, "Topology optimization of the permanent magnet type MRI considering the magnetic field homogeneity," *Journal of Magnetism and Magnetic Materials*, vol. 322, pp. 1651-1654, 2010.
- [16] J. Kennedy and R. Eberhart, "Particle swarm optimization," *IEEE International Conference of Neural Networks*, Perth, Australia, pp. 1942-1948, 1995.
- [17] Y. del Valle, G. Venayagamoorthy, S. Mohagheghi, J. Hernandez, and R. Harley, "Particle swarm optimization: Basic concepts, variants and applications in power systems," *IEEE Trans. Evolutionary Computation*, vol. 12, pp. 171-195, 2008.
- [18] J. Robinson and Y. Rahmat-Samii, "Particle swarm optimization in electromagnetics," *IEEE Trans. Antennas and Propagation*, vol. 52, pp. 397-407, 2004.
- [19] M. AlRashidi and M. El-Hawary, "A survey of particle swarm optimization applications in electric power systems," *IEEE Trans. Evolutionary Computation*, vol. 13, pp. 913-918, 2009.
- [20] J. Park, Y. Jeong, J. Shin, and K. Lee, "An improved particle swarm optimization for non-convex economic dispatch problems," *IEEE Trans. Power Systems*, vol. 25, pp. 156-166, 2010.
- [21] R. Eberhart and Y. Shi, "Tracking and optimizing dynamic systems with particle swarms," *Proceedings of the 2001 Congress on Evolutionary Computation*, pp. 94-100, 2001.



Yi-Yuan Cheng was born in Henan, China, in 1985. She received her B.E. degree in Biomedical Engineering from South-Central University for Nationalities, Wuhan, China, in 2008, and received Ph.D. degree in Biomedical Engineering from Zhejiang University, Hangzhou, China, in 2015. She is currently working as a Lecturer in the Department of Mechanical and Electrical Engineering in Nanyang Normal University, Nanyang, China. Her main research interests include MRI, design and optimization of magnet, artificial intelligence and so on.



Tao Hai was born in Henan, China, in 1974. He received his Ph.D. degree in Signal and Information Processing from Harbin Engineering University, Harbin, China. He is currently working as a Lecturer in the Department of Mechanical and Electrical Engineering in Nanyang Normal University, Nanyang, China. His main research interests include signal processing, image processing and so on.



Yang-Bing Zheng was born in Henan, China, in 1981. She received her M.Sc. degree in Detection Technology from China University of Geosciences (Wuhan), Wuhan, China, in 2008, and Ph.D. degree in Detection Technology and Automatic Equipment from China University of Mining and Technology (Beijing), Beijing, China, in 2014. She is currently working as a Lecturer in the Department of Mechanical and Electrical Engineering in Nanyang Normal University, Nanyang, China. Her main research interests include automatic control technology, intelligent instrument and so on.



Bao-Lei Li was born in Henan, China, in 1987. He received his Ph.D. degree in Information and Communication Engineering from Yunnan University, Kunming, China. He is currently working as a Lecturer in the Department of Physics and Electrical Engineering in Nanyang Normal University, Nanyang, China. His main research interests include intelligent optimization algorithm, path planning and so on.



Ling Xia was born in Zhejiang, China, in 1965. He received his B.E. degree in Automation and Ph.D. degree in Biomedical Engineering from Zhejiang University, Hangzhou, China. He is currently working as a Professor in the Department of Biomedical Engineering in Zhejiang University, Hangzhou, China. His main research interests include MRI key technical issues, biological effects of electromagnetic fields, Physiological simulation and modeling and so on.

Loss Analysis of Wideband RF MEMS Shunt Capacitive Switch in T and Π -Match Configurations

S. Suganthi, P. Thiruvallar Selvan, and S. Raghavan

¹Department of Electronics and Communication Engineering
K. Ramakrishnan College of Technology, Tiruchirappalli, Tamilnadu, India
tvssugi@gmail.com

²Department of Electronics and Communication Engineering
SRM-TRP Engineering College, Tiruchirappalli, Tamilnadu, India

³Department of Electronics and Communication Engineering
National Institute of Technology, Tiruchirappalli, India

Abstract — A wide bandwidth coplanar-waveguide (CPW) based RF MEMS capacitive shunt switch with π -matched & T-matched having high impedance transmission lines is designed and simulated for broadband (18-40 GHz) application. The effects of variation in membrane width (50 & 70 μm) of the switch and high-impedance transmission line length (300 – 600 μm) between the switch structures on scattering parameters are studied. The variation in beam width has very little effect on return loss of the switch in up-state. The reduction in high-impedance transmission line length yields marginal improvement in return loss. In the down-state configuration, the return loss showed negligible change with the variation in beam width and high-impedance transmission line length. The isolation is found improved with the increase in beam width and high-impedance transmission line length in whole frequency range. Simulating the technical performance demonstrates the greater improvement in RF characteristics of the switch particularly in return loss in up-state position. In order to validate the obtained result, Artificial Neural Network (ANN) has been trained using ADS result. Comparison shows good agreement between ADS and ANN results.

Index Term- High impedance short transmission line, matched section, return loss and isolation, RF MEMS, shunt switch, wideband.

I. INTRODUCTION

Design of RF MEMS switches is one of the interesting areas that facilitate the researcher with great potential to improve the performance of communication circuit and systems. At microwave frequencies, the rapid development and use of micro electromechanical systems (MEMS) have proved tremendous advancement

due to their high linearity and low losses [1] as well as low power consumption [2]. Among the various components of MEMS technology, MEMS switches are the basic building blocks replacing the conventional p-i-n diode and GaAs FET switches [3] at high frequency applications. Low cost MEMS switches are considered as prime category in MEMS technology due to their extremely low insertion loss (0.1dB) [4] and very high isolation upto 100 GHz, near zero power consumption (10-200 nJ/switching cycles) good isolation [5], lower insertion loss and low power consumption [3] properties. The analysis of MEMS switches from microwave to millimeter wave frequencies have revealed superior performance than the diode based switches which offer poor performance in terms of losses [6], tuning linearity and intermodulation distortion. The excellent linearity [7] due to the mechanical passive nature [8] of the device and wide bandwidth operation of MEMS switches makes it ideal for different wireless applications, reconfigurable antennas, filters and tuners, low loss phase shifters and high Q passive devices and resonators [5]. RF MEMS switches that are able to handle up to 20W and operating cycle of 10^{12} [1] have found applications in RADAR system, network analyzer, satellite communication system and in base stations [5].

MEMS switches are the devices which operate by the use of mechanical movement to achieve short or open circuit in RF circuits. The required force for mechanical movement can be obtained by different actuation mechanisms like electrostatic and magneto static [5]. MEMS switches can be designed in different configurations based on signal path (series or shunt), the actuation mechanism (electrostatic, thermal or magneto static), the type of contact (ohmic or capacitive) and the type of structure (cantilever or bridge) [9]. Extensive studies on various kinds of series and shunt

MEMS switches are available in literature [10, 11]. The practical first capacitive shunt switch was presented by Raytheon based on fixed-fixed metal beam structure [11]. Later on, lot of research works have been carried out on capacitive shunt RF MEMS (CSRSM) switches to achieve better performance [12].

In a CSRSM switch, a thin metal membrane bridge is suspended over the center conductor [13] and fixed on the ground conductor of CPW [14]. This switch performance depends on isolation which in turn depends on capacitance ratio (C_{\max}/C_{\min}). The MEMS switches performs excellently for 10-100 GHz frequency range applications with a typical isolation of -17 dB at 10 GHz and -35 to -40 dB at 30-40 GHz for a capacitance of 4 pF [7]. In these wide frequency range, Ka-band (18 – 40 GHz) can be the band of choice for many radio communication applications due to its increasing capacity availability and its applicability for broadband services. This band can encompass a new type of architecture, new transmission and bandwidth management to provide higher quality, better performance and faster speed [15].

The conventional RF parameters which characterizing the MEMS switches are: 1) The insertion loss in ON-state; 2) The isolation (i.e., $1/|S_{21}|$) in OFF-state; and 3) The return loss (i.e., $1/|S_{11}|$) in both states. Much effort has to be taken to improve these parameters to achieve higher isolation in OFF-state and low insertion and return losses in ON-state. Matching is necessary for the best possible energy transfer from stage to stage. The impedance of the devices (generally 50Ω internal impedance) connected in system must be matched in order to reduce the reflection and the related losses. Interstage matching has to be made between two complex impedances, which make the design still more difficult, especially if matching must be accomplished over a wide frequency band. In RF MEMS switches, either T-match or π -match configuration is used. In T-match configuration, the series inductors provide a good match at the design frequency. Whereas in π -match configuration, a short section of high impedance line is used between two shunt switches results in an impedance match. The π -match provides an excellent match in the upstate position over a wide bandwidth and wide isolation bandwidth compared to T-match. The double shunt capacitance ground the high frequency signal two times faster as compared to the T-match and improves the isolation [16-17].

In this paper, we analyze the RF design of coplanar waveguide based MEMS shunt switch in T and π -match configuration for Ka band applications. In T-match the capacitor is eliminated by using a distributed inductance of two short high impedance transmission lines (HITLs) and the π -matched consists of two bridges separated by a high-impedance transmission line. Scattering parameters of the T and π -matched shunt switch is studied as a function of:

- 1) Width of the switch membranes.
- 2) High impedance transmission line length.

The organization of the paper is as follows. Section two of this paper discusses the theory of capacitive shunt RF MEMS switch with its selection criteria and the proposed two types of matching network parameters. The electromagnetic simulation analysis of capacitive shunt switch in terms of insertion loss and isolation performance is discussed in Section 3. Section 4 presents applications of MEMS switch along the findings of our work.

II. CSRSM SWITCH

A. Selection of switch

As mentioned in Section I, there are several types of MEMS switches based on different design parameters. The major criteria for switch selection are its application and frequency of operation. Out of two types of switches based on contact, the shunt is preferred over series due to minimal parasitic involved and capable of handling more RF power. Shunt switches have the benefit of ease of fabrication and fewer parasitic due to continuous transmission line [9]. The capacitive MEMS switch has excellent performance up to 40 GHz [18] and life time in excess of 1 million cycles [19] under low power conditions.

B. Theory of capacitive shunt RF MEMS switch

The capacitive shunt RF MEMS (CSRSM) switch taken for analysis is based on a fixed-fixed beam [20] design and is shown in Fig. 1 (a). The MEMS Bridge with the gap of 'g' from the center conductor is connected to the CPW ground plane and the bridge is grounded.

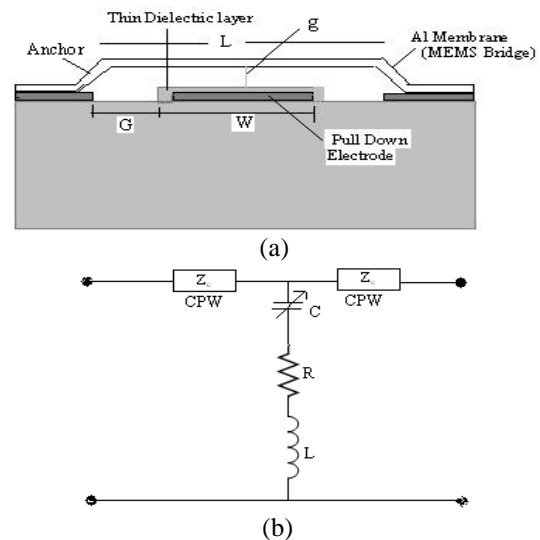


Fig. 1. Capacitive shunt RF MEMS switch: (a) cross section view, and (b) equivalent circuit.

The center pull down electrode provides both the

electrostatic actuation [22] and RF capacitance between the transmission line and ground. When the switch is down (OFF) state actuated, the capacitance to the ground provides good results in excellent short circuit and high isolation at microwave frequencies. The lumped element equivalent circuit model of CSRM switch is shown in Fig. 1 (b).

C. RFMEMS shunt switch in π -match configuration

The model of the single RF MEMS membrane switch can be used to design the high-isolation, low insertion-loss π -matched shunt switch [21]. The π -matched switch consists of two single MEMS shunt switches separated by a short length 'd' of high-impedance transmission line as shown in Fig. 2.

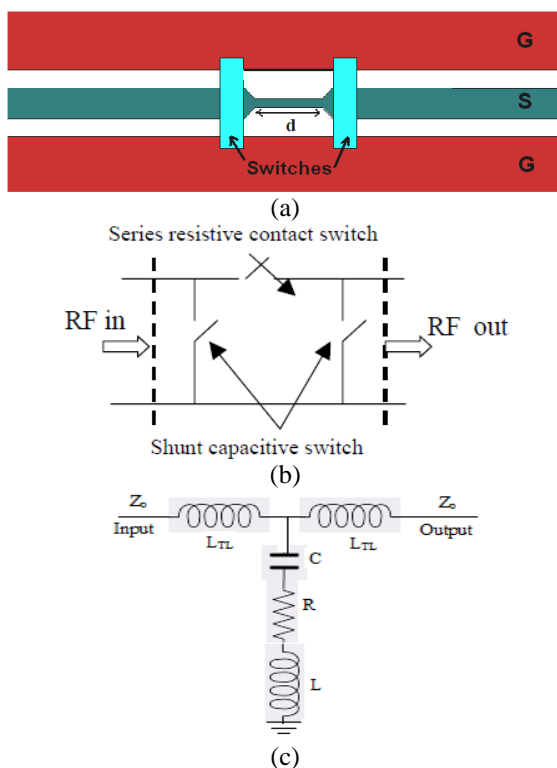


Fig. 2. (a) Schematic of RFMEMS shunt switch in π -match and its equivalent circuit in (b) π -match and (c) T-match.

The RF characteristic parameters of this switch are analyzed in terms of return loss, insertion loss and isolation. In our paper for getting broadband RF MEMS switch, we analyze the frequency response of the switch at different length of the midsection high impedance transmission line.

D. RFMEMS shunt switch in T-match configuration

The RF characteristics of a capacitive shunt switch depend on the capacitor of the switch in its up-state position. For lowering the actuation voltage, the gap-

height should be decreased which leads to an increase in the up-state capacitor [22, 23]. This deteriorates the RF characteristics of the switch. In this paper, the up-state position of the switch with two short high-impedance transmission lines (HITLs) having inductance ' L_{TL} ' is characterized by the C, L and R components. The capacitance 'C' is the more dominating component at high frequency in this model which causes the mismatch between input and output of the switch. We therefore match the circuit by using two additional short HITLs incorporating two inductors (L_{TL}) at the input and output of the switch which forms the T-matching circuit as shown in Fig. 2 (c). Though RF MEMS switches are 3D structures, they can also be seen as 2.5D structure due to their high aspect ratio. RF performance of the switch in terms of insertion and return loss is studied using ADS Momentum EM software. The characteristic impedance of CPW plays a major role which is determined by ground/substrate/ground (G/W/G) [24] dimension. In CPW line, the signal and two ground lines are on the same plane. In this proposal, the CPW line with dimensions G/W/G = $60 \mu\text{m}/100 \mu\text{m}/60 \mu\text{m}$ (50Ω) was designed and two values ($50 \mu\text{m}$ and $70 \mu\text{m}$) has been chosen for width of the membrane bridge.

E. Artificial neural network

ANNs are biologically inspired computer programs to simulate the way in which the human brain process information. Each neuron has weighted inputs, simulation function, transfer function and output. The weighted sum of inputs constitutes the activation function of the neurons. The activation signal is passed through a transfer function which introduces non-linearity and produces the output. The neural network architecture used in this paper called MultiLayer Perceptron Neural Network has use the back propagation [24] learning algorithms used in this work are based on multilayer correction learning algorithm called back propagation.

III. RESULTS AND DISCUSSION

Simulated scattering parameters of the π -matched & T-matched with HITLs switch structure are discussed in this section. Figures 3 (a) & (b) show the return loss (S11) and isolation (S21) for the up-state position for the switch for π section and T section with HITL length from 300 to $600 \mu\text{m}$ for the width of the membrane bridge of $W=50 \mu\text{m}$ and $70 \mu\text{m}$. The up-state S11 parameters of π section are found to vary between -5 dB to -35 dB in the $18 - 40 \text{ GHz}$ frequency range. The return loss of T section with HITL varies from -0.7 with highest minimum loss of -1.4 dB only. But for the same frequency range from 18 to 40 GHz , the π section gives the minimum return loss in the range from -4 dB to -32 dB .

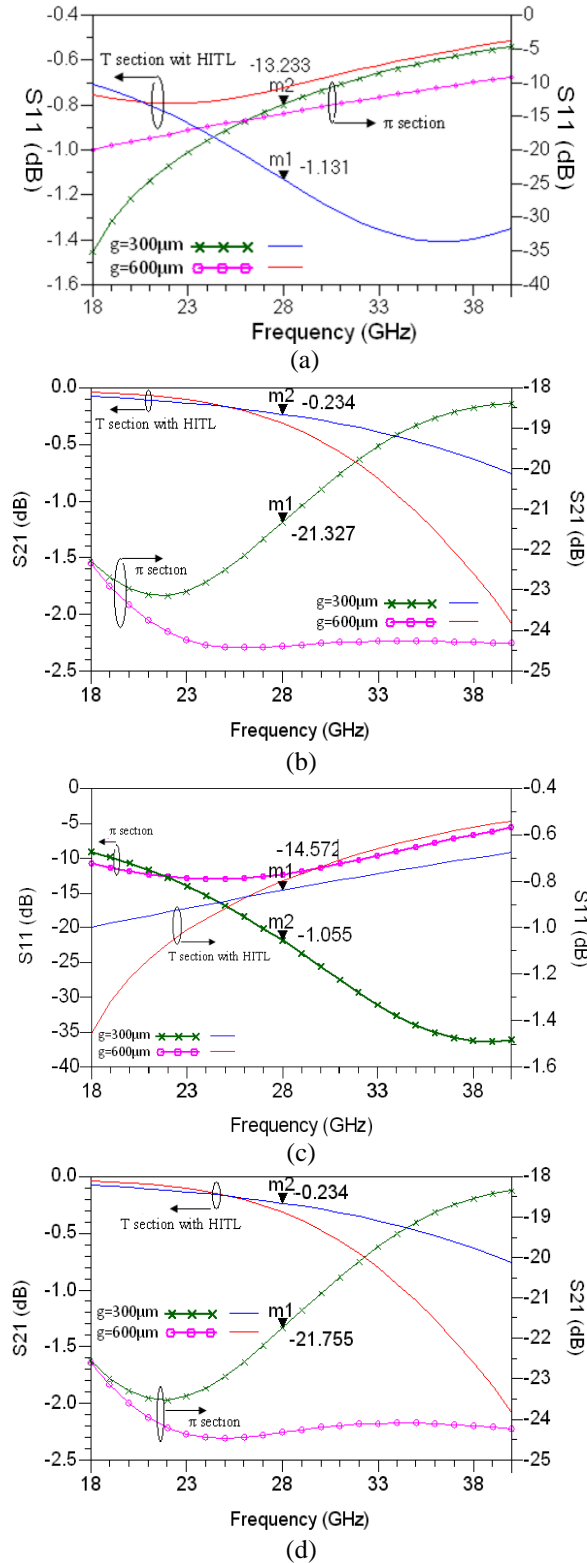


Fig. 3. UP-state insertion loss (S11) and isolation (S21) for π section and T section with HITL length from 300 to 600 μm and width of the membrane bridge (W) of (a) & (b) $W=50 \mu\text{m}$ and (c) & (d) $W=70 \mu\text{m}$

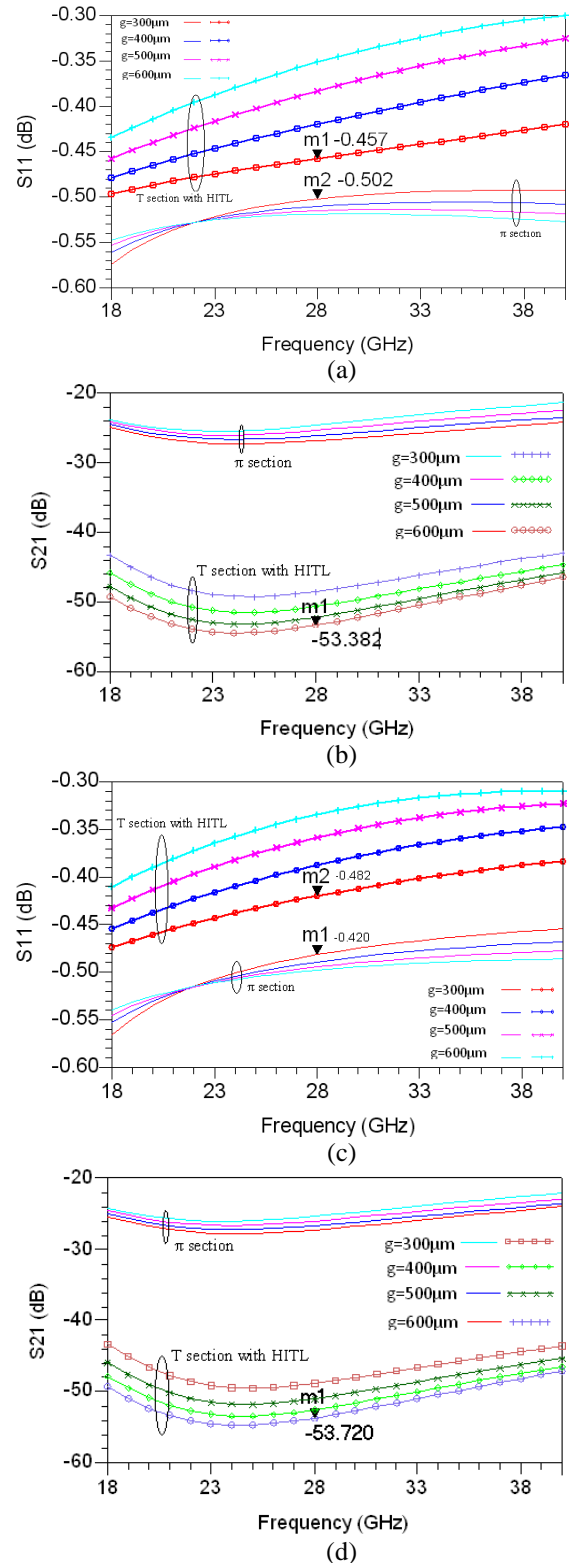


Fig. 4. Down-state insertion loss (S11) and isolation (S21) for π section and T section with HITL length from 300 to 600 μm and width of the membrane bridge (W) of (a) & (b) $W=50 \mu\text{m}$ and (c) & (d) $W=70 \mu\text{m}$

This shows that the π section performs well compared to T section in terms of their losses. Figures 3 (c) and (d) give the return loss with the width of the membrane bridge of 70 μm . This graph explains that there is no much difference in the loss performance with respect to the width of the membrane bridge.

Figure 4 gives the return loss and isolation performance of switch in π section and T section with HITL length from 300 to 600 μm and width of the membrane bridge of $W=50 \mu\text{m}$ & 70 μm in down-state configuration. In Fig. 4 (a), return loss (S11) for $W=50 \mu\text{m}$ is found to be varied from -0.5 to -0.3 dB for T section with HITL and this is reduced from -0.58 to -0.51 for π section. However, the S11 parameters do not show any noticeable change with the width of the switch as well as with high-impedance transmission line lengths. For the isolation performance as in Fig. 4 (b), the better performance of π section (isolation from -26 dB to -22 dB) can be noticed compare to T section with HITL (isolation from -54 dB to -44 dB). Though there is no much variation in isolation for 'g' values, we have achieved nearly 30 dB reduction in isolation for π -section. The isolation values seem to be decreasing with the increase in the high-impedance transmission line lengths, while it increases with increase in the beam width. As the beam width increases, the downstate capacitance increases, which results in better isolation as shown in Fig. 4 (d). As can be seen from the figures, the RF losses performance of the down-state position for the CSRM switch gives better results in the frequency greater than 25 GHz. Therefore, the switch provides desirable RF characteristics (S11 and S21) for the Ka frequency band applications.

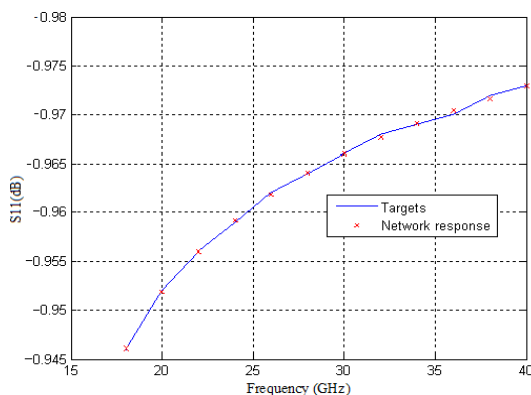


Fig. 5. Comparison of ADS and ANN trained values for insertion loss of CSRM with π section and T section.

In order to validate the obtained result, the neural network has been trained with the insertion loss ADS result obtained for down state insertion loss with $W=50 \mu\text{m}$ and $d=400 \mu\text{m}$ for π match configuration as shown in Fig. 5. After many trails, network having two hidden layers have been selected with dimensions of $4 \times 14 \times 10 \times 2$.

This means that the numbers of neurons were 4 for input layer, 14 and 12 for first and second hidden layers respectively and 2 for output layer respectively. The better agreement between the results from ADS and ANN shows that the proposed matching networks are optimized by simulation.

IV. CONCLUSION

This paper presents parametric analyses of scattering parameters of the π -matched and T-section with high impedance transmission lines for capacitive shunt RF MEMS switch for broad band (Ka-band) application. The variation in beam width has very little effect on up-state scattering parameters; whereas, the reduction in high-impedance transmission line length showed the marginal improvement in return loss. In the down-state configuration, there is no much change in return loss for the beam width of the switch and high impedance transmission line lengths. The isolation is found to be improved with the increase in beam width and high-impedance transmission line length. The achieved scattering parameters shows that the CSRM switch with proposed matching networks are best suited for high frequency band (25 - 40 GHz) which support for Ka band applications like satellites communications uplink in either the 27.5 GHz and 31 GHz bands, high-resolution, close-range targeting radars, aboard military airplanes, vehicle speed detection by law enforcement and for downlink of scientific data collected by the space telescope.

REFERENCES

- [1] V. Markovic, L. Vietzorreck, Z. Marinkovic, and O. Pronic, "Modeling of RF MEMS switches for application in communication system," *Simpozijum o Novim Tehnologijama u Postanskom I Telekomunikacionom Saobraćaju-PosTel 2012*, Beograd, 04, I 05, Dec. 2012.
- [2] R. W. Herfst, P. G. Steeneken, and J. Schmitz, "Identifying degradation mechanisms in RF MEMS capacitive switches," *MEMS 2009*, Tucson, AZ, USA, Jan. 13-17, 2008.
- [3] B. Pillans, J. Kleber, C. Goldsmith, and M. Eberly, "RF power handling of capacitive RF MEMS devices," *IEEE MTT-S*, pp. 329-332, 2002.
- [4] S. Suganthi, K. Murugesan, and S. Raghavan, "ANN model of RF MEMS lateral SPDT switches for millimeter wave applications," *JMOE*, vol. 11, no. 1, pp. 130-143, 2011.
- [5] Z. D. Milosavljevic, "RF MEMS switches," *Microwave Review*, pp. 1-8, June 2004.
- [6] M. Fernandez Bolaos, J. Perruisseau Carrier, P. Dainesi, and A. M. Ionescu, "RF MEMS capacitive switch on semi-suspended CPW using low loss high resistivity silicon," *Microelectronic*

- Engineering*, vol. 85, pp. 1039-1042, 2008.
- [7] D. Verma and A. Kaushik, "Analysis of RF MEMS capacitive switch based on a fixed-fixed beam structure," *IJESR*, vol. 2, no. 5, pp. 391-394, 2012.
- [8] S. Suganthi, K. Murugesan, and S. Raghavan, "RF MEMS switch beam position stabilization analysis using neural network," *IJMOT*, vol. 7, no. 2, pp. 107-115, 2012.
- [9] P. Verma and S. Singh, "Design and simulation of RF MEMS capacitive type shunt switch and its major applications," *IOSR Journal of Electronics and Communication Engineering*, vol. 4, no. 5, pp. 60-68, 2015.
- [10] C. M. Rebeiz and J. B. Muldavin, "RF MEMS switches and switch circuits," *IEEE Microwave Magazine*, Dec. 2001.
- [11] J. J. YAO, "Micro electromechanical RF switch," US Patent, Patent Assibnee: Rockwell International Corporation Patent No: 5578976, Nov. 1996.
- [12] D. Peroulis, S. Pacheco, K. Saarbadi, and L. P. B. Katehi, "MEMS devices for high isolation switching and tunable filtering," *IEEE MTT-S Digest*, pp. 1217-1220, 2000.
- [13] G. M. Rebeiz, *RF MEMS, Theory, Design and Technology*. John Wiley and Sons, Hoboken, 2003.
- [14] Y. Qian, G. P. Li, and F. De Flaviis, "A parametric model of low loss RF MEMS capacitive switches," in *Proc. APMC*, Asia Pacific, vol. 3, pp. 1020-1023, 2001.
- [15] L. Y. Ma, A. N. Nordin, and N. Soin, "Design, optimization and simulation of a low-voltage shunt capacitive RF-MEMS switch," *Microsystem Technologies*, 2015.
- [16] J. B. Muldavin and G. M. Rebeiz, "High-isolation CPW MEMS shunt switches – Part 1: Modeling," *IEEE Trans. on Microwave Theory and Techniques*, vol. 48, pp. 1045-1052, 2000.
- [17] J. B. Muldavin and G. M. Rebeiz, "High-isolation CPW MEMS shunt switches — Part 2: Design," *IEEE Trans. on Microwave Theory and Techniques*, vol. 48, pp. 1053-1056, 2000.
- [18] C. L. Golsmith, Z. Yao, S. Eshelman, and D. Denniston, "Performance of low loss RF MEMS capacitive switches," *IEEE Microwave and Guided Wave Letters*, vol. 8, no. 8, Aug. 1998.
- [19] C. Goldsmith, J. Ehmke, A. Malczewski, B. Pillans, S. Eshelman, Z. Yae, J. Brank, and M. Eberly, "Lifetime characteristics of capacitive RF MEMS switches," *IEEE International Microwave Symposium*, vol. 1, May 2001.
- [20] S. Suganthi, V. Krishnamurthi, and S. Raghavan, "Neural based optimization analysis of distributed MEMS transmission line phase shifters," in *Proc. IEEE - ICICIP*, pp. 639-643, Dec. 20-21, 2010.
- [21] U. Sharma, S. Dutta, and E. K. Sharma, "Scattering parameters of broadband (18 – 40 GHz) RF MEMS switch in π -match configuration," *Sensors & Transducers*, vol. 196, no. 1, pp. 37-42, Jan. 2016.
- [22] S. Suganthi, K. Murugesan, and S. Raghavan, "Neural network based realization and circuit analysis of lateral RF MEMS series switch," in *Proc. IEEE -ICCCET*, pp. 5-10, Mar. 18-19, 2011.
- [23] Y. Mafinejad, A. Z. Kouzani, K. Mafinezhad, and A. Kaynak, "Low actuation wideband RF MEMS shunt capacitive switch," in *Proc. IWIEE, Procedia Engineering*, vol. 29, pp. 1292-1297, 2012.
- [24] S. Suganthi, K. Murugesan, and S. Raghavan, "CPW dependant loss analysis of capacitive shunt RF MEMS switch," *The Applied Computational Electromagnetic Society Journal*, vol. 31 no. 4, pp. 410-416, Apr. 2016.

Interference Effects of Via Interconnect in Three Layer Printed Circuit Board

Avali Ghosh, Sisir Kumar Das, and Annapurna Das

Guru Nanak Institute of Technology
JIS Group, 157/F, Nilgunj Road, Sodepur, Kolkata-700114, India
avalighosh@gmail.com, dean_gnit@jisgroup.org, director_gnit@jisgroup.org

Abstract — Cylindrical vias are commonly used for interconnection in multilayered Printed Circuit Board (PCB) design. The RF current through vias causes radiated interference to adjacent traces. This paper describes an analytical method of computing the radiation from cylindrical via using the electromagnetic theory. Three layer printed circuit board consisting of three traces on the top of a dielectric substrate, a middle orthogonal trace and a ground plane at the bottom, is considered. The RF voltage coupling at the terminations of the traces due to the near field radiation from the via is computed. The reactive couplings between the traces are determined from the parasitic elements using transmission line equations. The total coupling obtained from analytical method is compared with those of modeling and simulation with Ansoft HFSS software tool. The total crosstalk is also measured using an available Network Analyzer. A good agreement is found. The changes of radiated coupling with the change of position of via, trace separation and trace length are also investigated. This paper shows that the analytical method is a useful tool for predicting interference in PCB without using expensive simulation software.

Index Terms — Crosstalk, electromagnetic compatibility, PCB, transmission line, via, via inductance.

I. INTRODUCTION

Analysis of reactive cross-talk between the traces in multilayer printed circuit board is described by Paul [1] using transmission line theory and results are well documented. In multilayer PCB, vias are placed to interconnect signals from one layer to another. Their locations are optimized for desired circuit operation with signal integrity and Electromagnetic Compatibility (EMC). Very costly software tools are utilized for this purpose. The effects of via interconnects are analyzed by many authors [2-12]. Pucel [2] developed an empirical formula for via inductance using image concept. Goldfarb and Pucel [3] developed empirical formula for via inductance based on measurements and numerical simulation. Cui et al. [4] described EMI problem due to via transitions through the DC power bus. Li et al.

[5] and Suntives et al. [6] have shown shielding of interference between PCB traces using an array of vias in a trace. Nam et al. [7] shown EMI mitigation in PCB using shorting vias around the signal via. Ndip et al. [8] described techniques to solve electromagnetic reliability problem due to return current paths through via by introducing layer stack up scheme. Jiang and Fan [9] has given an intrinsic via circuit model through rigorous electromagnetic analysis. Wu and Fan [10] analytically predicted crosstalk among multiple vias between infinitely large parallel planes. Pan and Fan [11] given an equivalent multi-conductor transmission line model to characterize via structures in multi-layer PCBs for signal integrity in high speed digital circuits. Isidoro-Munoz et al. [12] presented closed-form expressions for the via-pad capacitance and via-traces inductance for the performance assessment and optimization of signal integrity. None of the above publications described the analysis of radiation from via and its effects on the adjacent lines. Some results of radiation coupling from via placed in a fixed position are presented by the authors in international conferences [14,15].

In this paper the effects of via (interconnect) in a three layer PCB are described along with the reactive crosstalk between the traces. The three layer board consists of three parallel traces (Trace1, 2 and 3) on the top of a FR4 dielectric substrate (copper clad FR4 glass epoxy, S3110, CEM-1), a second layer trace (Trace 4) which is orthogonal to the top traces, and a bottom layer of ground plane as shown in Fig. 1. The single layer thickness of the substrate is h and having dielectric constant ϵ_r . The trace 1 and trace 4 are interconnected through a thin cylindrical via of diameter d . The RF current through via radiates electromagnetic signal in the hybrid medium formed by the solid dielectric substrate and the air on the top. The radiated magnetic field produces induced RF current on the adjacent traces. The net current gives rise to interference voltage at the ports terminated with matched loads.

Since the via model considered here does not have pad, and the length is very small due to thin substrate, the equivalent circuit of the via is an inductance. This

unknown inductance is computed from the transmission line model of the traces and using Ansoft HFSS software tool. For excitation of trace 1, the RF current through via is found and the radiation from the via is determined using Helmholtz equation in spherical domain [16]. The total interference coupling at the ports of the adjacent traces is the sum of radiated coupling voltage and the reactive coupling voltage. The reactive coupling is computed using empirical formulae of parasitic inductance and capacitance given by Sakurai [13].

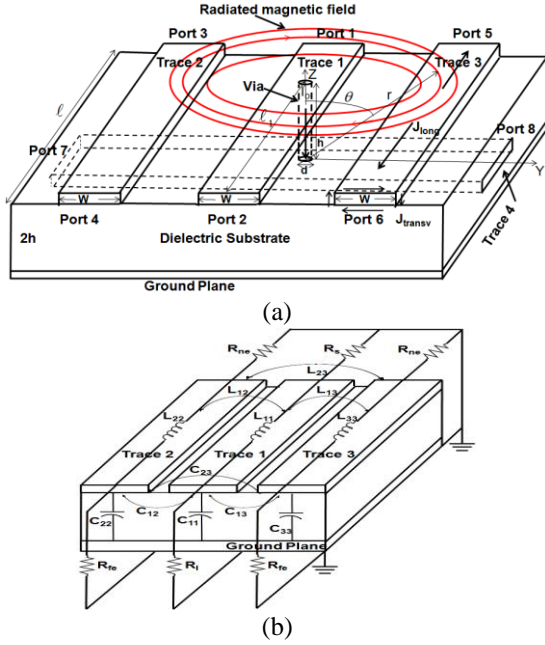


Fig. 1. Multilayer PCB structure: (a) via radiation coupling, and (b) reactive cross-talk coupling (via and orthogonal trace 4 are not shown).

The analytical values of the near field radiated coupling, reactive coupling and the total coupling are computed using MATLAB. Ansoft HFSS modeling and simulation of the structure is also done to find the resultant interference coupling on the traces at different frequencies for different locations of the via, trace length and trace spacing. Modeling and simulation results are compared with those obtained from analytical method and found good agreement. Experimental verification is also conducted for via position at the center of the trace along the length and results are found agreed well with those of simulation and analytical methods.

II. METHODS OF ANALYSIS

A. Analysis of radiation coupling from via RF current

As shown in Fig. 1, trace 1 is excited by RF current at Port 1. All the traces have width W and are matched

terminated by their characteristic impedances (50 ohm). A z -directed small via is a small dipole inside the substrate which radiates spherical waves in the hybrid medium around the via having non-zero field components E_r , E_θ and H_ϕ correspond to TM_r modes. Scalar magnetic potential A_r corresponding to these field components satisfies Helmholtz equations outside the via [16]:

$$\nabla^2 A_r + k^2 A_r = 0. \quad (1)$$

Here $k = k_0 \sqrt{\epsilon_e}$ in the hybrid medium consisting of dielectric substrate and air above it,

$$A_r = \frac{jkI_0h}{4\pi} \hat{H}_1^{(2)}(kr) P_1(\cos\theta), \quad (2)$$

and ϵ_e is the effective dielectric constant of the hybrid medium given by [17]:

$$\epsilon_e = \frac{\epsilon_r + 1}{2} + \frac{\epsilon_r - 1}{2} \left(1 + \frac{12h}{W}\right)^{-1/2}. \quad (3)$$

In (2) $\hat{H}_1^{(2)}(kr)$ is spherical Hankle function of 2nd kind, $P_1(\cos\theta)$ is Legendre polynomial of degree 1, and I_0 is RF current through via which will be determined from the via equivalent circuit and transmission line model of the traces.

Since the via is orthogonal to the traces on the top layer and on the middle layer, to a first degree of approximation, the scattering effects of these traces for the radiation from via is neglected. The magnetic field component H_ϕ induces transverse and longitudinal components of RF current on the surfaces of these traces. From (1) and (2), the radiated magnetic near field component:

$$H_\phi = -\frac{1}{r} \frac{\partial A_r}{\partial \theta} = \frac{jkI_0h}{4\pi r} \hat{H}_1^{(2)}(kr) \sin\theta. \quad (4)$$

Since the ground plane is considered as perfectly conducting, its effect on this emitted field is taken by replacing the ground plane with the image of the via (Fig. 2 (a)). The resultant radiated field component can be obtained from (4) for contributions of via and its image.

$$H_\phi = \frac{jkI_0h}{4\pi} \left[\frac{1}{r_1} \hat{H}_1^{(2)}(kr_1) \sin\theta_1 + \frac{1}{r_2} \hat{H}_1^{(2)}(kr_2) \sin\theta_2 \right]. \quad (5)$$

We can write [16]:

$$\hat{H}_n^{(2)}(kr) = \sqrt{\frac{\pi kr}{2}} H_{n+1/2}^{(2)}(kr), \quad (5a)$$

where $H_{n+1/2}^{(2)}(kr)$ is the cylindrical Hankle function.

From the geometry (Fig. 2 (a)), for field point $P(x, y, z)$,

$$r_1 = \sqrt{y^2 + (x - \ell_1)^2}, \quad (5b)$$

$$r_2 = \sqrt{r_1^2 + (3h)^2}, \quad (5c)$$

$$\theta_1 = \tan^{-1}\left(\frac{\ell_1}{2h}\right) \text{ and } \theta_2 = \pi - \theta_1, \quad (5d)$$

$$\cos\phi = \frac{-x}{r} = \frac{-x}{\sqrt{x^2 + y^2}}, \quad (5e)$$

$$\text{and } \cos\theta = \frac{(3/2)h}{r}. \quad (5f)$$

The induced surface current density on the top surface of the trace 2:

$$\vec{J}_{top} = \hat{z} x \hat{\phi} H_{\phi t} = -H_{\phi t} (\hat{x} \cos\phi + \hat{y} \sin\phi). \quad (6)$$

On the bottom surface of trace 2:

$$\vec{J}_{bottom} = -\hat{z} x \hat{\phi} H_{\phi b} = H_{\phi b} (\hat{x} \cos\phi + \hat{y} \sin\phi), \quad (7)$$

where suffices ϕt and ϕb represent top and bottom surfaces, respectively.

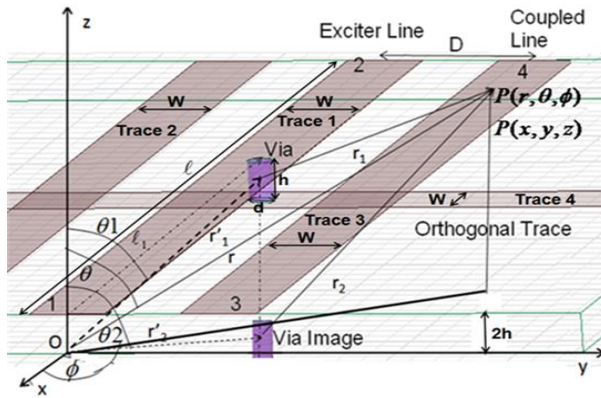


Fig. 2. Isometric view of the analytical model with via and its image below ground plane ($W=6.2\text{mm}$, $\ell_1=200\text{mm}$, $\ell_1=100\text{mm}$, $h=1.6\text{mm}$, $d=1\text{mm}$).

On the side outermost surface of trace 2:

$$\vec{J}_{rs} = \hat{y} x (\hat{\phi} H_{\phi}) = \hat{z} \sin\phi H_{\phi}. \quad (8)$$

On the side innermost surface of trace 2:

$$\vec{J}_{ls} = -\hat{y} x (\hat{\phi} H_{\phi}) = -\hat{z} \sin\phi H_{\phi}. \quad (9)$$

Therefore, it is seen that there is circulatory transverse current and also longitudinal current induced on the adjacent traces due to RF current through via along z . In PCB, the trace thickness is extremely small compare to width/wavelength. Therefore, in this analysis we can neglect the current on the side surfaces of the traces. The net current on top and bottom surfaces of the traces results in radiated coupling of signal at Ports 3, 4, 5 and 6 which can be obtained from (6) and (7). The resultant component of current density at P on a trace is given by:

$$J = \left| \vec{J}_{bottom} + \vec{J}_{top} \right| = H_{\phi b} - H_{\phi t}. \quad (10)$$

Therefore, the net current flow per unit length through adjacent victim trace can be expressed as:

$$I = \int_{D-W/2}^{D+W/2} (H_{\phi b} - H_{\phi t}) dy. \quad (11a)$$

The coupled voltages at ports are obtained by multiplying this current with port impedances $Z_L = Z_0$:

$$V = Z_L \times I. \quad (11b)$$

Equations (11a) and (11b) can be solved after determining the unknown excitation current I_0 through via.

B. Transmission line model of trace with equivalent circuit of via to find I_0

In general, the design of PCB is made using pad on a trace for connection of via with the associated trace. In this analytical model an assumption is made that the via with non-zero diameter $d \ll \lambda$ is connected between Trace 1 and 4 without pad. Therefore, the via offers an inductive path ($j\omega L_v$) as explained in Fig. 3 using transmission line model of the traces along with equivalent circuit of via, where L_v is the inductance of via.

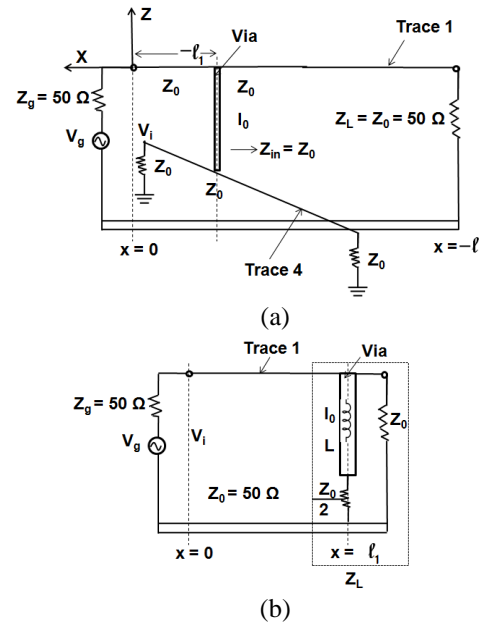


Fig. 3. (a) Equivalent circuit of via between traces 1 and 4, and (b) transformed equivalent circuit.

Considering a uniform lossless transmission line (Trace 1) of characteristic impedance $Z_0\Omega$ and length ℓ mm, excited at $x=0$ with a matched voltage source V_g , the equivalent load at the via point $x = -\ell_1$ is (Fig. 3),

$$Z_L = \frac{(j\omega L_v + Z_0/2)Z_0}{(j\omega L_v + Z_0/2) + Z_0}. \quad (12)$$

Based on formula developed by Pucel [2], the via inductance is given by:

$$L_v = \frac{\mu_0}{4\pi} \left[2h \cdot \ln \left(\frac{2h + \sqrt{\frac{d^2}{4} + (2h)^2}}{d/2} \right) + \left(\frac{d}{2} - \sqrt{\frac{d^2}{4} + (2h)^2} \right) \right]. \quad (13)$$

The line voltage at via point can be expressed by:

$$V(-\ell_1) = V_i (e^{+j\beta\ell_1} + \Gamma e^{-j\beta\ell_1}). \quad (14)$$

Here V_i = input signal voltage,

$$\beta = \frac{2\pi}{\lambda_e}, \quad \lambda_e = \frac{\lambda_0}{\sqrt{\epsilon_e}}, \quad \Gamma = \frac{Z_L - Z_0}{Z_L + Z_0}. \quad (15)$$

For excitation at Port 1, the via current can be calculated using (12) to (15) as:

$$I_0 = \frac{V(-\ell_1)}{j\omega L_v + Z_0/2}. \quad (16)$$

This I_0 is used in Equation 4 to find the radiated magnetic field and subsequently radiated coupling voltage at the trace end from (11a) and (11b).

C. Reactive and total coupling to the adjacent trace

There are direct crosstalk from the source trace to the adjacent parallel lines resulting in near end and far end cross-talk voltages due to reactive coupling. Since middle layer trace is orthogonal to top layer traces, there is no direct coupling to middle layer. The electrical equivalent circuit for inductive and capacitive coupling is shown in Fig. 1 (b).

At low frequency side of GHz range, crosstalk due to reactive coupling is well described by Paul [1] for lossless lines and are expressed by:

$$V_{ne} = \frac{j\omega R_{ne}}{(R_{ne} + R_{fe})(R_s + R_\ell)} [L_{12} + R_{fe} R_\ell C_{12}], \quad (17)$$

$$V_{fe} = \frac{j\omega R_{fe}}{(R_{ne} + R_{fe})(R_s + R_\ell)} [-L_{12} + R_{ne} R_\ell C_{12}], \quad (18)$$

where V_{ne} and V_{fe} are the reactive coupling due to via at Ports 3 and 4, respectively, $R_{ne} = R_{fe} = 50\Omega$, C_{12} and L_{12} are total mutual capacitance and inductance, respectively, per unit length. The capacitances and inductances are computed from the expressions given

by Sakurai [13]. The capacitance matrix can be written as:

$$[C] = \begin{bmatrix} (C_{11} + 2C_{12}) & -C_{12} & -C_{12} \\ -C_{12} & (C_{11} + C_{12}) & -C_{23} \\ -C_{12} & -C_{23} & (C_{11} + C_{12} + C_{23}) \end{bmatrix}, \quad (19)$$

where C_{ij} is the capacitance between the trace i and trace j , and C_{ii} is the capacitance between the trace i and the ground. Here $C_{23} = 0$ and $C_{12} = C_{13}$ for symmetry.

Since the inductance is not influenced by the lossless dielectric substrate the line inductance is derived from $[C]$ using the following relation:

$$[L] = \mu_0 \epsilon_0 [C]^{-1}. \quad (20)$$

The total coupled voltage at the port is the sum of the direct crosstalk voltage and the voltage due to radiation coupling from the via:

$$V_{31} = V_{r3} + V_{ne} \text{ and } V_{41} = V_{r4} + V_{fe}, \quad (21)$$

where, V_{r3} and V_{r4} are the radiated coupling due to via at Ports 3 and 4 respectively.

D. Simulation and Modeling

The PCB of Fig. 1 is simulated using Ansoft HFSS software with FR4 substrate having $\epsilon_r = 4.4$, $\tan \delta = 0.02$ and single layer thickness $h = 1.6\text{mm}$. All the traces have length 200mm, and are designed for 50 ohm impedance. The lines are matched terminated. A cylindrical via having diameter of 1mm, located at an arbitrary distance ℓ_1 from the input port, is used to connect the top source trace 1 and middle orthogonal trace 4. Ground plane is at the bottom of the substrate. The simulation and modeling in HFSS tool gives the true coupling, i.e., total coupling due to reactive cross talk and radiation coupling from RF current through via.

III. RESULTS

Following paragraphs describe the results obtained from the analytical, simulation and modeling using HFSS tool and experimental methods. Separate results are shown for radiation coupling, reactive coupling and total coupling (combined coupling due to radiation and reactive coupling).

A. Radiation coupling from via RF current

The radiated coupled voltage vs frequency at a Port 4 for 50 ohm termination is obtained from (11) and (16) using MATLAB, and the result is shown in Fig. 4, when via is placed at the middle along the length of the trace. The radiated couplings at all other ports can similarly be obtained.

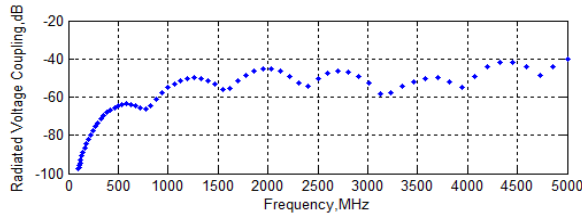


Fig. 4. Radiated coupled voltage vs. frequency using analytical method ($\ell = 200\text{mm}$, $\ell_1 = 100\text{mm}$).

B. Reactive and total coupling to the adjacent trace

The reactively coupled cross-talk voltages V_{ne} and V_{fe} are computed from (17) to (20), using MATLAB and the results are shown in Fig 5. It is seen that both the couplings increase with frequency.

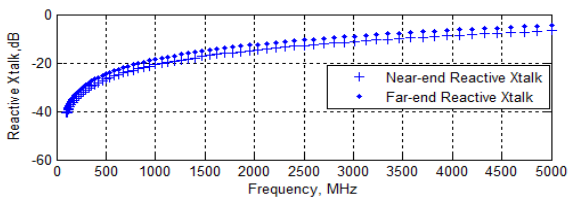


Fig. 5. Reactively coupled crosstalk voltages vs. frequency using analytical method ($\ell = 200\text{mm}$, $\ell_1 = 100\text{mm}$).

Finally, the total coupled voltage vs. frequency, expressed by (21), is shown in Fig. 6. It is seen from Fig. 4, Fig. 5 and Fig. 6, that the reactive coupling predominates coupling due to via radiation.

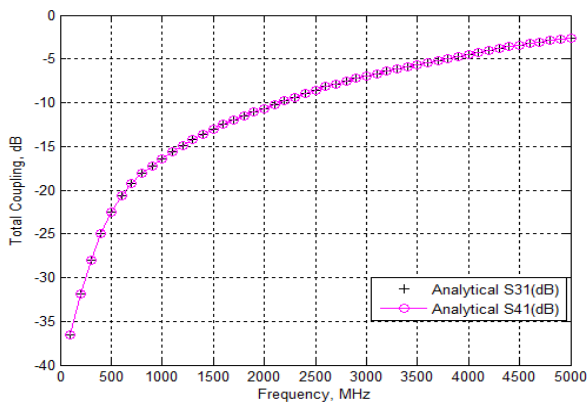


Fig. 6. Total coupled voltage vs. frequency using analytical method ($\ell = 200\text{mm}$, $\ell_1 = 100\text{mm}$).

C. Experimental and simulation results of coupling

The coupling parameters S31 (near-end) and S41 (far-end) are measured by using Rohde & Schwarz

ZVH4 Analyzer with the via at the center of the source trace as shown in Fig. 7.

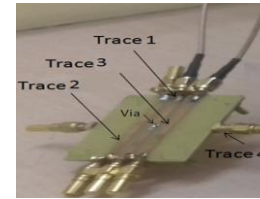


Fig. 7. PCB with via is at centre of Trace 1.

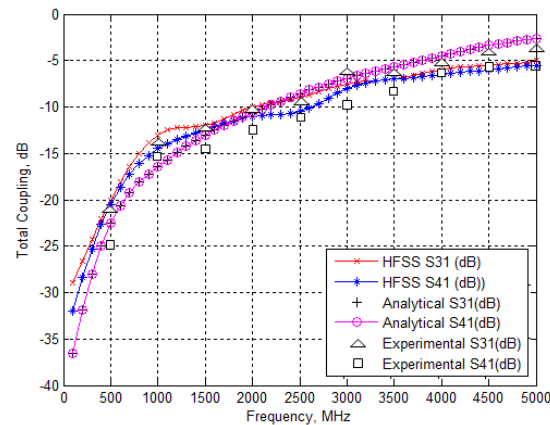


Fig. 8. Total coupled voltage vs. frequency (HFSS, analytical and experimental) when via is at centre of Trace 1.

The HFSS, analytical and experimental results of total coupled voltage at near end and far end ports of the adjacent victim trace versus frequency are compared and shown in Fig. 8. It is found that there is some deviation of 2-3 dB between the results which may be due to some assumptions made in the analytical method. At lower part of the frequencies, the deviation is slightly more. This may be due to the line losses which cannot be neglected at lower frequencies because propagation constant becomes complex and due to some experimental error.

D. Results of change in coupling with via position and line dimensions

The changes of radiated coupling with the other parameters, such as, (i) change of position of via, (ii) trace separation and (iii) trace length are investigated by using analytical method as discussed above. The effect of change of position of via on radiated coupling is shown in Fig. 9. It is observed that when the via is at the center along the length, then the radiated coupling voltage due to via is minimum and when it approaches towards the end of the traces, it increases.

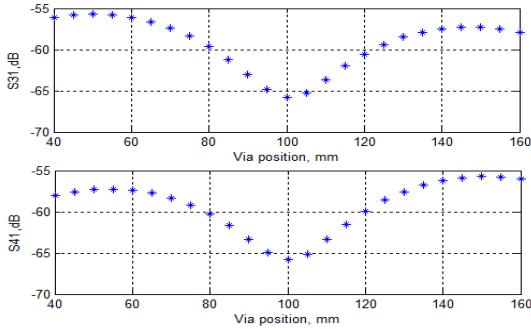


Fig. 9. Radiated coupling voltage vs. via position using analytical method.

The effect of trace length on radiated coupling is shown in Fig. 10. It is seen that when the length is increased the radiated coupling voltage is decreased.

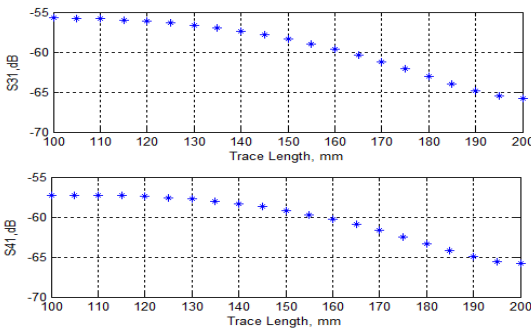


Fig. 10. Radiated coupling voltage vs. trace length using analytical method.

Figure 11 shows that when the trace separation is increased, the analytical results of radiated coupling voltage at different ports of the adjacent trace decrease with separation as expected.

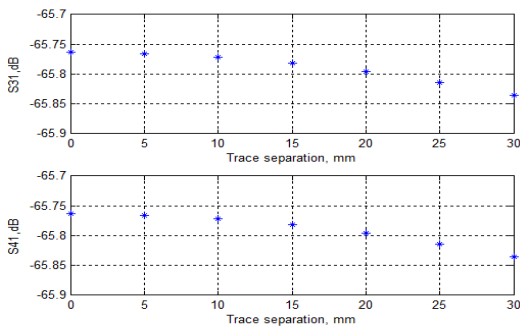


Fig. 11. Radiated coupling voltage vs. trace separation using analytical method.

The HFSS simulations are also carried out for (a) different positions of the via along the trace, (b) different trace lengths, and (c) different separation distances

between the traces. The simulated and analytical results of total coupling voltages at different ports of the traces for these cases are shown in Fig. 12 for two frequencies, 350 and 600 MHz. It is seen that the analytical results agree well with those of HFSS simulation and modeling with a maximum deviation of 15%.

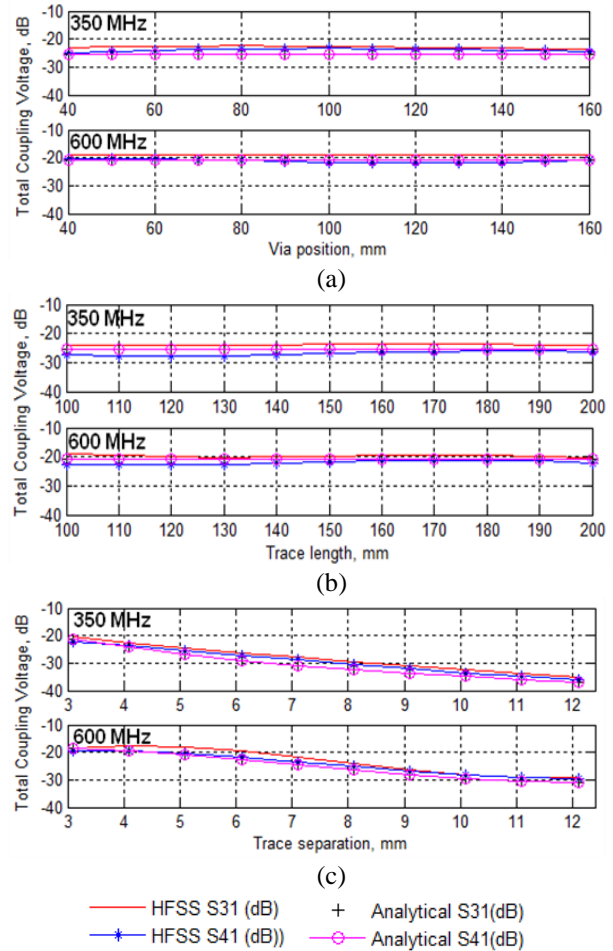


Fig. 12. Variation of coupling voltage: (a) with via position, (b) with trace length, and (c) with trace separation.

IV. DISCUSSION AND CONCLUSION

This paper describes radiation effect of via interconnect and reactive crosstalk between adjacent traces in a three layer PCB. The three layer PCB consists of three traces on the top, a middle orthogonal trace and a ground plane at the bottom. Centre trace 1 on the top layer is the source and interconnected to the orthogonal trace 4 through the via. The dielectric substrate used in the PCB is FR4-epoxy ($\epsilon_r = 4.4$). Each layer has thickness of 1.6mm. The traces are designed for 50 ohm impedance and terminated with matched loads. Analysis of radiation due to RF current through via is carried out using Helmholtz equation in spherical domain in hybrid

medium consisting of dielectric substrate and air on the top. The coupling of near field radiation from the via to the traces are calculated in terms of voltages due to the induced current on the traces. The total coupled voltage at a port is the sum of the radiated coupled voltage due to via radiation and the reactive crosstalk voltage from the adjacent traces due to line parasitic. It is seen that the reactive coupling is predominant over the radiated coupling voltage due to via.

Paper also describes the Ansoft HFSS analysis of the structure which takes care of both cross-talk due to reactive coupling between adjacent traces and radiated coupling due to via current. HFSS uses the Finite Element Method (FEM) in which automated adaptive meshing is generated. At the point of discontinuities smaller size of meshes and in the region of less complicated geometries, bigger meshes are generated. This helps to converge to the desired accuracy of the solution faster.

In general, total crosstalk increases with frequency. The via has little effect on the reactive coupling due to its small size and low values of inductance L_v . However, the effects of the variation in the position of via, change of trace length and trace separation, on the radiated coupling are also analytically investigated and verified with the help of HFSS simulation in this paper. It is seen that the position of the via alters the radiated coupling value giving a minimum when the via is at the center position of the trace length. It is observed that as the length and trace separation is increased, the radiation coupling from via is decreased.

The total crosstalk is measured using a network analyzer when the via is at the center of the length of the source trace 1. The overall observation shows that the results obtained with analytical and experimental methods have good agreement with a maximum deviation of 2-3 dB from those of HFSS simulation. The deviation of results may be due to some error in experimentation and assumptions made in the theory. The authenticity of the analytical work is verified by using very accurate modeling and simulation software tool Ansoft HFSS. However, deviation is maximum (> 5 dB) at lower parts of the frequency. This may be due to the line losses which are ignored in the theory. The analytical method described here shows that without using expensive software tools, interference coupling can be estimated applying electromagnetic theory.

REFERENCES

- [1] C. R. Paul, *Introduction to Electromagnetic Compatibility*. John Wiley & Sons, Inc., 1992.
- [2] R. Pucel, *Gallium Arsenide Technology*. D. Ferry, Ed., Indianapolis, IN: Howard W. Sams and Co., Ch. 6, pp. 216, 1985.
- [3] M. E. Goldfarb and R. A. Pucel, "Modeling via hole grounds in microstrip," *IEEE Microwave Guided Wave Letter*, vol. 1, no. 6, pp. 135-137, June 1991.
- [4] W. Cui, X. Ye, B. Archambeault, D. White, M. Li, and J. L. Drewniak, "EMI resulting from signal via transitions through the DC power bus," *2000 IEEE International Symposium on Electromagnetic Compatibility*, vol. 2, pp. 821-826, Aug. 21-25, 2000.
- [5] S. Li, Y. Liu, Z. Song, and H. Hu, "Analysis of crosstalk of coupled transmission lines by inserting additional traces grounded with vias on printed circuit boards," *Asia Pacific Conference on Environmental Electromagnetics, CEEM'2003*, Hangzhou, China, Nov. 4-7, 2003.
- [6] A. Suntives, A. Khajooeizadeh, and R. Abhari, "Using Via Fences for Crosstalk Reduction in PCB Circuits, 1-4244-0293-X/06/\$20.00(c) 2006 IEEE.
- [7] S. Nam, Y. Kim, J. H. Hur, S. Song, B. J. Lee, and J. Jeong, "Performance analysis of signal vias using virtual islands with shorting vias in multi-layer PCBs," *IEEE Transactions on Microwave Theory and Techniques*, vol. 54, no. 4, Part 11315-1324, June 2006.
- [8] I. Ndip, F. Ohnimus, S. Guttowski, and H. Reichl, "Modeling and analysis of return-current paths for microstrip-to-microstrip via transitions," *IEEE Electronic System-Integration Technology Conference (ESTC 2008)*, London, UK, Sep. 1-4, 2008.
- [9] Y.-J. Zhang and J. Fan, "An intrinsic circuit model for multiple vias in an irregular plate pair through rigorous electromagnetic analysis," *IEEE Trans. Microwave Theory Tech.*, vol. 58, no. 8, pp. 2251-2265, Aug. 2010.
- [10] S. Wu and J. Fan, "Analytical prediction of crosstalk among vias in multilayer printed circuit boards," *IEEE Transactions on Electromagnetic Compatibility*, vol. 54, no. 2, Apr. 2012.
- [11] S. Pan and J. Fan, "Characterization of via structures in multilayer printed circuit boards with an equivalent transmission-line model," *IEEE Transactions on Electromagnetic Compatibility*, vol. 54, no. 5, Oct. 2012.
- [12] A. Isidoro-Munoz, R. Torres-Torres, M. A. Tlaxcalteco-Matus, and G. Hernandez-Sosa, "Scalable models to represent the via-pad capacitance and via-traces inductance in multilayer PCB high speed interconnects," *2017 International Conference on Devices, Circuits and Systems (ICDCS)*, 2017.
- [13] T. Sakurai and K. Tamaru, "Simple formulas for two- and three-dimensional capacitances," *IEEE Transactions on Electron Devices*, vol. ED-30, no. 2, Feb. 1983.
- [14] A. Ghosh, S. K. Das, and A. Das, "Analysis of radiation coupling from via in multilayer printed

circuit board traces,” *14th International Conference on Electromagnetic Interference & Compatibility (INCEMIC 2016) and Workshop*, Bengaluru, India, Dec. 8-9, 2016. Electronic ISBN: 978-1-5090-5840-2. DOI: 10.1109/INCEMIC.2016.7921461

- [15] A. Ghosh, S. K. Das, and A. Das, “Analysis of crosstalk in high frequency printed circuit boards in presence of via,” *International Conference on Electromagnetics in Advanced Applications IEEE-APS Topical Conference on Antennas and Propagation in Wireless Communications 2017*, Verona, Italy, Sep. 11-15, 2017. Electronic ISBN: 978-1-5090-4451-1. DOI: 10.1109/ICEAA.2017.8065265
- [16] R. F. Harrington, *Time - Harmonic Electromagnetic Fields*. Donald G. Dudley, Series Editor, Wiley Publication.
- [17] C. A. Balanis, *Advanced Engineering Electromagnetics*. John Wiley & Sons, New York, 1989.



Avali Ghosh, obtained B.E degree from Nagpur University, M.Tech degree from West Bengal University of Technology (MAKAUT) and pursuing Ph.D degree in MAKAUT. Currently she is Assistant Professor in the Department of ECE, GNIT, Kolkata. She is Member of IEEE,

Life Member of ISTE and Society of EMC Engineers (India). Her current interests are microwaves and EMI/EMC.



Sisir Kumar Das, obtained B.Tech, M.Tech and Ph.D degrees from Calcutta University, IIT Kharagpur and Anna University, respectively, in India. He was Faculty in Delhi University during 1977-1980. Das led EMC evaluation and design of electronics products for 28 years under the ministry of communication and IT, Govt. of India, during 1980-2007. Presently he is Prof. and Dean – Research & Administration, GNIT, Kolkata. Das served as Associate Editor for IEEE EMC journal, USA (1994-2000) and now Chief Editor of EMC Journal of Society of EMC Engineers (India). He is Senior Member of IEEE.



Annapurna Das, obtained M.Sc. degree in Physics from University of Calcutta, M.Tech degree in Microwave Electronics and Ph.D degree in Electrical Engineering from the University of Delhi. She worked in the Department of ECE, Anna University during 1985-2007 as Professor. Presently she is Director of GNIT, Kolkata. She is the Life Member of Society of EMC Engineers (India) and ISTE, and Member of IEEE.

Data-Driven Arbitrary Polynomial Chaos for Uncertainty Quantification in Filters

Osama J. Alkhateeb and Nathan Ida

Department of Electrical and Computer Engineering
The University of Akron, Akron, Ohio 44325-3904
ida@uakron.edu

Abstract — A non-intrusive arbitrary polynomial chaos (aPC) method is applied to a problem of a band-stop filter with geometrical imperfections. The construction of aPC scheme only requires evaluating a finite number of moments, and does not involve assigning analytical probability density functions for the uncertain parameters of a stochastic model. Therefore, aPC is well suited for applications where the uncertain parameters are represented by raw data samples, as with the case of experimental measurements. The numerical examples show that the aPC approach is accurate even with a limited number of input samples.

Index Terms — Data-driven arbitrary polynomial chaos, generalized polynomial chaos, Monte Carlo sampling, uncertainty quantification.

I. INTRODUCTION

Methods of uncertainty quantification (UQ) have been widely used with computational electromagnetics (CEM) to address real-world problems that have probabilistic interpretation. Classically, the well-known Monte Carlo (MC) method is used to estimate the influence of the uncertain parameters on the output metrics of a stochastic model [1-3]. However, the MC method is a sampling method that requires large number of realizations to obtain accurate results. Therefore, in many cases applying the MC method is challenging, especially when incorporated with full-wave solvers. Alternatively, the generalized polynomial chaos (gPC) method [4,5] overcomes this drawback for a modest number of input parameters. In the gPC approach, the probability density function (PDF) of the output is interpolated by orthogonal polynomials defined uniquely for a given probability distribution. In [4], recursive relations of polynomial bases are provided for various types of parametric distributions.

Recently, Oladshkin and Nowak [6] introduced a moment-based polynomial chaos approach referred to as arbitrary polynomial chaos (aPC). The construction of the polynomial bases in aPC does not require an exact

knowledge of the input distributions and depends solely on the input moments. This allows aPC to be used with a broad range of applications, including applications with known input distributions (as in gPC), and with data-driven applications where only limited data samples are available (usually through measurements). Another advantage of aPC, is that since the input data are processed directly in the algorithm through the input moments, undesirable errors related to distribution fitting are avoided.

The objective of this paper is to introduce the non-intrusive aPC method [6] in uncertainty analysis of CEM applications. A band-stop filter based on an electromagnetic band gap (EBG) cell is considered as a model problem. The case studies address geometrical imperfections induced during the manufacturing process. This includes imperfections in the size and the corners of the EBG cell. To emphasize the data-driven concept, part of the work considers the treatment of limited input data sets.

II. MODEL PROBLEM

The notch filter considered in this paper consists of microstrip line suspended over a mushroom-type electromagnetic band gap (MSEBG) cell. The filter configuration is shown in Fig. 1. All the metals including the strip, the EBG cell, and the ground are assumed as perfect conductors. The filter is assumed to be placed in freespace. This is modelled by applying radiation boundary conditions (RBC) on a transparent box that encapsulates the computational domain. The size of the box is chosen such that its faces are located no less than a quarter-wave length from the filter, except at the two ends of the strip line, where waveports are placed to excite the structure. The resonance frequency (f_r) and the bandwidth (BW) are determined by computing the transmission coefficient (S_{12}). This is achieved here via 3D full-wave solver HFSS [9]. For a filter operating at $f_r = 94\text{GHz}$ and $\text{BW} = 7.62\text{GHz}$, the input parameters (see Fig. 1 (b)) are set as: $w = 0.21\text{mm}$, $\epsilon_1 = \epsilon_2 = 3.78$, $h_1 = h_2 = 1\text{mm}$, $r = 0.075\text{mm}$, and $t =$

0.05mm. Figure 2 shows the transmission coefficient of the filter with respect to frequency. BW is defined where S_{12} falls below -20 dB.

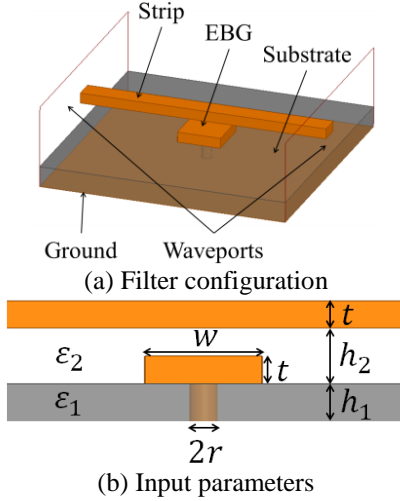


Fig. 1. Notch filter.

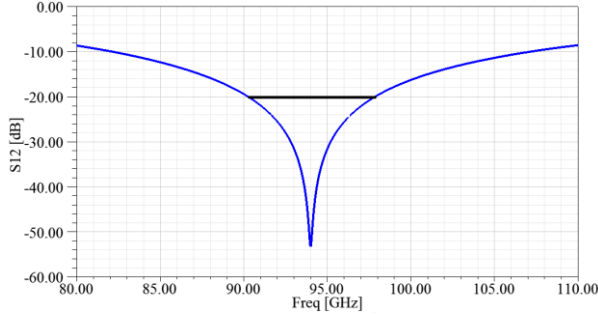


Fig. 2. S_{12} parameter.

III. STATISTICAL FRAMEWORK

A. Non-intrusive polynomial chaos

Consider a vector of independent random variables $\mathbf{x} = \{x_1, x_2, \dots, x_N\}$, defined on a sample space Ω , with a joint probability density function (PDF) $f_{\mathbf{x}}(\mathbf{x}) = \prod_{i=1}^N f_{x_i}(x_i)$. N is the dimension of \mathbf{x} and f_{x_i} is the marginal PDF of x_i . The k th moment of x_i is defined as:

$$\mu_{k,i} = \int_{\Omega_i} x_i^k f_{x_i}(x_i) \partial x. \quad (1)$$

However, in some problems f_{x_i} is not known and only M number of x_i samples is available. In this case the moments are given by:

$$\mu_{k,i} = \frac{1}{M} \sum_{j=1}^M x_{i,j}^k. \quad (2)$$

Let $y = g(\mathbf{x})$ be the model under consideration. x_i represents an input under uncertainty such as the geometrical sizes and the electrical parameters of the filter, while y represents an output of interest, i.e., the resonance frequency or the bandwidth. y can be approximated by the expansion:

$$y(\mathbf{x}) = y(x_1, x_2, \dots, x_N) = \sum_{i=0}^{P_{\text{out}}} \alpha_i \Phi_i(x_1, x_2, \dots, x_N), \quad (3)$$

where α_i are unknown coefficients, and P_{out} refers to the number of terms included in the expansion. Φ_i forms a set of multidimensional orthogonal polynomials with respect to $f_{\mathbf{x}}(\mathbf{x})$:

$$\langle \Phi_i, \Phi_j \rangle = \int_{\Omega} \Phi_i(\mathbf{x}) \Phi_j(\mathbf{x}) f_{\mathbf{x}}(\mathbf{x}) \partial \mathbf{x} = \|\Phi_i\|^2 \delta_{i,j}. \quad (4)$$

Based on the orthogonality condition in Eq. (4), the coefficients α_i can be determined by the spectral projection method:

$$\alpha_i = \frac{\langle y, \Phi_i \rangle}{\|\Phi_i\|^2}. \quad (5)$$

The expression in (5) is usually handled by Gaussian quadrature. However, with data-driven applications the locations of the Gaussian weights would vary with different realizations of input sample sets. This can be challenging, especially when full-wave solvers are used to evaluate the system response at these points. In a more convenient method, α_i can be determined from $P_{\text{out}} + 1$ fixed collocation points as:

$$\begin{bmatrix} \Phi_0(\mathbf{x}_0) & \Phi_1(\mathbf{x}_0) & \dots & \Phi_{P_{\text{out}}}(\mathbf{x}_0) \\ \Phi_0(\mathbf{x}_1) & \Phi_1(\mathbf{x}_1) & \dots & \Phi_{P_{\text{out}}}(\mathbf{x}_1) \\ \vdots & \vdots & \ddots & \vdots \\ \Phi_0(\mathbf{x}_{P_{\text{out}}}) & \Phi_1(\mathbf{x}_{P_{\text{out}}}) & \dots & \Phi_{P_{\text{out}}}(\mathbf{x}_{P_{\text{out}}}) \end{bmatrix} \begin{bmatrix} \alpha_0 \\ \alpha_1 \\ \vdots \\ \alpha_{P_{\text{out}}} \end{bmatrix} = \begin{bmatrix} y(\mathbf{x}_0) \\ y(\mathbf{x}_1) \\ \vdots \\ y(\mathbf{x}_{P_{\text{out}}}) \end{bmatrix}, \quad (6)$$

with $\mathbf{x}_0 = \{x_{1,i}, x_{2,i}, \dots, x_{N,i}\}$. The mean and the variance of y satisfy:

$$\mu_y = \alpha_0 \|\Phi_0\|, \quad \sigma_y^2 = \sum_{i=1}^{P_{\text{out}}} \alpha_i^2 \|\Phi_i\|^2. \quad (7)$$

B. Construction of orthogonal polynomials for an arbitrary distribution.

As already mentioned aPC is a moment-based method. Therefore, the next step is to express the polynomial basis Φ_i in terms of the statistical moments of \mathbf{x} . To do so we first write Φ_i in terms of univariate orthogonal polynomials using a multi-index I_j^i as:

$$\Phi_i(x_1, x_2, \dots, x_N) = \sum_{j=1}^N P_j^{(I_j^i)}(x_j). \quad (8)$$

$P_j^{(k)}$ refers to the j th univariate polynomial of degree k . It has the form:

$$P_j^{(k)}(x_j) = \sum_{i=0}^k p_{i,j}^{(k)} x_j^i, \quad (9)$$

with $p_{i,j}^{(k)}$ being the polynomial coefficients. In [6], it is shown that with straight forward algebra Eqs. (1), (2), and (4) can be used to find the coefficients $p_{i,j}^{(k)}$ in terms of the input moments. This relation is given by the matrix:

$$\begin{bmatrix} \mu_{0,j} & \mu_{1,j} & \dots & \mu_{k,j} \\ \mu_{1,j} & \mu_{2,j} & \dots & \mu_{k+1,j} \\ \vdots & \vdots & \ddots & \vdots \\ \mu_{k-1,j} & \mu_{k,j} & \dots & \mu_{2k-1,j} \\ 0 & 0 & 0 & 1 \end{bmatrix} \begin{bmatrix} p_{0,j}^{(k)} \\ p_{1,j}^{(k)} \\ \vdots \\ p_{k-1,j}^{(k)} \\ p_{k,j}^{(k)} \end{bmatrix} = \begin{bmatrix} 0 \\ 0 \\ \vdots \\ 0 \\ 1 \end{bmatrix}. \quad (10)$$

The moment matrix in Eq. (10) may become ill-conditioned when high order polynomials are required. One way to reduce the order of the polynomials without affecting the accuracy of the solutions is by using the multi-element approach [7,8].

C. Error estimation

In data-driven applications an input variable x_i is given as a set of M samples. The l -th realization of the input sample set can be represented as:

$$x_i(l) = \{x_{i,1}(l), x_{i,2}(l), \dots, x_{i,M}(l)\}, \quad l = 1, 2, \dots, L, \quad (11)$$

where L is the total number of realizations. Let $Z_{Approx}(l)$ be an output measure computed for the l -th realization. According to the central limit theorem when both M and L are big Z_{Approx} can be approximated by a normal distribution with a mean value $\mu_{Z_{Approx}}$ and a standard deviation $\sigma_{Z_{Approx}}$. Given that, the relative error of the output satisfy the bound:

$$P_r \left(\epsilon \leq \frac{\max\{\|\mu_{Z_{Approx}} \pm 3\sigma_{Z_{Approx}}\| - Z_{Exact}\}}{Z_{Exact}} \right) = 0.9973. \quad (12)$$

P_r and ϵ refer to the probability operator and the relative error of the output, respectively. Z_{Exact} is computed by the exact distribution. In a simpler form the error in Eq. (12) can be approximated by the expression:

$$\epsilon \approx \frac{\max\{\|\mu_{Z_{Approx}} \pm 3\sigma_{Z_{Approx}}\| - Z_{Exact}\}}{Z_{Exact}}. \quad (13)$$

IV. NUMERICAL EXAMPLES

A. Uncertainty in width

First we consider variations in the patch size w (see Fig. 1 (b)). In this case w follows a normal distribution $w \sim N(\mu_w, \sigma_w^2)$, truncated at $3\sigma_w$, i.e., $\Delta w = \pm 3\sigma_w \cdot \mu_w$ and the other parameters of the filter are fixed at the values provided in Section II. Figure 3 shows the maximum relative error obtained for the expected value and the standard deviation of the model outputs vs. number of input samples computed at $P_{out} = 2$ and $\Delta w = \pm 0.1t$ (t is the patch thickness). As the convergence rate in both cases is of order ~ 0.5 , it is clear that the error is due to the statistical sampling used to generate the input sets. However, the results show that acceptable accuracies are achievable with relatively small input sets ($100 \leq M \leq 1000$). For this example, Eq. (6) shows that only 3 input points are required to obtain the model coefficients. Thus, it is clear that the time consumption in aPC is substantially lower when compared with Monte Carlo simulations.

B. Uncertainty in corners

In this second example we study imperfections in the corners of the patch. To do so, a corner is

approximated by a cylinder of radius r_i , where $i = 1, 2, \dots, 4$. The configuration of this problem is shown in Fig. 4. The radius of the cylinders is assumed to follow a normal distribution $r_i \sim N(0, w^2/16)$, truncated on $[0, 3w/4]$.

The univariate polynomials used in this example are of order 2. Since this is 4-th dimensional problem, the system response in Eq. (6) is computed at 15 points (i.e., $P_{out} = 15$). Figure 5 shows the maximum relative error obtained for the expected value and the standard deviation of the model outputs vs. the total number of input samples generated for the 4 corners. As in the previous example the output error in this case study is also dominated by the sampling process (i.e., the convergence rate is of order ~ 0.5). The results here also show that good accuracies can be achieved with a relatively small number of input samples.

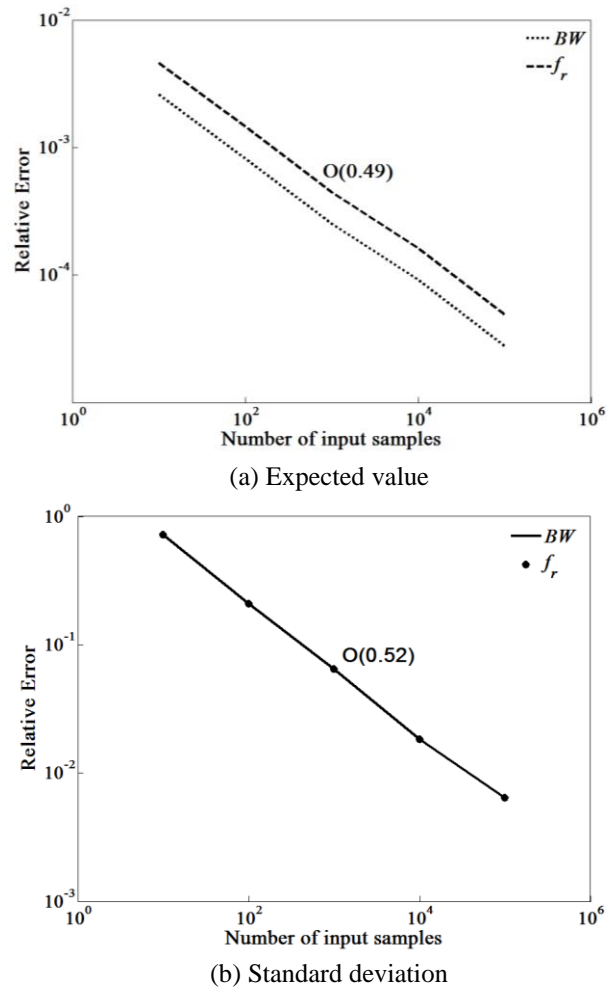


Fig. 3. Convergence rate of expected value and standard deviation vs. number of w samples, with $\Delta w = \pm 0.1t$ and $P_{out} = 2$.

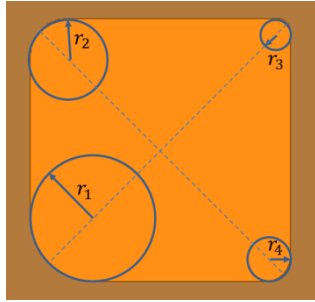


Fig. 4. MSEBG patch with imperfections in corners.

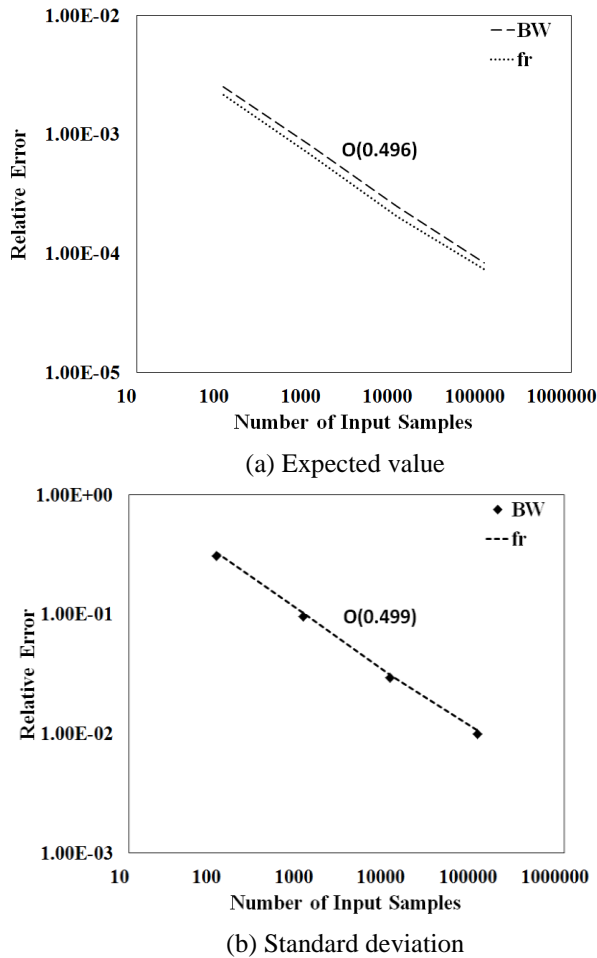


Fig. 5. Convergence rate of expected value and standard deviation vs. the total number of r_i samples, with $i = 4$ and $P_{out} = 15$.

V. CONCLUSION

A procedure based on data-driven arbitrary polynomial chaos (aPC) is introduced for uncertainty quantification (UQ) in filters. The filter imperfections are presented in terms of data samples. The main advantage of using this procedure is that the construction of the chaos polynomials is done by evaluating the input

moments directly from the input samples without necessarily knowing the input distributions. In this work the samples are provided by distribution sampling. However, in real-world problems they are obtained by measurements. The aPC approach is validated with a model problem of a band stop filter. Two case studies addressing geometrical imperfections induced during the manufacturing process are considered. The results show that even with low-order polynomials the accuracy of the approach is dominated by sampling process. Therefore, the convergence rate of this approach is of order ~ 0.5 .

REFERENCES

- [1] C. Chauvière, J. S. Hesthaven, and L. Lurati, "Computational modeling of uncertainty in time-domain electromagnetics," *SIAM Journal on Scientific Computing*, vol. 28, no. 2, pp. 751-775, Feb. 2006.
- [2] W. Ng, J. Li, S. Godsill, and J. Vermaak, "Tracking variable number of targets using sequential Monte Carlo methods," *13th European Signal Processing Conference*, pp. 1-4, Sept. 2005.
- [3] J. F. G. d. Freitas, M. Niranjana, A. H. Gee, and A. Doucet, "Sequential Monte Carlo methods to train neural network models," *Neural Computation*, vol. 12, no. 4, pp. 955-993, Apr. 2000.
- [4] D. Xiu and G. Em Karniadakis, "The Wiener-Askey polynomial chaos for stochastic differential equations," *SIAM Journal on Scientific Computing*, vol. 24, no. 2, pp. 619-644, 2002.
- [5] D. Xiu and G. Em Karniadakis, "Modeling uncertainty in steady state diffusion problems via generalized polynomial chaos," *Computer Methods in Applied Mechanics and Engineering*, vol. 191, no. 43, pp. 4927-4948, 2002.
- [6] S. Oladyshkin and W. Nowak, "Data-driven uncertainty quantification using the arbitrary polynomial chaos expansion," *Reliability Engineering & System Safety*, vol. 106, pp. 179-190, 2012.
- [7] X. Wan and G. Em Karniadakis, "Multi-element generalized polynomial chaos for arbitrary probability measures," *SIAM Journal on Scientific Computing*, pp. 901-928, 2006.
- [8] X. Wan and G. Em Karniadakis, "An adaptive multi-element generalized polynomial chaos method for stochastic differential equations," *Journal of Computational Physics*, vol. 209, no. 2, pp. 617-642, 2005.

ANSYS HFSS, 3D Full-wave Electromagnetic Field Simulation by Ansoft.